HRVATSKO DRUŠTVO
ZA STROJARSKE TEHNOLOGIJE

CROATIAN SOCIETY
FOR MECHANICAL TECHNOLOGIES

In association with:

University of Split
Faculty of Electrical Engineering, Mechanical Engineering and Naval Architecture

Slovak Academy of Science
Institute of Materials and Machine Mechanics

University of Split
University Department of Professional Studies

Croatian Society for Materials and Tribology

Dublin Institute of Technology

Rogante Engineering Office

ISSN 1847-7917

10th International Conference

Mechanical Technologies and Structural Materials 2021

General sponsors:
University of Split - FESB,
The Split - Dalmatia County,
The City of Split,
EVN Croatia Plin d.o.o.

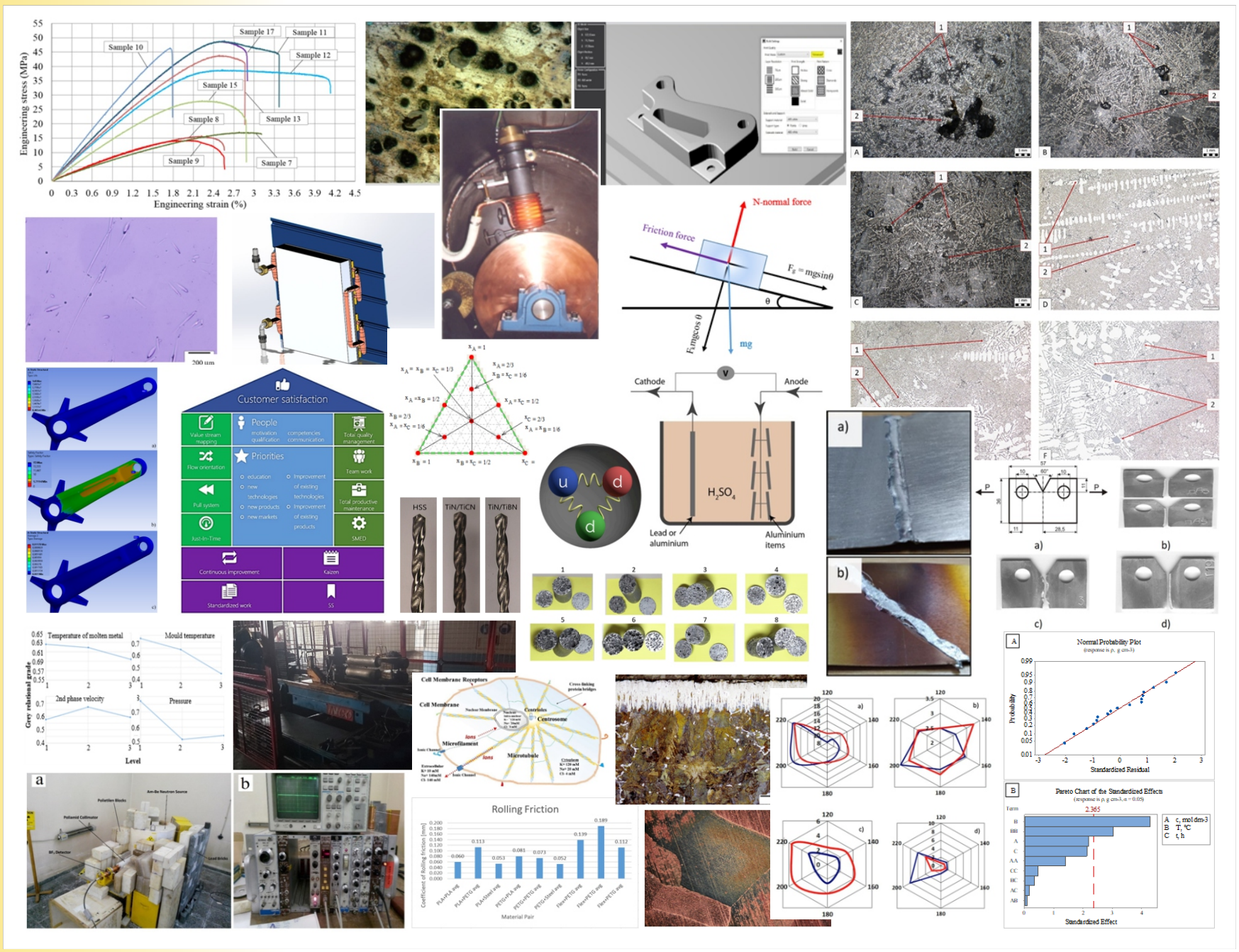

http://www.strojarska-tehnologija.hr

September, 23rd - 24th, 2021.
FESB, Ruđera Boškovića 32, Split

CONFERENCE PROCEEDINGS

MECHANICAL TECHNOLOGIES AND STRUCTURAL MATERIALS

Split

Croatia

23 - 24 September 2021

ORGANIZED BY:

CROATIAN SOCIETY FOR MECHANICAL TECHNOLOGIES, Croatia

CO-ORGANIZERS:

UNIVERSITY OF SPLIT
FACULTY OF ELECTRICAL ENGINEERING, MECHANICAL ENGINEERING AND NAVAL ARCHITECTURE

CROATIAN SOCIETY FOR MATERIALS AND TRIBOLOGY

DUBLIN INSTITUTE OF TECHNOLOGY

SLOVAK ACADEMY OF SCIENCE INSTITUTE OF MATERIALS AND MACHINE MECHANICS

ROGANTE ENGINEERING OFFICE

UNIVERSITY OF SPLIT
UNIVERSITY DEPARTMENT OF PROFESSIONAL STUDIES

SPONSORS:

UNIVERSITY OF SPLIT

SPLIT – DALMATIA COUNTY

CITY OF SPLIT

EVN CROATIA PLIN d.o.o.

TOURIST BOARD OF SPLIT

PUBLISHER:

CROATIAN SOCIETY FOR MECHANICAL TECHNOLOGIES, Croatia

HRVATSKO DRUŠTVO ZA STROJARSKE TEHNOLOGIJE, Hrvatska

c/o FESB, Ruđera Boškovića 32, 21000 SPLIT

tel.: +385 21 305 910; fax.: +385 21 463 877

e-mail: info@strojarska-tehnologija.hr

http://www.strojarska-tehnologija.hr

EDITORS:

PhD Sonja Jozić, Associate Professor
PhD Branimir Lela, Associate Professor
PhD Nikola Gjeldum, Assistant Professor

ISSN 1847-7917

ISSUE: 70

ORGANIZING COMMITTEE:

- Nikša Čatipović (Croatia) - Chairman
- Zvonimir Dadić (Croatia) – Vice Chairman

- Ante ALUJEVIĆ (Croatia)
- Amanda ALJINOVIĆ (Croatia)
- Andrej BAŠIĆ (Croatia)
- Marina CRNJAC ŽIŽIĆ (Croatia)
- Ivana DUMANIĆ (Croatia)
- Igor GABRIĆ (Croatia)
- Nikola GJELDUM (Croatia)
- Karla GRGIĆ (Croatia)
- Jure KROLO (Croatia)
- Petar LJUMOVIĆ (Croatia)
- Zvonimir MRDULJAŠ (Croatia)
- Stipe PERIŠIĆ (Croatia)
- Slaven ŠITIĆ (Croatia)

PROGRAMME AND REVIEW COMMITTEE:

- Dražen ŽIVKOVIĆ (Croatia) – President
- Dražen BAJIĆ (Croatia) – Vice President

- Boris ANZULOVIĆ (Croatia)
- Frane BARBIR (Croatia)
- Franjo CAJNER (Croatia)
- Goran CUKOR (Croatia)
- Krešimir GRILEC (Croatia)
- Dario ILJKIĆ (Croatia)
- Vinko IVUŠIĆ (Croatia)
- Zlatko JANKOSKI (Croatia)
- Jaroslav JERZ (Slovakia)
- Sonja JOZIĆ (Croatia)
- David KENNEDY (Ireland)
- Branimir LELA (Croatia)
- Zoran PANDILOV (Macedonia)
- Mladen PERINIĆ (Croatia)
- Massimo ROGANTE (Italy)
- Zdravko SCHAUPERL (Croatia)
- František SIMANČIK (Slovakia)
- Božo SMOLJAN (Croatia)
- Goran ŠIMUNOVIĆ (Croatia)
- Katica ŠIMUNOVIĆ (Croatia)
- Matej VESENJAK (Slovenia)
- Ivica VEŽA (Croatia)

Mechanical Technologies and Structural Materials MTSM2021

CONTENT

1. ***Andrej BAŠIĆ, Ivan PEKO, Jure KROLO, Petra BAGAVAC***
FUZZY LOGIC MODELING OF ULTIMATE TENSILE STRENGTH AND COST IN FUSED DEPOSITION MODELING PROCESS OF ADDITIVE MANUFACTURING 1

2. ***Nikša ČATIPOVIĆ, Dražen ŽIVKOVIĆ, Karla GRGIĆ, Petar LJUMOVIĆ, Josip PERINIĆ, Zvonimir DADIĆ***
THE INFLUENCE OF FURNACE ATMOSPHERE DURING AUSTENITIZATION ON MICROSTRUCTURE AND HARDNESS OF AUSTEMPERED DUCTILE IRON 11

3. ***Nikša ČATIPOVIĆ, Hasan AVDUŠINOVIĆ, Karla GRGIĆ, Petar LJUMOVIĆ, Josipa ŽIVALJIĆ, Zvonimir DADIĆ***
THE INFLUENCE OF SUBSEQUENT HIGH TEMPERATURE TEMPERING ON TENSILE STRENGTH AND ELONGATION OF AUSTEMPERED DUCTILE IRON 19

4. ***Nikša ČATIPOVIĆ, Nikola GJELDUM, Andrej BAŠIĆ, Ante TURKOVIĆ, Zvonimir DADIĆ***
USING REVERSE ENGINEERING FOR OPTIMIZATION AND MODELING OF MOTORCYCLE BRAKE CALIPER BRACKETS 23

5. ***Ivana DUMANIĆ, Sonja JOZIĆ, Deni DUMANIĆ, Luka NIMAC***
DESIGN AND IMPROVEMENT OF HIGH PRESSURE DIE CASTING PROCESS BASED ON NOVAFLOW&SOLID SOFTWARE 29

6. ***Arun GOPINATHAN, Jaroslav JERZ, Jaroslav KOVÁČIK***
STUDY OF HEAT TRANSFER CHARACTERISTICS OF ALUMINIUM FOAM FOR PCM-BASED THERMAL ENERGY STORAGE APPLICATIONS 35

7. ***Stanislav GYOSHEV, Nikolay STOIMENOV, Miglena PANEVA***
DETERMINATION OF THE FRICTION COEFFICIENT OF 3D PRINTED MATERIALS - PART II: SLIDING FRICTION 43

8. ***Aida IMAMOVIĆ, Mirsada ORUČ, Mustafa HADŽALIĆ, Admir MUMINOVIĆ, Amra TALIĆ –ČIKMIŠ, Fuad HADŽIKADUNIĆ***
SLAG AS AN IMPORTANT WASTE FOR RECYCLING 47

9. ***Jaroslav JERZ, Arun GOPINATHAN, Anton PUŠKÁR, Daniel SZABÓ, Jaroslav KOVÁČIK***
STRUCTURAL DESIGN OF THERMO-ACTIVE ALUMINIUM FOAM ROOFING 53

10. ***Borut KOSEC, Blaž KARPE, Mirko GOJIĆ, Aleš NAGODE, Ladislav VRSALOVIĆ, Stjepan KOŽUH, Ivana IVANIĆ, Matija ZORC, Milan BIZJAK***
THERMAL PROPERTIES OF COPPER BASE SHAPE MEMORY ALLOY 59

11. ***Maryna KOSTYKOVA, Larysa KOZACHOK, Andrii LEVTEROV, Anna PLEKHOVA, Viktoriia SHEVCHENKO, Anton OKUN***
A HEURISTIC METHOD FOR AN APPROXIMATE SOLUTION OF THE KNAPSACK PROBLEM 63

12. ***Franjo Kozina, Zdenka Zovko Brodarac, Barbara Tubić Bulat, Franjo Dominković***
THE IMPACT OF MELT RETENTION TIME ON THE STRONTIUM MODIFICATION EFFICIENCY 67

13. ***Jure KROLO, Zvonimir DADIĆ, Nikša ČATIPOVIĆ, Tin DOŽDOR***
ALUMINIUM WASTE REDUCTION IN AUTOMOTIVE COMPOSITE WEATHER STRIP SEAL MANUFACTURING 75

14. ***Olena KUZMENKO, Victor KUZMENKO, Anton OKUN***
FACTORS DETERMINING THE DURABILITY OF COLD EXTRUSION DIES 81

15. ***Darko LANDEK, Gorana BARŠIĆ***
WEAR OF SPIRAL DRILLS COATED BY HARD PACVD COATINGS 87

16. ***Darko LANDEK, Lidija ĆURKOVIĆ, Ivana GABELICA, Irena ŽMAK***
OPTIMIZATION OF VISCOSITY OF HIGHLY CONCENTRATED ALUMINA SUSPENSIONS FOR SLIP CASTING BY SURFACE RESPONSE METHODOLOGY 91

17. ***Branimir LELA, Jure KROLO, Karla GRGIĆ, Sonja JOZIĆ, Ivana DUMANIĆ***
PRODUCTION OF CLOSED CELL FOAMS FROM THE ALUMINIUM CHIP WASTE 95

18. ***Petar LJUMOVIC, Inoslav SVALINA, Igor GABRIC, Anela BARBARIC***
ALUMINIUM AND ALUMINIUM ALLOYS SURFACE PROTECTION BY THE USE OF ANODIZATION TECHNOLOGY 101

19. ***Marko MLADINEO, Marijan ĆUBIĆ, Nikola GJELDUM, Marina CRNJAC ŽIŽIĆ***
HUMAN-CENTRIC APPROACH OF THE LEAN MANAGEMENT AS AN ENABLER OF INDUSTRY 5.0 IN SMES 111

20. ***Sviatoslav MOTRUNICH, Anatoliy POKLATSKY, Ilya KLOCHKOV, Massimo ROGANTE, Anatoliy ZAVDOVEEV***
BASIC ADVANTAGES OF THIN-SHEET AA5056 ALLOY JOINTS PRODUCED BY FRICTION STIR WELDING 119

21. ***Miglena PANEVA, Peter PANEV, Nikolay STOIMENOV***
ROUGHNESS OF LOW CARBON STEEL AFTER COLD ROLLING OF REVERSING MILL 700 125

22. ***Massimo ROGANTE, Osman GENCEL, Erol KAM, Tuncay TUNA***
INVESTIGATION OF THE SHIELDING ABILITY OF CONCRETE SAMPLES REINFORCED WITH B4C AND IRON FILLINGS AGAINST NEUTRON RADIATION 129

23. ***Massimo ROGANTE, Franco G. CESARI, Massimo GIORGI***
DECOMMISSIONING OF NUCLEAR FACILITIES: GENERAL CONSIDERATIONS AND SUGGESTIONS NOT REGARDING ACTIVATED PARTS 133

24. ***Ivana ROPUŠ, Hrvoje CAJNER, Lidija ĆURKOVIĆ***
OPTIMIZATION OF DENSITY OF MICROWAVE SINTERED ALUMINA CERAMICS DUE TO THE CORROSION IN NITRIC ACID 139

25. ***Claudio SANTELLI***
CELL CYTOSKELETON STRUCTURE AND CONDUCTION OF ENVIRONMENTAL BIOPHYSICAL SIGNALS THROUGH MICROTUBULES AND MICROFILAMENTS 145

26. ***Nikolay STOIMENOV, Stanislav GYOSHEV, Miglena PANEVA, Peter PANEV***
DETERMINATION OF THE FRICTION COEFFICIENT OF 3D PRINTED MATERIALS PART I – ROLLING FRICTION 149

27. ***Kenan VARDA, Ernad BEŠLAGIĆ, Josip KAČMARČIK, Nermina ZAIMOVIĆ-UZUNOVIĆ***
FATIGUE NUMERICAL ANALYSIS COMPARISON ON BICYCLE PEDAL EXAMPLE USING DIFFERENT SOFTWARE 153

28. ***Ivan VIDAKOVIĆ, Goran HEFFER, Katica ŠIMUNOVIĆ, Goran ROZING***
APPLICATION OF HEAT TREATMENT IN WEAR PROTECTION FOR WORKING PARTS OF AGRICULTURAL MACHINERY 159

29. ***Ladislav VRSALOVIĆ, Senka GUDIĆ, Radosna JERČIĆ, Ivana IVANIĆ, Stjepan KOŽUH, Mirko GOJIĆ***
THE INFLUENCE OF CHLORIDE CONCENTRATION END ELECTROLYTE TEMPERATURE ON CuAlMnZn ALLOY CORROSION IN NaCl SOLUTION 165

30. ***Anatoliy ZAVDOVEEV, Massimo ROGANTE, Valeriy POZNYAKOV, Mark HEATON, Thierry BAUDIN, Alexander GAYVORONSKI, Yuriy DEMCHENKO, Serj ZHDANOV***
INFLUENCE OF PULSE CURRENT ARC WELDING MODES ON CHANGING THE PARAMETERS OF THE WELD AND HAZ OF WELDED JOINTS MADE BY LOW ALLOYED MATERIALS 171

ISSN 1847-7917

Fuzzy logic modeling of ultimate tensile strength and cost in fused deposition modeling process of additive manufacturing

***Andrej BAŠIĆ*[1)], *Ivan PEKO*[2)], *Jure KROLO*[1)], *Petra BAGAVAC*[1)]**

1) University of Split, Faculty of Electrical Engineering, Mechanical Engineering and Naval Architecture, Department for Production Engineering
Sveučilište u Splitu, Fakultet elektrotehnike, strojarstva i brodogradnje, R. Boskovica 32, 21 000 Split, **Croatia**
2) Magna Steyr, Liebenauer Hauptstraße 317, Graz, **Austria**

andrej@fesb.hr
ipeko@fesb.hr
Jure.Krolo@fesb.hr
Petra.Strizak@fesb.hr

Keywords

Additive manufacturing
Fuzzy logic modeling
Tensile strength
Cost

Original scientific paper

Abstract: Additive manufacturing is the modern technology that uses a computer-aided design product data to create its real physical replica. In the industry already exist a vast number of different additive manufacturing processes that use various types of materials, from polymers to metals, to create new products and prototypes. Fused deposition modeling (FDM) is one of the well-known additive manufacturing processes. It is able to create products that can be treated and used further in the manufacturing process. These products have very acceptable mechanical properties. These properties mostly depend and vary according to process parameters values and can be optimized by setting process parameters on appropriate levels. In this paper, a fuzzy logic modeling approach was used to analyze the influence of variable process parameters: top and bottom surface layers' number, fill spacing, and layer resolution on ultimate tensile strength and manufacturing cost. Experiments were conducted on the PLA (Polylactic Acid) biodegradable material but it can be also tested on some other materials such as ABS, PC, PSU, PEEK and etc. Developed models were used to describe the process and determine process parameters values that lead to maximal tensile strength and minimal cost. Findings in this paper can be significant for users involved in this type of process to obtain a higher quality product and desirable savings.

1. Introduction

Fused deposition modeling (FDM) is one rapidly growing technology of additive manufacturing (AM). It was developed almost 30 years ago. At that time, it was mainly focused on building conceptual models, but today it is present in the field of electronics, industry (machines, automobile, and space) but also in medicine, science, architecture, and military. The basic principle of FDM is that the melted polymer in a wire form passes through the nozzle. The polymer cures at room temperature, and thus, the heat of the melted material should be maintained a little above the curing temperature. The head of the extruder moves in the x-y plane, and after the production of the first layer, the platform moves down on the z-axis, thus extruding the new layer. The process of applying a new layer repeats, and a model is generated [1-3]. Depending on the geometry of the model, the extruder can build a supporting material for the model, which can be easily removed after printing. The surface of the model tends to be rough, and the model can be additionally processed after the printing, using techniques such as milling, grinding, and turning. Depending on the type of the used polymer, it can be treated with various chemicals to gain a smooth finish. For FDM, various polymers can be used: acrylonitrile butadiene styrene (ABS), polylactic acid (PLA), polycarbonates (PC), polypropylene (PP), polyethylene – high density (PE-HD) and polyethylene – low density (PE-LD) [3]. Investment is relatively small, as well as maintenance cost, material waste, and energy consumption [3]. Furthermore, an application is relatively simple, the material is stable and can be processed afterward. Several prototypes can be manufactured at one extrusion, and finally, low-cost products can be obtained, at least for low-cost 3D printers. On the other hand, the lack of this technology for building prototypes is that the created parts need to be finally processed after printing, and models usually require printing support. Furthermore, the process is sensitive to temperature changes. Dimensional accuracy of the model can be low and sharp edges cannot be produced due to the circular nozzle that shape the final product cross section [1]. Usually, material density is lower in the direction vertical to the printing direction, and the mechanical properties of the parts depend on the position of the product on the working surface (platform), especially in the z-axis direction [4, 5].

Considering the significant impact in most of the science and technology fields, the numerous studies on the efficiency of parameters of the FDM process is not surprising [6-19]. The main focus of these studies was based on the research on the impact of various parameters

that can affect the success of the process such as layer thickness, raster angle, and width, the orientation of the part build, air gap, strength (flexural and impact) [6-9]. Furthermore, numerous researches were conducted to investigate the influence of the FDM process parameters on the obtained samples properties: surface roughness [10], dimensional accuracy [11], material behavior (elasticity) [12], build time [13] and mechanical properties [14]. In most of the previous researches, efforts have been made to explain the relationship between the input process parameters obtained on the obtained samples properties using mathematical modeling methods [9-16, 18-19]. Several of research works were based on various optimization and modeling techniques such as response surface methodology (RSM), Taguchi method, full factorial, gray relational, fractional factorial, artificial neural network (ANN), fuzzy logic and genetic algorithms (GA) [17]. Nancharaiah et al. [10] studied the influences of process parameters such as layer thickness, road width, raster angle, and air gap on the surface finish of FDM processed ABS part through the Taguchi method and variance analysis (ANOVA) technique. The main conclusion was that surface roughness could be improved by using a lower value of layer thickness and air gap [10]. Peko et al. [16] utilized the design of experiments (DOE) approach in order to create mathematical models that can describe the influence of process parameters on maximal ultimate tensile strength and cost of the obtained samples. DOE was prepared using D-optimal response surface design. Optimization results showed that the samples with the best combination of tensile strength and cost were samples produced with 11 surface layers, fill spacing 15 mm, and layer resolution 70 μm. According to these results, it is possible to create samples that have 77.8 % of maximal UTS obtained in this research, but these samples also cost 45.9 % less than those with the maximal value of UTS [16]. Onwubolu et al. [18] analyzed the influence of layer thickness, part orientation, raster angle, raster width, and air gap on the tensile strength of test specimens. Mathematical models relating the response to the process parameters were developed using the group method of data handling (GMDH). Optimal process parameters that lead to maximized tensile strength were defined through the application of differential evolution (DE) algorithm. Sood et al. [19] made an extensive study to understand the effect of five FDM parameters such as layer thickness, part build orientation, raster angle, raster width, and air gap on the compressive stress of test specimens. They also developed statistically validated predictive equations using an artificial neural network approach and regression analysis and found optimal parameter settings through quantum-behaved particle swarm optimization (QPSO).

The main aim of this paper is to create mathematical models that should serve for description and prediction of the influence of additive manufacturing process parameters on the mechanical properties and cost of the obtained samples. As mentioned above, most of the previous researches deal with visual, mechanical, and physical properties of the obtained FDM samples, while in this research, economic perspective was also taken into consideration. The input process parameter was top and bottom surface layers number, fill spacing, and layer resolution. According to the comprehensive review paper published by Omar et al. [17], many studies have investigated the effects of FDM process parameters on ABS built part. However, in the case of other FDM materials, very little work has been done both in terms of material characterization and FDM process optimization. Therefore, considerable work remains to be done in DOE's for part fabrication and process optimization involving other FDM polymers such as PC, PPSF, PC-ABS, PC-ISO, elastomer, and nylon-12 [17]. For this reason, for the analysis in this paper PLA material is conducted. PLA is a biodegradable polymer, in contrast to ABS, which is not biodegradable but can be recycled. PLA has low printing temperature, and it can print sharper corners in comparison to ABS. Also, in contrast to ABS, it is significant in printing models for which the form is more important than its function [20-22].

Mathematical modeling in this paper will be conducted using the artificial intelligence method of fuzzy logic (FL). Fuzzy logic modeling provides a way to better understand the process behavior by allowing the functional mapping between input and output observations [23, 24]. Afterward, the quality of the obtained mathematical model will be estimated using the mean absolute percentage error (MAPE) and the coefficient of determination (R^2) between experimental and predicted response values. The created model will be used to determinate optimal area of input process parameters values that lead to maximal ultimate tensile strength and minimal cost of manufacturing. Obtained models should serve as a valuable tool in additive manufacturing investigation.

2. Experimental procedure

In order to develop mathematical models, design of experiment method (DOE) was utilized. These mathematical models will be able to predict output process responses and show the impact of variable input process parameters on them. In this paper, DOE was prepared using Taguchi L18 experimental plan. The impact of fill spacing, layer resolution and the number of top and bottom surface layers on built samples maximal tensile strength and manufacturing cost are investigated. Variable process parameters represent additive manufacturing machine settings that can be adjusted by operator. Fixed input parameters are building material: PLA, print mode: custom, print strength: strong, print pattern: honeycomb, outer walls: 1. Variable process parameters values and obtained ultimate tensile strength

values as well as cost for all experimental samples are shown in Table 1. Cost was calculated as:

$$Cost = mass\ of\ piece\ (g) * material\ price\ (EUR/g) \quad (1)$$

Table 1. Design of experiment and results

No. of experiment	Top and bottom surface layers number	Fill spacing (mm)	Layer resolution (μm)	Ultimate tensile strength, UTS (MPa)	Cost (EUR)
1.	3	2	70	25.150	1.77
2.	3	2	200	14.758	1.49
3.	3	2	300	15.258	1.59
4.	3	8.5	70	17.399	1.08
5.	3	8.5	200	15.818	1.16
6.	3	8.5	300	16.860	1.25
7.	3	15	70	17.130	0.94
8.	3	15	200	15.835	1.11
9.	3	15	300	14.372	1.09
10.	15	2	70	46.561	2.21
11.	15	2	200	49.046	1.84
12.	15	2	300	38.911	1.53
13.	15	8.5	70	43.994	1.71
14.	15	8.5	200	48.693	1.78
15.	15	8.5	300	28.092	1.53
16.	15	15	70	42.134	1.64
17.	15	15	200	48.861	1.77
18.	15	15	300	38.662	1.53

Experimental work was conducted on a CubePro (3D Systems) additive manufacturing machine. Experimental samples were generated according to HRN EN ISO 527:2012 standard (Figure 1b). Building material was applied in layers in z-axis while building platform lies in an x-y plane. Furthermore, ultimate tensile strength evaluation was performed on universal testing machine ''Instron 8801'' (Figure 1a). After the testing was finished a few random stress-strain diagrams for different experimental samples were generated (Figure 1c).

3. Fuzzy logic modeling

Fuzzy logic modeling is one of the most important modeling approaches in the field of artificial intelligence. It is very useful for modeling complex processes where the limited understanding of the physical laws that describe the underlying process does not allow development of accurate mathematical models. For complex processes where there are a few numerical data and where only ambiguous or imprecise information is available, fuzzy logic modeling provides a way to better understand the process behavior by allowing the functional mapping between input and output observations [23, 24]. The fuzzy system consists of four components (Figure 2): the fuzzification module, the fuzzy inference module, the defuzzification module, and the knowledge base. Fuzzification module converts all input variables into fuzzy (linguistic) variables using membership functions. A membership function is a curve that defines how each point in the input and output space is mapped to a membership value (or degree of membership) between 0 and 1. There are many available membership functions like triangular, trapezoidal, Gaussian etc. [24, 25]. The fuzzy inference module uses the knowledge base containing the fuzzy IF-THEN rules and the membership functions to obtain the fuzzy (linguistic) output values for the corresponding inputs. Finally, the defuzzification module converts the aggregated fuzzy output into a non-fuzzy value [24].

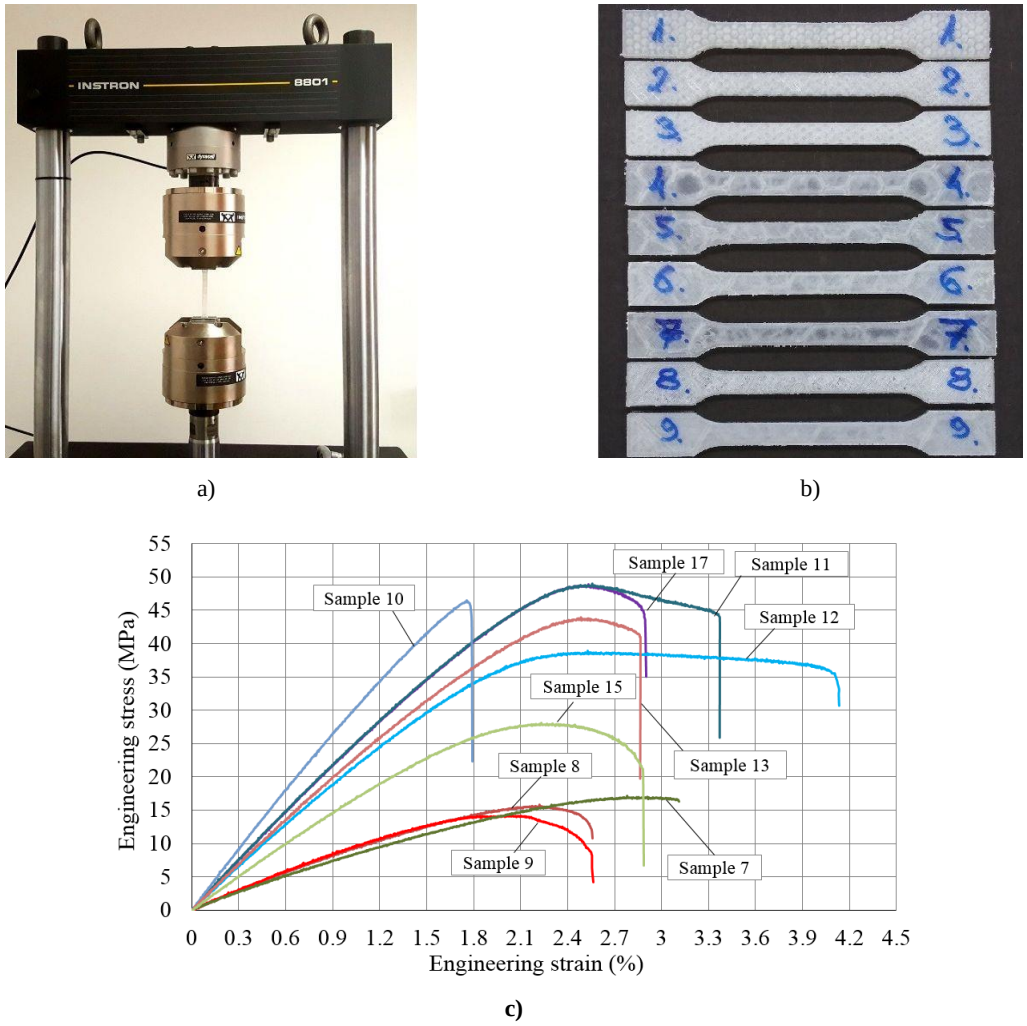

Figure 1. a) Universal tensile testing machine "Instron 8081", b) few experimental samples, c) Stress-strain diagrams for the few samples

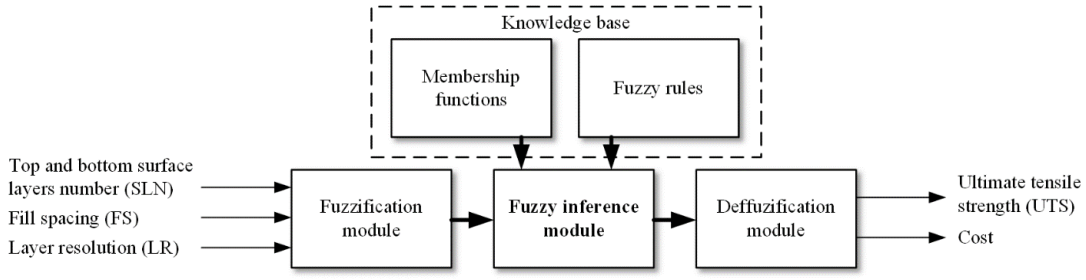

Figure 2. Structure of the fuzzy logic system with three input process parameters and two output responses

In this paper, for the purpose of FDM process analysis, Mamdani fuzzy inference system was used. Process parameters: top and bottom surface layers number (SLN) fill spacing (FS), layer resolution (LR) were considered as inputs, while ultimate tensile strength (UTS) and cost were considered as outputs. For SLN input two membership functions were used: Low and High, while for FS and LR inputs three membership functions were used: Low, Medium and High.

On the other side, for both outputs, five membership functions were used: Low (L), Low-Medium (LM), Medium (M), Medium-High (MH), High (H). Gaussian membership functions were employed to describe the fuzzy sets of inputs and outputs. Membership functions and their ranges are shown in Figure 3.

After selection of membership functions, based on conducted experiments, a set of 18 fuzzy IF-THEN rules with three inputs (SLN, FS, LR) and two outputs (UTS, Cost) was constructed. Each of these rules plays an important role in generating the fuzzy logic model and the accuracy of the numerical output [24, 26]. These rules are shown in Table 2. Fuzzy inference process was defined by the following: and method: min, or method: max, implication: min, aggregation: max and defuzzification method: centroid.

Centroid method is a widely accepted method of deffuzification where the deffuzified output z* is obtained by:

$$z* = \frac{\int \mu A(z) z dz}{\mu A(z) dz} \quad (2)$$

where $\mu_A(z)$ is the aggregated membership function and z is the output variable (the center value of the regions).

Table 2. Set of fuzzy rules

1. If (SLN is Low) and (FS is Low) and (LR is Low) then (UTS is M)(Cost is MH)
2. If (SLN is Low) and (FS is Low) and (LR is Medium) then (UTS is L)(Cost is M)
3. If (SLN is Low) and (FS is Low) and (LR is High) then (UTS is L)(Cost is M)
4. If (SLN is Low) and (FS is Medium) and (LR is Low) then (UTS is LM)(Cost is L)
5. If (SLN is Low) and (FS is Medium) and (LR is Medium) then (UTS is L)(Cost is L)
6. If (SLN is Low) and (FS is Medium) and (LR is High) then (UTS is LM)(Cost is LM)
7. If (SLN is Low) and (FS is High) and (LR is Low) then (UTS is LM)(Cost is L)
8. If (SLN is Low) and (FS is High) and (LR is Medium) then (UTS is L)(Cost is L)
9. If (SLN is Low) and (FS is High) and (LR is High) then (UTS is L)(Cost is L)
10. If (SLN is High) and (FS is Low) and (LR is Low) then (UTS is H)(Cost is H)
11. If (SLN is High) and (FS is Low) and (LR is Medium) then (UTS is H)(Cost is MH)
12. If (SLN is High) and (FS is Low) and (LR is High) then (UTS is MH)(Cost is M)
13. If (SLN is High) and (FS is Medium) and (LR is Low) then (UTS is MH)(Cost is MH)
14. If (SLN is High) and (FS is Medium) and (LR is Medium) then (UTS is H)(Cost is MH)
15. If (SLN is High) and (FS is Medium) and (LR is High) then (UTS is M)(Cost is M)
16. If (SLN is High) and (FS is High) and (LR is Low) then (UTS is MH)(Cost is M)
17. If (SLN is High) and (FS is High) and (LR is Medium) then (UTS is H)(Cost is MH)
18. If (SLN is High) and (FS is High) and (LR is High) then (UTS is MH)(Cost is M)

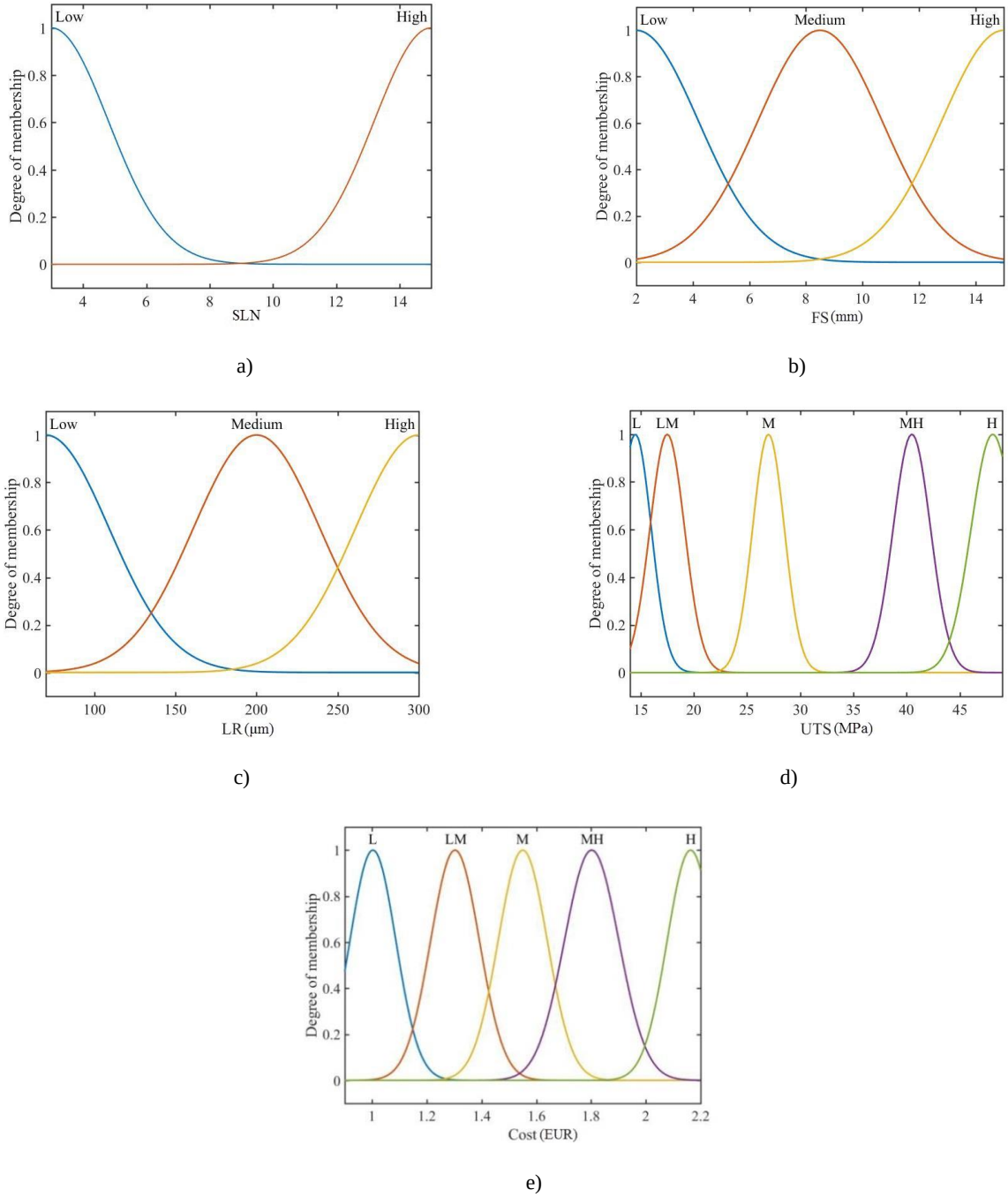

Figure 3. Membership functions for a) top and bottom surface layers number, b) fill spacing, c) layer resolution, d) ultimate tensile strength, e) cost

4. Results and discussion

In order to assess the prediction accuracy of the developed fuzzy logic model, the prediction and experimental data were compared. These comparison results with calculated mean absolute percentage errors (MAPE) and coefficients of determination (R^2) for both outputs are shown in Figures 4 and 5.

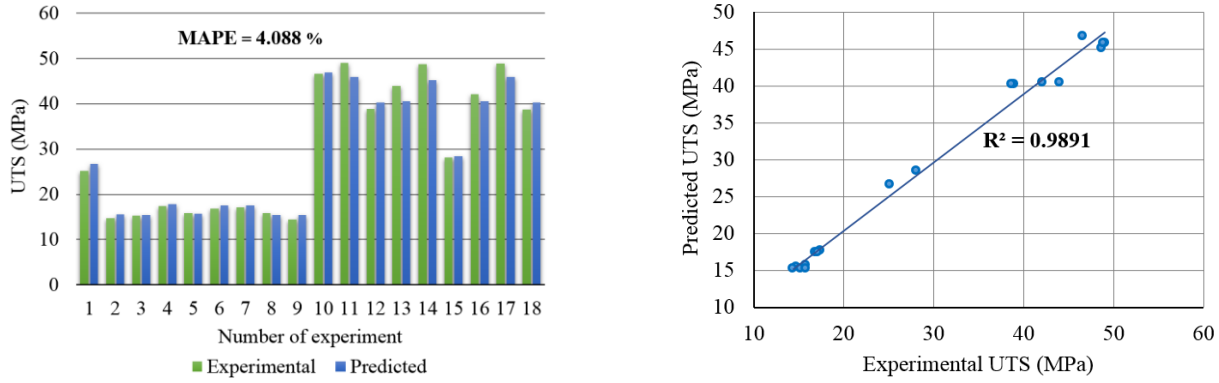

a) b)

Figure 4. a) mean absolute percentage error between experimental and predicted data for UTS, b) coefficient of determination between experimental and predicted data for UTS

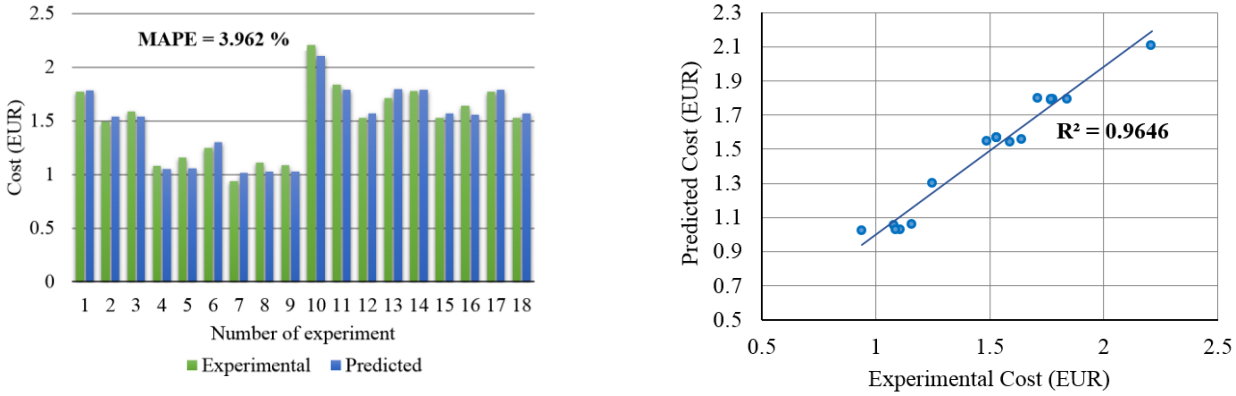

određivanja između eksperimentalnih i predviđenih podataka za UTS

a) b)

Figure 5. a) mean absolute percentage error between experimental and predicted data for cost, b) coefficient of determination between experimental and predicted data for cost

From the results in Figures 4 and 5, it is clear that developed fuzzy logic model has a good prediction performance. Once developed and validated fuzzy logic model can be used to analyze the effects of the fused deposition modeling process parameters on the ultimate tensile strength (UTS) and cost.

In order to that, three 3D surface plots for each of outputs were generated using a developed fuzzy logic model. These response surfaces are shown in Figures 6 and 7.

From the Figures 6 and 7, it can be observed that ultimate tensile strength and cost are quite sensitive to all fused deposition modeling process parameters. It is clear, from the Figure 6a) that higher top and bottom surface layers number at the layer resolution of 200 µm result with higher ultimate tensile strength. The fill spacing parameter doesn't have an influence on the ultimate tensile strength values change. At the same time, from the Figure 7a) it is obvious that, at the layer resolution of 200 µm, the area with higher ultimate tensile strength has also higher manufacturing cost values. In the area of the low top and bottom surface layers number, higher fill spacing values result in lower costs while in the area of the high top and bottom surface layers number fill spacing parameter doesn't affect the change in the manufacturing costs.

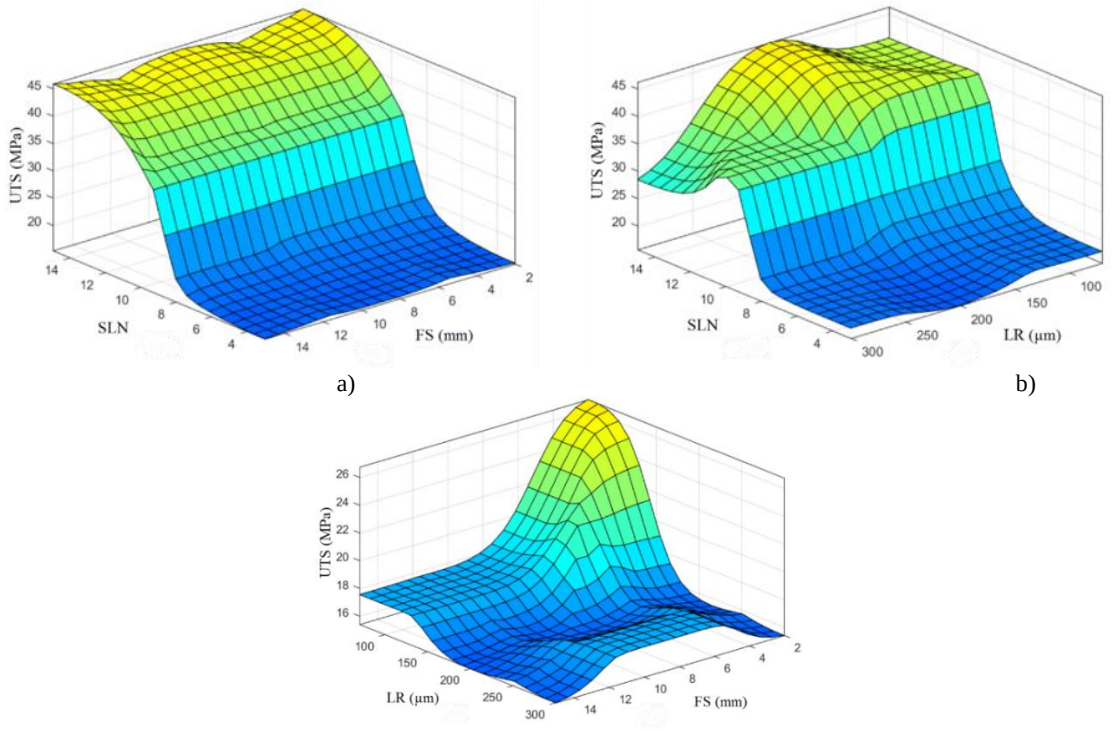

Figure 6. Effects of FDM process parameters on the UTS a) LR = 200 µm, b) FS = 8.5 mm, c) SLN = 3

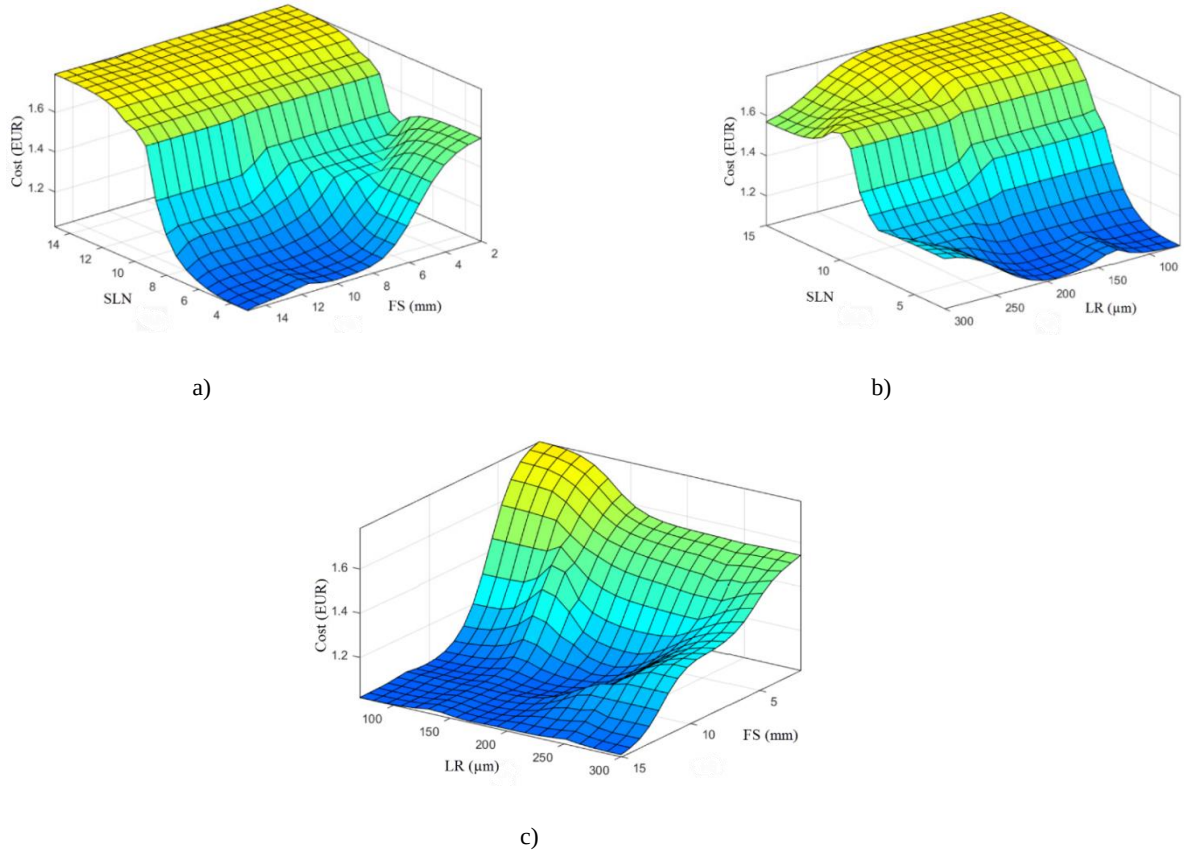

Figure 7. Effects of FDM process parameters on the cost a) LR = 200 µm, b) FS = 8.5 mm, c) SLN = 3

Figure 6b) shows that, at the fill spacing of 8.5 mm, layer resolution doesn't show influence on the ultimate tensile strength in the area of the low top and bottom surface layers number, while at the high top and bottom surface layers number, lowering layer resolution result in the ultimate tensile strength increment. On the other side, Figure 7b) shows that, at the fill spacing of 8.5 mm, low top and bottom surface layers number and the layer resolution of 70 μm result in the low costs. From the Figure 6c) it can be observed that lowering of the layer resolution at the fill spacing of 2 mm and in the area of the low top and bottom surface layers number, results in the higher ultimate tensile strength values. On the other fill spacing levels, the layer resolution parameter doesn't show significant influence on the ultimate tensile strength. Increasing of the fill spacing parameter at the layer resolution of 70 μm lead to the lowering of the ultimate tensile strength. On the other layer resolution levels, the fill spacing change doesn't affect the ultimate tensile strength. Figure 7c) shows that increasing of fill spacing results in lower costs at the all three layers resolution levels and in the area of the low top and bottom surface layers number. At the fill spacing of 2 mm lowering of layer resolution parameter lead to a noticeable increment of costs while at the fill spacing of 15 mm layer resolution doesn't show influence on the manufacturing costs. In the area of fill spacing parameter middle value, a costs increment is visible at the layer resolution of 300 μm. Further analysis of 3D response surfaces obtained from the fuzzy logic model can help to find an optimal result of ultimate tensile strength and costs and their process parameters values. Optimal solutions are compromising. They lead to maximal possible ultimate tensile strength values that will at the same time result with the acceptable manufacturing costs. Layer resolution parameter can be varied only on three levels and due to that, the optimal solutions will be defined for each of these levels. Optimization results are shown in Table 3.

Table 3. *Optimization results

$LR_{opt.}$, (μm)	$SLN_{opt.}$	$FS_{opt.}$(mm)	$UTS_{opt.}$ (MPa)	$Cost_{opt.}$ (EUR)
70	15	15	40.515	1.557
200	15	2	45.912	1.788
		8.5	45.248	1.788
		15	45.912	1.788
300	15	2	40.331	1.568
		15	40.331	1.568

5. Conclusion

In this paper, the influence of the fused deposition modeling process parameters: top and bottom surface layers number, fill spacing and layer resolution on the ultimate tensile strength and additive manufacturing cost was analyzed. The experimental work was carried out on the specimens generated from the PLA plastic material. Experimental results were used to establish a relationship between inputs and analyzed responses. Modeling was conducted using a fuzzy logic approach. The generated model was validated using statistical measures such as mean absolute percentage error and coefficient of determination between experimental and predicted responses values. After the prediction accuracy of the developed model was done, the effects of parameters and their interactions were explained using response surfaces obtained from the fuzzy logic model. From these figures, it was clear that tensile strength and costs are proportional what means that higher tensile strength leads to higher costs. Also, the developed model was effective for further analysis and optimization procedure. According to that, the process parameters values that lead to maximal tensile strength and acceptable manufacturing cost were found (Table 3). Obtained observations are useful for users involved in this kind of additive manufacturing process. Future research will focus on the examination, modeling, and optimization of other mechanical properties of FDM specimens built by ABS plastic material.

REFERENCES

[1] Peko I., Bajić D., Veža I. (2015), *Selection of additive manufacturing process using the AHP method*. In International Conference Mechanical Technologies and Structural Materials, Split

[2] Dandgaval O., Bichkar P., (2016), *Rapid prototyping technology-study of fused deposition modeling technique.* International Journal of Mechanical and Production Engineering 4, No. 4, p 44-47.

[3] Novakova-Marcincinova L., Novak-Marcincin J., (2012), *Applications of rapid prototyping fused deposition modeling materials.* In Annals of DAAAM for 2012 & Proceedings of the 23rd International DAAAM Symposium 23, No. 1, p 57-60

[4] Wiedemann B., Jantzen H. A. (1999), *Strategies and applications for rapid product and process development in Daimler-Benz AG*. Computers in Industry 39 No. 1, p 11-25.

[5] Levy G. N., Schindel R., Kruth J. P. (2003), *Rapid manufacturing and rapid tooling with layer manufacturing (LM) technologies, state of the art and future perspectives.* CIRP annals 52, No. 2, p 589-609.

[6] Raut S., Jatti V. S., Khedkar N. K., Singh T. P. (2014). *Investigation of the effect of built orientation on mechanical properties and total cost of FDM parts.* Procedia materials science 6, p 1625-1630.

[7] Mohamed O. A., Masood S. H., Bhowmik, J. L. (2016), *Mathematical modeling and FDM process parameters optimization using response surface methodology based on Q-optimal design.* Applied Mathematical Modelling 40, No. 23-24, p 10052-10073.

[8] Panda S. K., Padhee S., Anoop Kumar,S. O, Mahapatra S. S., (2009), *Optimization of fused deposition modelling (FDM) process parameters using bacterial foraging technique.* Intelligent information management 1,No. 2, p 89.

[9] Liu X., Zhang M., Li S., Si L., Peng J., & Hu Y. (2017), *Mechanical property parametric appraisal of fused deposition modeling parts based on the gray Taguchi method.* The International Journal of Advanced Manufacturing Technology 89, No. 5, p 2387-2397.

[10] Nancharaiah T., Raju D. R., Raju V. R. (2010), *An experimental investigation on surface quality and dimensional accuracy of FDM components.* International Journal on Emerging Technologies 1, No. 2, p 106-111.

[11] Sood A. K., Ohdar R. K., Mahapatra S. S., (2009), *Improving dimensional accuracy of fused deposition modelling processed part using grey Taguchi method.* Materials & design 30, No. 10, p 4243-4252.

[12] Laeng J., Khan Z. A., Khu S. Y. (2006), *Optimizing flexible behaviour of bow prototype using Taguchi approach.* Journal of Applied Sciences 6, No. 3, p 622-630.

[13] Nancharaiah T. (2011), *Optimization of process parameters in FDM process using design of experiments.* Int J Emerg Technol 2, No. 1, p 100-102.

[14] Rayegani F., Onwubolu G. C. (2014), *Fused deposition modelling (FDM) process parameter prediction and optimization using group method for data handling (GMDH) and differential evolution (DE),* The International Journal of Advanced Manufacturing Technology 73, No. 1-4, p 509-519.

[15] Nidagundi V. B., Keshavamurthy R., Prakash C. P. S. (2015), *Studies on parametric optimization for fused deposition modelling process.* Materials Today: Proceedings 2, No. 4-5, p 1691-1699.

[16] Peko I., Krolo J., Bagavac P., Đurić S., Kostić N., Bašić A. (2017, January), *Modeling and optimization of tensile strength of ABS parts manufactured by the fused deposition modeling process.* In International conference on Mechanical technologies and structural materials, Split

[17] Mohamed O. A., Masood S. H., Bhowmik J. L. (2015), *Optimization of fused deposition modeling process parameters: a review of current research and future prospects.* Advances in Manufacturing 3, No. 1, p 42-53.

[18] Onwubolu G. C., Rayegani F. (2014), *Characterization and optimization of mechanical properties of ABS parts manufactured by the fused deposition modelling process.* International Journal of Manufacturing Engineering 2014.

[19] Sood A. K., Ohdar R. K., Mahapatra S. S. (2012), *Experimental investigation and empirical modelling of FDM process for compressive strength improvement.* Journal of Advanced Research 3, No. 1, p 81-90.

[20] Chilson, L. (2013), *The Difference between ABS and PLA for 3D Printing.* ProtoParadigm Blog.

[21] Leigh, S. J., Bradley, R. J., Purssell, C. P., Billson, D. R., & Hutchins, D. A. (2012), *A simple, low-cost conductive composite material for 3D printing of electronic sensors.* PloS one, 7, No. 11, e49365.

[22] Wang X., Jiang M., Zhou Z., Gou J., Hui D. (2017), *3D printing of polymer matrix composites: A review and prospective.* Composites Part B: Engineering 110, p 442-458.

[23] Sivarao P. B., El-Tayeb N. S. M., Vengkatesh V. C. (2009), *GUI based mamdani fuzzy inference system modeling to predict surface roughness in laser machining*. International Journal of Electrical & Computer Sciences 9, No. 9, p 281-288.

[24] Madić M., Radovanović M., Ćojbašić Ž., Nedić B., Gostimirovic M. (2015), *Fuzzy Logic Approach for the Prediction of Dross Formation in CO2 Laser Cutting of Mild Steel.* Journal of Engineering Science & Technology Review 8, No. 3.

[25] Syn C. Z., Mokhtar M., Feng C. J., & Manurung Y. H. (2011), *Approach to prediction of laser cutting quality by employing fuzzy expert system.* Expert Systems with applications 38, No. 6, p 7558-7568.

[26] Sivarao S., Castillo W. J. G., Taufik T. (2009), *Machining quality predictions: comparative analysis of neural network and fuzzy logic*. International. Journal Electrical and Computer Sciences 9, No. 9.

ISSN 1847-7917

The influence of furnace atmosphere during austenitization on microstructure and hardness of austempered ductile iron

Nikša ČATIPOVIĆ, Dražen ŽIVKOVIĆ, Karla GRGIĆ, Petar LJUMOVIĆ, Josip PERINIĆ, Zvonimir DADIĆ

University of Split, Faculty of Electrical Engineering, Mechanical Engineering and Naval Architecture, Ruđera Boškovića 32, 21000 Split

Niksa.Catipovic@fesb.hr
Drazen.Zivkovic@fesb.hr
Karla.Grgic.00@fesb.hr
Petar.Ljumovic@fesb.hr
Josip.Perinic.00@fesb.hr

Keywords

Austempered ductile iron
Furnace atmosphere
Decarburization
Microstructure
Hardness

Original scientific paper

Abstract: The effect of furnace atmosphere during austenitization on properties of austempered ductile iron was investigated. Two sets of ductile iron samples were used. One set of samples was austenitized in normal furnace atmosphere, without protection of decarburization. Second set of ductile iron samples was austenitized in nitrogen protective atmosphere to prevent decarburization. All samples were austenitized at the same temperature of 850°C for 30 minutes. During austenitization in nitrogen atmosphere pressure of 0.3 bars was used. After that samples were austempered on 300°C for different times. Times ranged from 30 minutes to 60 minutes, following experimental plan. At the end, all the samples were air cooled to room temperature. Microstructural analysis was done, and hardness was measured on all samples. Results showed that samples austenitized in nitrogen atmosphere have higher hardness and more carbon rich phases in their microstructure. Mathematical models are derived that describe the hardness of ADI depending on the atmosphere in the furnace and the holding time at austempering temperature.

1. Introduction

Ductile cast iron combines good casting of gray cast iron and high tensile strength of cast steel. In the ductile cast iron graphite is excreted in the form of beads, or nodules. The spherical shape of the graphite gives the ductile cast iron a high yield strength and high elongation, as well as good toughness, castability and machinability.

Ductile cast iron is a type of iron-based cast iron, the composition of which is characterized by an increased amount of carbon, silicon and magnesium, which allow the excretion of graphite in the form of nodules. Ductile cast iron is an increasingly prevalent material on the iron castings market. Compared to gray cast iron, this cast iron has significantly higher strength, is less workable and has a slightly weaker ability to dampen vibrations. On the other hand, the vibration damping property and machinability are much more favorable with ductile cast iron than with cast iron. The yield strength is higher than that of gray cast iron and non-alloy cast iron [1].

To produce ductile cast iron, a backfill of special gray pig iron is used and melted in electric furnaces. The melt is then treated with nodulators and modulators and poured into molds. The interaction of graphitizers and nodulators, as well as the regulation of other influencing factors, enables the excretion and coagulation of the nodules. Nodulators are elements that enable the extraction of graphite in the form of nodules. Magnesium, calcium and cerium based nodulators are mainly used [2].

The microstructure of ductile cast iron consists of graphite beads in an austenitic matrix that is achieved by a stable eutectic transformation. The eutectic formed during solidification of the melt can be stable or metastable. Graphite and austenite are formed in stable crystallization, and cementite (Fe_3C) and austenite in metastable crystallization. There is a third possibility of the formation of a mixed structure of austenite, graphite and cementite [1].

The final microstructure of ductile cast iron is determined with [3]: the position of the grain boundaries, the influence of alloying elements on the phase boundaries, the ability to diffuse carbon in the solid, the way of alloying the alloying elements in the matrix and the ability to form nodules and grow grains.

Nodularity, i.e. the degree of sphericity, is the volume fraction of spherical clusters of graphite relative to the total number of graphite precipitates. The aim is to produce ducitle cast iron with as much nodularity as possible, preferably above 90% because the mechanical properties directly depend on the regularity of the graphite nodules [1, 4].

As the proportion of non-spherical graphite forms increases, the tensile strength and dynamic endurance decrease, while the nodularity does not have such an effect on the yield strength. In Figure 1. a diagram describing this phenomenon is shown. The shape of non-spherical graphite is important because thin sheets of graphite with sharp edges cause a significant drop in tensile strength. Reduced ductility also affects the modulus of elasticity, increases the ability of the material to dampen vibrations, lowers toughness, and increases thermal conductivity and reduces electrical resistance [1].

The matrix of ducitle cast iron can be: ferritic, perlite, ferritic-perlite or austenitic. To determine which type of matrix was formed, it is necessary to conduct a metallographic examination. Pre-sanded and polished samples are etched with nital to make the metal matrix visible. In Figure 2. the microstructure of (a) ferritic and (b) pearlitic - ferritic ductile cast iron, at a magnification of 100 times, etched with 4% nital is shown. By increasing the proportion of ferrite matrix, cast iron has higher elongation, lower tensile strength, lower impact fracture and higher toughness / brittle transition temperature [5]. Austenitic ductile cast iron is used primarily in the conditions of required resistance to high temperatures and resistance to wear and corrosion.

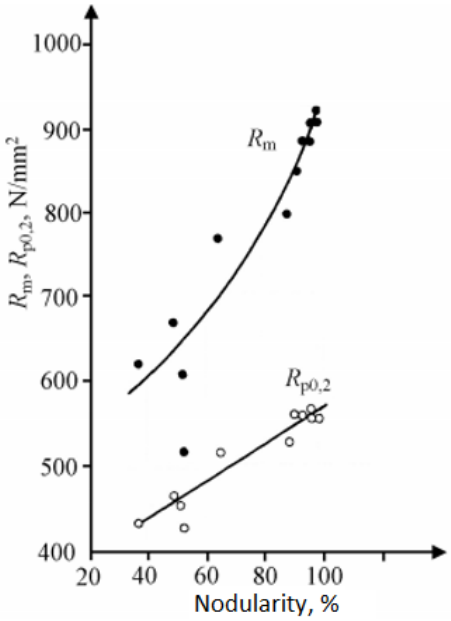

Figure 1: Nodularity impact on strength on ductile iron [5]

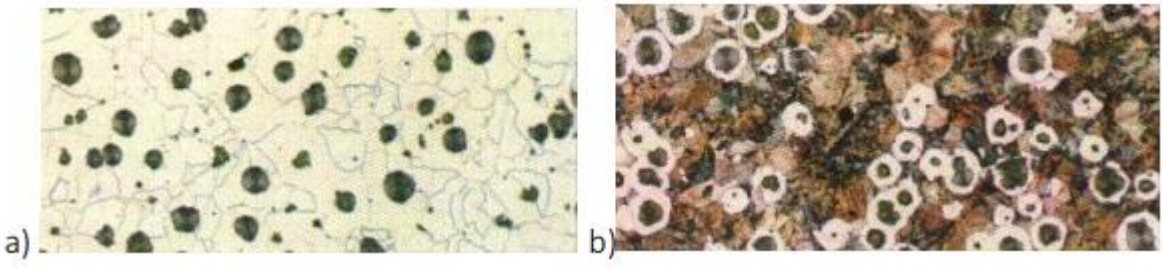

Figure 2: Microstructure of ferritic (a) and pearlitic (b) ductile cast iron, magnification 100x, etched with 4% nital [6]

By heat treatment as well as by adding alloying elements, we can significantly change the mechanical properties and microstructure of materials, especially iron-based metals. In practice, heat treatment is a technological process of heating a material to a certain specific temperature, keeping it at that temperature for a certain time and cooling it at an appropriate speed, whereby the structure of the material changes to achieve the desired material properties. The basic parameters of heat treatment are temperature and time.

Austempering is a heat treatment that originated as a version of classical tempering. While in the classical tempering (hardening + high temperature anneling) the products are cooled to room temperature after heating to the austenitization temperature, then heated to the anneling temperature again, in austempering the products are cooled from the austenitization temperature to the tempering temperature. Direct cooling to the tempering temperature and avoiding cooling to room temperature results in great savings of time and money in the production process. With the classic tempering, the energy consumption is higher due to double heating, and thus the consumption of money and time is higher.

As mentioned, there are energy and financial advantages of austempering, but there are also advantages in the form of improvement of mechanical properties, which are [3]: increased ductility, increased impact fracture, increased wear resistance and increased permanent dynamic strength.

The austempering process consists of: heating ductile cast iron to austenitization temperature (between 850°C and 950°C), holding at the austenitization temperature until complete austenitization of the workpiece, cooling of the workpiece in a bath at austempering temperature fast enough to obtain only ausferrite, holding at the austempering temperature long enough to obtain the desired microstructure and cooling in air to room temperature.

So, when the ductile cast iron is subjected to austempering, a completely new material is obtained, which is called Austempered Ductile Iron - ADI. ADI is twice as strong as classical tough cast iron and has high tensile strength and high impact fracture which combination of mechanical properties makes it wear-resistant and gives it high dynamic durability [7, 8].
ADI alloys undergo two stages of transformation during austempering. In the first stage of transformation, austenite (γ) decomposes into bainite ferrite (α) and carbon-enriched residual austenite (γ_{hc}), the so-called ausferrite [9,10, 11].

$$\gamma \rightarrow \alpha + \gamma_{hc}$$

In the second stage of transformation the carbon-enriched residual austenite (γ_{hc}) further decomposes into ferrite (α) and carbides. This conversion will occur if the workpiece is kept at austempering temperature for too long [9].

$$\gamma_{hc} \rightarrow \alpha + \text{carbides}$$

The appearance of carbides in the microstructure should be avoided because they make the material brittle, so the optimal mechanical properties of ADI are achieved after the end of the first stage of transformation, i.e. before the beginning of the second stage [12].
Due to its excellent mechanical properties and economic cost-effectiveness, the application of ADI alloys in industry is very wide [3]: industry (pumps and elements exposed to wear), agriculture (excellent wear resistance due to working with land), construction (elements exposed to wear, crushing, grinding, etc.), food industry (crushing, mixing, sorting, etc.) and car industry.

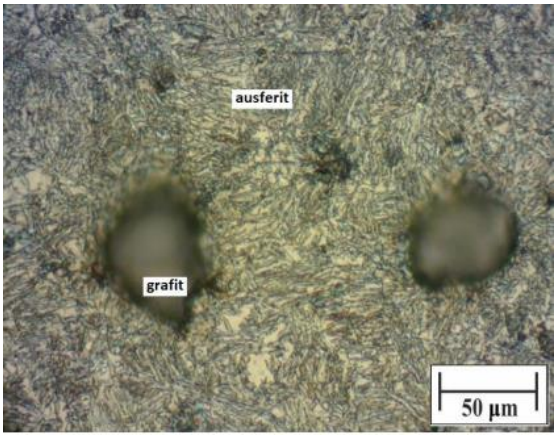

Figure 3: Microstructure od ADI [5]

The microstructure of ADI is shown in Figure 3. It consists of ausferrite and nodular graphite. Heat treatment significantly affects the microstructure of ADI alloys, as the austenitization temperature increases, so does the carbon content in the matrix. In addition, the carbon content of the matrix is also affected by the presence of alloying elements, their amount and their location within the matrix.

2. Experimental work

In the experimental part of the work, austempering of ductile cast iron was performed. After heat treatment, microstructure analysis and hardness test were performed. Considering the available literature and the research conducted so far, the heat treatment parameters used in the experiment were selected.
The experiment planning was performed using the computer program *State-Ease Design Expert*. In the first step, the input parameters are defined. Their category and the boundaries within which they change are selected. The first input parameter is a numerical, austempering time, ranging from 30 minutes to 60 minutes. The second parameter that will vary in the experiment is categorical, and refers to the atmosphere in the furnace, so the test samples will be heated to the austenitization temperature with or without nitrogen. Since there is only one numerical factor and one categorical factor, this is a relatively simple problem for the solution of which the "One factor" experimental plan was chosen. For the entered factors and their limitations, the program determines the experiment plan shown in Table 1.

Table 1: Experiment plan

Sample	Austempering time, min	Furnace atmosphere
1	30	With nitrogen
2	30	With nitrogen
3	38	With nitrogen
4	53	With nitrogen
5	60	With nitrogen
6	60	With nitrogen
7	45	With nitrogen
8	30	Without nitrogen
9	30	Without nitrogen
10	38	Without nitrogen
11	53	Without nitrogen
12	60	Without nitrogen
13	60	Without nitrogen
14	45	Without nitrogen

The number of output parameters, i.e., the number of tested properties of ADI, does not affect the final number of experiments. In this paper, only one of the mechanical

properties was tested, hardness, because the shape of the test samples was not made according to standards for testing other mechanical properties. Selected shape (Φ8x10mm) of the test samples is suitable for corrosion test that will be performed in the next phase of the overall research.

All test samples were first austenitized on 850°C, and the holding time at that temperature was 30 minutes, Figure 4. The test samples were austenitized in a *DEMITERM EASY 9* furnace which has the possibility of protective nitrogen atmosphere, shown in Figure 5a). The furnace has a power of 3 kW with a maximum temperature of 1150°C, and the temperature is measured with a thermocouple type "K" (NiCr-Ni).

Figure 4: Austenitization of test samples on 850°C

As stated in the test plan, half of the samples, i.e. 7, were austenitized with a protective nitrogen atmosphere and the other half without a protective nitrogen atmosphere. Nitrogen was released into the furnace at a pressure of 0.3 bar, Figure 5b). After holding for 30 minutes at the austenitization temperature, the test samples were quenched directly in a salt bath furnace to obtain ADI.

a)

b)

Figure 5: a) Laboratory furnace with protective atmosphere; b) Barometer

For austempering, a *JPA 6-600* furnace with a power of 3.1 kW and a maximum temperature of 600°C, shown in Figure 6, was used. For the salt bath, the salt AS 140 was used.

Figure 6: Salt bath furnace JPA 6-600

The salt bath was heated to 300°C and all samples were austempered at that temperature with different austempering times ranging from 30 min to 60 min. The samples were then removed from the salt bath and air cooled to room temperature, Figure 7.

Figure 7: Air cooling of test samples

After the heat treatment, the test samples had to be prepared for testing the mechanical properties and analysis of the microstructure. The samples were first grinded to remove heat-treated scale and then polished to a high gloss. Grinding was performed on a *Handimet Grinder* which has grinding tracks of fineness 240, 320, 400 and 600, which are constantly poured with water.

After grinding, the samples were polished on a polishing wheel. Aluminum oxide particles (Al_2O_3) in suspension with water were used as abrasive. Aluminum oxide particles are not soluble in water, but water only serves to transfer the particles to the rotating wheel.

3. Results

3.1. Microstructure

After hardness testing, the microstructures were analyzed using a light microscope. Pre-polished samples were etched on the surface to develop a microstructure that will be analyzed under a microscope. The reagent used to etch the surface of the samples was Nital. Nital is a 2% solution of nitric acid in 96% ethanol. The surface of each sample was etched for 10 seconds.

The sample surfaces were observed with the *OPTON Axioskop* light microscope shown in Figure 8. Said microscope has interchangeable lenses with magnifications of 50, 100, 200 and 500 times. An integrated *DinoEye* camera is built into the microscope, which is used to record metallographic images, and these images are processed using *DINOCAPTURE 2.0* software.

As can be seen from the microstructure images, ADI samples kept in the furnace for 30 minutes have significantly more dark phases compared to the samples held for 60 minutes, which means that they have more carbon and thus higher hardness. The atmosphere in the furnace affects in a way that the samples obtained in the nitrogen atmosphere have a darker microstructure because nitrogen prevents the diffusion of carbon into the atmosphere of the furnace and therefore have a higher hardness. It can be concluded that shorter austempering time gives higher hardness of ADI because carbon does not have enough time to diffuse, and longer austempering time has a positive effect on toughness.

Figure 8: OPTON Axioskop light microscope

Figures 9-12 show microstructures of test samples depending on different heat treatment parameters.

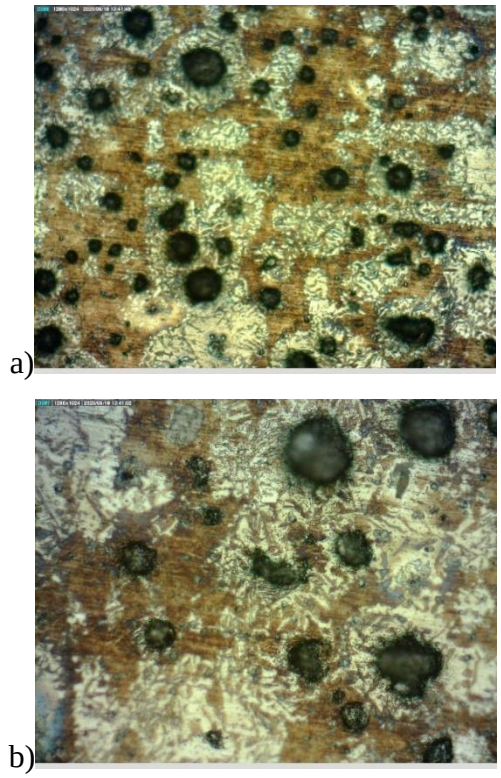

Figure 9: ADI microstructure after austenitization for 30 min in atmosphere with nitrogen: a) 100x and b) 200x magnification

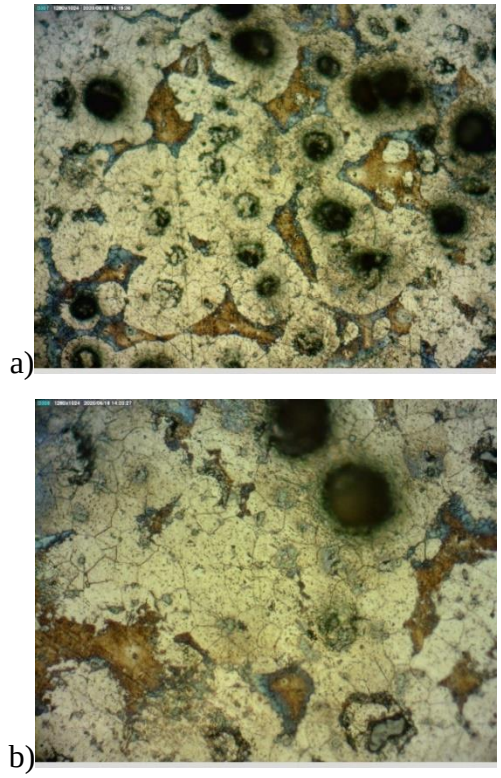

Figure 10: ADI microstructure after austenitization for 60 min in atmosphere with nitrogen: a) 100x and b) 200x magnification

a)

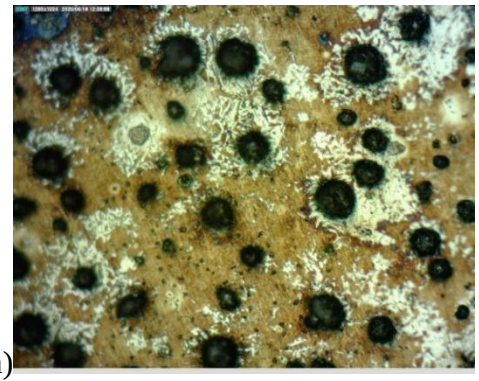

b)

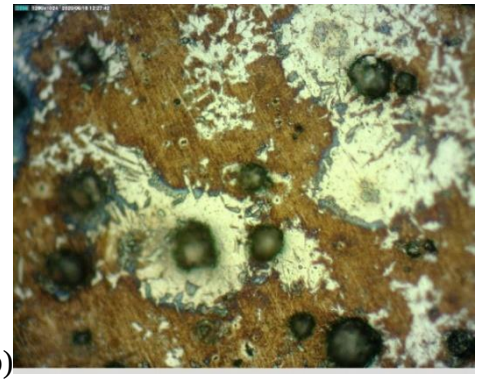

Figure 11: ADI microstructure after austenitization for 30 min in atmosphere without nitrogen: a) 100x and b) 200x magnification

a)

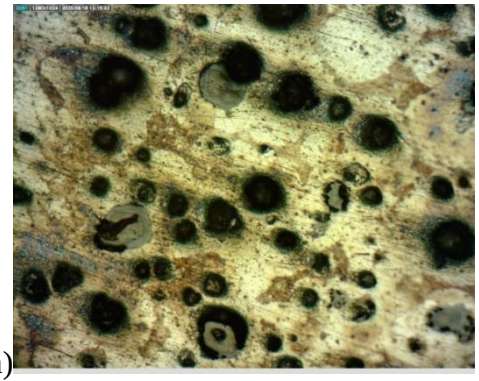

b)

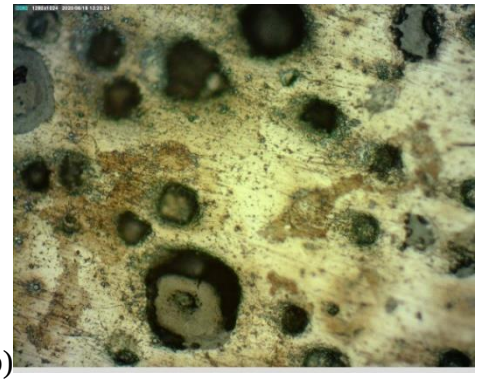

Figure 12: ADI microstructure after austenitization for 60 min in atmosphere without nitrogen: a) 100x and b) 200x magnification

3.2. Hardness

Hardness was tested on previously prepared samples using the *Dia Testor 2 Rc-S* device, Figure 11. Dia Testor 2 Rc-S is a hardness tester that uses three different test methods: Brinell, Vickers, and Rockwell. The Vickers method and force of 10 kP was used for this experiment. The test was carried out in such a way that the sample was placed on the device and a diamond four-sided pyramid with a top angle of 136 ° was pressed into its surface by means of a lever. The recess of the pyramid leaves a square trace on the surface, which is projected and enlarged by the machine. The length of the diagonals is measured in a square, their mean value is calculated, and the Vickers hardness value is read from the table. 3 measurements were performed on each sample and the mean hardness value was calculated. The measurement results are shown in Table 2.

Figure 11: Hardness testing machine

The obtained hardness results were entered into the computer program *Design Expert* and were statistically processed. Based on the performed regression analysis, according to the measured hardness, an algebraic model was obtained. The model analytically expresses the statistical relationship between variables.

Final equation for the hardness of ADI obtained in a nitrogen furnace atmosphere is:

$$HV = 657{,}13561 - 8{,}59452 \cdot t_a + 0{,}061256 \cdot t_a^2$$

Final equation for the hardness of ADI obtained in furnace atmosphere without nitrogen:

$$HV = 628{,}51656 - 8{,}27601 \cdot t_a + 0{,}061256 \cdot t_a^2$$

In stated equations, ta stands for austempering time. Since it was a relatively simple problem with one numerical and one categorical factor, the final expressions are simple.

Table 2: Hardness measurements

Sample	Austempering time, min	Furnace atmosphere	Hardness HV10 measurements			
			No. 1	No. 2	No.3	Mean
1	30	With nitrogen	464	450	450	455
2	30	With nitrogen	464	450	450	455
3	38	With nitrogen	421	417	425	421
4	53	With nitrogen	380	380	383	381
5	60	With nitrogen	366	366	370	367
6	60	With nitrogen	363	351	351	355
7	45	With nitrogen	394	390	383	389
8	30	Without nitrogen	442	442	421	435
9	30	Without nitrogen	442	433	437	437
10	38	Without nitrogen	383	421	401	402
11	53	Without nitrogen	366	376	366	369
12	60	Without nitrogen	357	351	348	352
13	60	Without nitrogen	351	351	348	350
14	45	Without nitrogen	383	360	390	378

There are 2 final expressions because the categorical factor had two options, so the first expression is given for the atmosphere of the furnace with nitrogen and the second for the atmosphere of the furnace without nitrogen.

The expressions show that for the same austempering time the hardness of the samples treated in the nitrogen atmosphere will be higher, which was confirmed by experiment. In addition, it is also evident from the expression that a longer austempering time negatively affects the hardness.

In Figure 12. a diagram is shown which illustrates how the furnace atmosphere and austempering time affect the hardness of ADI. Red curves represent the atmosphere of the furnace with nitrogen, and the green curves represent the atmosphere of the furnace without nitrogen.

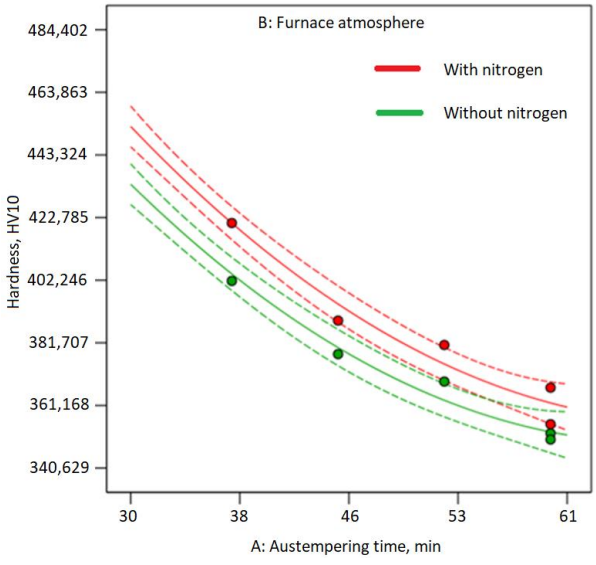

Figure 12: Influence of furnace atmosphere and austempering time on hardness

4. Conclusion

Ductile cast iron is a relatively new material whose production is growing day by day due to its extremely favorable mechanical properties with low production costs. When ductile cast iron is subjected to austempering heat treatment, a completely new material known as austempered ductile iron - ADI is formed, which has significantly better mechanical properties than ductile cast iron. The heat treatment parameters can significantly affect the mechanical properties and microstructure of ADI alloys.

The aim of this work was to study the influence of austempering time and furnace atmosphere on the hardness of ADI. The analysis of the hardness results obtained in the experimental part showed that the atmosphere in the furnace influences the hardness of ADI alloys in such a way that the samples obtained in the furnace with nitrogen have higher hardness than the samples obtained in furnace without nitrogen. This is because nitrogen atmosphere prevents the diffusion of carbon from sample surface and thus enables higher hardness as a result which was confirmed with microstructural analysis.

It was also found that the austempering time has a negative effect on the hardness, so the highest hardness has samples that were kept in the furnace for 30 minutes, and the lowest hardness samples were kept for 60 minutes. The reason for this is the transformation window during ausferrite formation. The longer the austempering time the more ausferrite decomposes into large amount of ferrite and small carbides and thus hardness decreases.

This paper shows how the choice of furnace atmosphere and isothermal time has a significant impact on the mechanical properties of ADI alloys. Mathematical models for a specific atmosphere in the furnace are given, which can be used to determine the optimal heat treatment parameters at which the desired mechanical properties will be achieved.

REFERENCES

[1] Žmak I., „Modeliranje strukture i svojstava žilavog lijeva neuronskim mrežama", Doktorski rad, FSB, Zagreb, 2008.

[2] Hrgović, D., „Tehnologija materijala",Zagreb 1984

[3] Gagne, M., „The Sorelmetal Book of Ductile Iron", Rio Tinto Iron & Titanium, Montreal, Kana da, 2004.

[4] Metals Hanbook, Ninth edition, Vol. 15, Casting, ASM International, Metals Park, Ohio, SAD, 1988.

[5] Čatipović N., „Utjecaj bakra i toplinske obrade na svojstva izotermički poboljšanog žilavog ljeva", Doktorski rad, FESB, Split, 2019.

[6] Nodular Iron, http://www.metallography.com/zechnotes/iron/nodular.htm.

[7] Behera G., Sohala S. R., „Effect of copper on the properties of austempered ductile iron castings", Bachelor thesis, Department of Metallurgical and Materials Engineering, National Institute of Technology, Rourkela, India, 2012

[8] Živković D., Gabrić I., Dadić Z., Čatipović N., Vrljičak I., „Analysis of austempering treatment parameters on properties of ductile iron EN-GJS-400", Zbornik radova = Proceedings, Hrvatsko društvo za strojarske tehnologije, MTSM 2015, Split, 2015.

[9] Sidjanin L., Smallman R. E., „Metallography of bainitic transformation in austempered ductile iron", Materials Science and Technology, Vol. 8, London, p. 1095-1103, 1992

[10] Elliot R., „Heat Treatments of Metals". 3, p. 55, 1997

[11] Harding R. A., „The production, properties and automotive applications of austempered ductile iron", Kovove Mater., 45, p. 1-16, 2007.

[12] Rajnovic D., Eric O., Sidjanin L., „The standard processing window of alloyed ADI materials", Kovove Mater., 50, p. 199-208, 2012

ISSN 1847-7917

The influence of subsequent high temperature tempering on tensile strength and elongation of austempered ductile iron

***Nikša ČATIPOVIĆ*[1)], *Hasan AVDUŠINOVIĆ*[2)], *Karla GRGIĆ*[1)], *Petar LJUMOVIĆ*[1)], *Josipa ŽIVALJIĆ*[1)] *Zvonimir DADIĆ*[1)]**

1) University of Split, Faculty of Electrical Engineering, Mechanical Engineering and Naval Architecture, Ruđera Boškovića 32, 21000 Split, Croatia
2) University of Zenica, Faculty of Metallurgy and Technology, Zenica, **Bosnia and Herzegovina**

Niksa.Catipovic@fesb.hr
hasan.avdusinovic@unze.ba
Karla.Grgic.00@fesb.hr
Petar.Ljumovic@fesb.hr
Josipa.Zivaljic.00@fesb.hr

Keywords

Austempered ductile iron
High temperature tempering
Tensile strength
Elongation

Original scientific paper

Abstract: The effect of high temperature tempering on austempered ductile iron was investigated in this paper. Five samples of ductile iron with 0,51% wt. % Cu were austempered without subsequent high temperature tempering and five samples of same ductile iron alloy were austempered with subsequent high temperature tempering. All samples were austenitized on 850°C for 60 minutes. Austempering was done on 250°C, 331°C and 420°C for 30, 68 and 120 minutes. High temperature tempering was done on 500°C for 60 minutes. At the end, all the samples were air cooled to room temperature. Tensile strength and elongation were measured on all samples thus compering results with and without high temperature tempering. Results showed that samples with subsequent high temperature tempering have slightly lower tensile strength and significantly higher elongation compered to samples without subsequent high temperature tempering. Also, samples with subsequent high temperature tempering show more uniform tensile strength when compared to samples without subsequent high temperature tempering.

1. Introduction

Ductile cast iron (spheroidal or nodular) is a type of cast iron that combines the advantages of steel cast iron (higher toughness and strength) and gray cast iron (good casting), [1]. Nowadays, the demand for solid and economically viable materials is increasing, and this type of material includes ductile cast iron.

Ductile cast iron has naturally more favorable mechanical properties than gray cast iron, but further heat treatment of ductile cast iron achieves significantly better properties, [2, 3]. By subjecting ductile cast iron to austempering, austempered ductile iron (ADI) is obtained. Such a cast has a unique, so-called, an ausferrite microstructure which is a mixture of needle ferrite and carbon-enriched retained austenite. One of the great advantages is that ADI also achieves twice the strength for a given level of ductility obtained by conventional heat treatment. Depending on the alloying elements of the ductile cast iron itself and the heat treatment parameters (austempering temperature and time), different mechanical properties are achieved. ADI has superior properties over many iron and aluminum alloys, [4].

The austenitization temperature is equal to the temperature of conventional hardening treatment of 840 - 900°C, [5]. The holding time depends on the chemical composition and size of the casting. The casting is quenched from the austenitization temperature in a warm isothermal salt bath for a defined time until the conversion is complete, Figure 1. Temperatures of salt baths range from 230 to 450°C, depending on which properties are to be achieved. As the temperature of the bath increases, the hardness and strength decrease after treatment. The cooling time of the workpiece in the salt bath is determined by the chemical composition of the casting and the temperature of the salt bath, [6].

Austempering of ductile cast iron is similar to austempering of steel, with a difference in the obtained microstructures and finally the desired properties. ADI produces a structure of ferrite and stable, carbon-rich retained austenite (ausferrite), [7-9]. The difference in structure is due to the high content of silicon in the ductile cast iron which limits the formation of carbides, [10-12]. After austempering, another heat treatment that was applied is the high temperature tempering which was carried out after austempering. High temperature tempering is performed at temperatures from 400°C to A1 temperature. The general purpose of this heat treatment is to eliminate residual stresses and increase toughness. The implementation of the high temperature tempering process strives to achieve optimum of

properties, by regulating the temperature and duration of tempering.

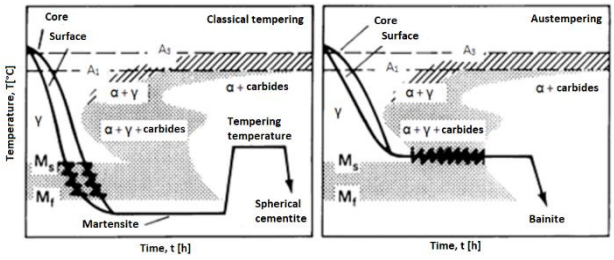

Figure 1. Comparison of classical tempering and austempering heat treatment, [13]

The castings should be tempered immediately after quenching to avoid residual stresses. High temperature tempering of ductile cast iron takes place in two stages. The first stage involves the excretion of carbides similar to that of steel. The second phase generates nucleation and growth of small, secondary graphite grains from carbides. Secondary graphitization results in a corresponding decrease in tensile strength. Since the wt.% of alloying elements affects the secondary graphitization, each alloying element has a unique range of tempering temperatures. The influence of the tempering temperature from 425°C to 700°C for tensile strength, tempered for 2 hours, are shown in Figure 2.

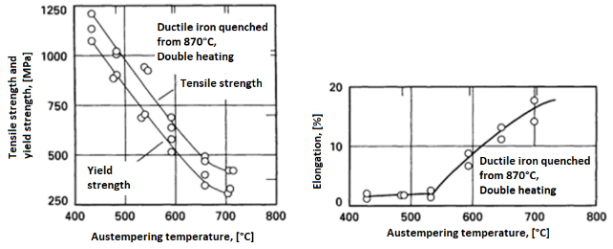

Figure 2: Impact of austempering temperature on mechanical properties of ductile iron quenched from 870°C and tempered for 2 hours. Chemical composition of used ductile iron: 3.52 - 3.68% C, 2.28 - 2.35% Si, 0.02 - 0.04% P, 0.22 -0.41% Mn, 0.91 - 0.99% Ni and 0.045 – 0.065% Mg, [13]

In this paper, heat-treated samples (5 samples of ductile cast iron with a 0.51 wt.% of copper) were tested on a tensile testing machine to obtain tensile strength, elongation and force-extension diagrams. The obtained results were compared with samples (with the same wt.% of copper) on which only austempering heat treatment was performed (with the same parameters) without subsequent high temperature tempering.

2. Experimental work

In this paper, 5 samples of ductile cast iron were prepared which were austepered and then high temperature tempered for tensile testing. Also, 5 samples of the same chemical composition were prepared which were heat treated without high temperature tempering for comparison with the previous samples. The exact chemical composition of the ductile cast iton is as follows: 3.63 wt.% C, 2.61 wt.% Si, 0.135 wt.% Mn, 0.51 wt.% Cu, 0.0035 wt.% S, 0.022 wt.% P, 0.005 wt.% Cr, 0.004 wt.% V, 0.085 wt.% Ni, 0.003 wt.% Mo, 0.017 wt.% Al, 0.013 wt.% Ti, 0.033 wt.% Sn, 0.017 wt.% W and 0.041 wt.% Mg. Proportionately short ductile iron samples for these tests were made in accordance with the ISO 6892-1:2009 standard, as shown in Figure 3.

Figure 3. Ductile iron samples before heat treatment

Ductile cast samples were first austenitized at 850°C for 60 min and then austempered (each sample at different austempering temperature and time). After austempering 5 samples were tempered at 500°C for 60 min. The results after high temperature tempering were compared with the results of austempering without subsequent high temperature tempering. The heat treatment parameters are given in Table 1.

Table 1: Heat treatment parameters

Samples ID		Austempering parameters	
Without high temperature tempering	**With high temperature tempering**	**Temperature, T_a [°C]**	**Time, t_a [min]**
705	719	250	30
715	720	250	120
706	721	331	68
718	722	420	30
709	724	420	120

Austenitization of the samples was performed in an Estherm DEMITERM Easy9 furnace, voltage 230V / 50Hz, power 3 kW, thermal element type K (NiCr-Ni) and maximum temperature of 1150°C. Immediately after the austenitization, the samples were immersed in a salt bath which was used to obtain austempered ductile cast iron. Austempering was performed at temperatures ranging from 250°C to 420°C with holding times at the austempering temperature ranging from 30 min to 120 min, [14]. After the austempering, all samples were cooled on air to room temperature. The austempering furnace is a JPA 6-600 furnace with a power of 3.1 kW and a maximum temperature of 600°C, and the temperature is controlled by a thermal element type K (NiCr-Ni). The type of salt used for the salt bath is AS 140 (50% $NaNO_3$ and 50% KNO_3), [15]. Figure 4 shows

the furnace in which the samples were austempered (left) and the furnace in which austenitization was performed (right).

Figure 4. Austempering salt bath (left) and austenitization furnace (right)

Figure 5 shows the appearance of the samples after high temperature tempering.

Figure 5: ADI samples after high temperature tempering

High temperature tempering was performed on 5 samples simultaneously after previous heat treatments. The furnace used for high temperature yield is a laboratory annealing furnace of ZLATARNA - CELJE, with a built-in controller of temperature and heating time. The maximum operating temperature is 1200°C.

3. Results

The tensile strength test was performed on an analog universal tensile testing machine WOLPERT 20 TUZ 750 with a maximum force of 200 kN. The machine consists of a control unit, an oil pump and a work unit with an integrated analog printer for printing stress diagrams F - ΔL. This test gives the magnitudes of the force, extension and final diameter of the sample. The obtained measurements are shown in Table 2, and the F - ΔL diagram is shown in Figure 6.

Tensile strength was calculated by the following formula:

$$R_m(\sigma_m) = \frac{F_{max}}{A} \quad (1)$$

Elongation was calculated by the following formula:

$$\varepsilon_k = \frac{\Delta l_k}{l_0} \cdot 100\% \quad (2)$$

The measurement results of this static experiment are shown in Table 3, in comparison with the results of tensile strength and elongation of the samples without subsequent high temperature tempering.

Table 2: Results obtained on tensile testing machine

Sample ID	Force, F_{max} [N]	Extension, Δl_k [mm]	Diameter, d_k [mm]
719	74000	7.23	9.6
720	64000	9.52	9.5
721	61600	10.37	9.8
722	66400	16.12	9.5
724	67800	12.8	9.4

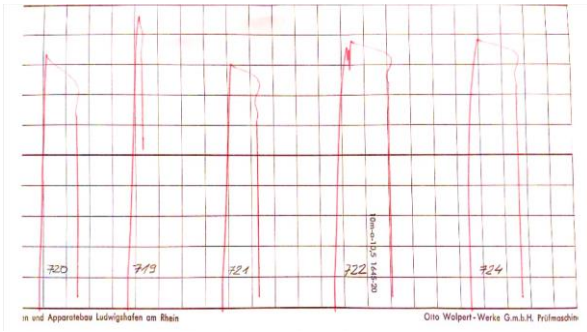

Figure 6: Force-extension diagrams obtained from tensile testing machine

A maximum tensile strength of 1022 MPa was measured on the sample 719 which is obtained at an austempering temperature of 250°C and a holding time of 30 min which also has the lowest elongation. The lowest tensile strength of 817 MPa was measured on the sample 721 which was austempered on 331°C, over a time of 68 min. Furthermore, the highest elongation of 32.24% belongs to sample 722 which was austempered at 420°C for a holding time of 30 min.

In the sample 719, in relation to the sample marked 705, a decrease in tensile strength of ~ 200 MPa is visible, while the elongation increased significantly. Also, in samples 720 and 721 in relation to 715 and 706 there is a decrease in tensile strength. Analogous to the previous alloy ratio, the elongation increases, which is the goal of high temperature tempering. For samples 718 and 709, the austempering temperature was 420°C, which affected a significant decrease in tensile strength compared to samples 722 and 724. The holding time for sample 718 was 30 min and a elongation of 10% was obtained. By holding for 120 minutes at the same temperature for sample 709, the elongation is 1%. Thus, it can be concluded that a longer holding time at a higher temperature negatively affects the elongation of the material. In samples 722 and 724, the high temperature tempering had a positive effect because better mechanical properties were obtained in the form of an increase in tensile strength and elongation.

Table 3: Tensile strength and elongation results

Without high temperature tempering			With high temperature tempering		
Sample ID	**Tensile strength, R_m [MPa]**	**Elongation, ε_k [%]**	**Sample ID**	**Tensile strength, R_m [MPa]**	**Elongation, ε_k [%]**
705	1240	1.3	719	1022	14.46
715	1180	2.2	720	903	19.04
706	929	4.8	721	817	20.74
718	697	10.0	722	937	32.24
709	855	1.0	724	977	25.6

From the obtained results it can be concluded that the tensile strength decreases with increasing austempering temperature, but on the other hand, after austempering at higher temperatures and high temperature tempering, the tensile strength increases again. Elongation increases with increasing austempering temperature, but with the example of sample 724 where the holding time is 120 min, there was a decrease in elongation which is still very good compared to sample 709 which is not tempered.

4. Conclusion

The heat treatment parameters affect the microstructure of the samples on which the mechanical properties of austempered ductile cast iron depend. Just as the chemical composition of the alloy itself is important, so are the temperature and heat treatment time. By varying these parameters, variations of mechanical properties are obtained, depending on what is needed to be achieved by heat treatment.

In industry, high temperature tempering is used as an effective heat treatment to reduce the brittleness of the material and remove residual stresses in the material. Elongation and strength are optimized, i.e. increased. The final mechanical properties depend on the tempering temperature and tempering time and the wt.% of alloying elements.

After high temperature tempering, the strength for the austempering temperatures of 250°C and 331°C decreased, while for the temperature of 420°C it increased in relation to the strength of the samples without tempering. Elongation increased significantly. The reason for the superior mechanical properties is the change in the microstructure of the samples with tempering, which will be focus of the next experiments. It is assumed that the obtained microstructure is more homogeneous, so the properties of different samples are more uniform. The ausferrite should be more uniform and there are fewer ferritic phases in the microstructure.

Since there is no previous research on the topic of this kind of heat treatment combination, it would be good to further apply electron microscopy to determine the exact phases that formed after the subsequent high-temperature tempering.

REFERENCES

[1] Labercque C., Gagne M., (1998), *Ductile Iron – Fifty years of continued development*, Rio Tinto Iron & Titanium, Quebec, Kanada.

[2] Žmak I., (2008), *Modeling the structure and properties of ductile cast iron by neural networks*, doctoral thesis, FSB, Zagreb.

[3] Global casting production trend and conclusion in 2014, http://www.pinepacific.com/news_detail.php?idnews=93.

[4] Čatipović N., (2018), *Influence of copper and heat treatment on the properties of austempered ductile iron*, doctoral thesis, FESB, Split.

[5] Stupnišek M., Cajner F., (2001), *Basics of metal heat treatment*, University of Zagreb, Zagreb, 2001.

[6] Engels G., (2003), *Half a century of foundry technical progress in the mirror of GIFA*, Proceedings of the 43rd Foundry Conference, CD-ROM edition, Portorož, Slovenija, September 2003.

[7] Foundry Industry 2020: Trends and Challenges, https://www.heat-processing.com/fileadmin/HPO/Dateien_Redaktion/Selected_Reports/150616_GIFA_Presentation_EN.pdf.

[8] Sponseller D. L., Scholz W. G., Rundle D. F., (1968), *Development of Low-Alloy Ductile Irons for Service at 1200-1500 F*, AFS Trans. 76, p 353-368.

[9] Sahoo S. K., (2012), *A study on the effect of austempering temperature, time and copper addition on the mechanical properties of austempered ductile iron*, NIT, Rourkela.

[10] Cast Metals Development Ltd., (1992), *Austempered ductile-iron castings — advantages, production, properties and specifications*, Materials & Design 13, No. 5.

[11] Keough J. R. Hayrynen K. L., Pioszak G. L. (2010), *Designing with Austempered Ductile Iron (ADI)*, Applied Process Inc. Technologies Division, Livonia, MI ; University of Michigan, USA.

[12] Nofal A., (1992), *Austempered Ductile Iron (ADI) Production, Properties and Applications* CMRDI, Kairo, Egipat.

[13] ASM Metals Handbook Volume 04 – Heat Treatment, *Heat Treating of Ductile Irons*

[14] Dubal G. P, (1991), *Salt bath Quenching*, Advanced Materials & Processes, Birmingham

[15] Hef Durferrit, http://www.hefdurferrit.de/en/

ISSN 1847-7917

Using reverse engineering for optimization and modeling of motorcycle brake caliper brackets

Nikša ČATIPOVIĆ, Nikola GJELDUM, Andrej BAŠIĆ, Ante TURKOVIĆ, Zvonimir DADIĆ

University of Split, Faculty of Electrical Engineering, Mechanical Engineering and Naval Architecture, Ruđera Boškovića 32, 21000 Split, **Croatia**

Niksa.Catipovic@fesb.hr
Nikola.Gjeldum@fesb.hr
Andrej.Basic@fesb.hr
Ante.Turkovic.00@fesb.hr

Keywords

Reverse engineering
3D modeling
3D printing
Motorcycle brake calipers

Professional paper

Abstract: Reverse engineering is a process of analyzing existing components to obtain enough data to replicate design or knowledge of those parts. Data obtained during reverse engineering can be used to lower production costs, improve component properties, or replace components. In this paper reverse engineering was used to obtain information from wooden model of the motorcycle brake caliper brackets to redesign and improve that component of the motorcycle. First step of the process was to 3D scan the wooden model. Then scan was transferred to CATIA design software for redesign. From there all precise dimensions were defined and final improved models could be 3D printed. Using reverse engineering process on this component allowed us to manufacture new brake caliper brackets so that larger brake discs could be installed thus improving braking power of the motorcycle. In this way original front forks and brake calipers could be used thus eliminating need of upgrading those components and lowering overall cost of the process.

1. Introduction

Reverse engineering is a process of analyzing existing product components for the purpose of replicating the design or knowledge that will be formed from the extracted information. A typical reverse engineering project involves working backwards on a particular product to establish the technology and design applied by the original manufacturer. The extracted information allows users of the reverse engineering process to reproduce or change the product, [1].

Designers and engineers are always looking for ways to improve new and existing products. The reverse engineering process provides access to the information and knowledge needed to change and improve the product manufacturing process and its working capabilities. Simplification of the production process can lead to cheaper and ultimately improved production, [1].

Reverse engineering process usually consists of three steps: 3D scanning, 3D modeling using CAD software and 3D printing of the prototype.

3D scanning is a non-contact non-destructive technology that digitally captures the shape of an object using a laser. 3D scanners create "position clouds" of data from the surface of the object. In other words, 3D scanning is a way of storing the exact size and shape of objects in a computer as a three-dimensional digital representation. 3D laser scanners measure to the smallest detail and record all types of shapes to recreate "position clouds" of data in a very short time. 3D scanning is the optimal method for measuring and inspecting objects of complex shapes that require a large amount of data for their correct description, [2, 3, 4].

CAD (computer aided design) software is a type of computer program used by designers and engineers to create two-dimensional and three-dimensional models of physical components, [5].

Also, CAD is a technology intended for the design and production of technical documentation that has replaced the classic manual drawing with an automated process, [4].

There are different ways of creating CAD 3D models, among which are creation by users or engineers or designers, through the user interface and reverse engineering. In the past, the problem was creating CAD 3D models by merging different surfaces because those surfaces would seemingly appear connected in CAD software, but a prototyping machine would generate something completely different from what was conceived and created in CAD. Today, such problems no longer exist because every CAD software register surfaces as design features and the software itself informs the user if an error has occurred when creating a 3D model, [6].

3D printing is a computer-controlled process of joining materials that form a three-dimensional object. One such

process for making prototypes or functional objects is called material extrusion.

The most used material extrusion technology is combined precipitation modeling. The low-melting thermoplastic mass is fed to an extruder where it is melted and applied to a working substrate on which it is immediately hardened.

This method significantly reduces the amount of material required for prototyping and makes it easier to create multiple variants of prototypes for testing. The application of the material is performed in layers so that each prototype is the application of layers of a certain thickness to the substrate, [7].

The advantages of 3D printing are:

- Easy prototyping to test different applications
- the speed of availability of the prototype depending on the complexity of the model itself
- repeatability, i.e. reprinting is easy and as such does not require a different acceptance on the machine or tool change
- the price is much lower compared to the standard manufacturing process on CNC machines, [7].

The disadvantage of 3D printing is the limited range of materials, [7].

Most additive manufacturing devices use the same coating method. This is mainly done via a vertically adjusting platform on which the workpiece is generated by depositing the material and forming layer by layer the cross section of the workpiece. Some 3D printers precipitate materials and form a cross section at the same time, while other 3D printers separate it. Each printer repeats the same operation repeatedly until the entire model is created or until the application material disappears. In this case, the device notifies the operator, [6].

2. Reverse engineering process

Aim of this paper was to modify and improve the existing brake caliper bracket of the Yamaha T-max motorcycle to improve braking performance.

The purpose of the customized mentioned bracket is to be able replace factory brake discs with a diameter of 267 mm, Figure 1, with larger brake discs with a diameter of 298 mm on the existing front forks, Figure 2. In this way, the braking momentum is increased which improves braking performance and the factory brake calipers are retained.

The reverse engineering process begins with a 3D scan of the obtained wooden model of Yamaha T-max bracket of inappropriate dimensions and surface quality, after which the obtained scan is transferred into the software for processing triangular meshes "*Mesh*". In the mentioned software, the object is placed in the basic XY plane, which serves for easier post-processing in the CAD software where the basic initial scan is corrected and improved in order to obtain the final model by 3D printing.

Figure 1. Factory brake disc 267 mm, [8]

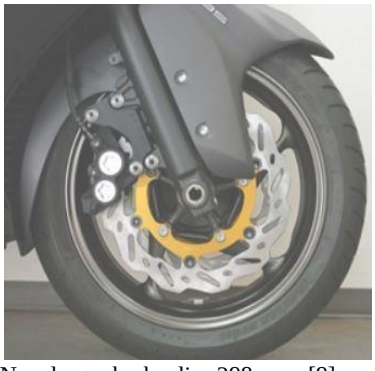

Figure 2. New larger brake disc 298 mm, [9]

2.1. 3D scanning and meshing

The initial wooden model, Figure 3, of the Yamaha T-max bracket was scanned with a "*David 3D Scanner Pro v4.5.3*" scanner.

Figure 3. Initial wooden model of the bracket

The first step consists of setting up the camera and projector of the scanner. The angle of the camera is set at 20-25 degrees to the projector, after which the bracket is placed so that it is in the center of the illuminated projection emitted by the projector. It then adjusts the focus of the projector making sure that the vertical and horizontal lines are clearly visible on the piece being scanned, which ultimately affects the correct 3D display by better describing the shape and depth of the workpiece.

The brightness of the projector is set to the maximum value and the shutter speed to 1/60 s. After adjusting the

camera and projector, a calibration process is required by which the scanner software obtains the necessary object size information for accurate scanning and display on a computer.

A calibration plate was used, which comes with the scanner, and a sample is selected on it, the size of which is a maximum of twice the size of the object to be scanned. The calibration plate is then moved to the location where the object was previously set relative to the camera and projector, after which the projector is self-calibrated and optimized for further scanning. After calibration, the bracket is placed in the intended place and scanning starts, Figure 4., whereby after each scan the object is rotated by approximately 15 degrees to capture each part of the surface of the scanned object.

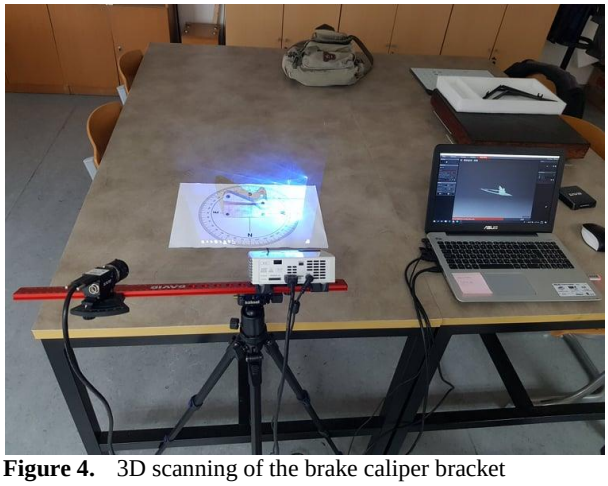

Figure 4. 3D scanning of the brake caliper bracket

Scanning is performed consecutively until the subject of the scan is completely covered, Figure 5., after which in the software with the tool "*Shape fusion*", Figure 6. all scans are merged into a single shape by recognizing the texture, Figure 6.

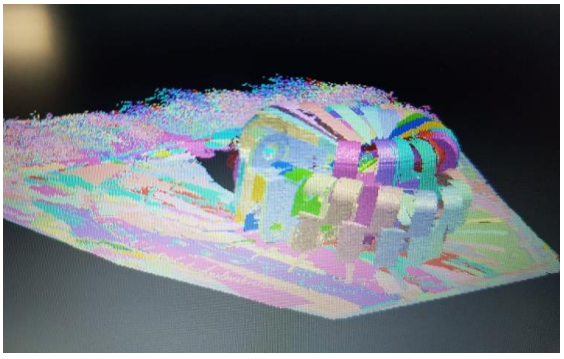

Figure 5. 3D scans of all bracket positions

After obtaining a unified scan in "*David 3D Scanner Pro v4.5.3*", the scan is saved in the form of a "*.obj*" file that needs to be converted to a "*.stl*" file in order to be used and processed in CAD software. The resulting "*.stl*" file can then be used in most "*mesh*" processing programs and for 3D preparation for 3D printing such as "*Meshmixer*".

Since the processed Yamaha T-max brake caliper bracket requires dimensional and surface accuracy, the "*Meshmixer*" program is not suitable for its precise processing, but only serves to position the piece in the XY plane for practical printing in the final phase of the reverse engineering process.

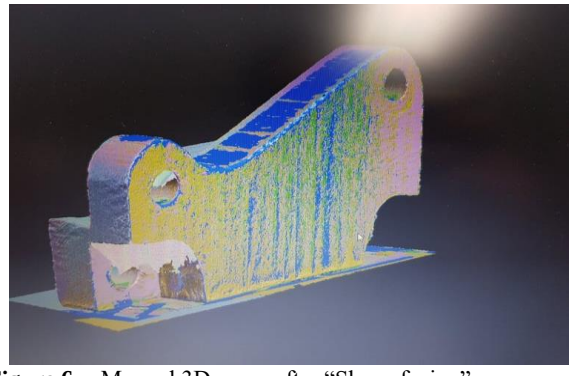

Figure 6. Merged 3D scans after "Shape fusion"

2.2. 3D modeling

As already mentioned, 3D modeling of objects, which must be dimensionally accurate and which must have a precise surface quality and meet certain engineering tolerances, cannot be performed in standard "mesh" processing programs, but it is necessary to select a program suitable for precise engineering use.

Therefore, the software for 3D CAD design "Catia V5" was used, in which it is possible to extract the full potential of the scanned adapter and prepare it for further processing and 3D printing.

The goal set in Catia is to get a ready-made model of adapter that is ready for 3D printing, which means that it is necessary to process the whole piece, ie smooth all surfaces, correct dimensional errors and properly install holes that will close due to distortion after scanning.

The initial procedure is reduced to placing planes around the entire adapter, so that in the end, by trimming and cutting the same planes, the shape of the desired object is obtained, i.e. the adapter, but with smooth surfaces.

Due to the previous positioning of the piece, the coordinate system is set correctly in advance and the creation of planes begins, and thus the shaping of the piece.

Figure 7. shows initial plane constructed on imported model from which final model will be made. Since the imported model is not perfect the plane does not lie perfectly on the model but that will be corrected with next steps of 3D modeling.

Due to irregularities of the initial wooden model and scanning errors, other planes must be constructed in a way that they are perpendicular to each other so that the final model can be 3D printed. The sides parallel to the YZ plane are made first and then sides under a 90-degree angle. In this way initial model is completely, Figure 8. Next step is to trim all the planes in order to obtain rectangular around initial wooden model, Figure 9.

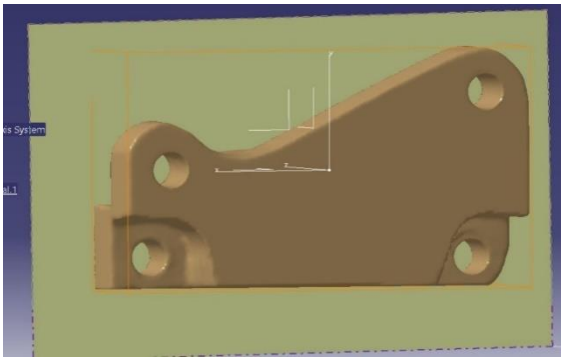

Figure 7. Initial plane constructed in CATIA V5

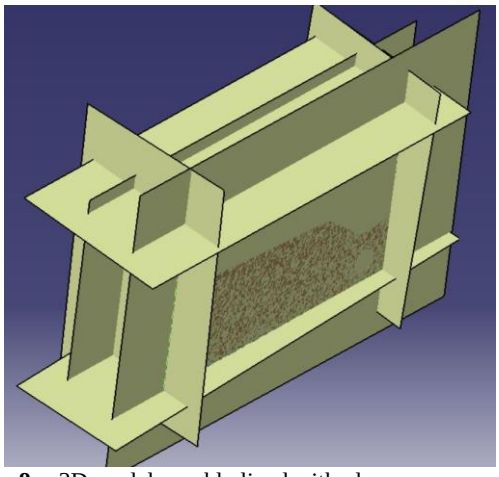

Figure 8. 3D model roughly lined with planes

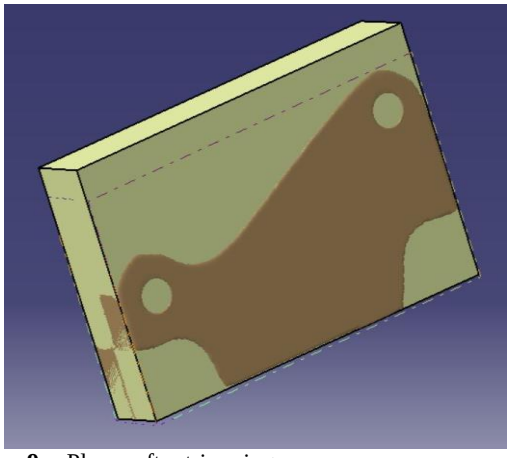

Figure 9. Planes after trimming

The resulting planes will in the future represent the sides of the bracket with satisfactory surface quality as opposed to the "mesh" condition originally imported in the CATIA V5. The display of all the rounded sides of the adapter is much more complicated to recreate precisely because of its shape, so it is necessary to apply a different approach when creating planar linings on the model.

In this case, it is necessary to use the tool "Planar sections" which serves to register all types of plane shapes and finally draw them on the model, which allows drawing a "sketch" and finally creates a complicated plane shape.

The curve that covers the piece of the selected plane allows the use of the tool "Sketch from scan" by selecting the scan achieved using "Planar sections". In the next step scan created in previous step is selected and used for curve creation, Figure 10.

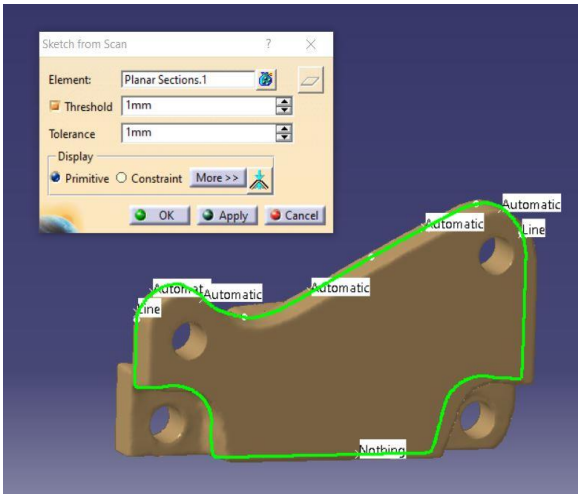

Figure 10. Using sketch from scan to form curved surface

Finally, using different tools, a drawing or "sketch" is created, which is extracted and a surface according to the shape of the scan from "Planar sections" is created, Figure 11.

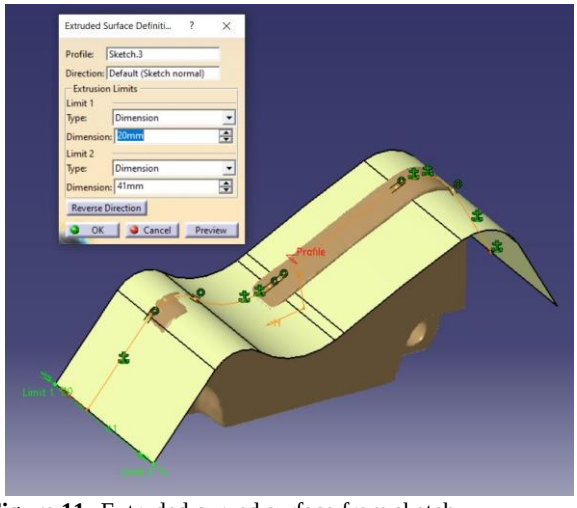

Figure 11. Extruded curved surface from sketch

The newly formed extruded plane is incorporated into the bracket model by a repeated trimming process. The same procedure creates all the complex planes that are joined by trimming into a base piece which was initially a rectangle, and ultimately the required shape of the bracket is obtained, still irregular in size and without needed holes. Holes are intentionally closed due to their distortion after scanning, which will later allow the holes to be made to the correct shape and dimensions.

By achieving the correct shape of the bracket using planes and trimming them, it is necessary to control the dimensions of the entire piece because 3D scanning is not able to show the exact dimensions of the bracket.
Correction of the dimensions is achieved with the tool "Scaling" which increases or decreases the model in a certain direction according to the instructions. By comparing the measures measured on the initial wooden model and the measures of the current condition of the model in CATIA, using the “Measure between” tool, a ratio of measures is obtained. With the help of the obtained ratio of measures, it is concluded how much and in which direction the current model is larger or smaller in relation to the initial wooden model.
Achieving the correct external dimensions of the bracket allows the hole to be machined. Holes are last to be machined because otherwise the dimensions of the holes would change and correct holes positions and measurements are the most important on the entire bracket for mounting both forks and brake calipers, which is the primary function of the bracket.
The holes are made with the "Hole" command in the "Part design" menu, the window of which allows the drawing ("sketch") to determine the exact position and dimensions of the hole and to give the choice of threading if necessary.
To make it easier to position the drill according to the required measures, it is necessary to reduce the background grid of the program interface in the CATIA settings so that the side of each square is one millimeter. After drawing the circle and its exact positioning in accordance with the dimensions in the drawing, the “Hole” tool window reappears, creating an opening in the place of the drawing of suitable dimensions. The procedure is repeated for the remaining three holes, all of which are eleven millimeters in diameter, Figure 12. The bottom two holes require a thread specified for the M10 screw.

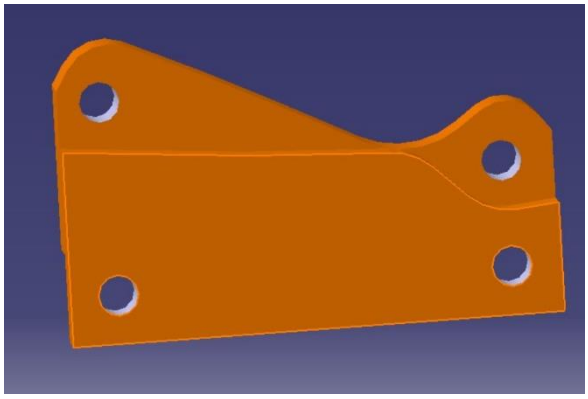

Figure 12. Finished holes on the model

Finally, the correct shape of the bracket with required dimensions has been achieved and it is necessary to improve the created model by reducing the mass for better performance.

The “Pocket” tool allows to sketch any shape and then select the depth of the same shape in the piece, Figure 13. The pocket is created according to the "sketch" and in a specific position on the drawing.

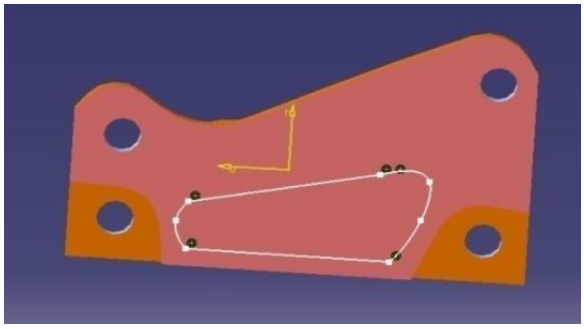

Figure 13. Positioning of the pocket sketch

Also, to reduce the stress concentration and the possibility of the formation of the initial crack, it is necessary to round all the sharp edges using the tool "Edge fillet". A radius of curvature of one millimeter is selected after which the modeling is completed and the final model is obtained, Figure 14.

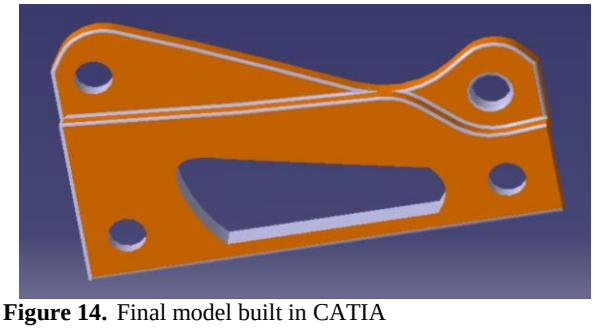

Figure 14. Final model built in CATIA

2.3. 3D printing

After obtaining the final model in CATIA V5, it is necessary to save it in the ".stl" format, which the 3D printer (in this case "CubePro") can recognize. In the "Build" tool located on the toolbar of the program 3D print settings are selected, Figure 15.
The layer resolution is set to two hundred microns, the print strength to "Almost solid" and the print pattern to "Honeycomb".
After entering the settings, the 3D print or layered stacking of the amorphous polymer "ABS" begins until the shape of the model entered as a ".stl" file is formed.
Due to the closedness of the "Cube Pro" 3D printer, high operating temperatures occur, which leads to the adhesion of the flat surface to the substrate, and thus to poorer surface quality, which makes it necessary to re-perform the printing process, Figure 16.

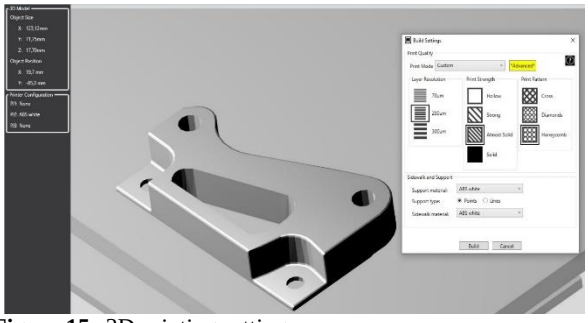

Figure 15. 3D printing settings

Figure 16. Results of first 3D printing

The second printing gave much better results which were further improved by subsequent abrasive surface treatment, Figure 17.

Figure 17. Results of second 3D printing from both sides

The polymer model obtained by 3D printing is suitable for checking how it fits on a real Yamaha T-max motorcycle. Based on this check, it is concluded that the manufactured model meets all dimensional and surface requirements and that it is suitable for the production of the final metal product on a CNC machine.

3. Conclusion

Reverse engineering plays a major role in the field of modern practical sciences and improves existing products and comparatively reduces the cost of manufacturing the same as shown in this paper by improving the existing Yamaha T-max brake adapter.

3D scanning of the initial model gave the possibility of detailed processing and improvement of objects by 3D modeling as seen on the processed bracket.

The scanning yielded many different scans that needed to be merged into a final scan that incorporates all the planes and each view of the adapter that was transferred to the CAD software tool "CATIA".

In CATIA, objects are processed and improved with various tools, which includes correcting the dimensions, symmetry, flatness of the planes, comparability and verticality of the planes and the quality of the surface and reducing the weight of the model itself.

The computer-aided design has achieved the conditions for mounting larger brake discs on the existing forks of the factory T-max motorcycle, thus enabling higher braking forces while retaining the factory brake calipers.

In the last step, the obtained finished model made in "CATIA" was printed with a 3D printer, thus gaining insight into the quality of previously completed processes.

This type of computer processing and subsequent retrieval of a physically enhanced object requires certain expensive computer tools, a 3D scanner, a 3D printer and, at the end of the process, a CNC machine. Also, a great knowledge of the modeling and processing process and a general thorough knowledge of the natural sciences is required.

REFERENCES

[1] Cambridge design technology, *Reverse engineering*, web: https://www.cambridge-dt.com/reverse-engineering/.

[2] Laserdesign, *3D scanning technology*, web: https://www.laserdesign.com/what-is-3d-scanning.

[3] Peko I., Bašić A., Aljinović A., (2018), *Computer aided design, additive manufacturing and 3D scanning of products*, FESB, Split.

[4] Autodesk, *What is CAD*, web: https://www.autodesk.com/solutions/cad-software.

[5] study.com, *What is CAD software*, web: https://study.com/academy/lesson/what-is-cad-software-definition-uses.html.

[6] Bajić D., Peko I., (2015), *Rapid prototyping, additive manufacturing*, FESB, Split, 2015.

[7] Enso, *3D printing*, web: http://enso.hr/3d-printanje/.

[8] Web: http://road.moto-nautika.com/yamaha-tmax-dx/.

[9] Web: https://www.webike.com.kh/products/21285560.html

ISSN 1847-7917

Design and Improvement of High Pressure Die Casting Process based on NovaFlow&Solid Software

Ivana DUMANIĆ[1)], Sonja JOZIĆ[1)], Deni DUMANIĆ[2)], Luka NIMAC[1)]

1) Faculty of Electrical Engineering, Mechanical Engineering and Naval Arhitecture, University of Split Ruđera Boškovića 32, 2100 Split, **Republic of Croatia**
2) Croatian Military Academy, Ilica 256b, 10000 Zagreb, **Republic of Croatia**

iduman00@fesb.hr
sonja.jozic@fesb.hr
ddnsc55@yahoo.com
lnimac00@fesb.hr

Original scientific paper

Abstract: In the present paper, investigation of the temperature of the molten metal, mould temperature, plunger velocity at the 2nd phase and pressure on shrinkage of the material and total casting time is presented. Simulation of the high pressure die casting process was observed. Therefore, the investigation of this casting process was based on simulation software NovaFlow&Solid. In addition, Taguchi based orthogonal array is adopted to set design of experiment. Grey relational analysis is used to identify the optimal process parameters. The optimal levels of the controllable parameters were the temperature of the molten metal of 640 °C, mould temperature of 150 °C, 2nd phase velocity of 2.5 m/s and pressure of 10 MPa.

Keywords

HPDC
NovaFlow&Solid
Taguchi method
Grey relational analysis
Multi-objective optimization

1. Introduction

Casting is a process in which molten metal is poured into a mould or die. The advantage of casting is the achievement of castings with complex geometry, with high dimensional accuracy, which would otherwise have to be assembled from several parts or machined. Setting the proper size of the gating system for casting is the basis for a proper and quality casting process. Casting is a complex process and many influential parameters need to be optimized. The final properties of the casting are influenced by many parameters such as alloy composition, construction of cast part, construction of tool (mould), process parameters, etc. Therefore, great importance is given to process optimization to achieve higher productivity and good mechanical properties of the final product. High pressure die casting (HPDC) is a process in which products are formed by injection of molten metal at high pressure and relatively high speed into the mould or die. With this procedure, it is possible to achieve castings of complex shape and thin-walled castings because the melt under pressure is able to fill all the places in the mould. The pressure in the mould is maintained until the solidification of the casting is complete. The most commonly cast materials, with this technology, are aluminium alloys, copper alloys, magnesium alloys and zinc alloys. These materials have good mechanical properties and have a low melting point. The HPDC is characterized by excellent surface finish and dimensional accuracy [1], [2]. The filling of the die cavity through the plunger motion takes place in three continuous phases. In the 1st phase, the molten metal fills the shot sleeve and the plunger begins to move at a low velocity. In the 2nd phase, filling of the die cavity is done at high velocity (2nd phase velocity) to avoid premature solidification at the gate and incomplete castings. In the 3rd phase, high pressure (in the next chapters is called 'pressure') is applied to the molten metal once the die cavity is full [3]. But, in HPDC process there are also a lot of essential parameters that influence the quality of the process. In other words, mechanical properties of the final product depend on the temperature of molten material, mould temperature, process pressure, injection speed and metal velocity at the gate [4]. Different phenomena can occur during casting such as turbulent flow, microporosity, unfilled phenomena, etc. Nowadays, there are various ways to reach the optimal process parameters and in practice this is done mainly on the basis of experience and using computer simulations. A lot of researchers, in order to reduce the performing of numerous experimentations (to save time and to reduce the costs), have used numerical simulations of high pressure die casting. Kwon and Kwon used the simulation software (AnyCasting) in order to optimize the gate and runner design of an automobile part in HPDC process. ProCAST simulation software was used to simulate the high pressure die casting of tensile test

samples [5] and automobile part [6]. Duan et al [7] concluded that simulation results of HPDC of automobile part are more accurate with FLOW-3D software in comparison to ProCAST software. Balikai et al [8] used Taguchi method to identify optimized parameters (pouring temperature, pressure, plunger velocity) in order to minimize porosity in HPDC processes. Minimum porosity formation was the aim of Hsu and Do [9] research. In addition, the Taguchi method was used in order to optimize holding furnace temperature, die temperature, plunger velocity and pressure.

Because of all noted, optimization of the temperature of the molten metal, mould temperature, plunger velocity at the 2nd phase and pressure is obtained in this work. First, for experimental planning, the Taguchi design approach is used. In addition, multi-objective optimization is achieved with the grey relational analysis. In order to eliminate empirical tests, all experiments were performed by a commercial software NovaFlow&Solid. The simulated results enable to optimize HPDC process what is meaningful for practical production.

2. Material

2.1. Material characteristics

In this research, aluminium alloy EN AC 46000 is used in simulations as casting material. The chemical composition is given in Table 1.

Table 1. Chemical composition of aluminium alloy EN AC 46000

Elements	Al	Si	Mg	Mn	Cu	Fe	Ni	Zn	Ti
Wt. [%]	84.04	10	0.2	0.3	3	0.8	0.15	1.5	0.01

Material's database (liquid fraction distribution, thermal conductivity, density) for different temperatures are adopted from software NovaFlow&Solid and presented in Figure 1.

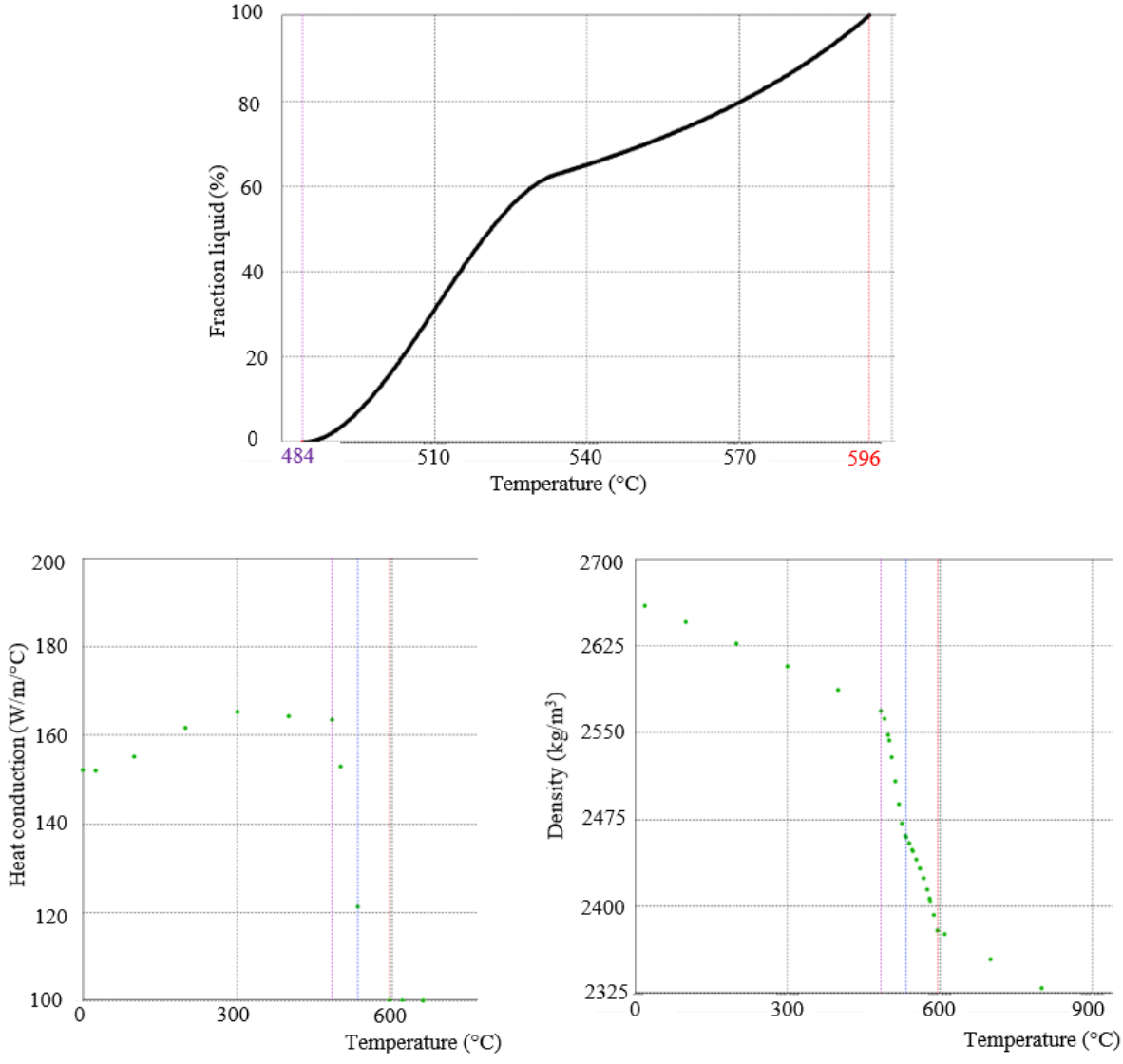

Figure 1. Material's properties of EN AC 46000 for different temperatures

2.2. Design of a casting model

A three-dimensional model of the casting (mechanical part) is conducted by means of SolidWorks. In addition, runner, gates and overflows are modelled taking into account the properties of the casting material and the properties of the HPDC process. Runner geometry and casting model with a total number of four cavities are presented in Figure 2.

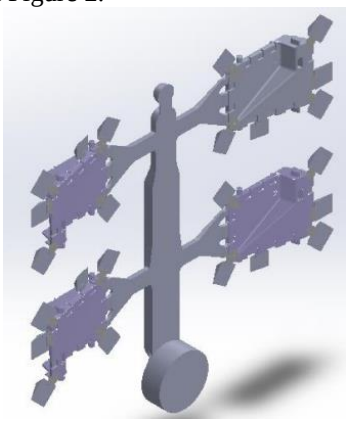

Figure 2. The three-dimensional model used for simulations

3. Methodology

After modelling the 3D casting model, the second step for production and optimization is defining the significant HPDC parameters that affect output variables. After selecting the number of significant variables and the number of levels for them, the appropriate design of experiments is defined. According to the design of experiments, simulations of the HPDC process are done and data analyses are obtained.

Table 2. Process parameters and their levels

Controllable parameters	Level 1	Level 2	Level 3
Temperature of the moleten metal, *Tmm* [°C]	640	670	700
Mould temperature, *Tmo* [°C]	150	200	250
2nd phase velocity, *v* [m/s]	1.5	2.5	3.5
Pressure, *p* [MPa]	10	20	30

The temperature of the molten metal, mould temperature, 2nd phase velocity and pressure were set as parameters that have influence on the total casting time and shrinkage of the material. All of these factors have three levels as shown in Table 2.

As noted earlier, four controllable parameters with three levels are considered in this research. Thus, Taguchi's orthogonal array (L9) is selected to organize the experiments. The plan of the experiments (with nine rows and four columns) is shown in Table 3.

Table 3. Taguchi's L9 orthogonal array

Simulation trials	*Tmm* [°C]	*Tmo* [°C]	*v* [m/s]	*p* [MPa]
1	640	150	1.5	10
2	640	200	2.5	20
3	640	250	3.5	30
4	670	150	2.5	30
5	670	200	3.5	10
6	670	250	1.5	20
7	700	150	3.5	20
8	700	200	1.5	30
9	700	250	2.5	10

4. Simulation setup

After modelling the 3D casting model, it is imported into the NovaFlow&Solid software as the *stp* file. The total number of control volume cells was around 500 598 and the dimension of the cell was 3.063 mm. The material of the mould was tool steel H13. Other casting process parameters are defined by the chosen design of experiments (Table 3).

5. Process simulation results

In the beginning, it is imported to confirm that casting parameters are correctly set and construction of the casting is correctly designed. It can be confirmed by the mould-filling process of the simulation, Figure 3.

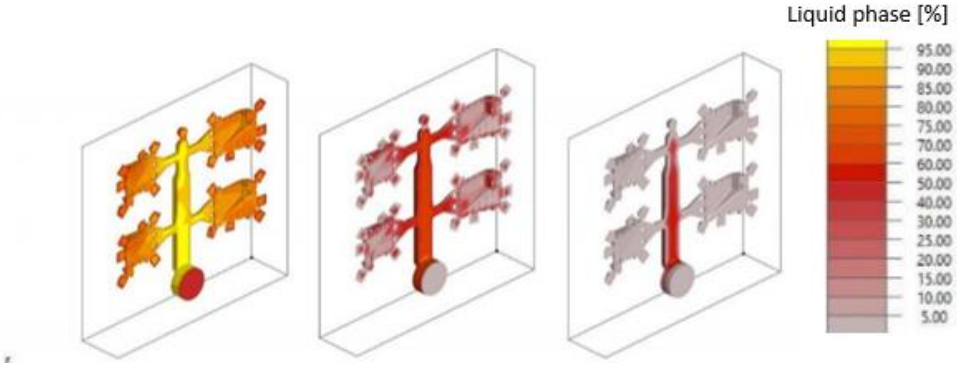

Figure 3. Solidification of molten metal

After each process simulation run, values of the total casting time and shrinkage of the material are obtained from the report, Table 4. The maximum value of the shrinkage is in the 3rd trial. On the other hand, the maximum value of the total casting time is in the last trial (9th trial). In the next chapter, multi-objective optimization will be performed by using grey relational analysis.

Table 4. Shrinkage and total casting time obtained from simulations

	Tmm [°C]	*Tmo* [°C]	*v* [m/s]	*p* [MPa]	Shrinkage [%]	Total casting time [s]
1	640	150	1.5	10	2.409	10.300
2	640	200	2.5	20	2.697	10.800
3	640	250	3.5	30	3.113	12.013
4	670	150	2.5	30	2.587	10.483
5	670	200	3.5	10	2.282	11.091
6	670	250	1.5	20	3.088	12.969
7	700	150	3.5	20	2.783	10.798
8	700	200	1.5	30	2.536	12.040
9	700	250	2.5	10	2.244	13.239

Shrinkage results of the 3rd trial (run with the largest shrinkage) and 9th trial (run with the smaller shrinkage) are presented in Figure 4.

6. Grey relational analysis

Grey relational analysis (GRA) is the method used for the optimization of controllable parameters as well as their mutual influence. Depending on the criteria, grey relational analysis gives the optimal combination of all parameters taken into consideration. To established mentioned, the required steps are described below.

At the beginning of the GRA, it is important to normalize the data to enable data comparability. Values of shrinkage formation and total casting time are normalized by the following formula:

$$y_{ij} = \frac{\max x_{ij} - x_{ij}}{\max x_{ij} - \min x_{ij}} \quad (1)$$

where y_{ij} is the value after the grey relation generation, x_{ij} is the value of the simulation data for the j_{th} response of i_{th} simulation (min – the smallest value, max - the largest value). It is important to mention that smaller-the better performance characteristic has been used because the small values of shrinkage of material and total casting time are desirable for the casting operations. It can be noticed from Table 5 that all normalized values are between zero and one.

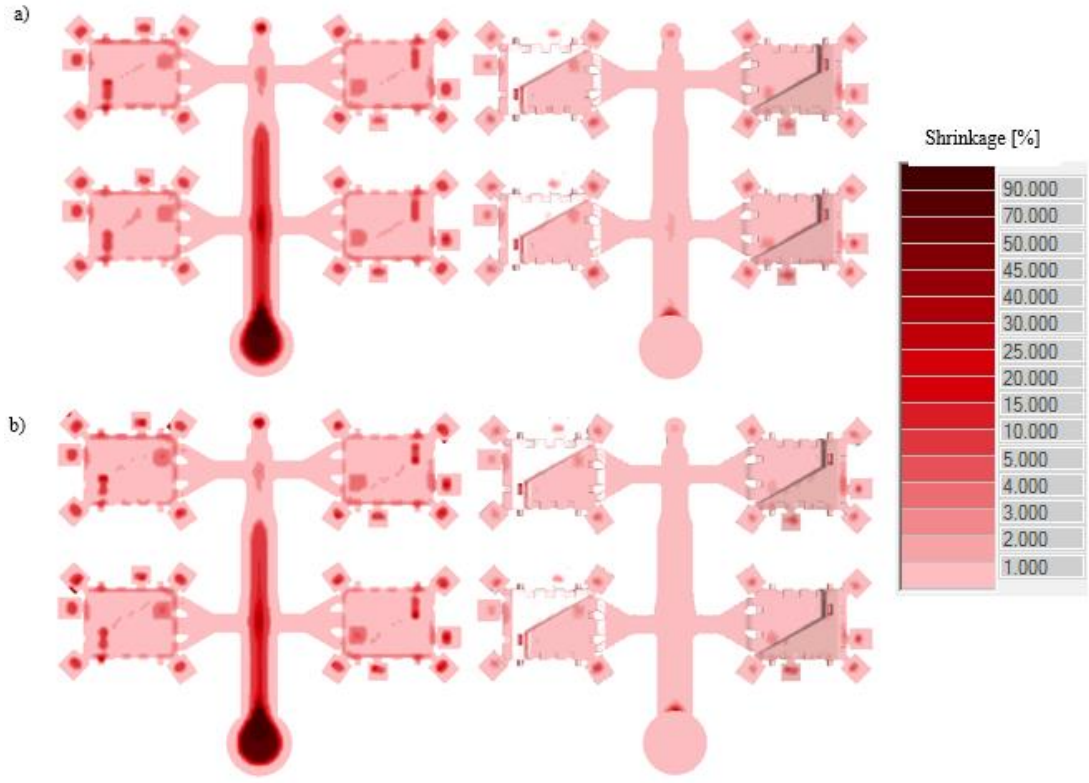

Figure 4. Comparison of shrinkage results for a) 3rd trial, b) 9th trial

Table 5. Normalized simulations results

	Shrinkage [%]	Total casting time [s]
1	0.810	1
2	0.479	0.83
3	0	0.417
4	0.605	0.938
5	0.965	0.731
6	0.029	0.092
7	0.380	0.831
8	0.633	0.408
9	1	0

The next step of the GRA is a determination of the referent value y_{0j} for j_{th} response. The normalised value y_{ij} closest to 1 is considered as the referent for the response j. Therefore, 9th simulation is considered as the referent for the shrinkage of material and 1st simulation for the total casting time. Table 6 shows the deviation of every simulation run in comparison to the reference sequence.

Table 6. Deviation sequences

	Shrinkage [%]	Total casting time [s]
1	0.190	0
2	0.521	0.17
3	1	0.583
4	0.395	0.062
5	0.044	0.269
6	0.971	0.908
7	0.620	0.169
8	0.367	0.592
9	0	1

Next, calculation of the grey relation coefficient ξ_{ij} is examined by the following formula:

$$\xi_{ij} = \frac{\Delta_{min} + \zeta\Delta_{max}}{\Delta_{ij} + \zeta\Delta_{max}} \quad , \quad \Delta_{ij} = \left| y_{0j} - y_{ij} \right| \tag{2}$$

where ζ is distinguishing coefficient, $\zeta \in (0,1]$. ζ_{ij} is used for determining the relation degree between simulation results and referent value. ζ is generally set at 0.5 to assign equal weights to every parameter [10].

The fourth step is the simplification of the complex multiple response optimization problem by determining a grey relational grade (GRG):

$$z_i = \frac{1}{n}\sum_{j=1}^{n} \xi_{ij} \tag{3}$$

The simulation with the highest GRG would be the best choice as this one have the closest corresponding controllable parameter combination to optimal, Table 7.

Table 7. Grey relational grade and grey relational order

	Shrinkage [%]	Total casting time [s]	GRG	Order
1	**0.725**	**1**	**0.862**	**1**
2	0.490	0.746	0.618	5
3	0.333	0.462	0.398	8
4	0.559	0.889	0.724	3
5	0.920	0.650	0.785	2
6	0.340	0.355	0.347	9
7	0.446	0.747	0.597	6
8	0.577	0.458	0.517	7
9	1	0.333	0.667	4

As A1B1C1D1 combination is only the nearest to optimal, it is necessary to calculate the means of the grey relation grades for each level of controllable parameters. The level with the highest grey relation grey is optimal, Table 8. Therefore, the optimal levels of the controllable parameters are the low temperature of the molten metal (640 °C), low mould temperature (150 °C), intermediate 2nd phase velocity (2.5 m/s) and low pressure (10 MPa), highlighted in grey in Table 8 (A1B1C2D1).

Table 8. Means for grey relational grades

Parameter	Level 1	Level 2	Level 3	Rank (max-min)
Temperature of the moleten metal, *Tmm* [°C]	0.626	0.619	0.594	0.032
Mould temperature, *Tmo* [°C]	0.728	0.640	0.451	0.277
2nd phase velocity, *v* [m/s]	0.576	0.670	0.593	0.094
Pressure, *p* [MPa]	0.771	0.521	0.546	0250

Graphs in Figure 5 shows the dependence of grey relational grade to temperature of the molten metal, mould temperature, 2nd phase velocity and pressure, separately.

After defining the optimal combination of controllable parameters it is desirable to know which controllable parameter affects the performance characteristic the most. It can be done by method called analysis of variance (ANOVA) [11], [12].

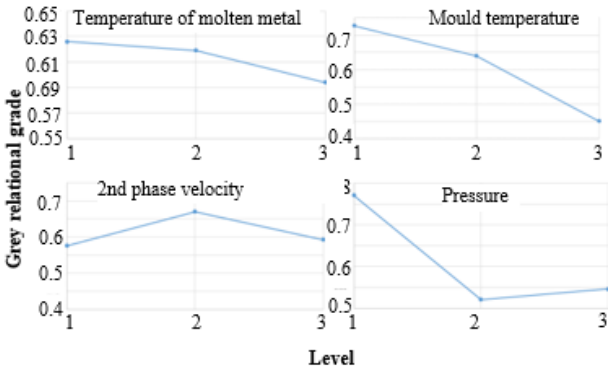

Figure 5. Relation of the grey relation grade to input parameters

The most significant controllable parameter is pressure (48.56%), then mould temperature (43.62%) and 2nd phase velocity (6.37%). Negligible impact on total casting time and shrinkage of material has temperature of molten metal, Figure 6.

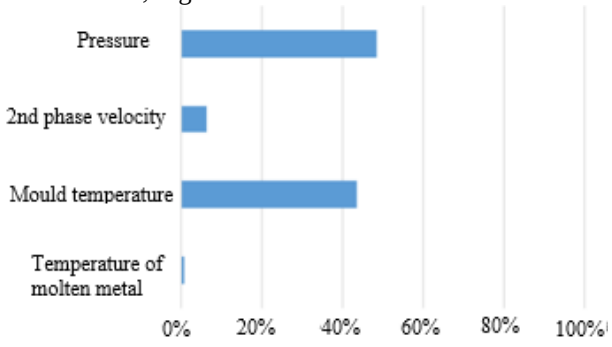

Figure 6. Percentage contribution of the input parameters to grey relational grade

7. Conclusion

The high pressure casting process of aluminium alloy is analysed based on NovaCast&Solid simulation software. Discussed output results of the simulations were shrinkage of material and total casting time. Based on simulation results, the largest shrinkage appeared in the gating system and overflows, indicating that casting parameters are correctly set and construction of the casting is correctly designed. In addition, Taguchi method and grey relational analysis were used to optimize controllable parameters (temperature of the molten metal, mould temperature, 2nd phase velocity and pressure). Based on ANOVA results of the grey relational grade it was found that pressure plays the most important role in affecting shrinkage and total casting time.

REFERENCES

[1] Heinz A., Haszler A., Keidel C., Moldenhauer S., Benedictus, R. Miller, W.S., (2000), *Recent development in aluminium alloys for aerospace applications*, Materials Science and Engineering: A, No. 1, pp.102-107.

[2] Sadeghi M., Mahmoudi J., (2012), *Experimental and theoretical studies on the effect of die temperature on the quality of the products in high-pressure die-casting process*, Advances in Materials Science and Engineering, Vol. 2012.

[3] Adamane A.R., Arnberg L., Fiorese E., Timelli G., Bonollo F. (2015), *Influence of injection parameters on the porosity and tensile properties of high-pressure die cast Al-Si alloys: a review*, International Journal of Metalcasting, No. 1, pp.43-53.

[4] Dumanić I., Jozić S., Bajić D., Krolo J., (2021), *Optimization of semi-solid high-pressure die casting process by computer simulation, Taguchi method and Grey relational analysis*, International Journal of Metalcasting, No. 1, pp.108-118.

[5] Dou K., Lordan E., Zhang Y.J., Jacot A., Fan, Z.Y., (2019), *Numerical simulation of fluid flow, solidification and defects in high pressure die casting (HPDC) process*, In IOP Conference Series: Materials Science and Engineering (Vol. 529, No. 1, p. 012058).

[6] Borlepwar P., Biradar S., (2019), *Study on reduction in shrinkage defects in HPDC component by optimization of localized squeezing process*, International Journal of Metalcasting, No. 4, pp.915-922.

[7] Duan H.Z., Shen J.N., Li, Y.P., (2012), *Comparative analysis of HPDC process of an auto part with ProCAST and FLOW-3D*, In Applied Mechanics and Materials, Vol. 184, pp. 90-94.

[8] Balikai V.G., Siddlingeshwar I.G., Gorwar M., (2018), *Optimization of process parameters of High Pressure Die Casting process for ADC12 Aluminium alloy using Taguchi method*, International Journal of Pure and Applied Mathematics, No. 6, pp.959-969.

[9] Hsu Q.C., Do A.T., (2013), *Minimum porosity formation in pressure die casting by Taguchi method*, Mathematical Problems in Engineering, No. 2013.

[10] Achuthamenon Sylajakumari P., Ramakrishnasamy, R., Palaniappan, G., (2018), *Taguchi grey relational analysis for multi-response optimization of wear in co-continuous composite*, Materials, No. 9, p. 1743.

[11] Singh G., Lamichhane Y., Bhui A.S., Sidhu S.S., Bains P.S., Mukhiya P., (2019), *Surface morphology and microhardness behavior of 316L in HAp-PMEDM*, Facta Universitatis, Series: Mechanical Engineering, No. 3, pp.445-454.

[12] Haque R., Sekh M., Kibria G., Haidar, S., (2021), *Improvement of surface quality of Ti-6Al-4V alloy by powder mixed electrical discharge machining using copper powder*, Facta Universitatis, Series: Mechanical Engineering.

ISSN 1847-7917

Study of heat transfer characteristics of aluminium foam for PCM-based thermal energy storage applications

Arun GOPINATHAN[1,2]***, Jaroslav JERZ***[1)]***, Jaroslav KOVÁČIK***[1)]

1) Institute of Materials and Machine Mechanics, Slovak Academy of Sciences, Dúbravská cesta 9/6319, 845 13 Bratislava, **Slovakia**
2) Faculty of Materials Science and Technology, Slovak University of Technology, JánaBottu 2781/25, 917 24 Trnava, **Slovakia**

arun.gopinathan@savba.sk
ummsjerz@savba.sk
ummsjk@savba.sk
ummsdvor@savba.sk

Professional article

Abstract: The heat transfer characteristic of the aluminium foam mainly depends on the structural parameters of the internal structure of the foam. It is one of the major factors which is needed to be studied for the application of aluminium foam in PCM based thermal storage system applications. The present study is focusing on the influence of pore morphology in the heat distribution at the internal structure of the aluminium foam, prepared by the powder metallurgical (PM) route. The produced high-density sample is characterised with X-ray tomography images and the image processing technology is employed to model the internal structure of the foam. The morphology of the struts and pore walls are examined to understand the possibility of achieving a uniform heat transfer rate at the inner structure of the foam. Further, the importance of pore size formation of the foam in addition to porosity is dealt which is one of the important criteria to achieve stable heat storage and release of the impregnated PCM into the aluminium foam.

Keywords

Aluminium foam
Thermal conductivity
Heat storage
Microstructure
Pore morphology

1. Introduction

Nowadays, energy savings is the newarea of interest that is getting popular among researchers to face environmental problems. Notably, the system or device which is capable of storing thermal energy is limited indefinably, and the need for it is bringing the interest in providing more concentration on developing the thermal energy storage (TES) system. The TES system is a storage device that allows storage and releases thermal energy by heating a storage medium [1]. Sensible heat storage, latent heat storage, and thermo-chemical storage are the three types of TES systems. The latent heat energy storage system is implemented in this work because of its advantages in storing a large amount of heat at a constant temperature. Phase change materials (PCMs) are the essential material for the latent heat thermal energy storage (LHTES) systems which absorb and release latent heat during the phase change transformation process [2]. By considering the small volume change and low-temperature variation, PCM is suggested as a suitable material for thermal storage applications for storing a large amount of energy [3]. A numerical study has been made in which PCM is used as a storage unit in thermal solar applications, which relates the solar plant parameters with the design variables [4]. Among different PCMs, paraffin wax having low vapour pressure in melting, high latent heat, thermal and chemical stability, and non-toxicity, is desirable. As PCMs have low thermal conductivity, different heat transfer enhancement is considered, such as the addition of nanoparticles [5], fins [6], porous graphite [7], and embedded with metal foams [2, 8-16]. This enhancer adds significant weight to the storage system. Among the different methods, high porosity metal foams are providing an effective way of improving the PCMs performance. Metal foams with porous structures are gaining interest for structural applications because of possessing unique properties such as appreciable density, high specific stiffness, energy and sound absorption, thermal insulation, fire resistance and recyclability [17]. Porous metal foams possess high thermal conductivity, large surface area to the volume ratio, and highly interconnected pore walls [13]. Much research has beenconducted to study the thermal conductivity of the metal foam and the influence of microstructure and porosity on the effective thermal conductivity of the PCM embedded with metal foam composites. Phase change kinetics is greatly influenced by the effective thermal conductivity of the PCM. When the effective thermal conductivity is increased, the heat transfer rate becomes higher, which increases the melting and

solidification rate of the PCMs. It brings an interest in studying the porosity and microstructure of the foam on thermal conductivity, which influences the rate of evolution of the liquid fraction.

This work is focused to study the internal porous structure of the aluminium foam produced through the powder metallurgical route. The different heat transfer mechanisms for PCM based heat storage applications are evaluated. The formation for the internal porous structure formation is analyzed with the help of a 3D model developed from X-ray tomography images. The importance of pore formation and distribution is studied. It is followed by the scope of using the research findings for developing the thermal energy storage system in the buildings sector for achieving indoor thermal comfort.

2. Heat transfer enhancement in PCMs

The thermal conductivity of the PCM can be increased by integrating highly conductive materials into the PCM [18]. From the literature [19,20], the heat transfer enhancement techniques can be grouped into the following categories.

- Addition of highly thermal conductive metallic particles
- Usage of graphite composites
- Usage of finned tubes
- Inserting porous structure

2.1 Selection of techniques for heat transfer enhancement

The advantages and disadvantages of the enhancement techniques explained above are listed and tabulated (Table1).

Table 1: Advantages and disadvantages of various impregnation techniques [19,21-28]

Impregnation Techniques	Advantage	Disadvantage
Fin and heat pipe	• Fabrication is easy • Less expensive	• Optimization of the system between metallic structure and amount of PCM is needed • Performance is less in comparison with porous structure
Nano-particles dispersion	• Simple to implement	• Energy density is increased by decreasing the particle fraction • Higher density causes the particles to settle at the bottom of the PCM container
Carbon fibre/brush	• Corrosion-resistant • Less in weight	• Availability of carbon fibres is less • Balancing between the fibre and PCM is considered to maximize the energy density
Graphite composite	• Stable. Resist chemical attacks and Corrosion	• Graphite flakes dispersion in PCMs is difficult
Metal foam	• Interconnected pore walls made of metallic ligaments provide excellent conductivity • Higher surface area by volume for heat transfer • Better heat transfer rate • Lightweight	• Pore walls become brittle after multiple heat cycles • Convective heat transfer is suppressed, but it is overcome by the conduction of solid and gas inside the foam
Metal mesh	• Inexpensive in comparison with foams	• Research on this approach is less

From the research made on the heat transfer enhancement, it is found that the selection of the technique is difficult. Implementing porous structured metal foam is bringing the interest among the researchers mainly for its better heat transfer, high specific area and insulation phenomenon.

2.2 Metal foam application

Porous matrices have gained their attention on impregnating it with PCM due to their high thermal conductivity. The lightweight porous matrix and higher surface area for transferring heat make it an exciting approach of utilizing the porous structure for PCM based TES applications.

Metal foam is a combination of solid metal-containing a large volume fraction of the pores filled with gas. It is divided into two – closed-cell foam, having closed spherical pores with ruptures and interconnected pore walls and open-cell foam, having interconnected networks of metals without closed cells. Impregnating PCM into the metal foam has the following advantages.

- The distribution of the foam ligaments makes the phase change process of the PCM more uniform
- High specific surface area for transferring the heat results in an increase in the effective thermal conductivity of the PCM/metal foam composite

Figure 1: Aluminium foam with the dimension $40 \times 40 \times 5$ mm^3

The primary parameter, which is considered while choosing the metal foam, is the porosity. The common materials used for making foam are aluminium, copper, stainless steel, and nickel. The material selected for the study is mainly based on balancing the thermal conductivity and its compatibility with the paraffin or other PCM materials to restrict corrosion.

Figure 2: Pores formation inside aluminium foam (cross-section)

3. Aluminium foam - heat transfer medium

The application of ultra-light aluminium foams with high porous structure as a heat exchanger medium is getting its interest nowadays for its high thermal conductivity and high porosity. Several manufacturing methods of aluminium foam, grouped into two categories, such as direct (injecting gas into the molten metal) and indirect method (foam produced from the foamable precursor containing compacted metal powder and gas agent), are available. It focuses on effective control of density by manipulating the manufacturing process parameters. Though the methods are effective, controlling the cellular formations during foaming is difficult, which leads to drawbacks in the structural and mechanical properties of the final products.

3.1. Aluminium foam by powder metallurgy (PM) method

The production of aluminium foam by PM method is classified into two stages,

- Foamable precursor made by compacting the mixture of metal and gas agent using the conventional technique
- Metal foams production by heating the foamable precursor at a temperature above its melting point

The production process of aluminium foam through the PM route is shown in figure 3 below. The most commonly studied aluminium alloys for aluminium foam production are pure aluminium, wrought alloys such as 6XXX alloy series, and casting alloys say AlSi7Mg. The selection of gas agents for foaming is essential for high-quality foams.

3.2. Powder selection and production

There are two main requirements to obtain high-quality foams,

- Uniform distribution of gaseous agent into the metal matrix of the precursor material
- Avoiding crack formations (before melting starts) to ensure the coordination of the thermal decomposition characteristics of the precursor material

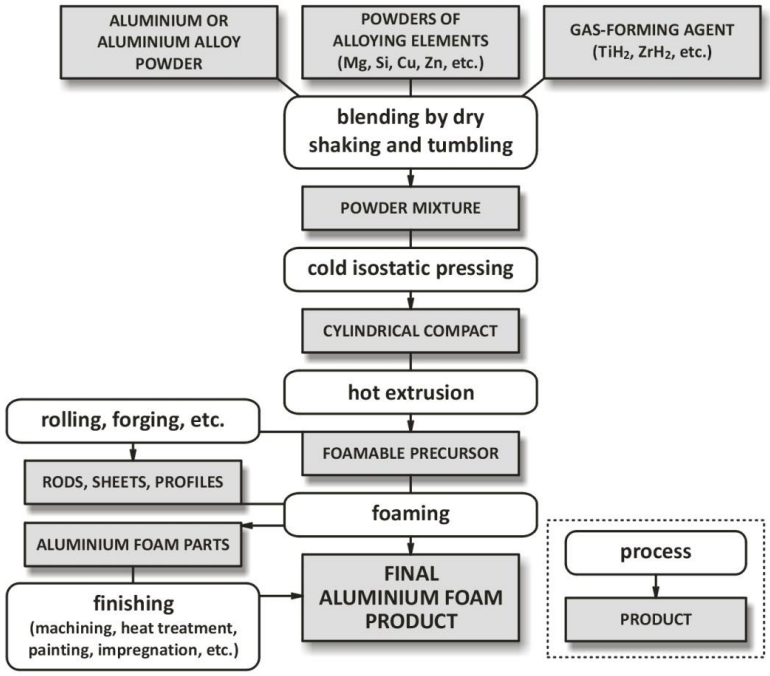

Figure 3: Schematic diagram aluminium foam production by PM method [29]

Therefore, the selection of the appropriate blowing agent and metal powder is of importance for successful foaming. In general, the formation of bubbles is the result of heating the blowing agent, which releases when heated. Furthermore, the study on the characteristics of the powder, such as particle size, alloy melting behaviour, thermal decomposition of the gaseous agent, purity, and the alloying chemical elements should be needed.

Among different blowing agents used for producing Al-alloy foam through PM routes such as titanium hydride (TiH_2), zirconium hydride (ZrH_2), carbonates and magnesium hydride (MgH_2), TiH_2 having the starting temperature of decomposition at 380 ^oC, is the preferable blowing agent among the researchers for producing aluminium foam through PM method. The disintegration of TiH_2 is delayed by the oxide layer formed on the surface of the particles as a result of preheating TiH_2 powders (~480 ^oC) in the air for 3 hours [18]. The blowing agent used less than 1% in weight in the mixture allowed for compaction.

Ibrahim et al. [30], in their work, explained the importance of TiH_2 particle size in the foam expansion process. From this study made, the coarser particle of TiH_2 leads to the formation of higher foam expansion and coarse macrostructure inside the foam. The finer macrostructure and lower expansion are recorded while using the finer particle of TiH_2 [30]. Moreover, the difference between the melting temperature of the aluminium and the thermal decomposition of the blowing agent is minimized to avoid the formation of irregularities in the final foam [30]. It has been achieved in two ways,

- Pre-treatment of the blowing agent to delay the release of hydrogen
- Change the alloy composition to obtain a lower melting point by adding more alloy elements

The steps involved in the production of aluminium foams through the powder metallurgical route are of four stages. It involves,

- Mixing of the powders – metal and gas-forming agent
- Powder compaction
- Foamable billets production by conventional methods
- Production of aluminium foam

3.3. Characterization of porous structure

Generally, the high porosity of metallic foams is preferred for better thermal conductivity, and it is characterized by the density, size, and shape of the cell, morphology, topology of the cell, and the interconnected pore wall properties [18]. It is also influenced by other factors such as moisture content and the temperature of the material. The porous, cellular structures evenly distribute the mass, and it increases the overall moment

of inertia of the foam. Ultimately, it is capable of providing high strength and required stiffness for the corresponding weight of the bulk material. Compared with solid metal panels; the foam structures are lighter with structural rigidity. Specific surface area needs to be considered when heat and mass transfer are of significant interest.

Generally, X-ray computed micro-tomography (μCT) is referred to as the non-destructive technique utilized for material characterization. Microtomography is following the same physical principle and mathematical algorithms as the classical medical CT scanner. In the μCT method, the imaging is done by passing an X-ray through the sample over 180 °C rotation, and the transmitted intensity is collected as a function of material composition and density.

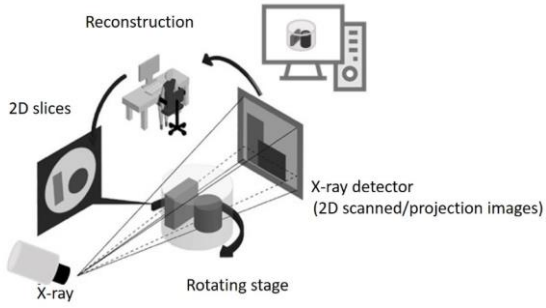

Figure 4: Schematic diagram of the μCT setup [31]

The X-ray slice image made along the aluminium foam is shown in the figure below.

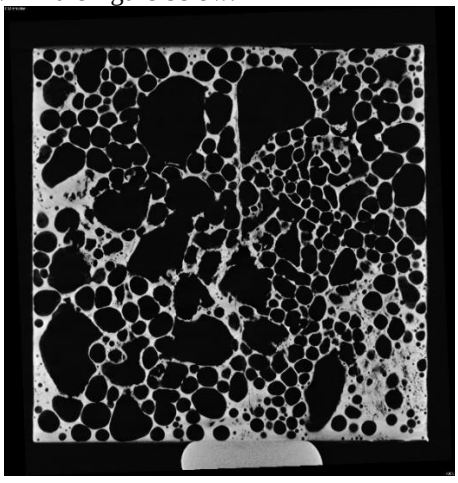

Figure 5: X-ray tomography image of aluminium foam of $40 \times 40 \times 5$ mm^3

4. Porosity

The high thermal conductivity of aluminium foam panels has the potential of improving the rate of heat transfer to the PCMs. From the previous studies made by the researchers [32], it has been found that the heat transfer rate is influenced by the effects of porosity and pore size of the foam panel. At steady-state temperature, the heat transfer rate of the foam panel with higher porosity and bigger pore size is reached faster as compared to the foam panel with lower porosity and smaller pore size [33]. But on the contrary, the lower porosity foam increases the melting rate compared to higher porosity foam due to the more significant heat conduction of the foam [34].

The porosity is calculated by using the following formulas [35].

$$Porosity = \frac{ApparentDesnity}{BulkDensity} = \frac{\rho^*}{\rho_s} \quad (1)$$

or,

$$Porosity = \frac{PoreVolume}{BulkVolume} = \frac{V_p}{V_T} \quad (2)$$

Where ρ^*, & ρ_s are the apparent and bulk density. V_p&V_T, refers to the pore volume and total volume of solid and pore.

When the foam density is increased, the conduction rate is getting improved, and the convective heat transfer is decreased, which leads to the reduction of heat storage capacity. So, it should be needed to maintain the appropriate porosity level while designing the foam panel for heat storage.

4.1. Importance of pore morphology

In general, the heat flux, q, induced by a temperature difference ∇T, is given by,

$$q = -\lambda \cdot \nabla T \quad (3)$$

where λ is the effective thermal conductivity of the solid. The equation for finding the amount of heat flow can be written as,

$$Q = \frac{\lambda \cdot L}{\nabla T \cdot A} \quad (4)$$

Where Q is the amount of heat transfer (W), L is the thickness of the solid (m), A is the surface area of the solid (m^2) [36].

The strut and pore wall formation is important to decide the uniformity of the heat flow rate inside the aluminium foam which is important for stable heat storage and release. The formation of the pores of different sizes is shown in figure 6.

The bigger pore size presence of the foam has thinner pore walls that experience a non-uniform heat transfer rate [36]. The smaller pores have thicker pore walls which enhance the heat flow rate to the PCM. At the same time, the presence of defects in the pore walls helps for the movement of molten PCM. The presence of the defects in the pore walls is shown in figure 7.

This could lead to understanding the importance of optimising the pore morphology in addition to the porosity of the foam. It can be achieved by synthesizing high-density foam with the usage of a very less amount of TiH_2 [36].

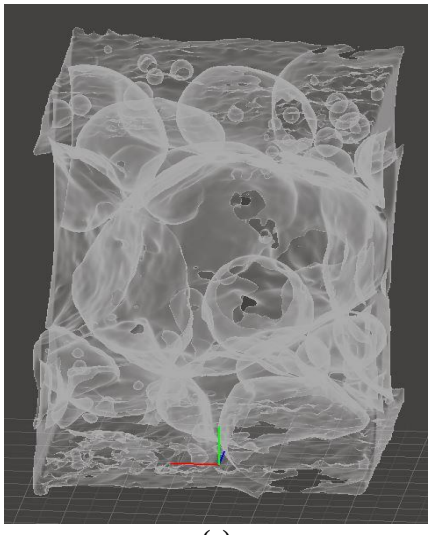

(a)

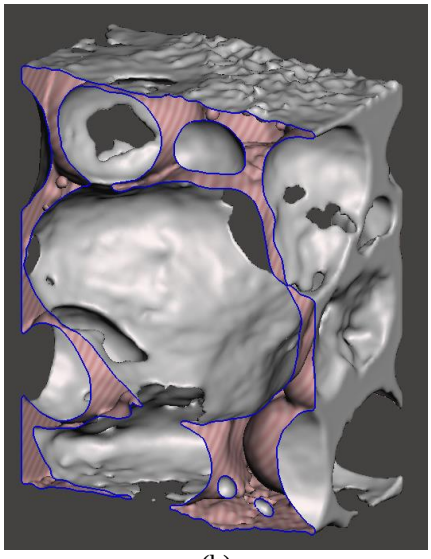

(b)

Figure 6: Inner structure of the aluminium foam 3D model (a) pores distribution (b) cross-section of the pores [36]

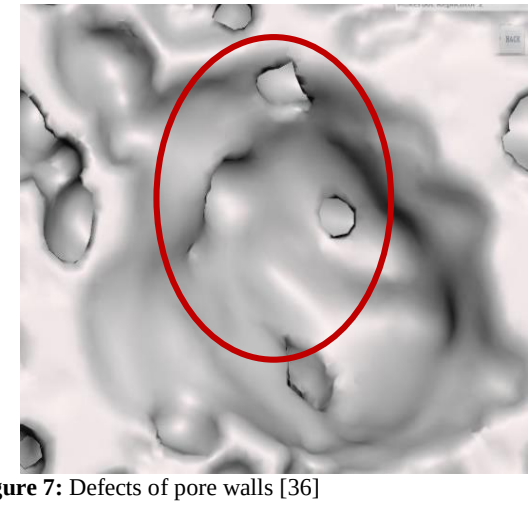

Figure 7: Defects of pore walls [36]

5. Conclusion

The role of pore morphology formed at the internal structure of the foam along with porosity to enhance the uniformity of the heat transfer to the PCM is highlighted in this contribution. Among different heat transfer enhancement techniques, porous aluminium foam application proved the higher efficiency of storing and releasing the heat. The combination of X-ray tomography along with the image processing technique is very helpful to characterize the pore formation of aluminium foam produced through the PM route in a non-destructive way. In addition to the porosity, the formation of smaller pores of microlevel is preferable for achieving better heat flow in comparison with bigger pores having thinner pore walls. The formation of microcracks and defects could help for the impregnation of PCM into the internal structure of the foam. This optimised inner structure of the high-density foam produced with the addition of the lesser amount of TiH_2 is highly promising and utilized to produce aluminium foam ceiling heat exchangers for the future PCM based heat storage application.

Acknowledgments

The financial support by the Slovak Research and Development Agency under the contract APVV-17-0580 (project: Research of roofing with the integrated function of the heat exchanger, acronym: RoofFoam) is gratefully acknowledged.

REFERENCE

1. Gil A., Medrano M., Martorell I., Lázaro A., Dolado P., Zalba B., and Cabeza L F., (2010), *State of the art on high temperature thermal energy storage for power generation. Part 1 – Concepts, materials and modellization*, Ren. Sust. En. Re., vol. 14, no. 1, pp. 31-55. DOI: 10.1016/j.rser.2009.07.035.
2. Mancin, S., Diani, A., Doretti, L., Hooman, K. and Rossetto, L., (2015), *Experimental analysis of phase change phenomenon of paraffin waxes embedded in copper foams*, Int. J. Therm. Sci., vol. 90, pp. 79-89. DOI: 10.1016/j.ijthermalsci.2014.11.023.
3. Zalba B., Marín J M., Cabeza L F., Mehling H., (2003), *Review on thermal energy storage with phase change: materials, heat transfer analysis, and applications*, Applied Thermal Engineering., vol. 23 (3), pp. 251–283.
4. Cammarata G., Monaco L., Cammarata L., and Petrone G., (2014), *A Numerical Procedure for PCM Thermal Storage Design in Solar Plants*, Int. J. Heat Tech., vol. 31, no. 2, pp. 105-110. DOI: 10.18280/ijht.3102.14.
5. Karunamurthy K., Murugu Mohan Kumar K., Suresh S., (2012), *Pcm based thermal energy storage system containing CuO nanoparticles*, IJNT: vol. 3, no. 1, pp. 13-16.

6. Casano LG., and Piva S., (2015), *Parametric Analysis of a PCM Energy Storage System*, Int. J. Heat Tech., vol. 33, no. 4, pp. 61-68. DOI: 10.18280/ijht.330408.
7. Jegadheeswaran S., Pohekar S D., Kousksou T., (2012), *Conductivity particles dispersed organic and inorganic phase change materials for solar energy storage–an exergy based comparative evaluation*, Energy Procedia., vol. 14, pp. 643–648.
8. Kováčik J., Španielka J., Dvorák T., Oslanec Jr P., Jerz J., (2017), *Closed-cell aluminum foams with phase change material*, Metallic foams., vol. 1, no. 1, pp. 42-48.
9. Lazzarin R M, Mancin S., Noro M., Righetti G., (2018), *Hybrid PCM- Aluminium Foam's Thermal storage: an experimental study*, International Journal of Low-Carbon Technologies.,vol. 13(3), pp. 286-291.
10. Beyne W., Bağci O., Huisseune H., Canière H., Danneels J., Daenens D., and De Paepe M., (2017), *Experimental investigation of solidification in metal foam enhanced phase change material*, Materials Science and Engineering.,251 012112, DOI:10.1088/1757-899X/251/1/012112.
11. Li W Q., Wan H., Jing T T., Li Y B., Liu P J, He G Q, Qin F., (2019) *Microencapsulated Phase change material saturated in metal foam as an efficient hybrid PCM for passive thermal management: A numerical and experimental study*, Applied Thermal Engineering., vol. 146, no. 5, pp. 413-421.
12. Deng Z., Liu X., Zhang C., Huang Y., Chen Y., (2017), *Melting behaviours of PCM in porous metal foam characterized by fractal geometry*, International Journal of Heat and Mass Transfer., vol. 113, pp.1031-1042, DOI: 10.1016/j.ijheatmasstransfer.2017.05.126
13. Moussa E I M., Karkri M., (2019), *A numerical investigation of the effects of metal foam characteristics and heating/cooling conditions on the phase change kinetic of phase change materials embedded in metal foam*, Journal of Energy Storage., vol.26, https://doi.org/10.1016/j.est.2019.100985.
14. Abishek S., King A J C., Nadim N., Mullins B J., (2018), *Effect of microstructure on melting in metal-foam/paraffin composite phase change materials*, International Journal of Heat and Mass Transfer., vol. 127, Part B, pp. 135-144.
15. Chen J., Yang D., Jiang J., Ma A., Song D., (2014), *Research progress of phase change materials (PCMs) embedded with metal foam (a review)*, Procedia Materials Science., vol. 4, pp. 389-394.
16. Shang B., Hu J., Hu R., Cheng J., Luo X., (2018), *Modularized thermal storage unit of metal foam/paraffin composite*, International Journal of Heat and Mass Transfer., vol. 125, pp. 596-603.
17. Bauer B., Kralj S., Busic M., (2013), *Production and application of metal foams in casting technology*, Tehnicki Vjesnik., vol. 20, pp. 1095–1102.
18. Duarte I., Oliveira M., (2012), *Aluminium Alloy Foams: Production and Properties: Powder Metallurgy*, DOI:10.5772/1992.
19. Al-Abidi A A., Mat S., Sopian K., Sulaiman M Y., Mohammad A T., (2013), *Internal and external fin heat transfer enhancement technique for latent heat thermal energy storage in triplex tube heat exchangers*, Applied Thermal Engineering., vol.53(1), pp. 147-156.
20. Medrano M., Yilmaz M.O., Nogues M., Martorell I., Roca J., Cabeza L. F., (2009), *Experimental evaluation of commercial heat exchangers for use as PCM thermal storage systems,* Applied Energy., vol. 86(10), pp. 2047-2055.
21. Agyenim F., Eames P., and Smyth M., (2009*), A comparison of heat transfer enhancement in a medium temperature thermal energy storage heat exchanger using fins*, Solar Energy., vol. 83(9), pp. 1509-1520.
22. Pakrouh R., Hosseini M J., Ranjbar A A., Bahrampoury R., (2015), *A numerical method for PCM-based pin fin heat sinks optimization*, Energy Conversion and Management., vol. 103, pp. 542-552.
23. Sharifi N., Faghri A., Bergman T L., Andraka C E., (2015), *Simulation of heat pipe-assisted latent heat thermal energy storage with simultaneous charging and discharging*, International Journal of Heat and Mass Transfer., vol. 80, pp. 170-179.
24. Zeng J L., Sun L X., Xu F., Tan Z C., Zhang Z H., Zhang J., Zhang T., (2007), *Study of a PCM based energy storage system containing Ag nanoparticles*, Journal of Thermal Analysis and Calorimetry, vol. 87(2), pp. 371-375.
25. Fukai J., Hamada Y., Morozumi Y., Miyatake O., (2002), *Effect of carbon-fibre brushes on conductive heat transfer in phase change materials*, International Journal of Heat and Mass Transfer., vol. 45(24), pp. 4781-4792.
26. Pincemin S., Olives R., Py X., Christ M., (2008), *Highly conductive composites made of phase change materials and graphite for thermal storage*, Solar Energy Materials and Solar Cells., vol.92(6), pp. 603-613.
27. Li W., Dong Y., Zhang X., and Liu X., (2019), *Preparation and Performance Analysis of Graphite Additive/Paraffin Composite Phase Change Materials*, *Processes.*, vol.*7*, p. 447.

28. Shuja S.Z., Yilbas B S., and Shaukat M M., (2015), *Melting enhancement of a phase change material with the presence of a metallic mesh*. Applied Thermal Engineering, vol. 79, pp. 163-173.
29. Jerz J., (1995) *Foamed Aluminium and Aluminium Alloys Prepared by Powder Metallurgy, Dissertation*, TU Wien.
30. Ibrahim A., Körner C., Singer R F., (2008), *The Effect of TiH2 Particle Size on the Morphology of Al-Foam Produced by PM Process*. Advanced Engineering Materials., vol. 10, pp. 845-848.
31. Duarte I., Fiedler T., Opara L K., and Vesenjak M., (2020), *Brief Review on Experimental and Computational Techniques for Characterization of Cellular Metals*, Metals., vol.10 (6), pp. 726, DOI:10.3390/met10060726.
32. Solórzano E., Reglero J A, Rodríguez-Pérez M A, Lehmhus D., Wichmann M., de Saja J A., (2008), *An experimental study on the thermal conductivity of aluminium foams by using the transient plane source method*. International Journal of Heat and Mass Transfer., vol. 51 (25-26), pp. 6259–6267.
33. Baetens R., Jelle B P., Gustavsen A., (2010), *Phase change materials for building applications: a state-of-the-art review*, Energy., and Buildings., vol. 42 (9), pp.1361–1368.
34. Tyagi V V., Buddhi D., (2007), *PCM thermal storage in buildings: state of the art*, Renewable and Sustainable Energy Reviews., vol. 11 (6), pp.1146–1166.
35. Zhang Y., Zhou G, Lin K., Zhang Q., Di H., (2007), *Application of latent heat thermal energy storage in buildings: state-of-the-art and outlook*, Building and Environment., vol. 42 (6), pp. 2197–2209.
36. Gopinathan A., Jerz J., Kováčik, J., Dvorák, T., Orovčík, L., (2021), *Investigation of the relationship between morphology and thermal conductivity of powder metallurgically prepared aluminium foams*. Materials., vol. 14, p. 3623.
37.

ISSN 1847-7917

Determination of the friction coefficient of 3D printed materials - Part II: Sliding Friction

Stanislav GYOSHEV[1)]***, Nikolay STOIMENOV***[1)] ***Miglena PANEVA***[1)]
1) Institute of Information and Communication Technologies – Bulgarian Academy of Sciences, Acad. G. Bonchev str., bl. 2, 1113 Sofia, **Bulgaria**

stanislavgyoshev@mail.bg
nikistoimenow@gmail.com
m.paneva7@gmail.com

Professional paper

Abstract: For most 3D printing materials, the basic physical and mechanical parameters such as tensile strength, modulus of elasticity, and coefficient of elongation are known and investigated. The coefficients of friction of the materials relative to each other and other materials are not determined. This paper is considered the determination of the coefficient of friction in sliding 3D printed samples of different materials (PLA, PETG, Flex). The aim is to determine the coefficient more precisely, thus in the presented work are made experiments with different sample sizes for each of the listed materials. Experiments have also been made with different pairs of materials.

Keywords

Friction
Sliding Friction
Friction Coefficient
3D Printing Materials
3D Printing

1. Introduction

The grinding of various materials is an industrial process with an important mission, in which the material is crushed and milled to a certain desired value. The sizes are due to the interaction between material, grinding bodies, and grinding media. The main factors influencing the grinding of material are grinding bodies and grinding media. Ball mills are used in various production areas, such as mining and mineral processing, metallurgy, chemical industry, cement production, ceramics, pharmaceuticals and cosmetics, laboratory research, and others. Depending on the specific field of application, the processed materials differ in hardness, size, chemical composition and structure, as examples in this regard are the different types of ores, minerals, limestones and others [1].

Modern mills must have increased production (operational) reliability, high productivity, with minimal energy consumption. Minimum energy consumption also includes electricity, heat costs, and costs for grinding bodies. Quality requirement - the output product must be in function of the requirements of BDS and ISO The main factor for increased productivity is the grinding time and operating speed.

Mills are influenced by some key factors that improve the productivity and quality of the output product (starting material). Key factors such as loading with a certain percentage of grinding material; percentage to be filled; the size of the grinding bodies used (if possible to be of the smallest dimensions, thus achieves a maximum contact area between the media and the grinding material); grinding time; it is not allowed to increase the temperature of the mill, etc [2].

The aim of the paper is to be experimentally determined the coefficient of friction of 3D printed materials, which will be used for simulation modeling of grinding processes in a laboratory ball mill.

2. Sliding friction coefficient

Sliding friction (also called kinetic friction) is a contact force that resists the sliding movement of two objects or movement between an object and a surface. Usually, the sliding friction is almost less than that of static friction. This causes the easier movement of an object once it starts moving rather than to get the object to begin moving from a static position [3, 4, 5].

$$Fk = \mu k \, . \, N \tag{1}$$

where Fk, is the force of kinetic friction;
μk is the coefficient of kinetic friction;
N is the normal force.

The acceleration process occurs when the external force is higher than the force of kinetic friction. The slowing down or so-called stopping occurs when the force of kinetic friction is higher than that of the external force. This also follows Newton's first law of motion as there exists a net force on the object.

Symbols

F	- frictional force, N			**Greek letters**
N	- Normal force, N	μ	-	coefficient of friction, dimensionless
F_k	- normal force (perpendicular to the surface), N	Θ	-	angle of inclination, º
F_g	- the component of the force of gravity in the direction of the incline, N			
m	- mass of the object, kg			
g	- newton's gravitational constant, , m/s^{-2}			
mm	- millimeters			
$°C$	- Temperature in Celsius			

The constant velocity is applicable when there is no net force on the object that is the external force is equal to the force of kinetic friction.
This case is shown in the free body diagram, shown in Figure 1. The component of the force of gravity in the direction of the incline is given by [4]:

$$Fg = mg\sin\theta \quad (2)$$

The normal force (perpendicular to the surface) is given by:

$$N = mg\cos\theta \quad (3)$$

Therefore, since the force of friction opposes the motion of the block,

$$Fk = \mu k \,.\, mg\cos\theta \quad (4)$$

To find the coefficient of kinetic friction on an inclined plane, first must be found the moment, where the force parallel to the plane is equal to the force perpendicular. This happens when the block is moving at a constant velocity at some angle θ:

$$\Sigma F = ma = 0 \quad (5)$$

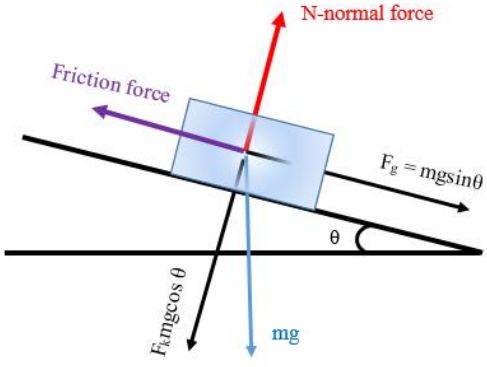

Figure 1. Free body diagram for a block subject to friction as it slides on an inclined surface

$$Fk = Fg \text{ or } \mu k mg\cos\theta = mg\sin\theta \quad (6)$$

From the equations above follows:

$$\mu k = mg\sin\theta / mg\cos\theta = \tan\theta \quad (7)$$

where θ is the angle at which the block begins moving at a constant velocity [5].

3. Experimental setup

3.1. Sample preparation

The samples were produced by a 3D printer. The 3D printing method nowadays is an affordable technology that provides various possibilities for complex-shaped objects to be made. It helps designers, based on a CAD model, to build real objects [5]. This technology is implemented in numerous fields such as agriculture, industry, medicine, etc. [6, 7, 8, 9]. Fused deposition modeling (FDM) is one of the most common additive manufacturing techniques, comprising extrusion of thermoplastic filaments for deposition as layer by layer [6].
Among other thermoplastic (filaments) materials utilized in the FDM technique, ABS (acrylonitrile butadiene styrene), PLA (polylactic acid), PETG (polyethylene terephthalate glycol-modified), and PC (polycarbonate) are the most popular ones [9]. The printed sample materials PLA, PETG, Flex (plastics with rubbery properties) were with the following settings: the dimension of the two sliding surfaces – 120x60x10 mm and 40x40x10 mm; Infill surfaces – 20%; Layer thickness – 0.16 mm. The printing temperature, as well as the printing speed, was different for the different materials, in compliance with the manufacturer requirements. The parameters of the 3D printed materials are as follows and with compliance of the manufacturer:

- Nozzle Temperature – PLA: 212 °C; PETG: 215°C; Flex: 230 °C;
- Bed Temperature – PLA: 60 °C; PETG: 60°C; Flex: 40 °C;
- Printing Speed – PLA: 60 mm/s; PETG: 50 mm/s; Flex – 30 mm/s;
- Tensile strength – PLA: 70 MPa; PETG: 50 MPa; Flex: 32 MPa;
- Manufacturer – PLA and PETG: 3D Jake; Flex: RECREUS.

3.1. Test preparation

Figure 2 shows the experimental setup for measuring the slip angle. Figure 3 shows three measurements from the experiments to determine the slip angle. Table 1 shows the measured angles in degrees and radians and the coefficient of sliding friction is calculated. Figure 4 shows the sliding friction coefficient data for all pairs of materials are shown graphically.

It can be seen that for harder materials such as PETG and PLA the coefficient of friction is in the range of 0.3-0.4, while for the more elastic material FLEX, the coefficient of friction is already in the range of 0.5-0.6 or with almost 50% higher. From the performed experiments it can be concluded that the friction coefficient of PLA material is lower than the PETG material, approximately by 15%.

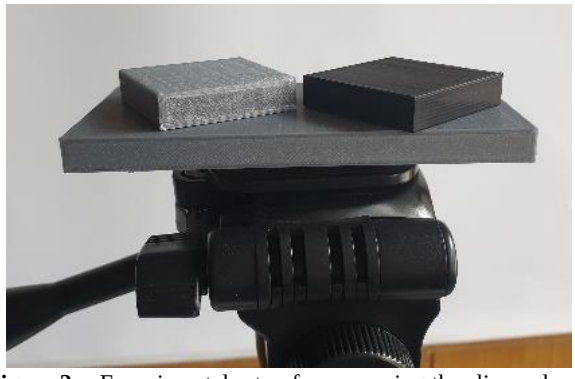

Figure 2. Experimental setup for measuring the slip angle

Table 1. Angle of friction and coefficient of sliding friction for different material pairs

Material	Angle of friction, θº	Angle of friction, θ rad	Coefficient of sliding friction tg θº
PLA+PLA (1)	15,850	0,277	0,284
PLA+PLA (2)	19,610	0,342	0,356
PLA+PLA (3)	22,590	0,394	0,416
PLA+PLA avg	19,350	0,338	0,351
PLA+PETG (1)	22,110	0,386	0,406
PLA+PETG (2)	23,590	0,412	0,437
PLA+PETG (3)	17,840	0,311	0,391
PLA+PETG avg	21,180	0,370	0,387
PETG+PLA (1)	16,830	0,294	0,302
PETG+PLA (2)	17,790	0,310	0,321
PETG+PLA (3)	21,760	0,380	0,399
PETG+PLA avg	18,793	0,328	0,340
PETG+PETG (1)	21,300	0,372	0,390
PETG+PETG (2)	20,810	0,363	0,380
PETG+PETG (3)	24,430	0,426	0,454
PETG+PETG avg	22,180	0,387	0,408
Flex+PLA (1)	32,960	0,575	0,648
Flex+PLA (2)	29,430	0,514	0,564
Flex+PLA (3)	31,680	0,553	0,617
Flex+PLA avg	31,357	0,547	0,609
Flex+PETG (1)	34,680	0,605	0,692
Flex+PETG (2)	24,980	0,436	0,466
Flex+PETG (3)	29,000	0,506	0,554
Flex+PETG avg	29,553	0,516	0,567

4. Future work

The experimentally determined coefficients of sliding friction will be used for setting the parameters of the specialized software for modeling and optimization of milling processes. The accurate coefficient of sliding friction gives more accurate results in the simulation process. The simulations from the software will be verified with a laboratory mill.

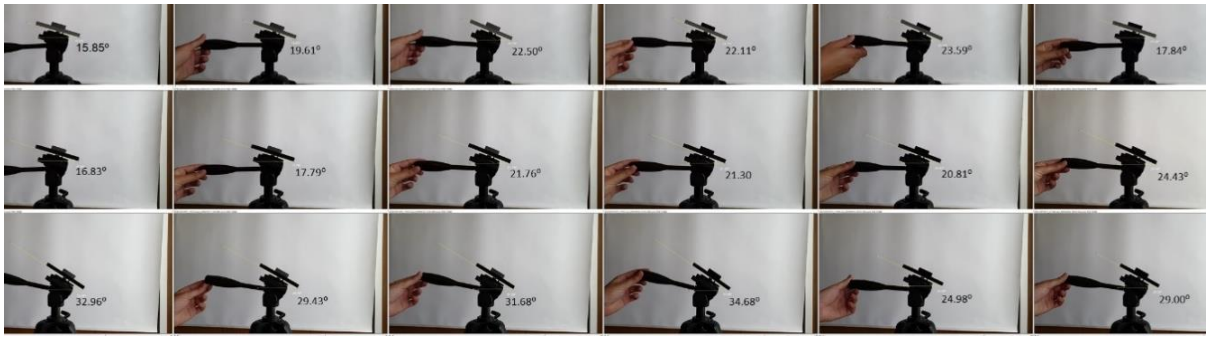

Figure 3. Three attempts for each pair of materials

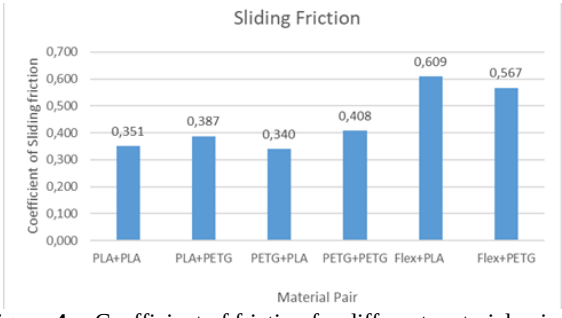

Figure 4. Coefficient of friction for different material pairs

5. Conclusion

The coefficient of sliding friction was experimentally determined by the gravitation-based device method. The sliding friction coefficients were conducted with different material pairs as follows: PLA+PLA; PLA+PETG; PETG+PLA; PETG+PETG; Flex+PLA; Flex+PETG. The material pairs were 3D printed by FDM 3D Printer. The experimentally obtained results will be used for simulations in EDEM Software aiming at optimization of the interaction between grinding bodies and media with an innovative shape.

Acknowledgments

This research was carried out as part of the project № KP-06-N47/5 "Research and optimization of the interaction between grinding bodies and media with an innovative shape", financed by the Bulgarian National Science Fund.

REFERENCES

[1] Ruzic J., Stoimenov N., (2016), *Advanced copper matrix composites, Monography in English, „Prof. Marin Drinov"* Publishing House of Bulgarian Academy of Sciences.

[2] Stoimenov N., Karastoyanov D., Klochkov L., (2022), *Study of the Factors Increasing the Quality and Productivity of Drum, Rod and Ball mills*, 2nd Int. Conf. on Environment, Chemical Engineering & Materials, ECEM '18, Publishing house AIP (American Institute of Physics), 2022, No. 1, p. 020024-1 - 020024-6.

[3] Bird J. O., Chivers P. J., (1993), Newnes Engineering and Physical Science Pocket Book.

[4] Malyshev V.N., (1871), Advances in Friction-Stir Welding and Processing, 201Benjamin Silliman, Principles of Physics, Or Natural Philosophy, Ivison, Blakeman, Taylor & company publishers.

[5] Ayrilmis N., Kariz M., Kwon J. H., Kitek Kuzman M., (2019), *Effect of printing layer thickness on water absorption and mechanical properties of 3D-printed wood/PLA composite materials*, Int. J. Adv. Manuf. Technol. 102, No. 5-8, p 2195-2200.

[6] Bikas H., Stavropoulos P., Chryssolouris G., (2016), *Additive manufacturing methods and modelling approaches: a critical review*, Int. J. Adv. Manuf. Technol. 83, No. 1-4, p 389-405.

[7] Rezayat H., Zhou W., Siriruk A., Penumadu D., Babu S.S., (2015), *Structure–mechanical property relationship in fused deposition modelling*, Mater. Sci. Technol. 31, No. 8, p 895-903.

[8] Cantrell J.T., Rohde S., Damiani D., Gurnani R., DiSandro L., Anton J., Young A., Jerez A., Steinbach D., Kroese C., Ifju P.G., (2017), *Experimental characterization of the mechanical properties of 3D-printed ABS and polycarbonate parts*, Rapid Prototyp. J. 23, No. 4, p 811-824.

[9] Hanon M. M. Zsidai L., Ma Q., (2021), Accuracy investigation of 3D printed PLA with various process parameters and different colors, Materials Today: Materials today, Proceedings 42, No. 5, p 3089-3096.

ISSN 1847-7917

Slag as an important waste for recycling

***Aida IMAMOVIĆ*[1)], *Mirsada ORUČ*[2)], *Mustafa HADŽALIĆ*[3)], *Admir MUMINOVIĆ*[4)], *Amra TALIĆ – ČIKMIŠ*[5)], *Fuad HADŽIKADUNIĆ*[6)]**

1) Metalurško-tehnološki fakultet, Travnička 1, 72000 Zenica, **Bosnia and Herzegovina**
3) Institut Kemal Kapetanović, Travnička 7, 72000 Zenica, **Bosnia and Herzegovina**
4) ArcelorMittal d.o.o. Zenica, Bulevar Kralja Tvrtka I,72000 Zenica, **Bosnia and Herzegovina**
5,6) Mašinski fakultet, Fakultetska 1, 72000 Zenica, **Bosnia and Herzegovina**

aida.imamovic@unze.ba
mirsada.oruc@unze.ba
mustafa.hadzalic@unze.ba
admir.muminovic@unze.ba
amra.talic-cikmis@unze.ba
fuad.hadzikadunic@unze.ba

Keywords

Blast furnace slag
Recycling
Mineral stone wool

Professional paper

Abstract: The paper presents the characteristics of blast-furnace slag of the company ArcelorMittal d.o.o. Zenica and a review of research done on this type of slag in order to increase its value as a useful waste, and increase the degree of utilization of blast furnace slag for recycling, and on the example of mineral wool production. This modern research has proven that metallurgical slag has properties similar to natural minerals, thus replacing their constant exploitation. Also on the concrete example of the use of blast furnace slag as a raw material, in addition to preserving natural resources and the environment, the possibility would be created for the production of mineral wool. Nanoindentation research of the primary layer mechanical properties based on mixture of blast furnace slag and diabase shows that the blast furnace slag can be used for production of mineral wool.

1. Introduction

One of the most important by-products of the metallurgical industry is slag. The slags from the production of iron and steel are especially significant, namely blast furnace slag and steel slag, figure 1, because the total production of iron and steel in the world has a growing trend.

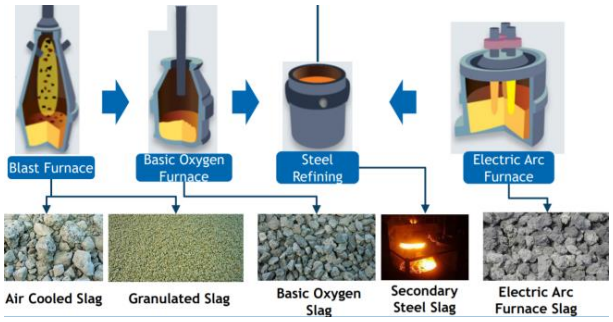

Figure 1. Slag as by-products of the metallurgical industry [1]

Environmental awareness and the concept of sustainable development, as well as the need to recycle by-products for economic and environmental reasons, have led to the development of metallurgical slag application especially in the construction industry, for the production of asphalt aggregate, portland cement, insulation materials, fertilizers, hydro-engineering, etc.

Blast furnace slag is an abundant and inexpensive raw material readily available from iron plants. The results of the survey on use of blast furnace slag (BF) in Europe 2016 are given by the following figure 2, [2].

Blast furnace slag is a safe raw material base for the usage in wide range of applications, which is guaranteed by the continuous operation of the blast furnace.

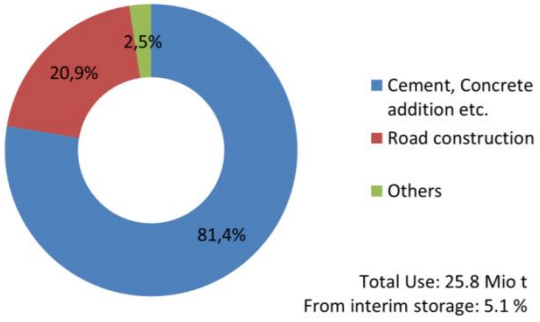

Figure 2. Usage of blast furnace slag in Europe 2016 [2]

The case study is based on evaluation of the potential for the usage of the blast furnace slag from ArcelorMittal steel company in Zenica, mixed with locally available mineral raw materials to prepare and fiberize the melt.
The amount of blast furnace slag generated in ArcelorMittal Zenica, BiH, in the period from 2014 to 2020 is shown in the diagram in Figure 3, which is approximately 480,000 tons annually.

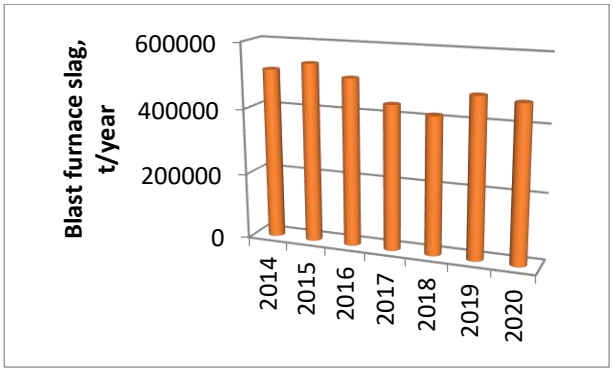

Figure 3. The amount of blast furnace slag generated in ArcelorMittal Zenica, in the period from 2014 to 2020 year

The present paper investigates the possibility to produce mineral stone wool by using blast furnace slag mixed with natural raw materials such as diabase.
With the usual technology, stone wool is obtained completely on the basis of natural materials, i.e. stone aggregate from basalt, diabase and dolomite minerals. Since the mineralogical composition of blast furnace slag is similar to the composition of these minerals, the basic idea of research is the possibility of using blast furnace slag for the production of mineral wool, [3].
Mineral wool is a general name for a non-metallic inorganic fibres, which has found wide application due to its combined advantages of excellent thermal insulation ability, sound insulation and fire resistance properties.
Mineral (stone) wool is produced by a technological process consisting of two basic operations:

- obtaining a silicate melt from a mixture of raw mineral components,
- changing of the obtained silicate melt into flying droplets which, in a stream of air, are transformed into mineral wool fibers.

The main factors that affect the process of formation mineral wool fibers from the melt, represent the modulus of acidity A, which means the amounts of acidic (SiO_2 + Al_2O_3) and basic (CaO + MgO) oxides in the mixture melt:

$$A= (SiO_2 + Al_2O_3)/ (CaO + MgO). \quad (1)$$

Other oxides present in the mineral mixture have no significant effect on the composition of the melt, however, they can to some significance affect the process of solidifying the melt, i.e. the quality of mineral wool fibers.

2. Experimental Part

The blast furnace slag used in this experiment was collected from ArcelorMittal Zenica.
The process of the mineral wool primary layer formation was studied experimentally on a spinning machine model with mineral mixture based on the blast furnace slag.
The mixture of 60% of a blast furnace slag and 40% of diabase, hereinafter referred to as blast furnace slag-diabase BS-D mixture, was melted in an induction furnace, and fibers made on the spinning wheel machine model with a laboratory centrifuge and a vertical collecting chamber, figure 4 [4].

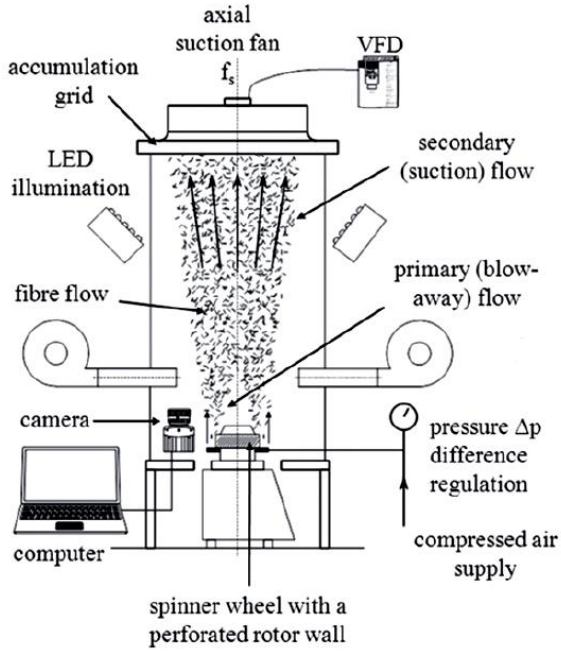

Figure 4. The spinning wheel machine model with a aboratory centrifuge [4]

The most commonly used measurement method is the camera visualization of the mineral wool primary layer. Examples of fiber formation (primary layers) are shown

in figure 5 from high-speed images of the formation process [5].

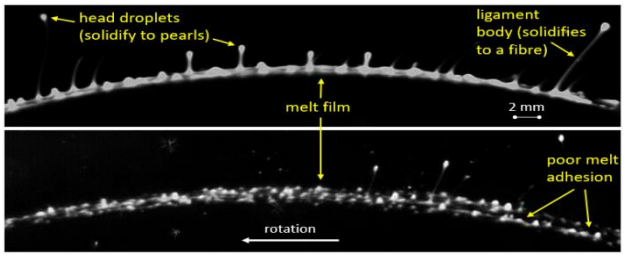

Figure 5: The fiberization process on spinning wheel machine [5]

The melt film is dispersed into liquid ligaments, which are then separated from the film and solidified into fibers. Ligament may be detached from the ligament body to solidify to "pearls" or droplets; or solidify to "ligaments" or fibers.

2.1. Chemical analysis

Sample chemistry was determined using the XRF method on the powdered BS-D sample. Due to the high Si content, a measurement was made at the same time on a standard SiO_2 sample.
The main component of blast furnace was CaO and SiO_2. Diabase as an additive was added to modify the blast furnace slag. Mineral fiber sample was produced on the basis of 60% of a blast furnace slag and 40% of diabase. Chemical composition of BS-D mixture is given in table 1.

Table 1. Chemical analysis of BS-D mixture

SiO_2	Al_2O_3	Fe_2O_3	MgO	CaO
40.4	14.05	4.1	5.0	30.3

The composition in table 1. gives an acidity modulus of 1.55.
The quality of the mineral melt obtained by melting the mineral mixture from which the mineral wool fiber are obtained, is defined by the following characteristics:
• chemical composition,
• melting viscosity,
• melting temperature,
• temperature interval of transition of the melt from liquid to solid state,
• fiber behaviour,
• physico-chemical properties of extracted mineral fibers.
Only if all the specified conditions set for mineral mixture in terms of melting temperatures, viscosity and surface tension are met, then fiber can be produced, and its quality is determined with:
• fiber diameter and length,
• fiber elasticity, hardness etc.

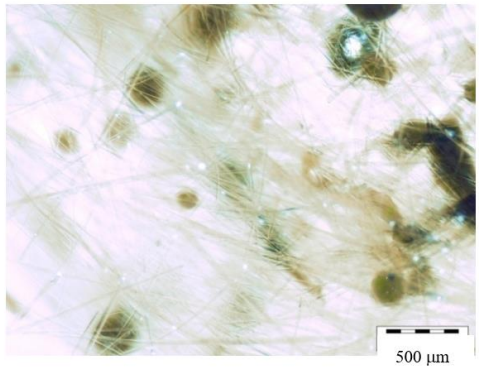

Figure 6a. Micro image of manufactured fibers of BS-D mixture [6]

Primary fiber layers were used in this chemical and thermal analysis. The cross-sectional diameter of the fiber is about 11 microns. Figure 6a) and 6b) show macro images of fibers produced from BS-D mixture combined with microscope images of fibers inserted in metallographic samples.

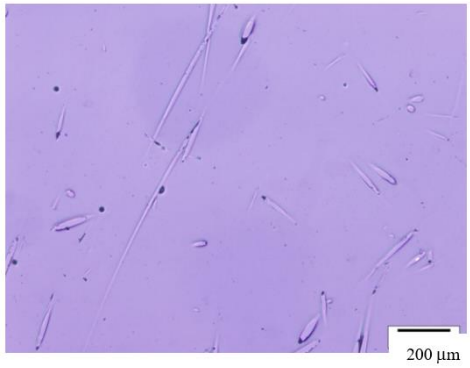

Figure 6b. Micro image of manufactured fibers of BS-D mixture [6]

2.2. Differential line calorimetry

The optimum melting temperature of the mineral melt should be about 1400 °C, where the actual temperatures depend on the ratio of acid and base oxides in the mineral melt. The temperature interval between the melting and solidification temperatures of the melt has a significant influence on the process of melting and fiber forming, on which the quality of mineral fibers depends.

The simultaneous thermal analyzer NETZSCH STA 449 was used for the measurement of thermal effects. This system was used to determine the differential line calorimetry of the curves and the latent heat of fusion. The experiments were performed at a defined heating rate in an Ar protective atmosphere, and with samples in graphite pots. Heating was performed to 1550 ° C, followed by cooling to room temperature. The results of BS-D sample are shown as DSC curves on the graph in Figure 7 for heating, and then in Figure 8 for cooling.

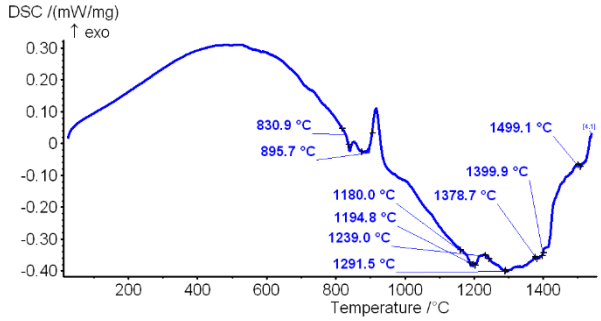

Figure 7. DSC heating curve of BS-D sample with characteristic temperatures [7]

In BS-D sample, the first exso term peak is present at a temperature between 860°C and 890°C, which represents a crystallographic change.

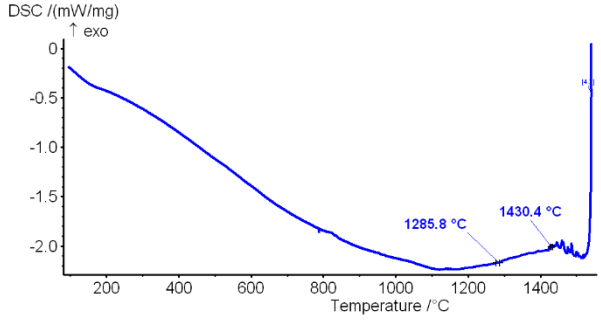

Figure 8. DSC cooling curves of BS-D sample with characteristic temperatures [7]

The chemical composition significantly affects the melting temperature range, and is related to viscosity.
In Table 2, the characteristic temperatures of BS-D sample is given.

Table 2. Characteristic temperature ranges of melting and solidification [7]

Mixture	Mixture Heating		Mixture Cooling	
	Tmin /ºC	Tmax /ºC	Tmax /ºC	Tmin /ºC
BF-D	1292	1499	1430	1286

3. Nanoindentation results

Mineral wool samples were inserted into the epoxy, and prepared by standard metallographic mode by grinding and polishing for optical microscopy and mechanical nanoindentation tests.
Nanoindenter Agilent G200 is a measuring setup for measurements of hardness and elastic modulus. It can apply and record small loads and displacements with high accuracy and precision that provides accurate, repeatable results compliant with ISO 14577 standard and allows dynamic properties characterization via continuous measurement of stiffness by indentation depth. Indentation of the specimen surface is performed with diamond Berkovich indenter tip on the end of indenter shaft. Force actuation to indenter is accomplished by coil-magnet assembly with high accuracy. It provides movements of the shaft in vertical direction (in both ways), while shaft vertical position inside machine frame is fixed with two leaf-springs. Displacement is measured by differential capacitance gauge of high precision. Knowing area function of indenter elastic modulus and hardness can be calculated using Oliver-Pharr methodology [8].
Mechanical tests were performed with a Nanoindenter AG200 using a DCMII measuring head with higher sensitivity at low loads with maximum load is 30 mN. The result is the modulus of elasticity and hardness of the test subject as a function of the depth of the impression.
The average value at a depth between 100 nm and 200 nm was taken as reference to determine the values of hardness and modulus of elasticity. Measurements on seven positions of BS-D fiber with different thicknesses are presented on images, figures 9 and 10 at 100x magnification.

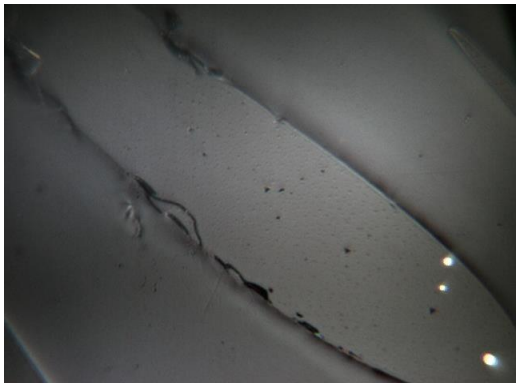

Figure 9. Measurements with thicker BS-D fiber, positions 1, 2, 3 and 4 (100x magnification) [7]

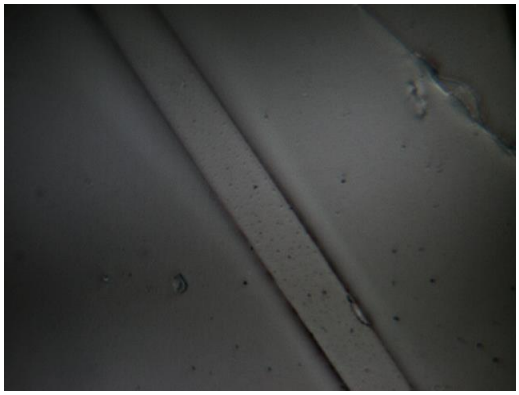

Figure 10. Measurements on a thinner BS-D fiber, positions 5, 6 and 7 (100x magnification) [7]

In the figures 11 and 12 are shown the values of modulus of elasticity and hardness to a depth of 500 nm.

4. Comparison of mechanical characteristics of fibers

Measurements of elastic properties on the BS-D sample, looking at the impressions presented in figures 7 are presented in table 3, [7].

The average elastic module of BS-D fiber samples is 72.6 GPa.

To more accurately determine the mechanical properties of the input raw material, a comparison was made with the allowable values of elastic modulus for characteristic fiber of industrial conditions.

Figure 13 shows the values of measured elastic properties for BS-D fibers.

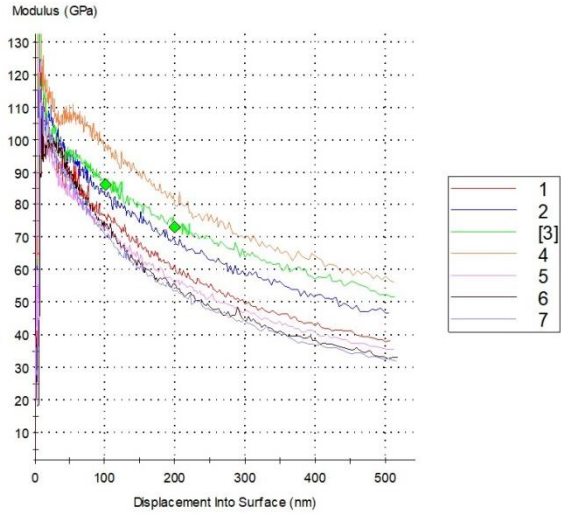

Figure 11. Modulus of elasticity to a depth of 500 nm [7]

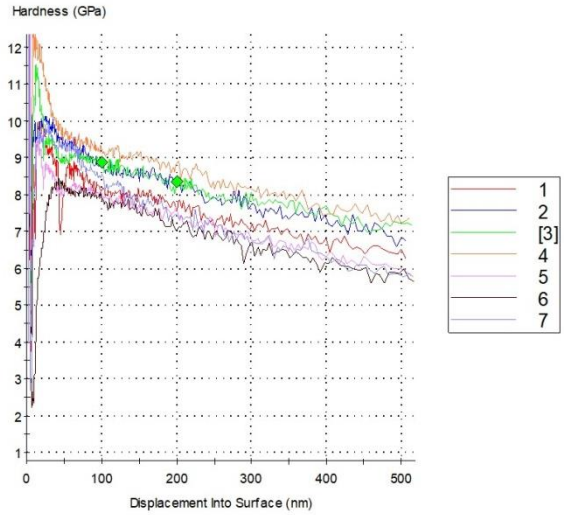

Figure 12. Hardness of BS-D fiber to a depth of 500 nm [7]

Table 3. Average elastic modulus of BS-D sample

Test	Average modulus, GPa
1	69.2
2	76.7
3	80.6
4	90.4
5	65.0
6	64.0
7	62.1
Mean	72.6

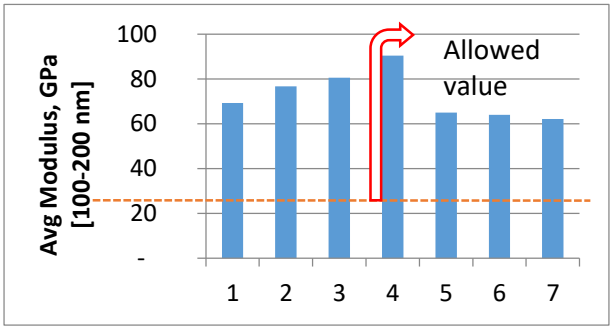

Figure 13. Comparison of measured elastic modulus for BS-D fiber and allowed value for fiber of industrial conditions.

It can be concluded that from the obtained BS-D mixture it is possible to make stone fibers.

Also the nanoindentation results of primary fiber layer mechanical properties based on mixture of blast furnace slag and diabase shows that the blast furnace slag can be used for production of mineral wool.

5. Conclusion

- The results show a positive trend in the use of blast furnace slag, as a replacement for natural mineral aggregates in the technology of stone wool production
- It is possible to produce stone wool of satisfactory characteristics on the basis of substitution of natural raw materials with blast furnace slag.
- The process of the mineral wool primary layer formation was studied experimentally on a model spinning machine with mineral mixture based on blast furnace slag.
- Chemical composition of mixture significantly affects the melt viscosity and mechanical properties of primary fiber layer.
- Nanoindentation results of primary fiber layer mechanical properties based on mixture of blast furnace slag and diabase show that the blast

furnace slag can be used for production of mineral wool.

Acknowledgement

The authors gratefully acknowledge the financial support by the Federation of Bosnia and Herzegovina Ministry of Science and Education.

REFERENCES

[1] Braconi A., Reiche T., (2019), *Session III: Case studies and views from other metal sectors & conclusions legal framework and secondary raw materials: Steel views and examples*, EUROFER/EUROSLAG WORKSHOP 06/11/2019

[2] https://www.euroslag.com/wp-content/uploads/2019/01/Statistics-2016.pdf

[3] Imamović A., Jovanović M., Hadžalić M., Oruč M: (2018), *Perspektiva upotrebe visokopećne troske kao zamjena prirodnim mineralnim agregatima u tehnologiji proizvodnje kamene vune*, 4. Međunarodna naučna konferencija „COMETa 2018"- Jahorina 27-20. November 2018

[4] Kraševec B., Bizjan B., Širok B., (2017),*Glass wool layer formation in the collecting chamber*, Glass Technol.: Eur. J. Glass Sci. Technol. A 58, No. 1, p 1–7

[5] Imamović A., Bizjan B., Seferović R., Mrvar P., Bombač D., (2019), M*echanical properties of mineral stone wool fibers based on mixture of blast furnace slag and diabase*, International journal of advanced research 7, No. 4.

[6] Seferović R., Imamović A., Mujagić D., Jovanović M., Zahirović A., Kasapović D., (2019), *Properties of stone wool primary fiber layers produced with different contents of blast furnace slag*, International journal of advanced research 7, No. 5.

[7] Bombač D., Balaško T., Lamut M., Mrvar P., (2018) *Analiza termičnih in mehanskih lastnosti kamenih vlaken M1, M2, M3 in M4 z različno mešanico diabaza in žlindre*, Ljubljana.

[8] https://web.fs.uni-lj.si/cem/en/infrastructure/laboratories/nanoindentation-characterization-laboratory/

ISSN 1847-7917

Structural design of thermo-active aluminium foam roofing

***Jaroslav JERZ*[1)], *Arun GOPINATHAN*[1,2)], *Anton PUŠKÁR*[3)], *Daniel SZABÓ*[3)], *Jaroslav KOVÁČIK*[1)]**

1) Institute of Materials and Machine Mechanics, Slovak Academy of Sciences, Dúbravská cesta 9/6319, 845 13 Bratislava, **Slovakia**
2) Faculty of Materials Science and Technology, Slovak University of Technology, Jána Bottu 2781/25, 917 24 Trnava, **Slovakia**
2) Faculty of Civil Engineering, Slovak University of Technology, Radlinského 11, 810 05 Bratislava **Slovakia**

ummsjerz@savba.sk
arun.gopinathan@savba.sk
anton.puskar@stuba.sk
daniel.szabo@stuba.sk
ummsjk@savba.sk

Keywords

Solar energy
Aluminium foam
Light-weight roofing
Energy efficiency
Heat exchangers

Professional article

Abstract: Light-weight aluminium foam roofing with embedded corrugated stainless steel pipes provides energy-efficient heat transfer between heat in building interior and surrounding environment utilizing proper non-freezing liquid as a heat transfer fluid. This roofing, therefore, facilitates during colder summer nights to dissipate the excessive heat accumulated in the building interior during the whole tropical days into the surroundings of the building. The various potential ways of using solar gains in future sustainable and energy-efficient buildings have been presented in this contribution, including the seasonal heat storage and year-round use of this energy with the interest to slow down global warming causing current undesirable climate changes.

1. Introduction

Solar energy is an essential source of renewable energy. The solar systems integrated into houses and residential buildings for heating of interiors and Domestic Hot Water (DHW) is, therefore, one of the key solutions to optimize energy efficiency and effectiveness. Based on the physics principle of conservation of energy, the Earth's radiation budget (Figure 1) represents the accounting of the balance between incoming radiation, which is almost entirely solar radiation, and outgoing radiation, which is partly reflected solar radiation and partly radiation emitted from the Earth system, including the atmosphere [6]. However, due to the temporal unbalance between solar energy supply and heat demand (Figure 2), it would be beneficial to exploit the excess of solar energy by carrying out storage for later heating use for daily as well as for long-term demand. Thermal Energy Storage (TES), including sensible, latent, and sorption energy storage, is one of the most reasonable solutions to rationalize the application of renewable energy by increasing the solar fraction in residential and commercial buildings sectors.

TES concerns:

- ✓ near-term storage of solar energy during daytime for use during the night
- ✓ seasonal storage of summer solar energy surpluses to compensate for the overconsumption of heat in winter.

2. Heat storage in the building sector

2.1. Energy demands for heating/cooling and DHW preparation

Application of the following technical solutions represents an opportunity to reduce significantly the energy demands for heating/cooling, preparation of DHW, leading to reduction of costs for construction and operation of future buildings as well as small family houses:

- ✓ the heat comfort of the interior is maintained during the whole year round by stabilization of the temperature using the system of aluminium foam

heating/cooling ceiling heat exchangers that allow short term storage of the heat for at least several hours in the form of latent heat of phase transformation of Phase Change Materials (PCMs) impregnated in the porous structure of aluminium foam for later use or, for removal of undesirable heat to the building surroundings during comparatively colder nights,

- ✓ an underground seasonal sorption energy storage tank in which a thermochemical reaction takes place as a result of which hydrates of metal halides are dehydrated and the biomass obtained as waste from agricultural production or the wood processing industry is dried effectively utilizing surplus summer heat for heating of interiors and DHW especially during the winter season,
- ✓ the thermo-active roofing is able not only to harvest the heat from the solar gains and use it for heating of the interiors and DHW but also to dissipate an undesirable heat from the interiors to the building surroundings during colder summer nights.

2.2. Roofing heat exchangers

The main requirements for thermo-active roofing of pitched roofs reducing the energy consumption of a building constructed according to this concept can be summarized as follows [3]:

- ✓ roofing must be sufficiently resistant to weathering, frost, intense solar radiation, summer heat, chemicals present in the air, chemically polluted water vapour, and to mechanical damage caused by adverse weather conditions (e.g. heavy rainfall, groats, etc.),
- ✓ roofing must provide considerable heat gains even when the temperature around the building is low, but the sunshine on the roof is sufficiently intense,
- ✓ the amount of the heat accumulated by roofing during hot summer days is low enough to dissipate it to the building surroundings during summer nights as efficiently as possible together with the heat of the liquid heat transfer medium flowing through the pipelines integrated into the structure of aluminium foam from which the roofing is made,
- ✓ the manufacturing cost of a thermo-active roof covering for pitched roofs of buildings must be only slightly higher compared with the manufacturing cost of classic roofing used in the current building which fulfills together with an additional heat insulation layer in particular only the functions of thermal insulation of the roof and the protection against the penetration of rainwater and water vapour into the interior,
- ✓ thermo-active roofing must be architecturally designed so that it is the part of the roof without being possible to recognize at first sight the places from which the heat of solar gains is gained from the rest of the roof.

The weight of 1 m^2 of aluminium foam heating/cooling ceiling heat exchangers is 5.4 kg. They can be filled with 7.24 kg of PCM RUBITHERM® RT28HC with a melting range of 27 – 29°C (PCM density in the solid-state is 0.88 g/cm^3, in the liquid stage 0.77 g/cm^3). Since 1 kg of PCM can accumulate about 250 kJ latent heat, and thus even 1810 kJ (e.g. ~ 503 Wh) of latent heat can be accumulated during phase transition of PCM into 1 m^2 of aluminium foam panels with pores filled by PCM in this way. There is enough heat during winter for keeping sufficient thermal comfort for about 9 hours without delivering additional energy from the source as an average winter monthly heat demand is ~ 40 kWh/m^2. The temperature of the ceiling panels does not drop below the phase transition temperature during this time even when they accumulate no more heat from the source. This means that during those days of the heating season that can be obtained from solar gains through a roof at least 500 Wh of heat (by heating the liquid heating medium to a temperature of at least 30°C) for every 1 m^2 of living space, sufficient thermal comfort can be assured by the daily charging and discharging of said ceiling heating/cooling panels. A sufficient amount of solar gains is available in the region of Central Europe for this purpose almost throughout the whole spring as well as autumn. The energy required to drive the circulating pump that distributes liquid heat transfer fluid heated by thermo-active roofing into the interior is almost negligible in comparison with the energy required for classical heating. The solar energy surpluses harvested during hot summer days can be stored in an underground seasonal sorption energy storage tank. Figure 3 shows an approximate estimate of the monthly energy demand for the operation of a self-standing single-storey family house built in the Central European region and the expected reduction of its energy demand in the case of use foamed aluminium heat exchangers described in this contribution supplemented by the seasonal storage of summer heat surpluses [3].

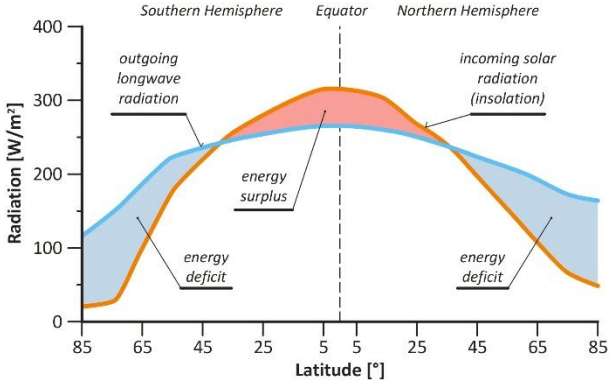

Figure 1. Earth's yearly radiation budget [6].

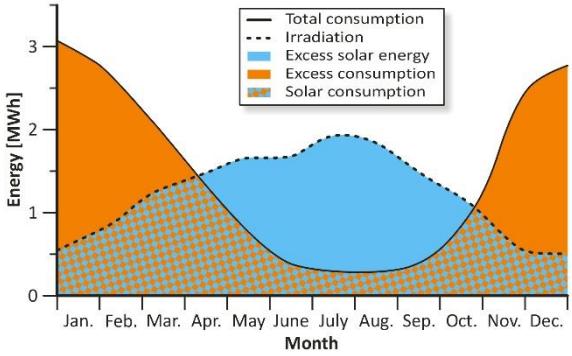

Figure 2. The seasonal mismatch between accessible solar energy and heating demand for the average family house [1].

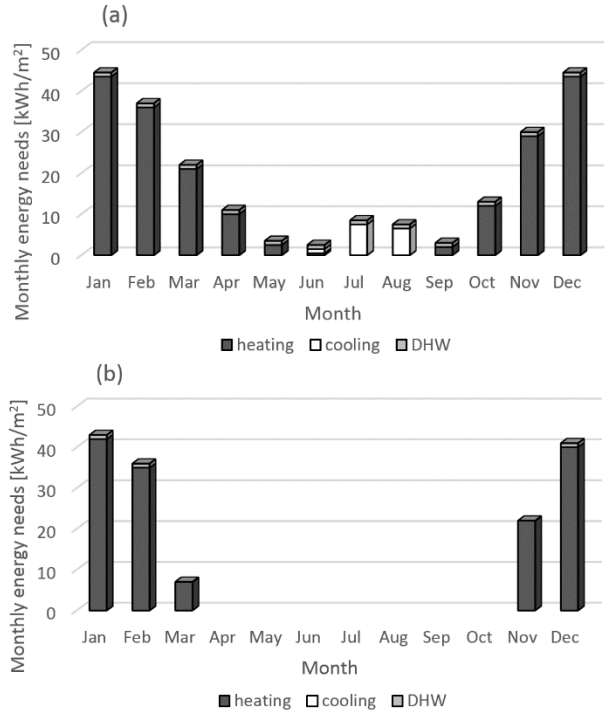

Figure 3. Comparison of energy needs for heating, cooling, and DHW preparation of (a) classic family house and (b) the house that uses novel aluminium foam heat exchangers, both built in the region of Central Europe [2].

3. The measurement of roofing heat transfer efficiency

3.1. Roofing design

The prototype of a functional demonstration area covered with two pieces of roofing tiles with the interconnected distribution of heat transfer fluid by copper pipes used for efficient heat dissipation from the roofing surface to the heat transfer fluid and vice versa if necessary to dissipate summer solar surpluses (Figure 4 and 5) has been investigated in this study. The samples of the roofing consist of a surface layer of trapezoidal steel sheet with the thickness of 0.35 mm with dimensions 680 × 580 mm^2, under which the distribution of heat transfer fluid is placed in the ventilation layer through copper pipes with an outer diameter of 18 mm and a wall thickness of 1 mm. The copper pipes are attached to the aluminum foam panel with the directions 480 × 400 × 10 mm^3 (Figure 7) utilizing brass clips, which serves the purpose of homogenous distribution of the temperature obtained from solar gains through the surface layer of the roofing tile and at the same time ensuring its sufficient bending stiffness. The thermal insulation in the form of polyurethane (PUR) foam plate with dimensions 480 × 400 × 30 mm^3, density 34 kg/m^3 and thermal conductivity 0.022 W/(m·K) is placed under the aluminum foam layer in a box made of 1 mm thick aluminum sheet.

3.2. Heat transfer measurement

Thermo-technical properties of demonstration area covered with two pieces of roofing tiles were investigated in the Faculty of Civil Engineering of the Slovak University of Technology in Bratislava (Laboratory of Building Physics of the Department of Building Structures) using a climate chamber for modeling of synergic effects of heat transfer, water vapor diffusion and air filtration (Figure 8). The air temperature in the outdoor and indoor chamber was at the beginning of the measurement stabilized at 35°C and maintained during the whole experiment by thermostats providing temperature control on both sides of the climatic chamber. The temperature of the surface of roofing tiles has been measured by 8 thermocouples and the average value was evaluated and shown in figure 6. as the outdoor temperature. The indoor air temperature, as well as the temperature of the inner surface of the roofing tile, have been measured separately. The water temperature in the copper tubes of the roofing heat exchanger was measured with 6 thermocouples to obtain information on the temperature distribution in the roofing during its irradiation with UV radiation.

The water providing heat dissipation from the surface of thermoactive roofing flowed through the copper pipes at a speed of 60 l/hod during the whole experiment. As can be seen from figure 6 the tested roofing tiles started to be irradiate after stabilizing their outdoor surface temperature to 35°C by 2 reflectors of the solar system (Figure 9) with the intensity of radiation 259 W/m^2 and after two hours the remaining 2 reflectors were turned on so that the radiation increased to 503 W/m^2. The radiation intensity was measured with a Kipp & Zonen CMP6 Pyranometer with a sensitivity of 15.05 μV/Wm^{-2}.

The experiment has shown that when irradiating a roofing sample with dimensions 0.4 × 0.96 m with 99.5 W radiation, the water temperature increases by 0.51°C under the abovementioned conditions. When the same roofing sample is irradiated with a radiation intensity of 193.2 W, the water temperature increases by 0.98°C.

4. The future potential of heat storage in buildings

4.1. The energy efficiency of buildings

The energy efficiency, e.g. the amount of energy used per unit of product (building construction, materials, equipment, etc.), is determined by improvements in energy conversion and reductions in energy use for environmental control.

The energy efficiency of a building is the extent to which the energy consumption per square meter of the floor area of the building measures up to established energy consumption benchmarks for that particular type of building under defined climatic conditions. Comparisons with simple benchmarks of annual energy use per square meter of floor area (kWh/(m^2·annum)) allow the standard of energy efficiency to be assessed and priority areas for action to be identified.

The annual energy use per square meter of floor area can be significantly reduced if:

- ✓ thermo-active roofing is capable of recovering the heat from solar gains as well as dissipating excessive summer heat surpluses,
- ✓ ceiling heat exchangers impregnated by Phase Change Materials (PCMs) can maintain sufficient thermal comfort in the interior in an energy-efficient way,
- ✓ collector working on the principle of thermochemical reaction incorporated into the air-handling system allows the seasonal storage of low-potential heat obtained from summer heat surpluses.

4.2. The approaches for heat storage

The common approaches for heat storage are through:

- ✓ sensible heat in which the heat is simply transferred from/to a material,
- ✓ latent heat in which a phase change occurs, or
- ✓ thermochemical heat which involves a chemical reaction to release or store heat energy.

Thermochemical heat storage systems can provide very high energy densities. Various economic systems with the right choice of materials based on carbonation, oxidation, hydration, and hydrogenation reactions are therefore currently receiving a great deal of attention from the scientific community.

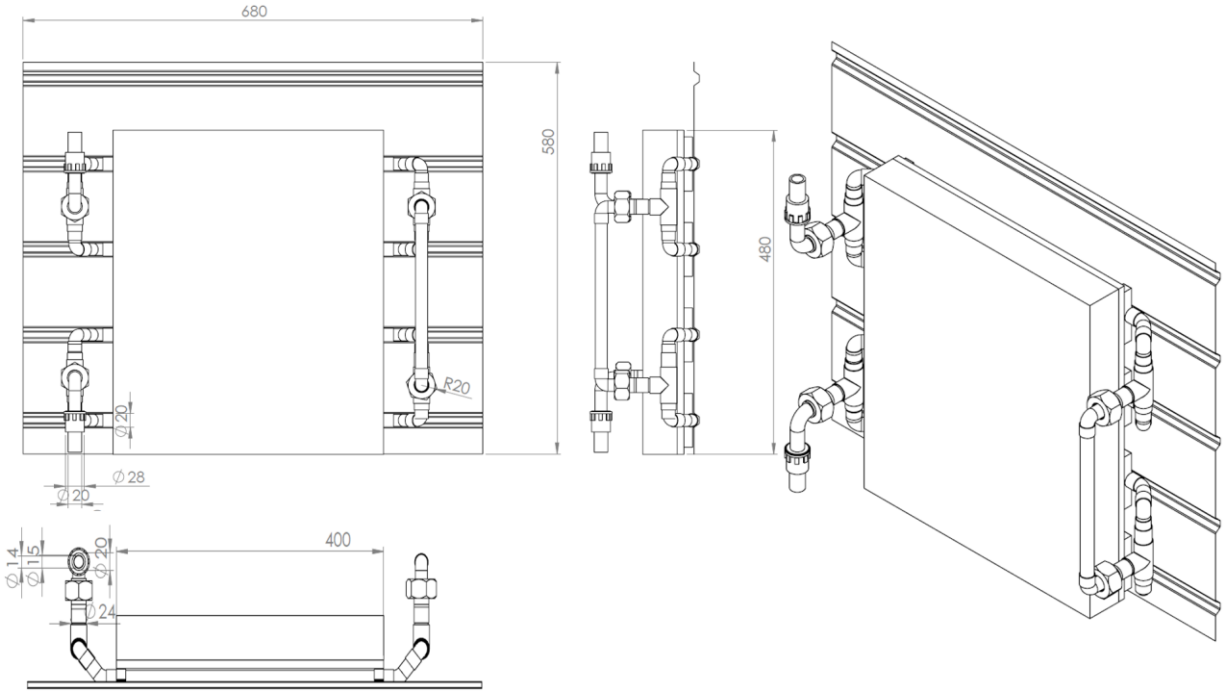

Figure 4. The structural design of a functional demonstration roofing tile was designed to test its thermophysical behavior in conditions corresponding to real weather conditions.

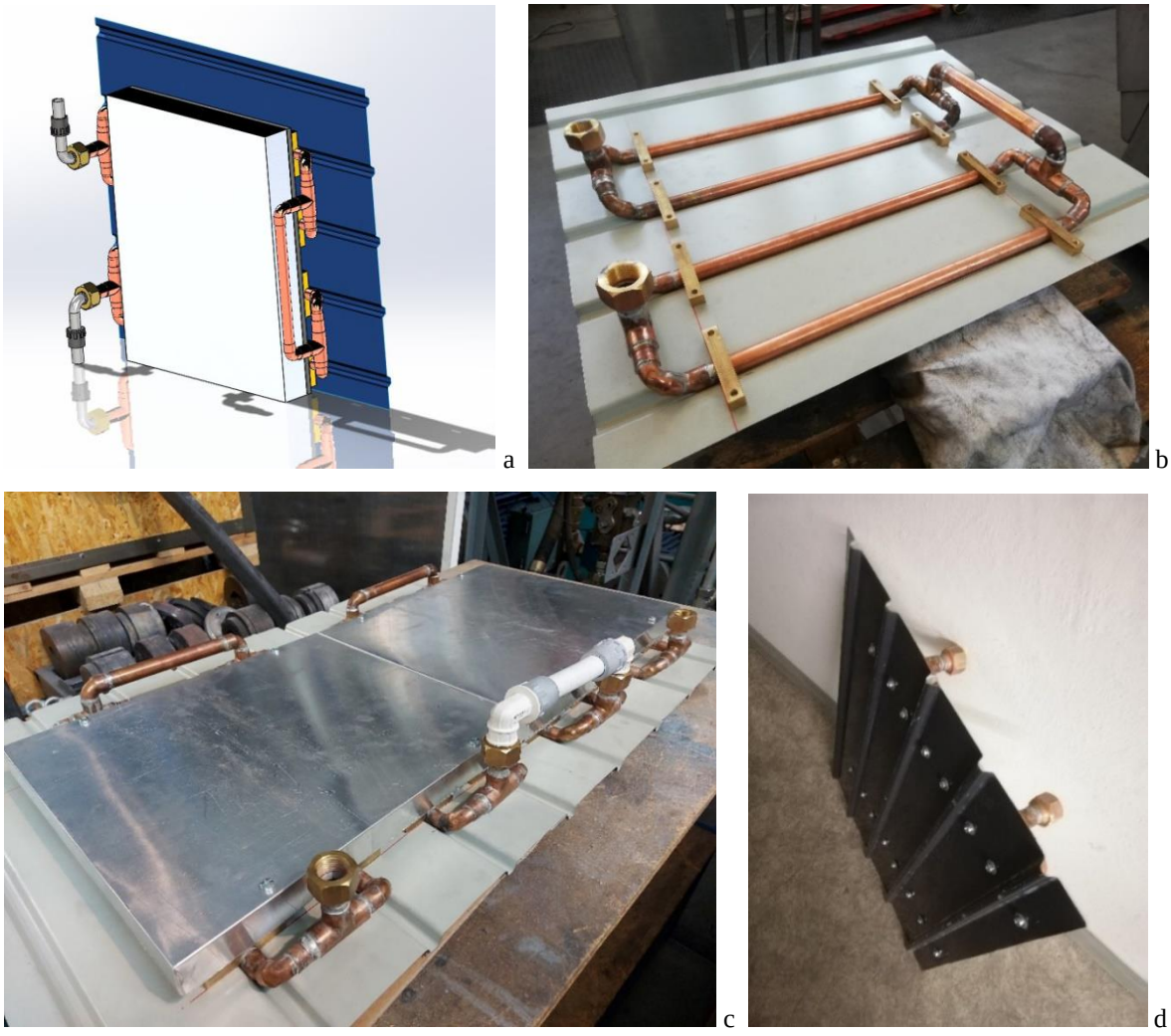

Figure 5. Prototype of a functional demonstration area with dimensions 680 × 1060 mm^2 covered with two pieces of roofing tiles (a) bottom view of a virtual model of roofing tile; (b) view of the piping system of heat transfer fluid distribution with copper pipes; (c) view of interconnected 2 prototype roofing tiles from below; (d) view of the part of the prototype roofing with the integrated function of the heat exchanger from the side of the covering surface trapezoidal sheet.

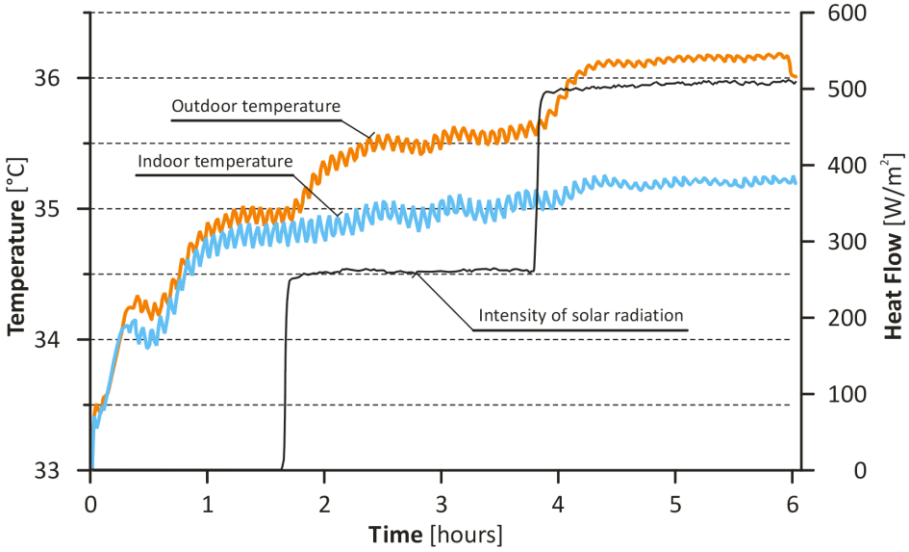

Figure 6. Thermal behavior of demonstration area covered with two pieces of roofing tiles during experiment modelling the synergic effect of heat transfer from the solar system to the heat transfer fluid flowing in the piping system.

Figure 7. Aluminium foam panel with the dimensions 480 × 400 × 10 mm^3 and weight 2138 g made of a foamable precursor prepared from fine-grained aluminum powder of 99.7% purity with a grain size of less than 63 μm with a content of 0.15 wt. % of TiH_2 powder as a foaming agent (panel density: 1.11 g/cm^3).

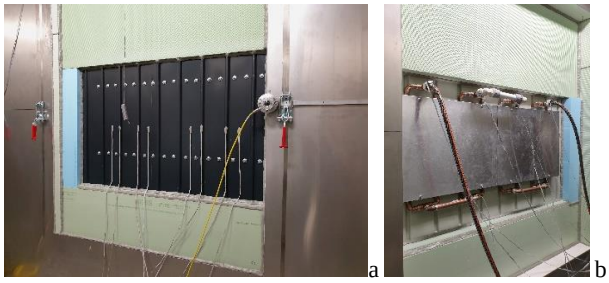

a b

Figure 8. View of tested roofing tiles in a climate chamber for modeling of synergic effects of heat transfer, water vapor diffusion, and air filtration from the exterior (a) and interior side (b).

5. Conclusions

This paper highlights the aluminium foam roofing system with the integrated function of the heat exchanger. This roofing can be designed to cover entire pitched roofs of the buildings to ensure energy-efficient cooling/heating through interior ceilings impregnated by PCM. The roofing is able effectively to gain low potential heat from (or dissipate it to) the building surroundings. The aluminium foam ceilings are therefore able to store a large amount of heat to ensure the constant temperature for several hours without the necessity to transport it to/from the roofing. The aluminium foam heat exchangers are able not only to reduce the building and operation costs of future buildings but simultaneously to increase significantly the thermal comfort for their users. The principles analyzed in this paper can be used in the building sector for designing any structural part forming an outer building envelope with an integrated function of the energy-efficient heat exchanger.

Acknowledgments

The financial support by the Slovak Research and Development Agency under the contract APVV-17-0580 (project: Research of roofing with the integrated function of the heat exchanger, acronym: RoofFoam) is gratefully acknowledged.

Figure 9. The solar system consisting of four reflectors of the Lightmaster 1000 CL1 type fitted with Osram HQI-TS 1000 W / D / S PRO lamps.

REFERENCES

[1] Chen B., (2020), *Study of ettringite-based thermochemical energy storage for buildings. Thermics*, Université de Lyon

[2] Jerz J., Simančík F., Španielka J., Šebek J., Kováčik J., Tobolka P., Dvorák T., Orovčík Ľ., (2018), *Energy demand reduction in nearly zero-energy buildings by highly efficient aluminium foam heat exchangers.* Materials Science Forum, vol. 919, p. 236-245. ISSN 0255-5476. DOI: 10.4028/www.scientific.net/MSF.919.236

[3] Jerz J., Simančík F., Kováčik J., Španielka J., *Aluminium foam for thermo-active pitched roofs of nearly zero-energy buildings*. (2017), 7th International Conference Mechanical Technologies and Structural Materials 2017. – Split: Croatian Society for Mechanical Technologies, p. 49-58. ISSN 1847-7917.

[4] Jerz J., Gopinathan A., Kováčik J, (2021), *Phase Change Materials Reinforced with Aluminium Foam for Latent Heat Storage.* In: Vid. Proc. Adv. Mater., Volume 2, Article ID 2021-0146, DOI: 10.5185/vpoam.2021.0146. (https://www.proceedings.iaamonline.org/article/vpoam-2021-0146)

[5] www.illustrationsource.com/stock/image/507120/the-difference-between-the-solar-radiation-absorbed-and-the-thermal-radiation-emitted-determines-earths-radiation-budget/

[6] https://science.nasa.gov/ems/13_radiationbudget

[7] Gopinathan A., Jerz J., Kováčik J. - Dvorák T., (2021), *Investigation of the Relationship between Morphology and Thermal Conductivity of Powder Metallurgically Prepared Aluminium Foams.* In: Materials, vol. 14, no. 3623. ISSN 1996-1944

ISSN 1847-7917

Thermal properties of copper base shape memory alloy

***Borut KOSEC*[1)], *Blaž KARPE*[1)], *Mirko GOJIĆ*[2)], *Aleš NAGODE*[1)], *Ladislav VRSALOVIĆ*[3)], *Stjepan KOŽUH*[2)], *Ivana IVANIĆ*[2)], *Matija ZORC*[1)] *and Milan BIZJAK*[1)]**

1) University of Ljubljana, Faculty of Natural Sciences and Engineering, Askerceva 12, 1000 Ljubljana, **Slovenia**
2) University of Zagreb, Faculty of Metallurgy, Aleja naodnih heroja 3, 44103 Sisak, **Croatia**
3) University of Split, Faculty of Chemistry and Technology, ul. Ruđera Boškovića 35, 21000 Split, **Croatia**

borut.kosec@omm.ntf.uni-lj.si

Keywords

Thermal properties
Thermal conductivity
Measurement
Copper base shape memory alloy
Rapid solidification

Original scientific article

Abstract: The mechanical properties and microstructure of copper base shape memory alloys are relatively well known, while data on thermal properties (thermal conductivity, specific heat and temperature conductivity) are not available. In the frame of our investigation work thermal properties of rapidly solidified Cu-Al-Ni-Mn alloy were determined.

As the first part of the work, a study and evaluation of the operation of the device for determining the thermal properties of Hot Disk TPS 2200, today one of the more modern and high-quality instruments for determining thermal properties has been carried out.

In the second part of the work, the measurements and analysis of thermal properties of rapidly solidified Cu-Al-Ni-Mn shape memory alloy in accordance with the standard ISO 22007-2 at ambient and elevated temperatures has been done.

1. Introduction

Shape memory alloys (SMA) are relatively a new class of advanced functional materials which are able to memorize and recover its original shape after being significantly deformed from heating over the phase transformation temperature [1].

The main advantage of Cu-based SMA are their low price compared to other SMA. Properties of Cu-Al-Ni alloys are superior to those of Cu-Zn-Al alloys due to their wide range of useful transformation temperature and small hysteresis. Although Cu-Al-Ni alloys have a better thermal and electrical stability and a higher operating temperatures, their practical applications are sometimes restricted by very small shape changes due to their poor workability and susceptibility to brittle intergranular cracks [2]. Their very high elastic anisotropy and large grain size cause brittle and poor mechanical properties owing to the high degree of order in the parent phase.

Typically, composition of Cu-Al-Ni SMA is in the range Cu-(13-15 m. %)Al-(3-4.5 m. %)Ni [3]. Adding some alloying elements such as Mn, Fe, Ti, Zr, B etc. to the alloys can significantly improve their ductility and other properties which modify their operating temperatures [4,5].

In the frame of our investigation we have investigated thermal properties of rapidly solidified Cu-Al-Ni-Mn shape memory alloy [6] produced by melt-spinning procedure (Figure 1). The chemical composition of the testing Cu-Al-Ni-Mn alloy is in Table 1.

Table 1. Chemical composition of the testing Cu-Al-Ni-Mn alloy (in m.%)

Mn	Ni	Al	Cu
2.4	4.2	12.7	rest

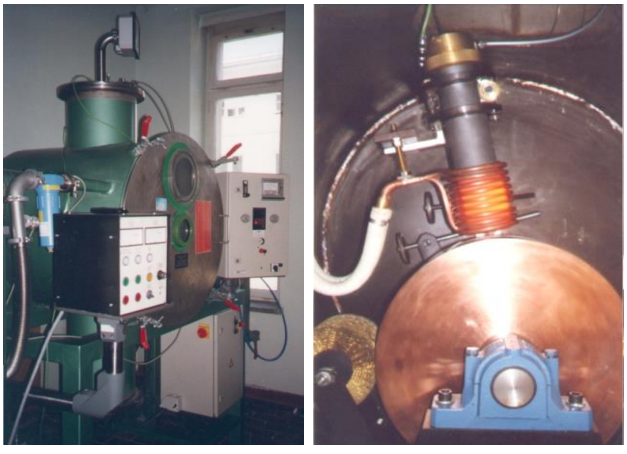

Figure 1. Melt spinner at Faculty of Natural Sciences and Engineering University of Ljubljana [7].

Single Roll Melt Spinning is the most commonly used process for the production of rapidly solidified thin metal foils or ribbons with amorphous, microcrystalline or even combined microstructure. In this type of a process, a molten material is introduced onto a surface of the spinning wheel, where melt puddle is formed, and as final results a metal ribbons are formed (Figure 2).

The final products are in the form of thin and narrow ribbons, which could be in further production steps subjected to milling and molded into useful shapes by different methods of powder metallurgy. In our cas we have made disks from ground and molded alloys (Figure 3). From them testing samples to perform measurements of thermal properties of dimensions Ø40 x 13 mm have been done.

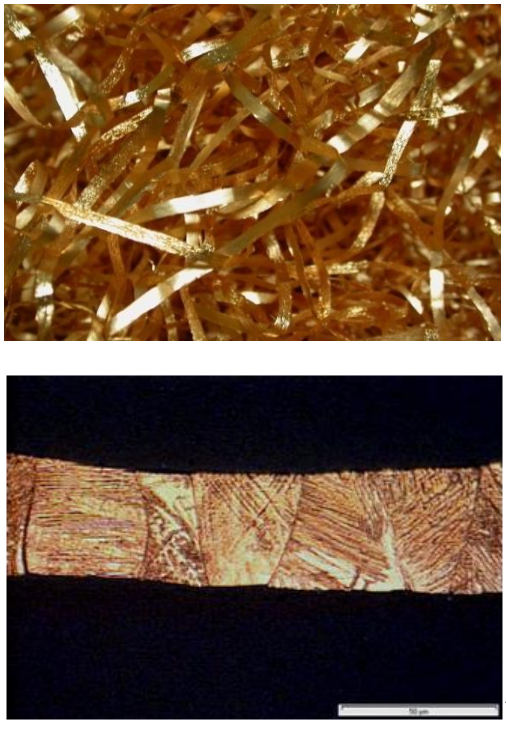

a)

b)

Figure 2. Rapidly solidified Cu-Al-Ni-Mn shape memory alloy thin ribbons (a), microstructure (b).

Figure 3. Disks from ground and molded rapidly solidified Cu-Al-Ni-Mn shape memory alloy.

2. Temperature properties measurement

In our research, we used one of the most advanced instruments for determining the thermal properties, Hot Disk TPS 2200, a product of Hot Disk AB company, Gothenburg, Sweden (Figure 4) [8].

Figure 4. Instrument Hot Disk TPS 2200.

The instrument can be used for determining thermal properties of various materials including pure metals, alloys, minerals, ceramics, plastics, glasses, powders and viscous liquids with thermal conductivity in the range from 0.01 to 500 W/mK, thermal diffusivity from 0.01 to 300 mm^2/s and heat capacity up to 5 MJ/m^3K.

Measurements can be perform in a temperature interval between -50 °C up to 750 °C [9].

Figure 5. Measuring sensor sandwiched between two halves of a sample during measurement.

Hot disk measuring method is a transient plane source technique (TPS). Based on the theory of TPS, instrument utilizes a sensor element in the shape of 10 μm thick double spiral, made by etching from pure nickel foil. Spiral is mechanically strengthening and electrically insulated on both sides by thin polyimide foil (Kapton ®Du Pont) for measurements up to 300 °C or mica foil for measurements up to 750 °C.

Sensor acts both as a precise heat source and resistance thermometer for recording the time dependent temperature increase. During measurement of solids,

encapsulated Ni-sensor is sandwiched between two halves of the sample and constant precise pre-set heating power is released by the sensor, followed by 200 resistance recording in a pre-set measuring time, from which the relation between time and temperature change is established. Based on time dependent temperature increase of the sensor, thermal properties of the tested material are calculated

2.1. Experimental

Measurements and analysis of thermal properties of testing samples from the testing rapidly solidified copper base shape memory alloy were performed in accordance with ISO 22007-2 standard [10] in the Laboratory for Thermotechnical Measurements, Faculty of Natural Sciences and Engineering, University of Ljubljana. In Figure 6 complete results of thermal properties measurements are presented.

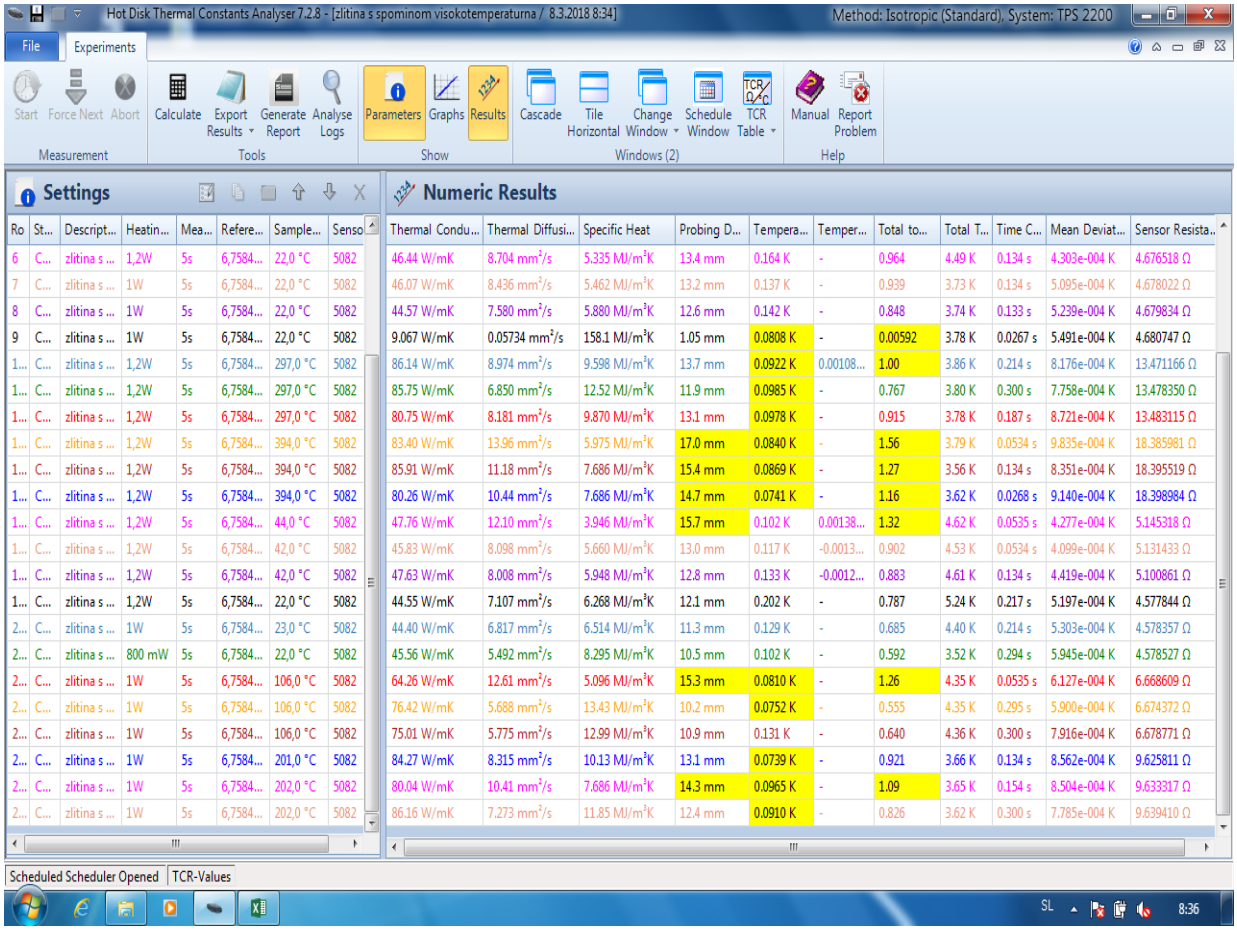

Figure 6. Results of TPS measurements.

In Table 3 thermal properties (thermal conductivity, specific heat and temperature conductivity) of analysed rapidly solidified Cu-Al-Ni-Mn shape memory alloy at ambient temperature (approx. 22 °C) are presented. In Figure 7 shows thermal conductivity of analysed Cu-Al-Ni-Mn shape memory alloy on the temperature interval between ambient temperature (approx. 22 °C) and temperature 400 °C.

Table 2. Thermal properties of analysed Cu-Al-Ni -Mn shape memory alloy at ambient temperature

	Cu-Al-Ni-Mn
Thermal conductivity	45.30 W/mK
Specific heat	6.29 MJ/m^{3}K
Temperature conductivity	7.36 mm^2/s

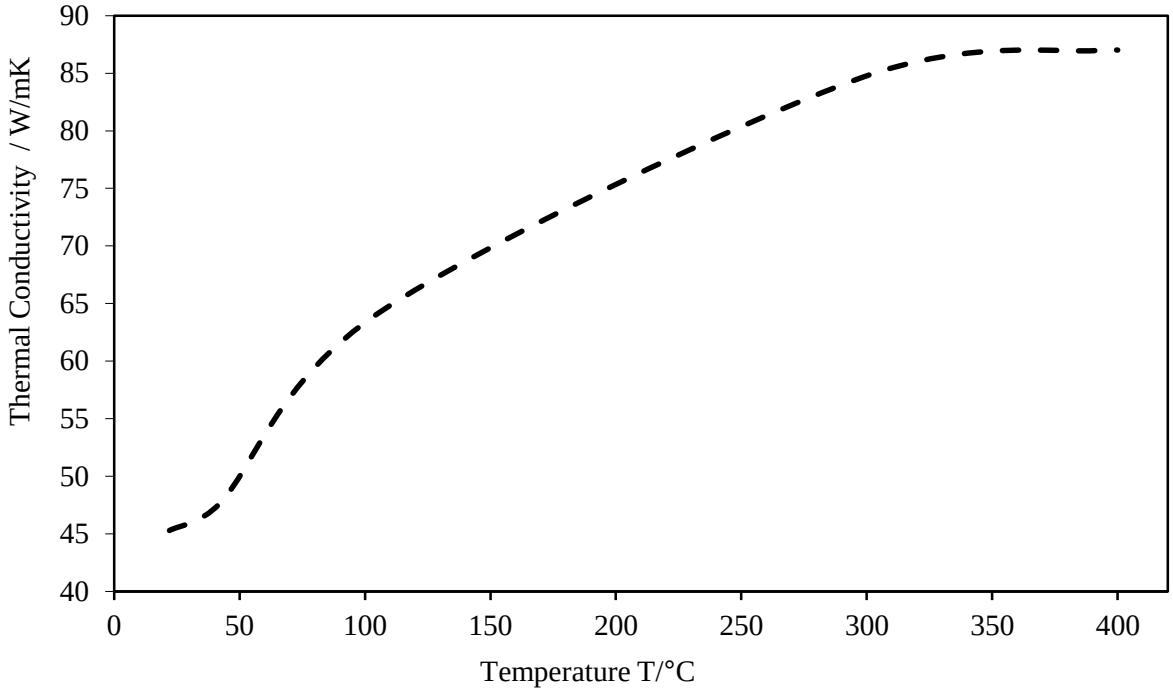

Figure 7. Thermal conductivity at elevated temperatures.

3. Conclusions

In the frame of investigation thermal properties of rapidly solidified Cu-Al-Ni-Mn shape memory alloy were determined. The measurements and analysis of thermal properties of rapidly solidified Cu-Al-Ni-Mn shape memory alloy has been done.in accordance with the standard ISO 22007-2 at ambient and elevated temperatures.

The values of thermal properties of Cu-Al-Ni-Mn steel at ambient temperature (approximately 22 °C) are:
thermal conductivity 45.30 W/mK,
specific heat 6.29 MJ/m^{3}K, and
temperature conductivity 7.36 mm^2/s.

We found that investigated rapidly solidified Cu-Al-Ni-Mn shape memory alloy at ambient temperature has almost 100 % lower heat conductivity as at temperature 400 °C.

REFERENCES

[1] L.A. Dobrzanski, Technical and Economical Issues of Materials Selection, Silesian Technical University, Gliwice, 1997.

[2] H.H. Libermann, Rapidly solidified alloys, Marcel Dekker, London, 1993.

[3] M. Gojić, L. Vrsalović, S. Kožuh, A.C. Kneissl, I. Anžel, S. Gudić, B. Kosec, M. Kliškić, Electrochemical and microstructural study of Cu-Al-Ni shape memory alloy, Journal of Alloys and Compounds, 509 (2011) 41, 9782-9790.

[4] G. Lojen, I. Anžel, A.C. Kneissl, E. Unterweger, B. Kosec, M. Bizjak, Microstructure of rapidly solidified Cu-Al-Ni shape memory alloy ribbons, Journal of Materials Processing Technology, 162/163 (2005), 220-229.

[5] I. Ivanić, S. Kožuh, F. Kosel, B. Kosec, I. Anžel, M. Bizjak, M. Gojić. The influence of heat treatment on fracture surface morphology of the CuAlNi shape memory alloy. Engineering failure analysis.77 (2017), 85-92

[6] Ivanić, M. Gojić, S. Kožuh, B. Kosect. Microstructural analysis of CuAlNiMn shape-memory alloy before and after the tensile testing. Materiali in tehnologije. 48 (2014) 5, 713-718.

[7] Kosec, Device for rapid solidifying of metal alloys, Euroteh, 3 (2004), 32-33.

[8] Kosec., B., Karpe, B., Instrument for the thermal properties analysis Hot Disk TPS 2200, IRT3000, 1 (2017), 67.

[9] B. Karpe, M. Vodlan, I. Kopač, I. Budak, A. Nagode, A. Pavlič, T. Puškar, B. Kosec. Thermal properties of materials used in dental medicine. Advanced technologies and materials. 43 (2018) 1, 7-10.

[10] International standard ISO 22007 (2009). Plastics – Determination of thermal conductivity and thermal diffusivity – Part 1: General principles. Reference: ISO 22007:2009(E).

ISSN 1847-7917

A heuristic method for an approximate solution of the knapsack problem

Maryna KOSTYKOVA[1)]***, Larysa KOZACHOK***[1)]***, Andrii LEVTEROV***[1)]***, Anna PLEKHOVA***[1)]***, Viktoriia SHEVCHENKO***[1)]***, Anton OKUN***[2)]

1) Kharkiv National Automobile and Highway University
25 Yaroslava Mudrogo St., Kharkiv, 61002, **Ukraine**
2) National Technical University "Kharkiv Polytechnic Institute"
2 Kyrpychova St., Kharkiv, 61002, **Ukraine**

kmv_topaz@ukr.net
larisak2010@ukr.net
lai@khadi.kharkov.ua
plehovaanna11@gmail.com
vicashev@gmail.com
okunanton@gmail.com

Keywords

Algorithm
Value
Loading
Weight
Approximate solution

Original scientific paper

Abstract: The basic concepts and possibilities of solving the knapsack problem by the heuristic method are presented and substantiated. This problem is being actively researched; its popularity is due to the large number of applications. The main areas of application are in the planning and management of economic, production and transport systems. The implementing method and algorithm are described. The research consists in the development of a heuristic method for solving the knapsack problem, which gives approximate solutions to the problem. The problem considered is NP-complete, and there is no polynomial algorithm that solves it in a reasonable time. The computational characteristics of the algorithm obtained experimentally on various sets of generated initial data are presented in the paper. Recommendations for its practical application in real problems are given.

1. Introduction

It is known that the knapsack problem is a classical discrete optimization problem (e. g. [1] and [2]). This problem and its variants are widely used to simulate a large number of practical problems. In general, the problem can be formulated as follows: from a given set of items with the "value" and "weight" properties, it is required to select a certain number of items in such a way as to obtain the maximum total value while observing the limit on the total weight.

The problem got its name from the maximization problem of packing as many valuable things as possible into a knapsack, provided that the total volume (or weight) of all items that can fit into the knapsack is limited. The term "knapsack" itself can be interpreted broadly enough. The knapsack problem and its modification often arise in economics, cryptography, genetics, applied mathematics and logistics to find the optimal loading of a transport (car, plane, train, container, ship's hold) or warehouse.

The knapsack problem is a model for a large number of industrial tasks such as positioning of goods in a warehouse with a minimum area; cutting fabric, namely from the available piece of material to obtain the maximum number of patterns with a certain shape; calculation of the optimal investment.

The knapsack problem is one of the essential problems in the field of cryptography. This is the task on the basis of which the first public key encryption algorithm (Merkle–Hellman knapsack cryptosystem) was developed. A solution to the knapsack problem was used to encrypt messages. There are a number of modifications of the Merkle-Hellman cryptosystem.

Many other problems of different dimensions can be reduced to the classical problem setting. Completely different characteristics and even their combinations as value and weight can be used. In this matter, it is only necessary to have some transformation (function), which will reduce the required problem to the classical one (e. g. [3] and [4]).

There are various exact and approximate algorithms for solving the knapsack problem. Exact algorithms include brute force method, branch-and-bound method and dynamic programming. The approximate algorithms are greedy and genetic (e. g. [5] and [6]).

Symbols

A	- number of weight units	x	- items that maximize the total value of the load and are placed in the knapsack by weight
a	- weight of an item	X	- vector of item indices
c	- value of an item	Y	- values vector of load units
D_e, D_r	- confidence interval	z	- value of load
I	- set of items		
L	- weight of a knapsack		**Greek letters**
N	- number of items	Δ	- error
O	- running time		
Q	- estimate for each vertex of the search tree		**Subscripts**
R_e	- underloading of a knapsack	i	- i-th kind of item
S_t	- deviation		
V	- total value of items	max	- maximum
W	- maximum weight capacity	s	- average

When choosing a solution algorithm, one has to choose between exact algorithms, which are not applicable for large knapsacks, and approximate ones, which operate quickly, but do not provide an optimal solution to the problem. The choice of using one method or another is a controversial task. It all depends on the setting of the task, as well as what goals are set (e. g. [5] and [6]).
Comparison of various methods for solving the knapsack problem is widely presented in the literature and on the Internet. Much attention has been paid to the development of methods for solving the problem, and primarily effective ones (e. g. [7], [8] and [9]).

2. Problem setting

The aim of the study is to develop a heuristic method for solving the knapsack problem, which gives approximate solutions to the problem. An analysis of this algorithm is provided, on the basis of which recommendations for their practical application are given.
The problem we are considering is NP-complete, and the problem is that there is no polynomial algorithm that solves it in a reasonable time.
In general, the knapsack problem is formulated as follows. Before journey a knapsack with a capacity of no more than A weight units, from a set $I = \{1, 2, ..., n\}$ of items, each with weight a_i and value c_i, it is necessary to put those items x_i, $i \in I$, that maximize the total value of the load and are placed in the knapsack by weight.
In mathematical form, the problem is presented as follows: it is required to find x_i, $i \in I$, delivering

$$\max \sum_{i \in I} c_i x_i = W \tag{1}$$

under conditions

$$\sum_{i \in I} a_i x_i \le V \tag{2}$$

$$x_i = \begin{cases} 1, & \text{if the item is placed in a knapsack,} \\ 0, & \text{if the item is not placed in a knapsack.} \end{cases} \tag{3}$$

Thus, the knapsack problem is an integer linear programming problem with Boolean variables. Its solution is achieved on a certain subset 2^n of combinations formed by different sets of variables x_i, that meet the condition (2).
It is known that the problem is NP-complete, and for such problems, theoretically speaking, there is no time-polynomial solution to the algorithm [1]. Among the exponential algorithms, the most suitable are, apparently, those that implement the branch-and-bound scheme, the dynamic programming method, the Balas additive algorithm [2], and other developed algorithms. These algorithms are estimated in terms of computational complexity, but together they do not have practical estimates for solving problems, estimates of the algorithms on average, which is very important for application. Therefore, sometimes it is necessary to choose either a fast algorithm, but it does not always solve the problem in the best way, or choose an exact one, which is not workable for large values.

3. Algorithm development

As it known, in the branch-and-bound method, there are two aspects of algorithmization, determined by the specifics of the problem, namely partitioning the original set of combinations into subsets with a further choice of a subset for the next partition and calculating the lower (upper) bounds (estimates) of the values of the optimized function on subsets. Partitioning a set into subsets is called branching, and choosing a subset for partitioning

is called its strategy. The calculation of errors is interpreted as the solution of estimation problems.

An illustrative result of branching and solving estimation problems is *n*-tiered solution search tree with estimates of the subset vertices of each tier. The estimate of the last tier vertex (a record) represents the current value of the function being optimized, which is then compared with the estimates of the vertices of the previous tiers, as a result of which unpromising for branching subsets are eliminated, and promising ones are partitioned, complementing the solution tree. The algorithm ends its operation when all current and newly generated vertex estimates are compared with the record.

Practice shows that algorithms which build binary solution trees are more efficient, namely they implement the partition of each next set into two subsets. The choice of a subset for branching is carried out according to the maximum (minimum) estimate of the function being optimized, the estimation problems are formed in such a way that estimates are calculated more accurately.

Therefore, when developing an algorithm and having a choice you should adhere to these rules.

As for the problem under consideration, the process of partitioning the next set is carried out into two subsets, the first of which contains combinations of the vector component from $x_i = 0$, the second one from $x_i = 1$. The branching strategy is to choose the next subset for partitioning according to the maximum estimate of the upper bound of the function being optimized.

To calculate the estimates of the upper bounds of the optimized function on subsets, the following estimation problem is formed:

$$Q = \max \sum_{i \in I} c_i x_i \tag{4}$$

under conditions

$$\sum_{i \in I} a_i x_i \le V \tag{5}$$

$$0 \le x_i \le 1,\ i \in I. \tag{6}$$

In other words, for some x_i it is assumed that it is not Boolean, but lies in the interval $[0,\ 1]$. This relaxation of the severity of the problem conditions leads to the fact that the estimate Q for each vertex of the search tree turns out to be larger W, namely it really is the upper bound of the optimized function on subsets of combinations.

At the same time, the estimation problem is easy to solve. According to [3], it is necessary to find the unit values of the load weights c_i/a_i, $i = 1,\ 2,\ ...,\ n$ and arrange them in descending order $c_1/a_1 \ge c_2/a_2 \ge ... \ge c_n/a_n$. Then all $x_i \in I$ chosen in the order of values sequence and such $\sum_{i=1}^{k} a_i < V$ that are set equal to one. The next value x_{k+1} is such $\sum_{i=1}^{k+1} a_i \cdot x_i > V$ that it is calculated by the expression $x_{k+1} = (V - \sum_{i=1}^{k} a_i) / a_{k+1}$, namely the value of the variable x_i, $i \in I$ that is assumed to be non-Boolean is searched for. The other x_i, $i = k+2,\ ...,\ n$ are taken equal to zero. As a result, we get an estimate $Q = \sum_{i=1}^{k+1} c_i x_i$ and a limitation $\sum_{i=1}^{k+1} a_i < V$.

Let's consider a heuristic algorithm that approximately solves the estimation problem (4).

The following steps are included.

- Step 1. Install n. Form the values vector of load units $Y = (c_1/a_1,\ c_2/a_2,\ ..,\ c_n/a_n)$.
- Step 2. Arrange the components of the vector Y in descending order and get the corresponding vector of item indices X.
- Step 3. Set the initial weight of the knapsack equals to $L = 0$, the initial value of the load is $z = 0$.
- Step 4. Set $i = 1$.
- Step 5. Calculate $L = L + A(x_i)$.
- Step 6. If $L \le V$, calculate $z = z + c(x_i)$, otherwise calculate $L = L - c(x_i)$ and go to step 8.
- Step 7. Set $i = i + 1$; if $i \le n$, go back to step 5.
- Step 8. Calculate the knapsack underloading $\Delta V = V - L$ and stop.

4. Practical Algorithm Research

The experimental characteristics of the algorithm are obtained by solving a representative set of random numbers. The programs are written in $C\#$.

The problem was solved in accordance with the proposed algorithm for 6 sets of random tasks of 10, 20, 30, 40, 50, 60 items with 100 tasks in each set.

For the heuristic algorithm, the average Δ_s and maximum $\Delta_{\max}$ errors were calculated in relation to the exact solution of the problem. The standard deviation S_t, the 95 % confidence level D_e, D_r for the average Δ_s and the average backpack underloading R_e were taken into account. The data obtained are shown in Table 1.

5. Conclusions

The scientific novelty of the development lies in the fact that the algorithm has been designed and experimentally investigated. The algorithm implements the solutions of the knapsack problem by a heuristic method.

The practical significance of the research lies in the fact that an estimate of the problem solution and an estimate of the developed algorithm operation are obtained, which is an important factor in its application.

Table 1. Experiment data

The number of items N	Δ_s	$\Delta_{\max}$	S_t	D_e	D_r	R_e
10	1.78	9.87	2.54	2.49	2.59	9.44
20	1.36	6.25	1.43	1.40	1.45	4.31
30	0.99	3.66	0.90	0.88	0.92	2.76
40	1.05	2.87	0.80	0.78	0.81	1.90
50	0.82	2.19	0.57	0.56	0.58	1.65
60	0.73	2.25	0.50	0.49	0.51	1.20

The data in the table show that the average Δ_s and maximum $\Delta_{\max}$ errors of the heuristic algorithm are quite low. So, for the size of the problem $N=10$, they are less than 2 % and 10 % respectively. Moreover, with an increase in the size of the problem N, the errors decrease significantly so that, for example, for $N=60$ they are less than 1 % and 3 %. There is a very small scatter of random S_t and a narrow confidence interval $[D_e, D_r]$ for the average, which indicates the statistical stability of these algorithm characteristics.

Thus, in terms of the counting time, the dynamic programming method is more preferable. However, it is required a significant amount of memory, which grows as $2\cdot\left[N\cdot(V+1)\right]$, namely something like $O(N^2)$.

In practice when operational planning, if a quick approximate solution to a problem is required, then a heuristic method for solving the problem can be successfully applied.

This problem is very important from the point of view of its application in real life. There are many algorithms for solving the knapsack problem. However, each of these algorithms successfully solves a certain range of problems. The interest in solving this problem is growing. All transport loading optimization programs solve the problem known in science as the knapsack problem. So, for example, the optimal loading of transport, taking into account a variety of restrictions, helps to reduce costs, get more profit from the transportation of loads.

REFERENCES

[1] Papadimitriu H, Steiglitz K., (1985), *Combinatorial optimization. Algorithms and complexity*, Mir, Moscow,

[2] Korbut A., Finkelstein Y., (1969), *Discrete programming*, Nauka, Moscow,

[3] Shkurba V., (1976), *Tasks of 3 machine tools*, Nauka, Moscow,

[4] Saati T., (1973), *Integer optimization methods and related extremal problems*, Mir, Moscow,

[5] Cormen T., Leiserson C., Rivest R., Stein K., (2013), *Algorithms: development and analysis*, Williams, Moscow,

[6] Burkova I., Puzhanova E., Marin O., (2014), *The knapsack problem and its modification*, Scientific Bulletin of the Voronezh State University of Architecture and Civil Engineering. Series: Construction Management No. 1, p 103-111,

[7] Fedorin A., (2007), *Evolutionary genetic algorithms for solving knapsack problems*, Information technologies for modeling and control No. 9, p 1054-1062,

[8] Vasilchikov V., (2018), *About a recursive-parallel algorithm for solving the knapsack problem*, Modeling and analysis of information systems 25, No. 2, p 155-164,

[9] Chebakov S., Serebryanaya L., (2019), *Determination of the structure of the optimal subset in the knapsack problem*, BGUIR Proceedings No. 6, p 72-79.

ISSN 1847-7917

The impact of melt retention time on the strontium modification efficiency

***Franjo KOZINA*[1)], *Zdenka ZOVKO BRODARAC*[1)], *Barbara TUBIĆ BULAT*[1)], *Franjo DOMINKOVIĆ*[2)]**

1) University of Zagreb Faculty of Metallurgy
Aleja narodnih heroja 3, 44 000 Sisak,
Croatia

2) Proizvodnja OSO d.o.o.
Vukomerička 9, 10410 Velika Gorica,
Croatia

fkozin@uizg.simet.hr
zovko@unizg.simet.hr
tubicb@unizg.simet.hr
franjo.dominkovic@dalekovod.hr

Keywords

AlSi12 alloy
Strontium
Eutectic modification
Modification efficiency

Original scientific article

Abstract: The modification of eutectic ($\alpha_{Al}+\beta_{Si}$) phase is frequently performed during processing of aluminum-silicone (Al-Si) based foundry alloys leading to a structural transformation of the eutectic β_{Si} phase from a course plate to a fine fibrous morphology. The morphological refinement of the brittle eutectic β_{Si} phase improves ductility, tensile strength, and elongation. This research was performed to estimate the influence of melt retention time on strontium (Sr) modification efficiency. For this purpose, the AlSi12 alloy with eutectic composition was produced and processed by the addition of AlSr10 master alloy. The samples for chemical, mechanical and microstructure analysis were taken with melt retention time of 20 min, 40 min and 80 min. The results of chemical composition analysis indicated the decrease in Sr content with the increase in melt retention time. The poor Sr recovery was a result of the subsequent addition of chemical degassing agents led to the gas entrapment in the melt. Consequently, the highest gas index and most severe porosities were found in sample with retention time of 20 min. The fully modified eutectic ($\alpha_{Al}+\beta_{Si}$) phase morphology was only obtained in sample with retention time of 20 min. After melt retention time of 40 min the unmodified plate-like eutectic β_{Si} phase particles were found. Additional prolongation of melt retention time to 80 min led to the coarsening of eutectic β_{Si} phase particle. The plate-like eutectic β_{Si} phase particles were located near the primary α_{Al} dendritic network and surrounding the primary β_{Si} phase particles. This phase distribution suggests that the transformation of the primary α_{Al} dendritic network is followed by solidification of unmodified eutectic β_{Si} phase particles.

1. Introduction

The modification of eutectic ($\alpha_{Al}+\beta_{Si}$) is frequently performed during processing of aluminum-silicone (Al-Si) based foundry alloys [1]. The modification leads to a structural transformation of the eutectic β_{Si} phase from a course plate to a fine fibrous morphology [2]. The morphological refinement of the brittle eutectic β_{Si} phase improves mechanical properties, especially ductility, tensile strength, and elongation [3]. The modification of eutectic ($\alpha_{Al}+\beta_{Si}$) can be performed chemically, by high cooling rate, electromagnetic stirring, and ultrasonic vibration [4]. The ultrasonic melt processing is an effective method of grain and intermetallic phase refinement through the mechanisms of fragmentation and nucleation. The fragmentation of primary solidified intermetallic phases allows for the heterogeneous nucleation of α_{Al} solid solution and eutectic ($\alpha_{Al}+\beta_{Si}$) phase [5]. The magnetic stirring enables cast microstructure refinement by promoting dendritic fragmentation ahead of the solidification front. The increased liquid convection can result in either bending of dendritic branches or dendritic root remelting [6]. In the hypereutectic Al-Si alloys the electromagnetic stirring enables refinement of the primary β_{Si} particles through cavitation effect [7]. At the cooling rates higher than 400 μms^{-1} the solidification of the eutectic β_{Si} phase transitions from faceted to non-faceted, followed by the decrease in undercooling and twin density [8]. The chemical modification of eutectic ($\alpha_{Al}+\beta_{Si}$) phase is based on the addition of microstructure modifying elements that can affect eutectic β_{Si} phase nucleation and growth [9]. Although, chemical modification can be performed by adding alkaline, alkaline earth and rare earth metals, phosphorus (P), sodium (Na) and strontium (Sr) are most frequently used in foundry practice [4].

The nucleation of eutectic β_{Si} phase is affected by poisoning of aluminum phosphide (AlP) particles necessary for the heterogeneous nucleation. Since poisoned Na_2P, Sr_3P_2 and Al_2Si_2Sr particles solidify prior to the eutectic reaction [4], the reduced number of heterogeneous nucleation sites forces the eutectic transformation to higher undercooling and reduces the number of eutectic grains [10].

The two most established restricted growth theories for eutectic ($\alpha_{Al}+\beta_{Si}$) modification are the impurity-induced twining (IIT) and the twin plane re-entrant edge (TPRE) mechanism. The IIT mechanism is based on the modifier adsorption at the growth surfaces of eutectic β_{Si} phase

facilitating the formation of new twins and enabling growth in many different directions [11]. The TPRE modification mechanism proposes that the modifier retards eutectic β_{Si} phase growth by being selectively adsorbed at the growth surfaces. Consequently, modified eutectic β_{Si} phase grows isotropic in different directions. Due to the increased branching of eutectic β_{Si} phase, the decrease in undercooling is expected [12]. The level of undercooling influences both nucleation and growth of microstructure constituents during solidification process However, since the undercooling occurs in the melt before eutectic reaction starts and modification begins, the higher undercooling can occur due to the Na and Sr poisoning effect [13].

The chemical modification using P is a commonly used methods for modification of primary β_{Si} phase in hypereutectic Al-Si foundry alloys. The P, added in form of phosphorus salt, phosphorus copper master alloy or aluminum phosphorus master alloy, reacts with Al to form AlP particles with high melting point. The similarity in crystal structure between AlP particles and primary β_{Si} phase enables its heterogeneous nucleation and structure refinement [14]. The Na is added to a melt in the elemental form or as a salt at the lowest practical temperature. With the drop in melt temperature a large amount of highly dispersed sodium silicate (NaSi) particles is formed. The NaSi particles are adsorbed on the eutectic (α_{Al}+β_{Si}) nucleation sites retarding the grain growth. In the Al-Si alloys with eutectic composition, Na additions increase undercooling and promote primary α_{Al} dendritic network transformation [15]. Due to the high vapor pressure, Na has a short modification period with poor and unpredictable recovery (10 – 50 % of the addition [16]) [17]. The modification using Sr is mainly performed due to its higher retention time and lack of overmodification issue [18]. Compared to Na, Sr is usually added as master alloy exhibiting more complex dissolution characteristics with better recovery (80 – 90 % of the addition [16]). Dissolution of Sr in the melt strongly depends on its content in the master alloy. Master alloys with high Sr content are added at the lowest practical temperature, while master alloys with lower Sr content give better recovery at the higher temperatures. To achieve satisfactory modification effect 0.2 – 0.5 g/kg of Sr is added to the melt [16]. Due to its high tendency towards hydrogen (H_2), the Sr is never added to the melt in combination with chemical degassing agents. Their interaction reduces the absorption of Sr into the melt, hydrogen trapping and appearance of gas porosities in the castings. The Sr modification is based on the TPRE mechanism comprehending its adsorption at the growth surfaces of eutectic β_{Si} phase and increased branching [17].

The goal of the research is to estimate the influence of melt retention time on the Sr modification efficiency during processing and casting of AlSi12 alloy. The efficiency of Sr modification was estimated by chemical composition, mechanical properties, and metallographic analysis.

2. Experimental work

In order to estimate the efficiency of Sr modification the AlSi12 alloy was produced. The input materials used in melt production and processing are given in Table 1.

The production of the melt began by remelting 80 kg of the AlSi12 master alloy with the addition of 0.8 kg Coveral 1 fluxer. The chemical composition was mended through the additions of 0.32 kg AlMn75, 0.4 kg, AlTi10 and 2.4 kg AlSi50 master alloys.

Table 2. The input materials used in AlSi12 alloy production and processing

Input material		Amount, kg
Master alloy	AlSi12	80
	AlMn75	0.32
	AlTi10	0.4
	AlSi50	2.4
Fluxes	Coveral 1%	0.8
Microstructure modifiers	AlTi5B1	0.22
	AlSr10	0.23

The grain refinement was performed by adding 0.22 kg of AlTi5B1 master alloy. The AlSr10 master alloy was added to the melt at the temperature of 780°C before stirring with argon (Ar). After chemical modification the melt was transported into a holding furnace with constant temperature and chemical degassed. The casting process was delayed for 20 min after modification. The melt was cast into a permanent steel mold at the pouring temperature of 720±20 °C.

During the solidification in a permanent steel mold Simple Thermal Analysis (STA) was performed using temperature measuring device "National Instruments" NI-9211 with NI cDAQ-9172 thermo-module and LabVIEW Full Development System software support. The obtained cooling curves were used to identify the following characteristic temperatures: minimum liquidus temperature (T_{Lmin}), maximum liquidus temperature (T_{Lmax}), minimum eutectic temperature (T_{Emin}), maximum eutectic temperature (T_{Emax}) and solidus temperature (T_S). The obtained characteristic temperatures enabled calculation of changes in liquid (ΔT_L) and eutectic (ΔT_E) temperature as well as estimation of temperature (ΔT_{L-S}) and time (Δt_{L-S}) solidification interval.

The samples for the chemical composition analysis, density measurements, mechanical properties determination and microstructure analysis were taken 20 min (sample 1), 40 min (sample 2) and 80 min (sample 3) after the addition of Sr.

The chemical composition was analyzed using SPECTRO MAX x LMM 04 spectrometer.

Based on the Archimedes' law density values for the samples solidifying on air and under vacuum were calculated. Comparison of the calculated density values enabled determination of gas index.

The use of Radiographic measurements enabled determination of discontinuities in the clamp castings. The Radiographic measurement were performed according to the ASTM E 155-05 on the YXLON MU 2000 device.

The samples for metallographic analysis were prepared using standard grinding and polishing techniques. The samples for light microscopy were etched using 0.5 aqueous fluoric acid solution (0.5HF). The Olympus GX51 inverted metallographic microscope was used to perform light microscopy.

The tensile strength was determined using Zwick tensile testing machine. The castings were loaded under a constant speed of 5 mm/min.

3. Results

The results of chemical composition analysis are given in Table 2. The chemical composition of the produced alloy is in accordance with EN AB 44100. The amount of Si present in all three samples (Table 2) corresponds to the eutectic composition indicating solidification of eutectic ($\alpha_{Al}+\beta_{Si}$) phase. The amount of Sr is highest in the sample 1 (0.0069 wt.%). After retention time of 40 min, content of Sr drops to 0.0056 wt.%. The lowest amount of Sr was measured in sample 3 obtained after 80 min of retention time (Table 2). Based on the amount of Sr in all three samples a complete modification of eutectic ($\alpha_{Al}+\beta_{Si}$) structure is not expected (Table 2).

The cooling curve recorded at the beginning of the casting is given in Figure 1 with characteristic temperatures indicated in Table 3.

Table 2. The results of chemical composition analysis

Sample	Chemical composition, wt. %									
	Si	Fe	Cu	Mn	Mg	Ni	Ti	Na	Sr	Al
1	12.190	0.112	0.0016	0.180	0.0054	0.0024	0.056	0.0003	0.0069	balance
2	12.120	0.113	0.0015	0.182	0.0055	0.0025	0.056	0.0002	0.0056	balance
3	12.250	0.113	0.0015	0.182	0.0053	0.0024	0.057	0.0002	0.0034	balance
EN AC 44100	10.35-13.5	≤ 0.55	≤ 0.10	≤ 0.55	≤ 0.10	≤ 0.10	≤ 0.15	-	-	balance

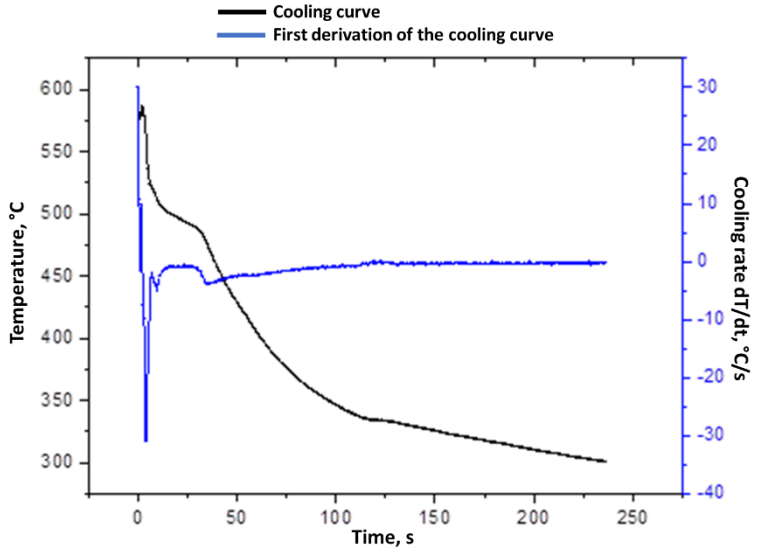

Figure 1. The cooling curve and the first derivation of the cooling curve recorded at the beginning of casting

Table 3. The characteristic temperatures identified from the obtained cooling curves and its first derivation

T_{Lmax}, °C	T_{Lmin}, °C	T_{Emax}, °C	T_{Emin}, °C	ΔT_L, °C	ΔT_E, °C	T_S, °C	ΔT_{L-S}, °C	Δt_{L-S}, °C
586.57	585.64	526.52	525.9	0.93	0.62	507.43	78.21	32.38

The cooling curve exhibits a typical behavior for Sr modified melts with minimal undercooling and recalescence (Figure 1). The solidification of the melt began by transformation of primary phase at T_{Lmin} of 585.64 °C (Table 3) increasing the liquidus temperature to T_{Lmax} of 586.57 °C. The nucleation of eutectic ($\alpha_{Al}+\beta_{Si}$) phase started at T_{Emin} of 525.90 °C followed by the increase of the eutectic growth temperature to T_{Emax} of 526.52 °C. The nucleation and solidification of the eutectic ($\alpha_{Al}+\beta_{Si}$) phase caused recalescence ΔT_E of 0.62 °C. The solidification sequence lasted for 32.38 s and ended at T_S of 507.43 °C with a cooling rate of 2.42 °C/s. The results of density measurements are indicated in Table 4. The samples solidified on air exhibited higher density values compared to the vacuum solidified samples (Table 4). From the samples solidified on air, the sample 2 had the highest density value of 2.29 gcm^{-3}. Samples 1 and 3 have the same density value of 2.27 gcm^{-3} (Table 4). From the vacuum solidifying samples, the sample 1 exhibits the lowest density value of 2.05 gcm^{-3}. Increasing the melt retention time to 40 min increased the density of the vacuum solidified sample to 2.09 gcm^{-3}

Table 4. The results of melt density measurements

Sample	Density of the sample solidified in air, gcm^{-3}	Density of the sample solidified in vacuum, gcm^{-3}	Gas index, %
1	2.27	2.05	9.63
2	2.29	2.09	8.62
3	2.27	2.16	5.04

(Table 4, sample 2), while melt retention time of 80 min increased density to 2.16 gcm^{-3} (Table 4, sample 3). The highest gas index of 9.63 % was calculated for the sample with retention time of 20 min (Table 4). Increasing the melt retention time to 40 min decreased the gas index to 8.62 %, while the lowest gas index of 5.04 % was calculated for the sample taken at the melt retention time of 80 min.

The radiographs of the samples 1, 2 and 3 with the corresponding cross-sections of the clamp castings are given in Figure 2.

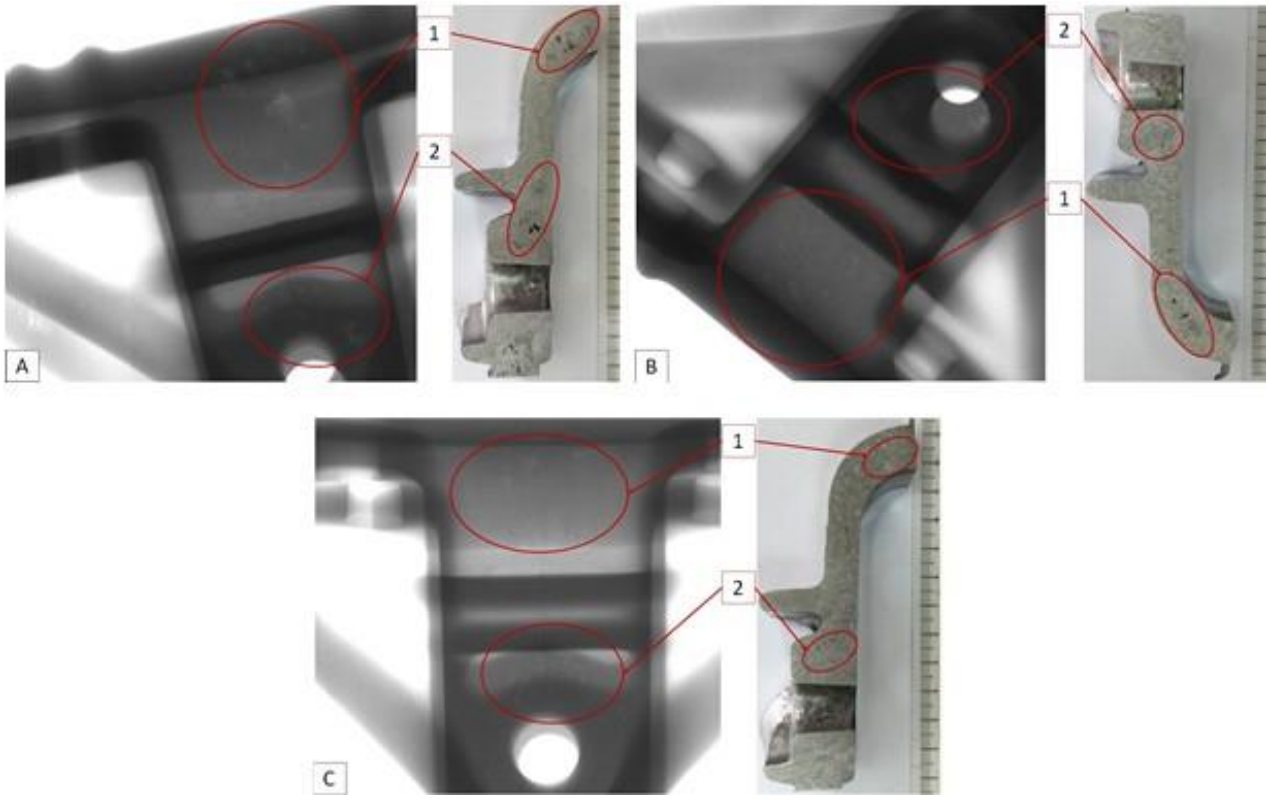

Figure 2. Radiographs and corresponding cross-sections of the samples taken after the melt retention time of: a) 20 min, b) 40 min, c) 80 min.

The results of Radiographic measurements indicate the presence of discontinuities located in the thick sections of the clamp castings (Figure 2, the darkest areas). Based on their morphology the discontinuities can be identified as porosities (Figure 2). The most prominent properties were obtained in the sample taken 20 min after the Sr

addition. The porosities were equally distributed through the thick section of the sample 1 (Figure 2 a). The increase in the melt retention time decreased the severity of porosities (Figure 2 b and c). In the sample with melt retention time of 80 min the porosities can be seen in the last solidifying areas (Figure 2 c). Comparison of the radiographs with the corresponding cross sections of the clamp castings samples indicated the presence of both gas and shrinkage porosities. The gas porosities were most severe in the sample 1 at the positions 1 and 2, and in sample 2 at the position 1 (Figure 2 a and b). The shrinkage porosities were found at the thick sections of the sample 2 (Figure 2 b, position 2) and sample 3 (Figure 2 c, position 2) that are characterized as the last solidifying areas.

The macrostructure and microstructure of the samples 1, 2 and 3 are given in Figure 3.

The macrostructure of sample 1 indicates the presence of shrinkage (Figure 3 a, detail 1) and gas porosities (Figure 3 a, detail 2). In samples 2 (Figure 3 b) and 3 (Figure 3 c) the shrinkage (Figure 3 b detail 1, Figure 3 c detail 1) and gas (Figure 3 b detail 2, Figure 3 c detail 2) porosities are less severe compared to the sample 1. The structure of all three samples consists of primary α_{Al} dendritic network (Figure 3 a, b and c, bright areas) and eutectic (α_{Al}+β_{Si}) phase (Figure 3 a, b and c, dark areas). In sample 1 the eutectic (α_{Al}+β_{Si}) phase morphology is fully modified with slightly course eutectic β_{Si} phase particles solidified at the boundaries of eutectic cells (Figure 3 d detail 1). The primary β_{Si} phase particles with polygonal morphology can also be found in the microstructure of the sample 1 (Figure 3 d detail 2). In sample 2 the morphology of eutectic (α_{Al}+β_{Si}) phase is partially modified (Figure 3 e).

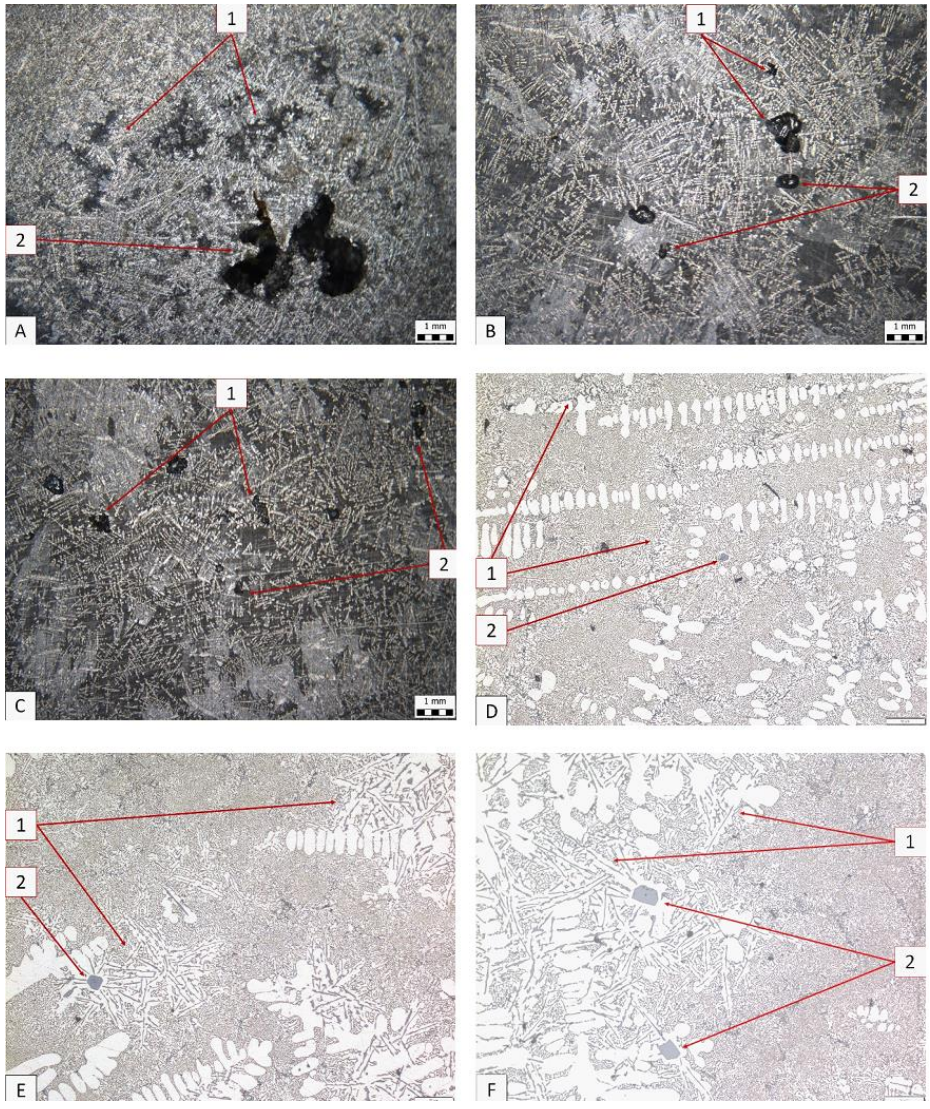

Figure 3. The results of metallographic analysis: a) macrostructure of sample 1, b) macrostructure of sample 2, c) macrostructure of sample 3, d) microstructure of sample 1, e) microstructure of sample 2, f) microstructure of sample 3

The unmodified plate-like eutectic β_{Si} phase particles can be found near the primary α_{Al} dendritic network (Figure 3 e detail 1) and surrounding the primary β_{Si} phase particles (Figure 3 e detail 2). The coarsening of the eutectic β_{Si} phase particles was further enabled by the increase in melt retention time to 80 min (Figure 3 f).

The results of Tensile testing are given in Table 5.

Table 5. The results of melt density measurements

Sample	R_m, MPa
1	133.1
2	93.1
3	87.9

The highest tensile strength of 133.1 MPa was obtained for the samples with the melt retention time of 20 min. Increasing the retention time to 40 min decreased the tensile strength to 93.1 MPa. The lowest tensile strength of 87.9 MPa was measured for the sample 3 obtained after the melt retention time of 80 min.

4. Conclusions

The research was performed to estimate the impact of melt retention time on the Sr modification efficiency. The investigation comprehended determination of chemical composition, density, mechanical properties, and structure investigation of AlSi12 alloy clamp castings taken with retention time of 20 min, 40 min and 80 min. The results of chemical composition analysis indicated the decrease in Sr amount with the prolongation of melt retention time. Despite appropriate addition of AlSr10 master alloy during melt processing, the sufficient amount of Sr required for eutectic (α_{Al}+β_{Si}) phase modification was not achieved. The poor Sr recovery was a consequence of subsequent addition of chemical degassing agents. Their reaction led to the gas entrapment in the melt. Consequently, the highest gas index and most severe porosities were found in sample 1. Prolongation of melt retention time to 40 min and 80 min resulted in the reduction of both gas index and porosities. The fully modified eutectic (α_{Al}+β_{Si}) phase morphology was only obtained in sample 1. After melt retention time of 40 min the unmodified plate-like eutectic β_{Si} phase particles were found. Additional prolongation of melt retention time to 80 min led to the coarsening of eutectic β_{Si} phase particle. In both cases the unmodified plate-like eutectic β_{Si} phase particles were located near the primary α_{Al} dendritic network and surrounding the primary β_{Si} phase particles. This phase distribution suggests that unmodified eutectic β_{Si} phase particles solidify at the beginning of solidification sequence following the transformation of the primary α_{Al} dendritic network.

Acknowledgements

The investigation was performed within the research topic "Design and Characterization of Innovative Engineering Alloys", Code: FPI-124- 2020-ZZB funded by University of Zagreb within the Framework of Financial Support of Research and Infrastructural scientific projects: Center for Foundry Technology, Code: KK.01.1.1.02.0020 and VIRTULAB - Integrated Laboratory for Primary and Secondary Raw Materials, Code: KK.01.1.1.02.0022 funded by European Regional Development Fund, Operational Programme Competitiveness and Cohesion 2014 - 2020.

REFERENCES

[1] Gursoy O., Timelli G., (2020), *Lanthanides: a focused review of eutectic modification in hypoeutectic Al–Si alloys*, Journal of Materials Research and Technology 9, p 8652-8666

[2] Abboud J., Mazumder J., *Developing of nano sized fibrous eutectic silicon in hypereutectic Al–Si alloy by laser remelting*, Scientific Reports 10

[3] Mao F., Qiao Y., Zhang P., Chen C., Zhang C., (2021)., *Modification Mechanism of Rare Earth Eu on Eutectic Si in Hypoeutectic Al-Si Alloy*, International Journal of Metalcasting, 1-12.

[4] Li J. H., Wang X. D., Ludwig T. H., Tsunekawa Y., Arnberg L., Jiang J. Z., Schumacher P., (2015) *Modification of eutectic Si in Al–Si alloys with Eu addition*, Acta Materialia 84, p 153-163

[5] Chankitmunkong S., Eskin D. G., Limmaneevichitr C., (2021), *Effects of Ultrasonic Melt Processing on Microstructure, Mechanical Properties, and Electrical Conductivity of Hypereutectic Al–Si, Al–Fe, and Al–Ni Alloys with Zr Additions*, Light Metals 2021: 50th Anniversary Edition. Springer International Publishing, Oslo, Norway.

[6] Bustos O., Allende R., Leiva R., Sanchez C., (2021), *Effect of magnetic stirring, grain modification and refinement on the solidification structure of an A356 aluminum alloy*, Matéria (Rio de Janeiro) 26.

[7] Yu J., Ren Z., Deng K., (2011), *Refinement and migrating behaviors in Al-Si hypereutectic alloys solidied under electromagnetic vibration*, Acta Metallurgica Sinica 24, p 301-308.

[8] Khan S., Elliott R., (1996), *Quench modification of aluminium-silicon eutectic alloys*, Journal of Materials Science 31, p 3731-3737

[9] Li J. H., Zarif Z. M., Dehm G., Schumacher P., (2014), *Influence of impurity elements on the nucleation and growth of Si in high purity melt-spun Al–Si-based alloys*, Philosophical Magazine 92, No. 31, p 3789-3805.

[10] Cho Y. H., Lee C. H., OH K. H., Dahle A. K., (2008), *Effect of Strontium and Phosphorus on Eutectic Al-Si Nucleation and Formation of β-*

Al_5FeSi in Hypoeutectic Al-Si Foundry Alloys, Metallurgical and Materials Transactions A 39A.

[11] Li, J. H., Barrirero J., Engstler M., Aboulfedl H., Mucklich F., Schumacher P, (2014), *Nucleation and Growth of Eutectic Si in Al-Si Alloys with Na Addition*, Metallurgical And MATERIAls Transactions A 46A, p 1300-1311.

[12] Li J. H., Zarif M. Z., Albu M., McKay B. J., Hofer F., Schumacher P., (2014), *Nucleation kinetics of entrained eutectic Si in Al–5Si alloys*, Acta Materialia 72, p 80-98.

[13] Lu S. Z., Hellawell A., (1987), *The Mechanism of Silicon Modification in Aluminum-Silicon Alloys: Impurity Induced Twinning*, Metallurgical and Materials Transactions A 18A, p 1721-1733.

[14] Hong X., Chen D., Xu Y., Zhu H., Zhang J., Liu Y., Peng Y., Hou L., (2021), *Effect of Different Phosphorus Modifiers on Microstructure and Properties for Al-Si Alloy*, Earth and Environmental Science 692.

[15] Makhouf M. M., Guthy H. V., (2001), *The aluminum–silicon eutectic reaction: mechanisms and crystallography*, Journal of Light Metals 1, p 199-218.

[16] Liao C., Chen J., Li Y., Chen H., Pan C., (2014), *Modification performanceon 4032 Alalloy by using Al–10Sr master alloys manufactured from different processes*, Progress in Natural Science: Materials International 24, p 87-96.

[17] Chen G., Fu G., Yang K., Lin C., (2019) *Study on the Modification Effect of Al-Sr Master Alloy on A356 Aluminum Alloy*, Materials Science Forum 998, p 3-8.

[18] Giovani M., Kaduk J. A., Srirargam P., (2019), Modification of Al-Si Alloys by Ce or Ce with Sr, Jom 71, p 426-434.

ISSN 1847-7917

Aluminium waste reduction in automotive composite weather strip seal manufacturing

Jure KROLO, Zvonimir DADIĆ, Nikša ČATIPOVIĆ, Tin DOŽDOR
Faculty of Electrical Engineering, Mechanical Engineering and Naval Arhitecture, University of Split
Ruđera Boškovića 32, 2100 Split, **Croatia**

jkrolo@fesb.hr
zdadic@fesb.hr
ncatipov@fesb.hr
tin.dozdor@gmail.com

Keywords
Aluminium recycling
Weather strip seal
Soldering
Waste re-use

Professional paper

Abstract: Motivated with both ecological and economic benefits this paper summarizes how aluminium industrial waste was returned into the production without conventional recycling and melting. Aluminium usage in the automotive industry is on the rise and aluminium recycling is very important due to the energy savings and reduced CO_2 emission compared with primary aluminium production. Paper presents how residual aluminium waste for automotive composite weather strip seal was joined with low-cost soldering procedure and returned to the manufacturing process. Aluminium waste material was in form of strips which enter the production process in roll forming stage followed by polymer extrusion process around formed aluminium profile. Because of requirement to preserve 0.4 mm aluminium strip thickness due to the extrusion tool geometry and fine tolerances, butt and scarf soldering joint configurations were chosen. This method enabled joining residual aluminium waste strips in order to preserve manufacturing process continuity and prevent high-cost process interruption. While conventional thin aluminium strips recycling leads to increased materials and energy losses and involves subsequent costly and complex strip production this approach has multiple advantages. Production process is more economical, energy and materials savings are significant which brings increased profit in the production industry. Soldered joints were evaluated with tensile test and proven in actual manufacturing conditions.

1. Introduction

Aluminium usage in automotive and aerospace industry over the last two decades is constantly rising due to its excellent strength to weight ratio [1-3]. In 2000 each automotive vehicle contained an average of 100-120 kg of aluminium, in 2012 it was around 158 kg and by 2025 it is expected to be 250 kg. Benefits of reduced weight will continue to increase the demand for aluminium components [3]. Another advantage of aluminium is possibility of recycling without loss of its properties [3,4]. Aluminium primary production is a high energy consumption process which uses about 160 GJ per ton. On the other hand, secondary production processes use only about 10 GJ per ton, depending on the waste type [4]. Some of aluminium parts in modern automobile include engine block, cylinder head, transmission housings, radiators, chassis, suspension (cradle and axle), wheels, steering systems, doors, front structure and bumper beams [5, 6]. Because the average mass of passenger car has dramatically increased since the 70's, and because vehicle weight directly impacts fuel consumption, lightweighting can significantly reduce CO_2 emissions. Reducing 100 kg from car mass saves 8 grams of CO_2 per km at the exhaust pipe. Aluminium is the ideal light-weighting material, as it allows a weight saving of up to 50% over competing materials in most applications without compromising safety [6]. Lately, automobile window weather strips seals are produced as composite material which consists of lightweight but strong aluminium profile core surrounded with appropriate polymer material. Core metal inserted in weather strip plays a key role to maintain the appropriate shape and strength [7]. Automotive window seals are embedded between metallic panels and non-metallic door glass. They can be classified as header, frontal run-channel, rear run-channel and belt-line [8]. Associated with human sensibility intimately, windows seals have great influence on customer's perception of design and manufacturing quality [9]. The automotive weather strips market will register a revenue of more than USD 14 billion by 2022. The global automotive market accounted for 96.85 million units in 2017 and is projected to grow to 117.72 million units by 2022. [10]. The weather strips are used for preventing the water leakage, dust and exterior noise entering passenger cabin. At the same time, they must keep interior air in thus saving energy used for heating and air conditioning. They also absorb vibrations of car body and impact of door closing. The mechanical properties of the product, along with dimensional accuracy are of importance for the life cycle of the weather strip [11, 12].

Manufacturing of the composite weather strips is usually initiated with aluminium strip roll forming followed by

polymer extrusion process around formed aluminium profile on the extruder ("coextrusion"). The extruder is indisputably the most important piece of machinery in the polymer processing industry. Material is extruded when it is pushed through an opening. The part of the machine containing the opening through which the material is forced is referred to as the extruder die. As material passes through the die, it acquires the shape of the die opening. This shape generally changes to some extent as the material exits from the die. The extruded product is referred to as the extrudate [13]. In this case extrudate were outer door composite weather strips (sometimes referred as beltlines).

In this case, during continuous production of the composite weather strip seals a lot of aluminium waste was generated. When process was terminated, it was not economically justifiable to use the rest of the aluminium strips for new weather strip production cycle (few hundred meters length instead of kilometres of the starting aluminium strip material). The main reason for this was because it was too expensive to start the process again for small number of aluminium strips, and then to stop process again after rapid strip run out (each start costs at least 200 €). In this way a lot of aluminium strip residuals were generated in form of industrial waste. Allwood et al. [14] did a research where they suggested that industrial waste should be innovatively recycled without conventional melting. One of the examples is steel sheet reuse in Abbey Steel in UK. Company purchases blanking skeletons and other trims (such as the window cut-out in door panels) from car manufacturers. They cut regular shapes from these skeletons thus finally supplying it to other firms making small parts from them [14]. Other example of diverted scrap usage was employed during construction of the Olympic Stadium in London. The truss structure for the stadium uses 2500 tons of "non-prime" unused steel tube, over-ordered from an oil and gas pipeline project [14]. There are multiple advantages using this approach, energy and materials savings are significant and production process is much more economical which brings increased profit in the production industry.

Motivated with both ecological and economic benefits this paper summarizes how aluminium industrial waste was returned into the production without conventional recycling and material melting. For this purpose, shorter aluminium waste strips were joined using low-cost soldering process. This procedure enabled continuous production of the automotive weather strips windows seals without costly interruption. Soldering joints were evaluated with tensile test and proven in actual manufacturing conditions.

2. Experimental procedure

Manufacturing of the composite weather strips are initiated with aluminium strip roll forming followed by polymer extrusion process around roll formed aluminium profile, Figure 1. Strip width and thickness were 43 mm and 0.4 mm, respectively. Aluminium strip alloy was EN AW 3015 in H 48 condition which stands for strain-hardened and painted or lacquered - 4/4 hard (fully hardened).

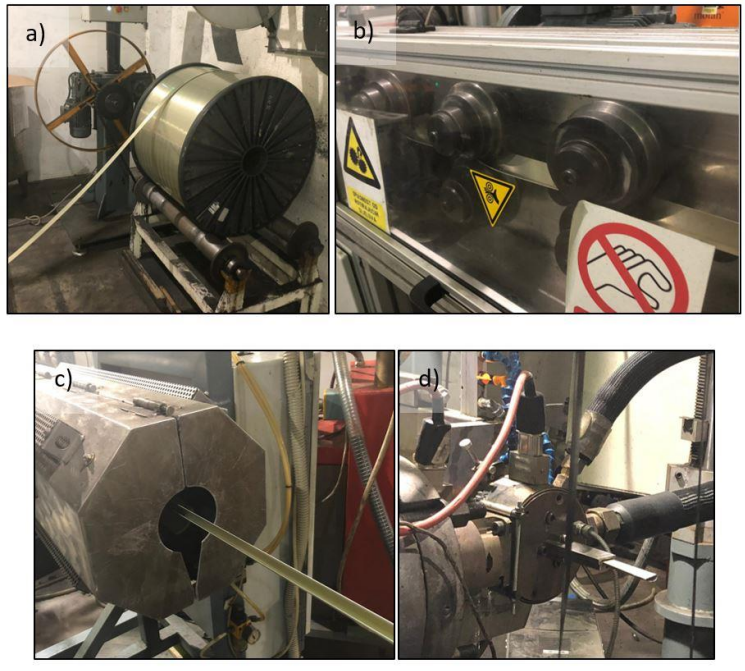

Figure 1. Composite weather strip seal production steps: a) aluminium strip rolls b) roll forming c) entering in polymer extrusion die d) composite weather strip at die exit

Joint between aluminium waste-strips must be strong enough to withstand roll forming and tensile force during entering phase in the polymer extrusion device. Joining very thin (0.4 mm) strips is not easily feasible using conventional electric arc welding processes such as Tungsten Inert Gas (TIG) or Metal Inert Gas (MIG) welding. Their power sources usually deliver welding current that is too high for joining very thin metal. Relatively expensive alternatives such as Micro TIG, Micro Plasma or laser welding could be used instead. Although preliminary experiments with resistance spot welding showed promising results they were rejected. Reason is that forming tool could not accept strips welded in lap joint configuration which is inevitable in this welding process. Strip thickness should be preserved, meaning that every excess must be avoided or grinded. In subsequent attempt strips were joined by low-cost soldering process and successfully tested on production line. Filler metal (zinc and aluminium alloy) has melting point below 450°C which classifies this process as soldering, not brazing [15, 16]. Compared to welding, soldering does not melt the base metal, has relatively low processing temperatures and heat input which results in reduced impact on the properties of the base metal. Soldered joints rely on metallurgical bonds and mechanical interlocking at interface. Due to abovementioned restrictions, butt and scarf joint configuration was used. It should be mentioned that this joint configuration is not commonly used for soldering because of relatively small load-bearing surface area. However, these joints were strong enough to resist all forces during weather strip production. Area around the joint was thoroughly degreased using acetone before soldering. In addition, aluminium-oxide and thin paint film from the strip surface were eliminated by brushing it with stainless steel brush. After brushing obtained surface roughness was 1.47 μm, while surface roughness of unbrushed aluminium strips was 0.39 μm. Filler metal rod was rubbed along the joint during soldering to break up aluminium oxide below molten filler thus enabling better solder-base metal contact which results in high-quality bond [17]. Aluminium strips were preheated around 400°C before soldering. Propane-butane fuel gas flame was used as the heat source. Both butt and scarf joint configuration (Figure 2) were investigated and compared. Soldered joint quality was determined for both cleaned and uncleaned aluminium strips to determine if cleaning step should be omitted. There is a possibility that, during preheating, paint film and any residual grease on aluminium strips would burn out. Figure 2 shows aluminium strips after soldering process. Figure 2 a shows butt joint of the brushed and acetone cleaned aluminium strips, while Fig. 2 b shows scarf joint of the uncleaned aluminium strips covered with paint.

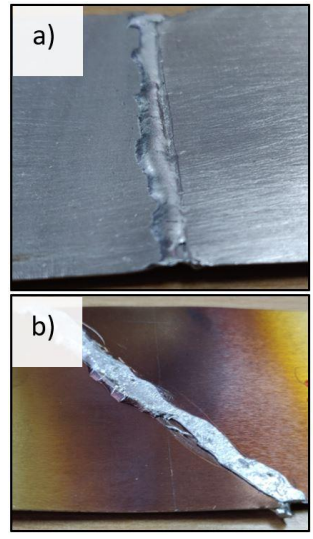

Figure 2. Aluminium strip soldered joints: a) butt joint (brushed and acetone cleaned) b) scarf joint

In order to evaluate joint quality, three tensile tests were performed for each joint type. Tensile testing was conducted on the 1 MN hydraulic press, while the force and displacement were measured with HBM load cell C6A 1 MN sensor and WDS-1000-P60-SR-U sensor, respectively. Tensile test was used for comparison of conventionally used and soldered aluminium strips. The main aim was to investigate strength of the various soldered joints and compare it with base metal. Specimens length was 240 mm and total distance between testing device grips was 170 mm.

3. Results analysis and discussion

Tensile test results for different soldered joints are presented in table 1. According to the results, all soldered joints endured lower tensile force compared to original aluminium strip (base metal). Average maximal tensile force for soldered joints and base metal was 1168 N and 2875 N respectively.

Table 1. Maximal average tensile force* for different soldered joints and base metal (original aluminium strip)

	Original Al-strip	**Butt joint**	**Scarf joint**	**Butt joint**	**Scarf joint**
		Brushed and acetone cleaned		**Covered with paint**	
Maximal tensile force [N]	2875	1218	1168	1084	1199

** calculated from 3 measurements*

Most of the samples break at heat affected zone (HAZ) during testing, Figure 3. It clearly indicates that soldered joints had good metallurgical bonds and mechanical interlocking at interface. Base metal had cold rolled microstructure which increased overall strength by strain hardening phenomena. However, during preheating and soldering procedure aluminium recrystallized in HAZ which reduced its strength. It seems that for brushed and acetone cleaned joints butt configuration was somewhat stronger than scarf joint. Opposite is true for the joints of the strips covered with paint where scarf joint seems to be stronger. Nevertheless, it should be noted that if quality joint was obtained soldered specimens always break in HAZ despite of joint configuration. In addition, there is no significant difference in strength if specimens are brushed and cleaned or not. It would probably be more important factor in lap joint configuration where paint and grease would cause severe problems at the interface.

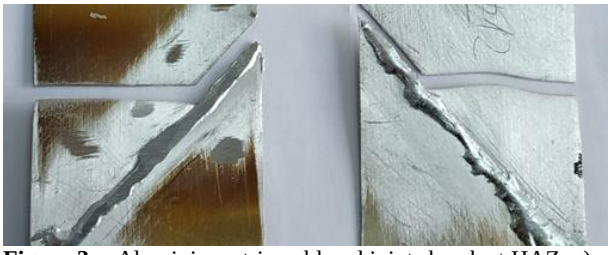

Figure 3. Aluminium strip soldered joints break at HAZ: a) scarf joint (unbrushed covered with paint) a) scarf joint (brushed and acetone cleaned)

Figure 4 presents roll-formed aluminium profile for both butt and scarf soldered joints. These final tests are conducted in real manufacturing conditions to confirm method suitability. This can be considered as most important criteria for accepting or rejecting joint quality. Main requirement is that the obtained joint should be strong enough to pull rest of the aluminium strip during coextrusion process. Roll-forming accompanied with tensile pulling force during material entrance in the polymer extrusion die are the most demanding part of the process that obtained joints must endure. As indicated in the Figure 4 butt joints endured the process without any visible cracks, while scarf joint cracked during the process. This test eliminated scarf join configuration which did not perform well under complex load in production process. It also confirmed that butt joint is more appropriate solution that can withstand load requirements. Chosen soldering process is good enough to be used in real manufacturing conditions despite strength reduction in HAZ that it causes. It should be noted that more concentrated heat source and higher soldering speed could lower heat input thus reducing HAZ area.

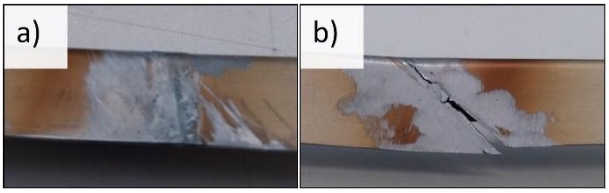

Figure 4. Roll formed aluminium profile a) at butt joint soldered region b) at scarf joint soldered region

Of course, the parts of the produced weather strip seals which contains soldered joints will be discarded due to the high-quality standards of the automotive industry. However, this will be only a small, neglectable fraction of the discarded weather strip seal (10-15 cm) compared with total produced weather strip length (kilometres) with continuous polymer extrusion process.

4. Conclusion

Tensile testing and in-production-test of soldered aluminium strips confirmed possibility of their re-usage in composite automotive weather strip seals. Soldered joints break in HAZ during tensile test. Although maximum tensile strength was considerable reduced in HAZ compared to base metal, real manufacturing conditions showed that butt joint was strong enough to withstand roll forming process and loads prior entrance in polymer extrusion die. Scarf joint had quite similar tensile strength but did not withstand roll forming production stage. Furthermore, both cleaned, and paint-covered aluminium strips were suitable for the soldering process because breaks occurred in HAZ in both cases. Therefore, aluminium strip brushing and acetone cleaning before soldering process, although recommended, is not necessary. More concentrated heat source and higher soldering speed should be used to reduce heat affected zone. Presented approach is both economically and environmentally beneficial with significant savings of material and energy, reduced CO2 emissions and increased profit.

REFERENCES

[1] The Aluminum Association, *LCA Report: EDAG Silverado Body Lightweighting*, http://1pp2jy1h0dtm6dg8i11qjfb1-wpengine.netdna-ssl.com/wp-content/uploads/2018/09/AA-LWT-Body-Design_Final-LCA-Report_August-2018.pdf, Accessed 10 September 2019

[2] European Aluminum, (2015), *Sustainability Highlights, Reporting on the European aluminium industry's performance*, https://www.european-aluminium.eu/media/1836/20170323-sustainability-performance-report.pdf, Accessed 10 September 2019

[3] European Aluminum, Aluminium: *Benefits in Transport* (2015), http://www.world-aluminium.org/media/filer_public/2015/11/30/alum

inium_in_transport.pdf, Accessed 11 November 2019

[4] Stacey M., (2015), *Aluminium Recyclability and Recycling; Towards Sustainable Cities, Published by Cwningen Press*, International Aluminium Institute, Nottingham + Llundain, ISBN 978-0-9930162-1-9.

[5] European Aluminium Association: *Aluminium in cars- unlocking the light-weight potential*, https://european-aluminium.eu/media/1326/aluminium-in-cars-unlocking-the-lightweighting-potential.pdf, Accessed 12 November, 2019.

[6] Hirsch J., (2014), *Recent development in aluminium for automotive applications*, Trans. Nonferrous Met. Soc. China 24.

[7] Park J. S., Lee H. W., Jung S. Y., Bae J. H., Kim H. Y. and Kim C., (2011), *Process Planning for Insert Metal of Weather Strip Using High Speed Rolling-Type*, Journal of the Korean Society for Precision Engineering Vol. 28, No. 11, pp. 1279-1287.

[8] Lin C., (2004) *Robust Design of Glass Run-Channel Seal*, SAE Technical Paper 2004-01-1687, https://doi.org/10.4271/2004-01-1687.

[9] Zhu W. F., Jiang X. H., Chen X., Lin P. J., (2016), *Automotive window seal design considering external aerodynamic load and surrogate constraint modeling*, International Journal of Automotive Technology 17, No. 5, p 853−864.

[10] Technavio; *Global Automotive Weatherstrips Market 2018-2022*, https://www.technavio.com/report/global-automotive-weatherstrips-market-analysis-share-2018, Accessed 12 November 2019.

[11] Stavropoulos P., Alexopoulos H., Papacharalampopoulos A., Mourtzisa D., (2018), *Automotive weather strip manufacturing: Process modeling and extrudate dimensional accuracy evaluation*, Procedia CIRP 72, p 375-380.

[12] Park J., (2012), *Development of New Test Method for Compression Load and Permanent Deformation of Weather Strip*, SAE Technical Paper, https://doi.org/10.4271/2012-01-0021.

[13] Rauwendaal C., (2014), *Polymer Extrusion*, 5th Edition, Hanser Publishers, Munich Hanser Publications.

[14] Allwood J. M., Cullen J. M., Carruth M. A., *Sustainable Materials with Both Eyes Open*, (2012), UIT Cambridge, ISBN 190686005X, 9781906860059.

[15] O'Brien E. A., (2004), *Welding Handbook*, 9th Edition Vol 2, American Welding Society, ISBN: 0-87171-729-8.

[16] ASM HANDBOOK, (1993), *Vol. 6, Welding Brazing and Soldering*, ASM international, ISBN 0-87170-377-7(V.1).

[17] O'Brien E. A., Kathy E., (2015), *Welding Handbook*, 9th Edition Vol 5, American Welding Society, ISBN: 978-0-87171-856-3.

ISSN 1847-7917

Factors determining the durability of cold extrusion dies

Olena KUZMENKO[1)]***, Victor KUZMENKO*** [1)]***, Anton OKUN***[1)]
1) National Technical University "Kharkiv Polytechnic Institute"
2 Kyrpychova St., Kharkiv, 61002,
Ukraine

vileta@gmail.com
vileta067@gmail.com
okunanton@gmail.com

Keywords
cold extrusion
durability
extrusion tools
structure
heat treatment

Professional paper

Abstract: The factors, which influence on the implementation effectiveness of cold extrusion processes of steel billets are considered. Economic feasibility and effectiveness of the implementation primarily depends upon the durability of extrusion tools. The research results of the ways to increase durability of tools for cold extrusion, which performed in four different directions: improving the structure and fabrication technology of dies; billet surface preparation for extrusion; improving material properties of extrusion tools using heat treatment; improving deformability of billet material. The procedure of heat treatment which increases the lifetime of extrusion tools made of high-speed steel is considered. Moreover, the conditions of heat treatment for obtaining the uniform structure of globular pearlite in hot-rolled and extrusion with different degree steel for the deformability improvement are proposed. The results of the research have been tested and implemented in the manufacture of the bicycle brake sleeves.

1. Introduction

Cold extrusion is one of the most efficient low-waste steelmaking processes, the implementation of which instead of cutting and hot extrusion provides a significant increase in labor productivity, the utilization of metal and surface quality. Compared to casting and hot extrusion, up to 50 % of metal is saved, compared to cutting processing, waste into shavings is reduced by 2–3 times. During cold extrusion, the material utilization rate can reach 0.9–0.95. The accuracy of the executive dimensions of the parts obtained by cold extrusion corresponds to 8th tolerance grade, and the surface roughness does not exceed 16–32 μm.

The drawback of cold extrusion is the high resistance to deformation due to reduced plasticity of steel at room temperature, which requires the use of equipment with increased power and process lubricants, which leads to an increase in the number of die transitions and a decrease in the durability of die tooling. In order to prevent destruction of the forming tool, the deformation ratio during one transition is recommended to limit to 40−55 %.

The durability of cold extrusion dies is one of the main indicators that affect the feasibility and economic efficiency of implementing the developed technologies into manufacture. The durability is the ability of the tool to not break down, as well as preserve its original dimensions and properties, and it depends on the operating life and wear resistance of the dies. But if the operating life is determined by the number of cycles of loading the tool to its destruction in the case of breakage or under the influence of fatigue, then wear resistance is the number of extruded parts that caused a change in the size of the forming elements within the specified tolerance [1], [2].

The problem of increasing the durability of an extrusion tool for cold extrusion is a complex task, the solution of which must be carried out in the following four main directions:

- The development of cold extrusion technology, improving the design of dies;
- Preparation of the workpiece surface for extrusion;
- Improving the punchability of the workpiece material;
- Improving the properties of the tool material by heat treatment.

The aim of this work is to show the effectiveness of a comprehensive approach to solving the problem of increasing the durability of dies.

2. Development of cold extrusion technology, improving the design of dies

In order to ensure the stability of the cold extrusion process and reduce the specific operating loads on the tool, it is necessary to choose a rational arrangement of component parts and die assemblies that provide the given strength and rigidity when centering the punch and die, as well as strict alignment and parallelism of the mating elements [1].

Symbols		**Greek letters**	
A_{C1}	- critical point of transformation of pearlite to austenite	γ	austenite, or gamma-phase iron (γ-Fe)
		α	ferrite, or alpha-phase iron (α-Fe)

This is achieved by precision manufacturing. In case of misalignment, eccentric loads on the punch arise (especially during reverse extrusion), which sharply reduces its durability, and also degrades the quality of the manufactured parts, leading to a thickness variation. The higher the wear resistance of the tool, the more accurate the extruded parts are.

The centering of the punch relative to the bottom die is more reliable and more accurate due to inoperative elements of the matrix and the punch, which prevents premature breakage of the punch due to excessive bending moments that occur during eccentric loading. It is known that dies with guide columns provide parts with a thickness variation that does not exceed 0.3 mm, while with the die directly centered on the die, parts with a thickness variation of no more than 0.03 mm are obtained. However, the direction of the punch in the bottom die has its drawbacks, limiting the use of dies. An increase in the length of punches and dies adversely affects tool life. In addition, the diameter of the guide part of the punch during operation changes due to its heating and elastic deformations during extrusion, which significantly breaks the alignment conditions and can lead to breakdown [1].

The design parameters of the punch and the bottom die should create the most favorable stress diagram of these heavily loaded parts. To reduce the loading on the punch can be a rational choice of the shape of its head [3]. The radii and the cone angle of the transition zones from the cylindrical part of the punch to the calibrating girdle and from the calibrating girdle to its end part also have a great influence. The longevity of the working parts of the die will be higher, and the likelihood of their destruction from fatigue is less with a decrease in tensile stresses that occur during the reverse move. Dies must be designed so that the efforts to extract the punches are insignificant, the inserts of the bottom dies are installed with sufficient interference, the supports of the punch and ejector work with minimal bending stresses [4].

Extrusion of the brake sleeve was carried out on K0032 press for cold extrusion in specially designed dies taking into account the recommendations [1], [2], [4], [5]. Rigid construction dies were used with massive lower and upper plates, strong mounting units, with guide columns. This required subsequent mechanical completion of the sleeve.

3. Preparation of the surface of the workpieces for extrusion

The durability of the dies largely depends on the quality of the surface preparation of the workpieces and the lubrication of the deforming and deformable surfaces [6], [7], which affect tool wear, increasing it several times with unsatisfactory technology. The right choice of lubricant coating will help to reduce the specific extrusion force. Breaking of the continuity of the lubricating coating can lead to the setting of the punch material and the workpiece, causing damage to the punch.

In contrast to the operations of hot and sheet extrusion during cold extrusion steel parts contact stresses reach the maximum values for the tool material of 2000-2500 MPa, therefore very high demands are made on their lubrication. The coating process is carried out on mechanized galvanic lines and it includes over 10 operations: descaling, degreasing, etching, washing with cold and hot water, applying a lubricant porous layer with a thickness of 10-40 microns based on zinc phosphates, followed by impregnation with zinc stearate or laundry soap [6], [7].

4. Improving the punchability of the workpiece material

The advantages of the cold extrusion process are most fully realized when using low-carbon steels, the hardness of which does not exceed 125 HB. In this case, deformations up to 70–85% are allowed in one transition, and the tool loading is much lower than 2 GPa.

In a multi-transition process, in order to improve the subsequent punchability of the workpieces between different transitions, softening heat treatment of deformed steel is carried out. As a rule, when assigning annealing modes, the inhomogeneity of the deformed state of the workpieces obtained by cold extrusion and the presence of sections with very different degrees of deformation are not taken into account. For example, in the preparation of a bicycle brake sleeve obtained by heading on cold heading machines, with an average degree of deformation of 45%, there are areas in which local deformation is close to critical (about 20%), and areas in which local deformation exceeds 80%.

It is generally accepted that low-carbon steels with a uniform granular perlite structure, when carbides are uniformly distributed in a ferrite matrix, have optimal punchability. The plasticity of steel with a uniform structure of granular perlite is higher than that of the same steel with a differentiated structure of ferrite and grains of granular perlite [8]. The loading on the punching tool depends on the state of the carbide phase even with a small amount of perlite in the structure. For example, at the same hardness of 125 HB, the hardening curves of 15X steel with a homogeneous granular perlite structure are lower than the hardening curves of this steel with plate carbides [9].

As the studies [10], [11] have shown, under certain temperature-time conditions of heating, a kind of "annealing interval" on granular perlite can also appear in mild steels. So, during the slow heating of 15X steel, from which the bicycle brake sleeve is made, to a temperature of A_{C1} point (740 °C), with average speeds not exceeding 1–2 °C per minute (heating of the charge with the furnace), austenite as a rule, it nucleates at the boundaries of ferrite grains far from pearlite regions, which makes it difficult to dissolve carbides in it. In order for carbides to dissolve in the γ phase, they must first go from perlite carbides to the α phase. Due to the increased number of crystal structure defects that arise during the α–γ transformation, carbon is retained in ferrite, accumulating around dislocations arising from phase hardening [11].

In the course of research [9], unexpected results were obtained on the effect of the heating rate to temperatures of A_{C1} point temperature on the decomposition products of austenite during subsequent cooling with a furnace or in air. When heating is accelerated to 100 ° C per minute, austenite sections nucleate predominantly at the boundaries of ferrite-pearlite grains, which contributes to the dissolution of carbides in the γ phase and its saturation with carbon. This increases the stability of austenite to decomposition upon subsequent cooling, since it shifts the C-shaped curves to the right. As a result, the phase transformation develops at lower temperatures of the subcritical interval, when carbon atoms lose their diffusion mobility and austenite, cooled in air or even with a furnace, decomposes with the formation of sections of lamellar perlite or sorbitol of increased hardness (over 138 HB) [11].

Cold plastic deformation, as is known, provides spheroidization of carbides during heating, which is explained by the influence of an increased number of "recrystallization vacancies" that accelerate the diffusion of carbon. In the case of deformations of 5–10%, leading to the development of stabilizing polygonization upon heating, which suppresses the primary recrystallization of ferrite, the intensity of spheroidization processes is almost the same as in hot-rolled steel.

In addition, as was established by the authors of [12], the rate of carbon diffusion is much lower than the rate of movement of the recrystallized boundaries; therefore, at the locations of the disappeared initial boundaries, an increased carbon concentration is retained, which can lead to the formation of cementite here. All this contributes to the redistribution of carbides in the recrystallized matrix and to obtain a homogeneous structure of granular perlite after heating.

Due to the greater degree of spheroidization of carbides in deformed steel when heated in a subcritical temperature range above the temperature of A_{C1} point, their stability with respect to dissolution in austenite is greater than in hot rolled metal. Thus, in steels deformed by 20% or more, carbides practically do not dissolve in the γ phase in the temperature range of A_{C1} point − A_{C1} point + 20 °C during slow heating. This allows us to recommend this mode for production conditions. A rather uniform structure of granular perlite in inhomogeneously deformed billets made by cold extrusion is obtained after three hours of annealing at temperatures of the "annealing interval" [10], [11].

The regime, including heating the planted billets from 15X steel with a furnace to temperatures of 740–760 °C, was introduced at the bicycle factory and allowed to halve the annealing time, increase the service life of retorts and baskets made of heat-resistant steels, and, most importantly, to obtain a fairly uniform grain structure perlite, to improve the formability of the workpiece material and thereby reduce the consumption of dies and punches of cold extrusion by 15−25%.

5. Improving the heat treatment of the die material

In addition to the requirements of high hardness and heat resistance, which are necessary for a cutting tool, a number of additional requirements are imposed on the material of dies, which are determined by the specific conditions of the tool's operation. To determine the quality criteria of the material of a punching tool, it is necessary to know the conditions of its operation, the nature of the breaking stresses and the cause of the failure of the tool. Most punches usually wear out, however, in the case of punches for backward extrusion of deep cavities, destruction from cyclic compressive-tensile stresses or bending loads is possible [13], [14]. As is known, in the forward move, the punch experiences significant compressive stresses, and in the opposite, tensile stresses. Some working parts of cold forming dies (bottom dies, ejectors, supports) fail due to the appearance of fatigue cracks. That is, in each case, the structural strength of the material will be determined either by the level of hardness, or by the yield strength during bending or tension, or by some other criterion.

Fractographic studies of fractures and average durability of punches of the first and second transitions from P6M5 steel during two-transition extrusion of the brake sleeve, carried out for several years at the Kharkov Bicycle Plant, showed the following [13]. The longevity of the punches of the first transition is determined by the level of bending stresses and, on average, is 7 thousand loading cycles, and the punches of the second transition are subjected to cyclic compressive-tensile loads and squeeze 20 thousand parts to failure. Thus, for the punches of the first transition, it is necessary to increase the bending strength, for the punches of the second transition, the ultimate compressive and tensile strength and hardness.

Systematic studies of the influence of the first tempering regimes on the structure and properties of steel after the standard second tempering made it possible to distinguish three stages of the first tempering - "primary

softening”, “maximum hardening” and “secondary softening” and to develop the following recommendations for designating the heat treatment mode of die tools made of P6M5 steel [14]:

- if the tool material must have high values of hardness, yield strength under compression, resistance to brittle fracture and heat resistance, the first tempering of hardened high-speed steel must be interrupted at the stage of “primary softening”;
- if a high resistance to bending loads is required from the tool material, the first tempering should be completed at the stage of “secondary softening”.

In the standard mode, the first tempering is completed at the stage of “maximum softening”, which leads to a decrease in strength properties after the second tempering [13], therefore, the generally accepted heat treatment regime should not be recommended for stamping tools made of P6M5 steel.

According to the developed principle of choosing the temperature and time parameters of the first tempering, for the punches of the first transition, the first tempering must be completed at the stage of “secondary softening”, which increases the tensile strength in bending from 3000 to 3250 MPa, although it slightly reduces the hardness and yield strength in compression.

For punches of the second transition, the first vacation must be completed at the stage of "primary softening". This increases the hardness and tensile strength by compression by 1–1.5 HRC and 150 MPa, respectively, compared with the parameters obtained after standard heat treatment. The effect of hardening by almost double grinding of tempering carbides and their more uniform distribution in the bottom die is explained [14].

Experimental industrial tests showed that after heat treatment according to the proposed technologies, the average resistance of the punches of the first transition was 11 thousand loading cycles, and the punches of the second transition were 40 thousand cycles, which is 1.6 and 2.0 times higher than the durability of punches, issued according to the standard technology. Thus, the change in the mode of the first tempering significantly increased the durability of the punch tool made of P6M5 steel.

6. Conclusions

The factors determining the durability of a punching tool during cold extrusion, which were used in the design of tooling and the development of technologies for cold extrusion and surface preparation of blanks, are considered. The results of scientific research, pilot tests and industrial introduction of the multi-transition process of cold extrusion of a bicycle brake sleeve made of steel 15X at the Kharkov Bicycle Plant are presented.

It is shown that punches of different transitions of one extrusion technological process made of P6M5 high-speed steel can be destroyed by different stresses, therefore, a differentiated approach to the choice of heat treatment modes is required. The principle of choosing the temperature-time parameters of the first tempering is proposed, depending on the operating conditions of a punch tool made of P6M5 steel. For punches, which must have high values of hardness and yield strength under compression, the first tempering of hardened high-speed steel must be interrupted at the stage of "primary softening". For punches, which require high resistance to bending loads, the first vacation should be completed at the stage of "secondary softening".

A mode of softening heat treatment of inhomogeneously deformed billets of steel 15X has been developed, which allows one to obtain the most homogeneous structure of granular perlite with the best punchability and includes slow heating with a furnace to temperatures of so-called A_{C1} point − A_{C1} point + 20 °C.

As a result of the implementation of the development, the average durability of the punches of the first transition amounted to 11 thousand loading cycles, and the punches of the second transition - 40 thousand cycles.

REFERENCES

[1] Evstratov V., (1987), *Fundamentals of extrusion and die technology*, Kharkov University, Kharkov,

[2] Chukhlib V., Klemeshov E., Gubskyi S., Okun A., Biba N., (2020), *Theoretical and Experimental Studies of Changes in the Workpiece Shape During Narrow Die Indentation*, Lecture Notes in Mechanical Engineering, p 361-370,

[3] Afanasyeva G., Evstratov V., (1974), *On the types and causes of failure of punches for cold extrusion of steel parts*, Forging and extrusion production No. 4, p 7-10,

[4] Cold and half-hot extrusion on presses: guidelines, (1981), NIIMASH, Moscow,

[5] Evstratov V., Eremin V., (1981), *Ways to increase the resistance of punches for cold extrusion*, Automotive industry, No. 11, p 30-31,

[6] Evstratov V., Kuzmenko V., (2008), *The study of friction during plastic deformation*, Tribology and Reliability, p 7-10,

[7] Danilenko V., Evstratov V., Kuzmenko V., (2010), *Cold extrusion friction test*, Forging and extrusion production, No. 5, p 11-18,

[8] Jonck R., (1974), *Gluhen auf Best Umfor Barkeit bei der Kaltformgebung*, ZwF 6, No. 11, p 525-532,

[9] Dyachenko S., Kuzmenko E., Kuzmenko V., (1997), *Ways to improve the quality of parts and improve the technology of cold forging*, Forging and extrusion production, No. 6, p 12-15,

[10] Dyachenko S., Kuzmenko V., Polyanychka A., (1989), *Development of a mode of softening annealing of inhomogeneously deformed*

workpieces, Metallurgy and heat treatment of metals No. 6, p 6-9,

[11] Kuzmenko E., Kuzmenko V., (2008), *Improving the stampability of hypereutectoid steels in the processes of cold deformation*, Metal forming No.1, p 163-167,

[12] Bockstein S., (1962), *The effect of carbon on the movement of grain boundaries during iron recrystallization*, MITOM No.3, p 8-13,

[13] Evstratov V., Oprishchenko T., Khristoforov A., Dyachenko S. (1995), *Breaking stresses and heat treatment of reverse extrusion punches*, Forging and extrusion production No. 8, p 21-22,

[14] Evstratov V., Oprishchenko T., Khristoforov A., Dyachenko S. (2011), *The role of the parameters of the first holiday in increasing the tool life of P6M5 steel*, New materials and technologies in metallurgy and mechanical engineering No. 2, p 34-37.

ISSN 1847-7917

Wear of spiral drills coated by hard PACVD coatings

Darko LANDEK[1)], **Gorana BARŠIĆ**[1)]
1) University of Zagreb, Faculty of Mechanical Engineering and Naval Architecture, Ivana Lučića 5, 10000, Zagreb, Croatia, **Croatia**
dlandek@fsb.hr
gbarsic@fsb.hr

Keywords
PACVD
TiN/TiCN
TiN/TiBN
Coating adhesivity
Drill bit wear

Original scientific paper
Abstract: The paper examines the wear of the blade of helical drills with diameter 4 mm. The helical drills were made of high-speed steel and tested in uncoated state and coated with two-layer plasma assisted chemical vapor deposition (PACVD) coatings, TiN/TiCN and TiN/TiBN. The thickness of coating was characterized by light microscopy, and the adhesivity of coatings was evaluated with the VDI 3198 indentation test. The surface roughness, before and after coating, was determined by a contact profilometry. Blade wear was examined by determining the drill diameter decreasing and drilling time to make a series of 1 to 15 bores in a 3 mm thick strip of non-alloy structural steel. The results show an extension of the drilling time for uncoated drill bits after the third bore, compared to the coated drills. Coated drills withstood drilling of 15 holes without significant reduction of diameter and with slow increasing of drilling time. Drilling times with PACVD coated drill bits are three to four times shorter and the feed rate is twice as large compared to drilling with uncoated drill bits for the same rotation speed and drilling force.

1. Introduction

Hard coatings are usually applied to reduce friction, heating, and wear of cutting tools. For this task they should have low coefficient of friction, high resistance to adhesion and abrasion wear, good adhesivity to the substrate, high resistance to contact pressure, and good adhesion of lubricant and cooling media [1, 2]. Such a combination of properties on the surface of the cutting tools cannot be achieved by conventional monolayer coatings but with multilayer and composite coatings. In hard multilayer coatings boundaries between thin layers inhibit the motion of dislocations and the propagation of micro cracks, which results in a tougher coating with a higher resistance to abrasive wear. The top layer of the coating is usually produced with low friction material such as TiN or diamante like coating (DLC) which significantly reduces adhesive wear of the tool surface. To create multicomponent and multilayer tribological coatings, good adhesion between the coating and the substrate material is required together with good adhesion between layers. The conditions of good adhesion between the coating and the substrate and between layers of the coating can be achieved commercially by the physical vapor deposition (PVD) and plasma-assisted chemical vapor deposition (PACVD) processes [3].

In both processes, PVD and PACVD, the coating is created in a single multiphase process carried out in a vacuum chamber, without contaminating the workpiece surface by oxygen and other gases or humidity from the environment. Commercial PVD processes can produce multicomponent and multilayer coatings with different chemical compositions and microstructures, but the clear visibility between the workpiece surface and the coating material source (the targets) must be ensured. This problem can be partially solved by rotating the parts during the application of coating and by using advanced PVD processes such as magnetron sputtering and cathodic arc evaporation. The multilayer PVD coating required different targets installed into a vacuum chamber. The temperature of the PVD process is between 200 °C and 550 °C [3, 4].

In the PACVD process direct visibility of the parts surface and the coating material source is not necessary, because the vapor of precursors can be uniformly distributed inside the vacuum chamber. Also, for different coating compositions only the specific precursor should be introduced into the vacuum chamber. The temperature for PACVD process is between 450 °C and 600 °C. The energy required for an activation of chemical reactions for the creation of the coating are obtained from a plasma created between the parts (cathode) and the vacuum furnace walls or the auxiliary anodes. In the PACVD process, plasma can be activated by the pulsed direct current (DC) or alternating current (AC), by the electric field discharge in the range of radio frequencies (RF) or by microwaves (MW). The thickness of the multilayer PACVD coatings is between 1 to 10 μm [4].

The aim of this research is comparison of wear of high-speed steel drills uncoated and coated by the PACVD multilayer coatings TiN/TiCN and TiN/TiBN. The PACVD coating was carried out in the pulsed direct current (DC) plasma in a Rübig GmbH type PC 70/90 industrial vacuum furnace.

2. Materials and methods

For PACVD coating process the set of nine helical drills with diameter 4 mm were used. Drills were made form high speed steel HS18-0-1 in hardened and tempered state with hardness of 59 ± 2 Rockwell C. A set of three drills with diameter 4 mm was PACVD coated by multilayer TiN/TiCN. The other similar set was PACVD coated by multilayer TiN/TiBN, while one set remain uncoated. The tested coatings have different microhardness. For the TiN/TiCN coating it is between 1600 and 2200 HV0.01 and for the TiN/TiBN coating it is between 2000 and 2500 HV0.01 [4]. Before plasma deposition, all drills were cleaned in an ultrasonic bath and placed in an industrial furnace, the Rübig GmbH type PC 70/90 (with the inner diameter of the deposition chamber of 700 mm and the height of 900 mm) equipped with a bipolar DC voltage-controlled micro pulse plasma generator. The parameters of the PACVD coating process were given in Table 1.

The surface roughness of samples was tested with five repetitions using an electromechanical device with a stylus, i.e. the Surface Roughness Tester Perthometer S85. The testing length for the measurement of roughness parameters was 5.60 mm and the Gauss filter was used for filtering data (λ_c= 0.8 mm).

The thickness of the PACVD coatings was determined after cutting spiral drill and metallography preparation of its cross section. The coating thickness was measured in a light microscopy picture of drill surface made with the optical microscope Olympus GX51. The adhesivity of coatings was evaluated with the VDI 3198 indentation test. In this test, a diamond indenter with a load of 1470 N is imprinted into the coating. Plastic deformation, microcracks or delamination of the coating appear around the place of embossing. Acceptable degrees of adhesion of the coating are denoted from HF1 to HF4 according to the appearance of the coating shown in Figure 1. Poor adhesion of the coating with circular cracks and delamination, is indicated by grades HF5 and HF6 [5]. The appearance of the coating around the indenter injection site was analyzed by light microscopy with a magnification of 50:1.

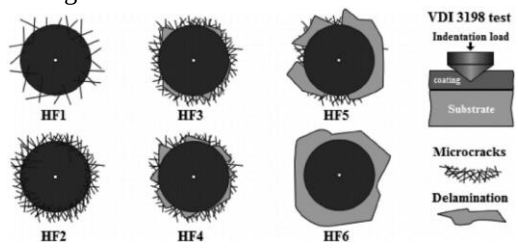

Figure 1. Evaluation of adhesion of the coating according to the VDI 3198 norm [5]

The wear tests of the uncoated and coated drills were performed in a drilling machine Bosch PBD-40 with maximum output power of 700 W. The workpiece material for drilling is a strip 50 mm width, 3 mm thick and 1000 mm long made of nonalloyed structural steel EN 10025-2: S355JR. In all drilling tests the rotation speed of spindle was 1000 rpm, the drilling force was constantly hold at 100 ± 10 N and the drilling was performed without coolants. The drilling time for every hole was measured as output value. At the initial state and after drilling of 10 and 15 holes the diameter of drill was measured by micrometer with three repetitions.

Table 1. Parameters of heat treatment and PACVD coating of test drills made of the HS18-0-1 tool steel

Test drill labels:	**Coating processing conditions**: Pulsed voltage: 500 V DC; Pressure 2 mbar; Gas mixture $N_2/Ar/H_2/CH_4$; Precursors for PACVD process $TiCl_4$, TiB_3	
	Sputtering-cleaning process	DC PACVD coating process
D1	500°C /2 h	+[500°C/(TiN/1.5 h +TiCN/6 h)]
D2	500°C /2 h	+[500°C/ (TiN/2 h + TiBN/10h)]

3. Results and discussion

3.1. Coatings characterization

Test results of the surface roughness before and after the PACVD deposition are shown in Table 2 using the parameters *Ra*, *Rz* and *Rmax*. The PACVD process practically does not change the initial surface roughness. The multilayer coatings grow uniformly and homogeneously on the cleaned surface.

The growth of the coating formed the profile roughness with an increased number of microhills and micro depressions with respect to the initial state.

The thickness of the coating was determined by light microscopy on the cross section of the drill bit. The thickness of the TiN/TiCN coating is 1.3 ± 0.2 μm and the thickness of the TiN/TiBN coating is 5.5 ± 0.2 μm. The indents made on the coatings by the indenter after the Rockwell-C indentation test are shown in Figure 2. In both coatings one could note the delamination of the

coating around the indent, together with a small number of radial micro cracks. According to the VDI 3198 method, the look of the indent indicates slightly weaker adhesion and increased brittleness in both coatings tested.

Table 2. Roughness parameters of the tested drills made of the HS18-0-1 tool steel in the initial stage (D0) and after the PACVD process (samples D1 and D2)

Drill label	*Ra*±*σ*, µm	*Rz*±*σ*, µm	*Rmax*±*σ*, µm
D0	0.562±0.145	4.311±0.705	5.444±0.336
D1	0.706±0.079	4.814±0.609	5.710±0.676
D2	0.515±0.027	3.903±0.240	4.619±0.280

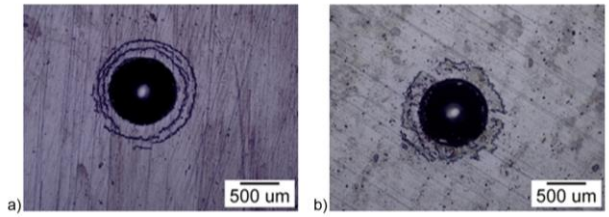

Figure 2. Micrographs of Rockwell-C indents on the PACVD drills coated with multilayer: a) TiN/TiCN (sample D1), b) TiN/TiBN (sample D2)

3.2. Drill wear

Drilling of 15 holes in the strip of non-alloy low-carbon steel S355JR was carried out on a column drill Bosch PBD-40 with a constant speed and drilling force. Table 3 shows the appearance of the drill bit tip with a diameter of 4 mm before the start of drilling and after 15 drilled holes.

Table 3. Appearance of 4 mm diameter drill bit tip before drilling and after 15 drilled holes in 3 mm thick S355JR steel strip

Drill label	Drill bit tip before starting drilling	Drill bit tip after 15 drilled holes
D0 (uncoated)	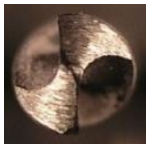	
D1 (TiN/TiCN)		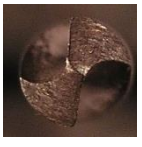
D2 (TiN/TiBN)	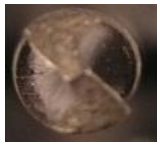	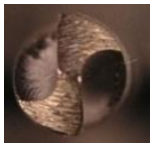

Figure 3 shows the drills in full length after drilling 15 holes. Remains of glued separate particles can be seen on the spiral surfaces of the drill.

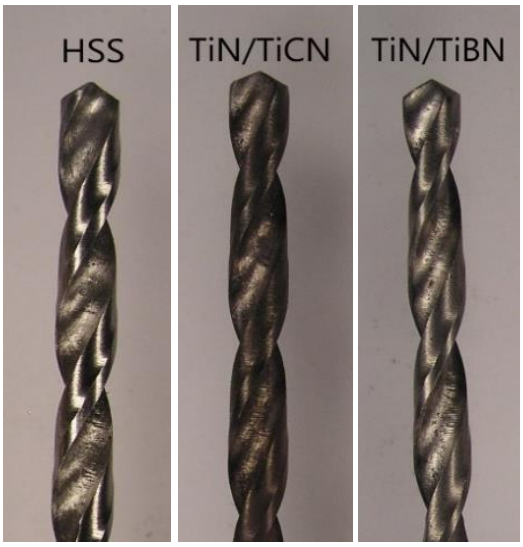

Figure 3. Appearance of a 4 mm diameter drill bit after 15 drilled holes in a 3 mm thick S355JR steel strip

Figure 4 shows the mean drilling time of 15 holes calculated based on three repetitions of drilling. A new spiral drill was used for each drilling. The mean value of the diameter reduction at the top of the drill bit after drilling 10 and 15 holes is given in Table 4.

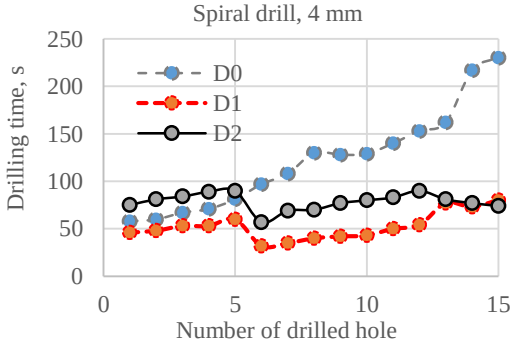

Figure 4. Drilling time of 4 mm diameter sheet metal 3 mm thick depends on the number of drilled holes

Table 4. Average reduction of the drill diameter after drilling 10 and 15 holes

Test label	Reduction of diameter after drilling:	
	10 holes, µm	15 holes, µm
D0	- (78 ± 37)	- (143± 14)
D1	- (94 ± 65)	- (130± 66)
D2	- (29 ± 11)	- (47 ± 19)

In the conducted experiments, the drill was loaded with a constant drilling force of 100 N and penetrated the

material at different feed rates whose mean values can be determined from the measured drilling time (Figure 4) and the thickness of the strip (3 mm). The mean value of the drilling offset depending on the number of drilled holes is shown in Figure 5. The display shows a decrease in the feed rate of the uncoated drill bit with an increase in the number of drilled holes due to drill bit wear. The drilling offset of coated drills after 12 drilled holes stabilized at 0.04 mm / s.

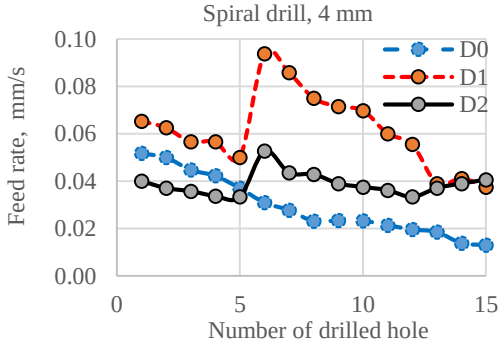

Figure 5. Average value of feed rate during drilling hole in 3 mm thick steel track depending on the number of drilled holes

During the drilling of holes, the temperature change was monitored with an optical pyrometer at the point of entry of the drill into the material. However, this method did not prove reliable for predicting drill wear due to large deviations of measurement results during drilling of the observed hole dependent on the formation of deposits of chips around the drill and the change of focusing point of the pyrometer. From the measured values, an increase in the temperature of the material around the drilling site and an increase in the temperature of the drill blade after drilling a hole, ie a series of holes, were observed. The temperature of the drill blade increased in the range from 20 °C at the beginning of drilling the first hole to 65 °C after successive drilling of five holes.

From the appearance of the worn drill blades shown in Table 3, the occurrence of adhesive wear of the rear surface is observed, which becomes rougher with glued separate particles. The drilling time of the first 5 holes is equally increased for all three drill states. Between drilling 5 and 6 holes and 10 and 11 holes, the drill blade was photographed during which the drills cooled to room temperature.

Continued drilling with uncoated drill bits (label D0) caused a further extension of the drilling time, which was 230 s for the fifteenth hole. Wear was confirmed by the appearance of the rear surface of the drill bit shown in Table 3 and by measuring the reduction in the diameter of the drill bit listed in Table 4. PACVD coated drill bits showed shorter drilling times after the fifth hole, compared to uncoated drill bits (Figure 4). This phenomenon can be explained by the beneficial effect of the coating on reducing the friction between the drill and the workpiece and the drill and the separated particle, increasing the resistance to abrasion wear of the blade and reducing the tendency of the blade to form bonded chips. The TiN/TiCN coated drill bits (marked D1) showed the shortest drilling time with drill diameter wear similar to uncoated drill bits (Table 4). The TiN/TiBN coated drill bits (label D2) showed the lowest diameter wear (Table 4) with about 10% longer drilling time compared to D1 drill bits. This can be explained by the greater thickness of the TiN/TiBN coating compared to the TiN/TiCN coating and the appearance of rounding of the transverse blade tips due to coating deposition. After drilling 10 holes, the transverse blade of the TiN/TiBN coated drill bits reduces the tip radius and the drilling time becomes equal to the TiN/TiCN coated drill bits.

4. Conclusion

The paper compares the wear of a spiral drill with a diameter of 4 mm with and without PACVD coatings after drilling 15 holes in a strip of low-carbon non-alloy steel 3 mm thick with a drilling force of 100 N and a drilling speed of 1000 rpm. Uncoated drills became blunt after drilling 12 holes, which caused the drilling time to be extended to more than 200 s per hole with a feed rate of 0.02 mm/s. PACVD coated drills did not become significantly worn after drilling 15 holes. The drilling time of the hole with drills protected by PACVD coatings is three to four times shorter compared to drilling with an uncoated drill bit with a feed rate of 0.04 mm/s. The lowest blade wear and reduction of the drill diameter was achieved after coating with a multilayer coating PACVD TiN/TiBN, which is also higher in hardness than the coating TiN/TiCN.

REFERENCES

[1] Graham T. S., (2008), *Cutting tool technology: industrial handbook*, Springer-Verlag London, UK

[2] Dolinšek, S. Kopač, J.(2006), *Mechanism and types of tool wear particularities in advanced cutting materials*, Journal of Achievements in Materials and Manufacturing Engineering, Vol. 19/1, p.11-18

[3] Holmberg, Matthews, A.,(2009), Coatings Tribology: Properties, Mechanisms, Techniques and Applications in Surface Engineering Elsevier, Oxford, UK

[4] Martin, P.M (2010), *Handbook of Deposition Technologies for Films and Coatings – Science, Applications and technology*, Elsevier, Oxford, UK

[5] Vidakis, N, Antoniadis, A. Bilalis, N, (2003), *The VDI 3198 indentation test evaluation of a reliable qualitative control for layered compounds*, Journal of Materials Processing Technology Vol. 143–144 p.481–485

ISSN 1847-7917

Optimization of viscosity of highly concentrated alumina suspensions for slip casting by surface response methodology

Darko LANDEK[1)]***, Lidija ĆURKOVIĆ***[1)]
Ivana GABELICA[1)]***, Irena ŽMAK***[1)]
1) University of Zagreb, Faculty of Mechanical Engineering and Naval Architecture, Ivana Lučića 5, 10000, Zagreb, Croatia, **Croatia**

dlandek@fsb.hr
lcurkovic@fsb.hr
igabelica@fsb.hr
irena.zmak@fsb.hr

Keywords
Alumina suspension
Darvan C-N
Tiron
Citric acid monohydrate
Simplex lattice mixture design

Original scientific paper

Abstract: In this work highly concentrated (70 wt.%) aqueous suspensions of alumina (Al_2O_3) were prepared for slip casting. The suspensions were stabilized with different combinations of three dispersants (A) disodium salt monohydrate (Tiron), (B) Darvan C-N, 4,5-dihydroxy-1,3-benzenedisulfonic acid, and (C) citric acid monohydrate. Amounts of three dispersants were selected due to the simplex lattice mixture design in aim to evaluate the effect of dispersant content and their combination on rheological properties of highly concentrated alumina suspensions. The regression analysis and the response surface plots showed synergistic effect on decreasing suspension viscosity below 12 mPas, after addition small concentrations of the dispersants Tiron and the citric acid to the Darvan. The antagonistic effect of mixture of dispersants was obtained, after addition small amounts of the Darvan and the citric acid to the Tiron, with increasing viscosity up to 20 mPas.

1. Introduction

Alumina is high-performance engineering material which can replace metals, and improve product properties in many demanding applications. Sintered alumina cutting inserts can cut hard materials faster and las longer than the best tool steels. It can be used in applications with high temperature and corrosive environment or in human body as part of artificial joints. Compared to other ceramics, alumina has three key advantages [1,2,3]: a good combination of mechanical, tribological, dielectric properties and chemical inertness; availability of cheap raw powder and it can be shaped and sintered to full density in without protective atmosphere. The production of sintered products from aluminum ceramics is carried out in three interdependent steps consisted from [4, 5]: (i) preparation of a stable suspension, (ii) a green body formation and (iii) densification of body during sintering.

For the production of high-quality aluminum oxide ceramics by slip casting, a powder of Al_2O_3 with particle sizes between 1nm and 1 mm is used, which is mixed with water, dispersants and additives to form a stable highly concentrated suspension (a slip). The slip casting method is simple process for the production of ceramic green bodies by casting a slip into gypsum molds and their drying into molds with absorption of water. For the production of a quality sintered product, it is necessary to ensure the stability of the suspension which determines the homogeneity of the composition and isotropic properties of the green body. The stability of the suspension is disturbed by the occurrence of grain adhesion into aggregates that fall to the bottom in the form of sediment or the lifting of the grain by hydromechanical buoyancy and the formation of a surface film. Both phenomena result in the appearance of inhomogeneous areas in the suspension composition and later with formation of porosity and poorer properties in the sintered product. The application of dispersants reduces the viscosity of the suspensions with very high solids content, and increases the suspension stability, which allows good filling of the mold and obtaining a uniform formation of the green body [5, 6]. The influence of dispersant content and combination was investigated at number of papers [7, 8, 9]. The usually industrial dispersant is ammonium polymethacrylate ("Darvan C") [10,11], 4,5-dihydroxy-1,3-benzenedisulfonic acid disodium salt ("Tiron"), carbonic acid salt ("Dolapix CE 64") [12], polycarbonic acid salt ("Dolapix PC 33"), carbonic acid ester ("Dolapix ET 85") [13] etc. In [14, 15] was found that the minimal viscosity (7 mPas) of highly concentrated alumina (70 wt. % of Al_2O_3 powder) and water suspension was obtained with addition of 0.75 wt. % of Darvan, or 0.1 wt. % of Tiron or 0.3 wt. % of citric acid.

In this research the influence of combinations of three dispersants Tiron (4,5-dihydroxy-1,3-benzenedisulfonic acid disodium salt monohydrate), Darvan C-N (an ammonium polymethacrylate water solution) and citric

acid monohydrate on viscosity of highly concentrated alumina suspensions for slip casting was investigated and statistically analysed.

2. Materials and methods

2.1. Suspension preparations

Aqueous alumina suspensions with a solid loading of 70 wt.% were prepared from high purity Al_2O_3 powder with average particle size of 300–400 nm (Alcan Chemicals, Stamford, CT, USA) deionized water and three dispersants denoted as "A", "B", and "C". A dispersant "A" is 4,5-dihydroxy-1,3-benzenedisulfonic acid disodium salt monohydrate (Sigma-Aldrich Chemie GmbH, Germany) commercially named Tiron. A dispersant "B" is an ammonium polymethacrylate water solution (Vanderbilt Chemicals, LLC, USA), commercially named Darvan C-N. A dispersant "C" is citric acid monohydrate, > 99,7 % purity (VWR Chemicals, BDH Prolabo, Belgium). The pH value of alumina suspension was 6.00 ± 0.5, which was set by addition of 1 M NaOH aqueous solution. All suspensions were prepared by adding deionized water, dried ceramic powder and dispersant into the grinding jar of a planetary ball mill. The grinding jar and ten balls used for homogenization are made of alumina ceramics to prevent the contamination of suspensions. Each of the prepared suspensions was homogenized for 90 min at a rate of 300 rpm in the planetary ball mill (PM 100, Retsch, Germany). To remove air bubbles and to achieve homogeneity of prepared suspensions, each of them was treated in an ultrasonic bath.

2.2. Rheological tests

Rheological measurements were conducted using a rotational viscometer DV-III Ultra (Brookfield Engineering Laboratories, Inc., USA) in a small sample chamber with spindle SC4-18. Pre-shearing lasted for 2 min at a shear rate of 100 s^{-1}. The shear rate was gradually increased from 0.1 to 180 s^{-1}, and then reduced back to 0.1 s^{-1}. The shear rate increase/decrease interval was divided in 50 equal time frames, which lasted for 3 seconds each. Rheological measurements were conducted just before each shear rate change. Temperature was kept constant at 25±1 °C using a thermostatic bath Lauda EcoRE 415 (LAUDA-Brinkmann, LP, USA). Flow curves were recorded for each dispersant type and each dispersant concentration

2.3. Design of experiments

The simplex lattice mixture design was used to evaluate the effect of different amount of dispersants: Tiron (x_A), Darvan (x_B) and citric acid (x_C) on dynamic viscosity of highly concentrated alumina suspensions. Concentrations of each dispersant were expressed as fractions of the mixture as shown in Figure 1. The content of dispersant was prepared as shown in Table 1**.** The three tested combination were obtained with three single-dispersant (label 1 to 3), three combination used two-dispersant (label 5, 7, and 9) and four test combination used three-dispersant mixtures (label 4, 6, 8, and 10).

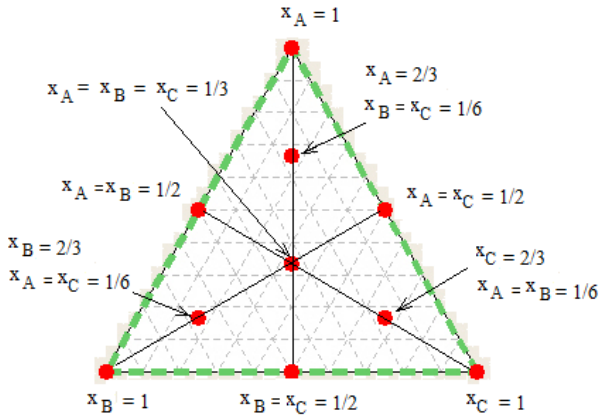

Figure 1. A simplex lattice mixture test design for addition of dispersants used in preparation of the 70% alumina suspensions

Table 1. Variation of amounts of dispersants (Tiron, Darvan C-N and Citric acid) in 70% alumina suspensions

Label of test sample	*wt. (dispersant), %*		
	A: Tiron	**B: Darvan C-N**	**C: Citric acid**
1	0.50	0	0
2	0	1	0
3	0	0	0.30
4	0.16	0.66	0.23
5	0.30	0	0.20
6	0.36	0.66	0.13
7	0.3	0.80	0
8	0.16	0.86	0.13
9	0	0.80	0.20
10	0.23	0.73	0.16

Experimental results of viscosity measurements were analyzed using software Minitab with combination of response surface and regression analysis.

3. Results and discussion

3.1. Viscosity measurements

Suspension stability was estimated by rheological measurements at shear rate, of 50 s^{-1}. This shear rate is usually achieved during the gravity slip casting.

Measured values of dynamic viscosity and pH values are presented in Table 2. From results showed in Table 2 one can see that the lowest dynamic viscosities were obtained in suspensions 7 (0.3 wt.% Tiron, 0.8 wt.% Darvan), 8 (0.16 wt.% Tiron, 0.86 wt.% Darvan, 0.13 wt.% Citric acid) and 9 (0.8 wt.% Darvan, 0.2 wt.% Citric acid). These results showed the synergistic effect of a combination of dispersants A + B, and also A+B+C. The suspensions 1 and 5 showed the highest values of viscosity, and the antagonistic effect of combination of dispersants A+C. The measured pH value of suspensions 2 and 7 were higher than was planned with experimental design but it seems that this result did not have a significantly effect on measured viscosity.

Table 2. **Viscosity and pH value of** suspensions **made from** 70% alumina **and 30% deionized water with variation of added** dispersants

Label of test sample	pH	η, mPas
1	6.74	23.9366
2	8.70	13.6231
3	6.06	15.0854
4	5.63	13.7770
5	6.23	22.2433
6	6.20	14.8545
7	7.75	12.1607
8	6.57	12.6225
9	6.20	13.0073
10	6.15	13.6231

3.2. Statistical analysis

A contour plot of a response surface of viscosity measured in mPas dependent from dispersant content is shown in Figure 2. From the contour view of the measured viscosity of the suspension in Figure 2, the area of lower viscosity values in the lower left corner of the view is observed. These favorable lower viscosity values are achieved by a combination of dispersants B (Darvan C-N) and C (citric acid), with possibly a small addition of dispersant A (xA < 1/3).

Regression analysis of the response surface of dynamic viscosity dependent from type and content of dispersants is conducted in the software Minitab. The influence of interactions among the dispersants Tiron (factor A), Darvan C-N (factor B) and Citric acid (factor C) on dynamic viscosity are shown in Table 3.

The terms x_A, x_B and x_C are the wt, % of dispersants. The coefficient of determination of model (1) is $R^2 = 0.9082$.

The calculated regression model also indicates a significant synergistic effect of dispersants A and B on the reduction of suspension viscosity. This significance of action is indicated by the *p*-value of their regression coefficient, which is 0.021 and satisfies the condition of statistical significance of the action of the observed effect in the experiment ($p < 0.05$).

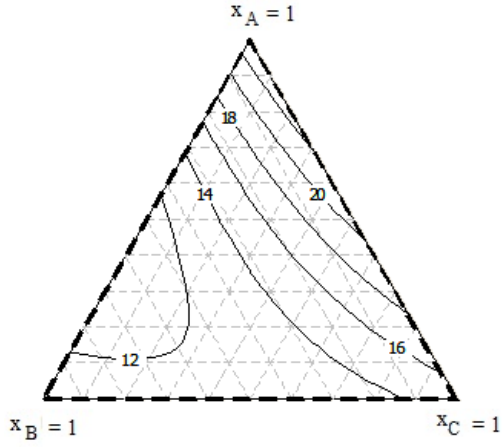

Figure 2. Mixture contour plot of dynamic viscosity (mPas) of the 70% alumina suspensions after addition of dispersants

From regression analysis and results in Table 3 the following regression equation for prediction of dynamic viscosity **(η, mPas)** of 70% alumina suspensions dependent from wt, % of added dispersants is estimated:

$$\eta = 23.42x_A + 14.28x_B + 15.00x_c - 30.61x_Ax_B + \\ +5.32x_Ax_C - 8.66x_Bx_C \quad (1)$$

Table 3. **Estimated regression coefficients in a linear model of dynamic viscosity (η, mPas) of** 70% alumina suspensions **dependent from added** dispersants

Term	Coefficient	Sum of error of coefficient	*p*-value
x_A	23.42	1.807	
x_B	14.28	1.807	
x_C	15.00	1.807	
x_A*x_B	-30.61	8.326	0.021
x_A*x_C	5.32	8.326	0.557
x_B*x_C	-8.66	8.326	0.357

Mixing of dispersants B and C also shows a synergistic effect on the reduction of viscosity, which can be deduced from the negative value of the regression coefficient with the product of their weight fractions. However, the combined effect of dispersants B and C on the viscosity reduction is not statistically significant,

because the *p*-value of the product of their weight fractions is higher than 0.05. The antagonistic effect of mixture of dispersants was obtained, after addition small amounts of the Darvan and the citric acid to the Tiron, with increasing viscosity up to 20 mPas.

The addition of only one dispersant to the Al_2O_3 aqueous suspension also reduces the viscosity of the suspension, but only for certain values of the weight fraction of the dispersant with small variations in values around the optimal content. The addition of two or three dispersants at the same time will result in a decrease in viscosity with a wider range of allowable variation around the range of optimal dispersant proportions.

Based on equation (1) and Figure 2 the combination of dispersants can be optimized by looking for combinations that will give a minimum dynamic viscosity of high concentrated Al_2O_3 suspension suitable for slip-casting.

4. Conclusion

The focus of this research was the influence of three different dispersants on dynamic viscosity of highly concentrated alumina suspensions with 70 wt. % of dried Al_2O_3 powder. The simplex lattice mixture design was used to evaluate the effect of different amount of dispersants: Tiron, Darvan C-N and Citric acid on dynamic viscosity. From analysis of rheological testing results the synergistic effect in decreasing the 70 *wt.* % alumina suspension viscosity was found for mixtures of dispersants Tiron and Darvan C-N (0.3 wt.% Tiron, 0.8 wt.% Darvan), as well as for Darvan C-N and Citric acid (0.8 wt.% Darvan, 0.2 wt.% Citric acid). A mixture of all three dispersants in the weight content: 0.16 wt.% Tiron, 0.86 wt.% Darvan, 0.13 wt.% Citric acid also gave the acceptably low suspension viscosity. For optimization of dispersant contents, a linear regression model is proposed estimated from statistical analysis of rheological measurement.

Acknowledgements

This work has been fully supported by the Croatian Science Foundation within the project IP- 2016-06-6000: Monolithic and Composite Advanced Ceramics for Wear and Corrosion Protection (WECOR).

REFERENCES

[1] Lee, W. E. (1996), *Ceramic processing and sintering*, International Materials Reviews, No.41, p. 36–37

[2] .F. Shackelford, R.H. Doremus (2008), *Ceramic and Glass Materials: Structure, Properties and Processing*, Springer, New York, USA

[3] Ćurković, L., Kumić, I., Grilec, K. (2011), *Solid particle erosion behaviour of high purity alumina ceramics*, Ceramic International, 37, p. 29–35.

[4] Landek, D.,Ćurković, L., Gabelica, I, Kerolli Mustafa, M., Žmak, I. (2021), *Optimization of Sintering Process of Alumina Ceramics Using Response Surface Methodology*, Sustainability 2021, 13, 6739.

[5] Yuan, C.S.; Wang, Z.J.; Zhi, Q.; Zhang, Y.M.; Wang, X.D.; Yang, J.F. (2018), *The preparation and properties of alumina ceramics through a two-step pressureless sintering process*. Mater. Sci. Forum, 922, p.47–54.

[6] Boch, P, J Niepce, C. (2010), *Ceramic Materials: Processes, Properties, and Applications*., ISTE Ltd, London, UK

[7] Tsetsekou, A., Agraotis, C., Milias, A. (2001), *Optimization of the rheological properties of alumina slurries for ceramic processing applications Part I: Slip-casting*, Journal of the European Ceramic Society 21, p.363-373

[8] Majić Renjo, M., Lalić, M., Ćurković, L., Matijašić, G. (2012) *Rheological properties of aqueous alumina suspensions*, Materialwissenschaft und Werkstofftechnik, 43, p.979–983.

[9] Wu, L., Huang, Y., Liu, L. Meng,L. (2010), *Interaction and stabilization of DMF-based alumina suspensions with citric acid*, Powder Technology., 20, p. 477–481

[10] Singh, B.P.; Bhattacharjee, S.; Besra, L.; Sengupta, D.K.(2004), *Evaluation of dispersibility of aqueous alumina suspension in presence of Darvan C*, Ceramics International, 30 (6), p.939–946.

[11] Tsetsekou, A.; Agrafiotis, C.; Leon, I.; Milias, A. (2004), *Optimization of the rheological properties of alumina slurries for ceramic processing applications Part II: Spray-drying*, Journal of the European Ceramic Society, 21 (4), p.493–506

[12] Gulicovski, J.J.; Čerović, L.S.; Milonjić, S.K. (2008), *Rheology of alumina suspensions stabilized with Tiron*, Korea-Australia Rheology Journal, 20 (2), p.65–71

[13] Mohanty, S.; Das, B.; Dhara, S. (2013), *Poly(maleic acid) - A novel dispersant for aqueous alumina slurry*, Journal of Asian Ceramic Societies, 1 (2), p.184–190.

[14] Sever, I., Žmak, I., Ćurković, L., Švagelj, Z. (2018) *Stabilization of Higly Concentrated Alumina Suspensions by Different Dispersants*, Transactions of FAMENA, Vol. 43, No. 3, p.61- 70

[15] Vukšić, M., Žmak, I. Ćurković, L., Ćorić, D. (2019), *Effect of Additives on Stability of Alumina—Waste Alumina Suspension for Slip Casting: Optimization Using Box-Behnken Design*, Materials, 12, 1738, p. 1-16

ISSN 1847-7917

Production of closed cell foams from the aluminium chip waste

***Branimir LELA*[1)], *Jure KROLO*[1)], *Karla GRGIĆ*[1)], *Sonja JOZIĆ*[1)] *and Ivana DUMANIĆ*[1)]**

1) Faculty of Electrical Engineering, Mechanical Engineering and Naval Architecture, University of Split
Ruđera Boškovića 32, 21 000 Split,
Republic of Croatia

blela@fesb.hr
jkrolo@fesb.hr
kgrgic00@fesb.hr
sonja.jozic@fesb.hr
Ivana.Dumanic.00@fesb.hr

Keywords

Closed cell foam
Aluminium foam
Energy absorption
Microhardness
Waste recycling

Original scientific paper

Abstract: Aluminium metal foams represent a new generation of materials that are characterized by their lightweight structure and unique properties. This research is based on the production of closed cell foams which are made of aluminium alloy chip waste and TiH_2 as a foaming agent. The main task was to investigate the influence of different times and temperatures of foaming as well as a different percentage of TiH_2 on mechanical and physical properties of foams. Microhardness, energy absorption, density, and compression properties were observed. Compressive strength and energy absorption are higher with the increase in density, while densification strain is lower. It is also concluded that a longer time and higher temperature of foaming lead to lower density values.

1. Introduction

In the last a few decades, metal foams became desirable materials for many purposes. They have cellular structures modeled on forms in nature like bones, sponges and coral [1]. Foams are investigated because of their unique properties such as low density, high strength to weight ratio, energy absorption capacity as well as high stiffness. They are characterized by great sound and heat insulation properties. The usage of this material is in many industries such as automotive, construction, naval and aerospace. In these industries metal foams are most commonly applied as energy and sound absorbers, various automotive and machine parts,heat exchangers foam sandwich panels and foam-filled beams. Their properties depend on cell structure, density, anisotropy, and homogeneity. Some of the most commonly used materials for metal foams are aluminium, nickel, copper, steel and titanium [2–4]. Aluminium foams are recyclable, and their main advantage is their non-toxicity. Therefore, they are often used [2], [3]. In addition to the above parameters, the properties of aluminium foam also depend on the base alloy [5], [6]. They are divided into open and closed metal foams [2].. The main property and aplication of closed cell foams is the absorption of energy. They can also be used for thermal insulation, flotation and vibration reduction [7]–[9]. Ther are two manufacturing methods for obtaining metal foams: melt and powder metallurgical route. Regardless of the used production route the most used foaming agents for closed cell foams are TiH_2 and $CaCO_3$.

Most of the authors investigated closed cell foams made by aluminium alloy powder. One of the studies included metal foams which were made by coarse and fine aluminium powder with TiH_2 at different foaming temperatures. Compression properties and densities were analyzed [2]. The study of compression tests on closed cell foams exhibited that mechanical properties are related to density and temperature of testing. With an increase in temperature, there is a decrease in energy absorption and compression strength [5]. Other authors studied aluminium foam made with an addition of calcium and TiH_2. Energy absorption and compression properties were observed with changing compression temperature. An increase in the temperature resulted in the reduction of the main mechanical properties [10]. Closed cell metal foams were studied with micro-computed tomography. A geometry of foams and their properties were investigated with and without deformation [6]. Another study included foams made with TiH_2 which decomposes at high temperatures into Ti and H_2 and creates bubbles. The structure of foams and their mechanical properties were investigated with the influence of the human factor [3]. Foam can also be made from melting alloy with the addition of TiH_2 and Ca

stabilizer. The influence of porosity on compression properties was examined. With an increase in the porosity, the value of mechanical properties decreased [11]. Two-layer foams were made in the study. The first part is open cell foam, and the second is closed cell foam with different porosities. After foaming of precursors, mechanical properties were observed by compressive test [12]. Static and dynamic properties of closed cell foams made of aluminium alloy with TiH_2 were analyzed and the influence of densities on mechanical properties and energy absorption were researched. With the higher strain rate, there is an increase in compressive strength and energy absorption [13], [14].

A great disadvantage of producing metal foams is the price of the process. Producing aluminium foams from chips leads to a reduction of costs and greater recyclability. When producing aluminium foams from machined chips, it is needed to maintain homogeneity of foaming powder in the mixture and to achieve consolidation of machined chips. This part is more difficult than the process with aluminium powder due to the difference in particle size of aluminium powder and foaming agent. One of the studies included foams made by aluminium burrs and TiH_2 powder in the process of friction stir back extrusion. Porosity and compression properties were investigated [9], [15]. Another study described the solid-state consolidation process of foam production with machine waste and TiH_2. The influence of the foaming agent value and the addition of ceramic particles were investigated. The addition of Al_2O_3 led to the increase in the expansion of the foam [16]. Dynamic characteristics of aluminium foams with closed cells were analyzed using modal analysis and the Finite element method. These methods can serve for optimization of foams properties [8]. Another study was made with aluminium foams produced with different alloys chip waste and TiH_2. Aluminium oxide (Al_2O_3) was used as a stabilizer. Foaming behavior was analyzed as well as the shape and size of pores [17]. The study included measurement of oxygen level in closed cell aluminium foam. The foam was made of chip waste and TiH_2 with the addition of Al_2O_3 as well as Mg. Greater values of Mg resulted in lower densities and homogenous structures [18].

This study is based on the closed cell metal foam production out of waste material, which is important for considerable cost reduction of foams. The foaming time and temperature were investigated as well as their influence on mechanical properties.

2. Experimental procedure

The main aim of this research was to produce metal foams from the A380 (EN AC-46500) aluminium alloy machining chip waste and TiH_2 as a foaming agent. Table 1 shows chemical composition of the A380 alloy. Machining chips were produced by the milling process, Figure 1.

Table 1. Chemical composition of the alloy A380 according to the ASTM B179 standard

Alloy	Si	Fe	Cu	Mn	Mg	Ni	Zn	Ti	Other	Al
EN A 380	7.5 - 9.5	max 1.3	3.0 - 4.0	max 0.5	max 0.1	max 0.5	max 3	max 0.35	max 0.5	rest

Figure 1. Aluminium alloy A380 chip waste

As a foaming agent, TiH_2 was added to aluminium chips with the mass percentage of 0.25 and 0.5 %. After that, a small amount of distilled water was added and mixed with a previous compound in a glass container in different directions to achieve a compact and homogenous distribution. The mixture was then set on a hydraulic press and compressed in a mold with a diameter of 38 mm. Compaction steps were carried out by 1 MN hydraulic press. All compaction steps were performed with 200 kN force, while the final step was performed with 300 kN force. Measurement of the compacting force was taken by force sensor HBM C6A. Furthermore, to achieve compact precursor, compacted billets were direct hot extruded with the die and container preheated at 400°C and with a 7.1 extrusion ratio. Prior to extrusion, billets were preheated for 20 minutes on 400°C. After extrusion, round precursor bars with 15 mm in diameter were obtained. Precursor specimens were then placed in a mold with a diameter of 22 mm and height od 100 mm. Foaming of precursors was made at temperatures of 590 °C and 610 °C, as can be seen in Table 2. Temperatures were controlled with the digital temperature controller OMRON E5CC and type K thermocouple. One part of specimens (1, 3, 5, 7) was held with the shortest foaming time and taken from a heater when the foam fulfill the mold diameter. Other specimens (2, 4, 6, 8) had longer foaming time and were left in the mold until they reached the height of 70 mm. Figure 2 shows obtained samples after foaming process. Laser sensor OMRON ZX 1 – LD300A61 was used for measuring the height of the foam.

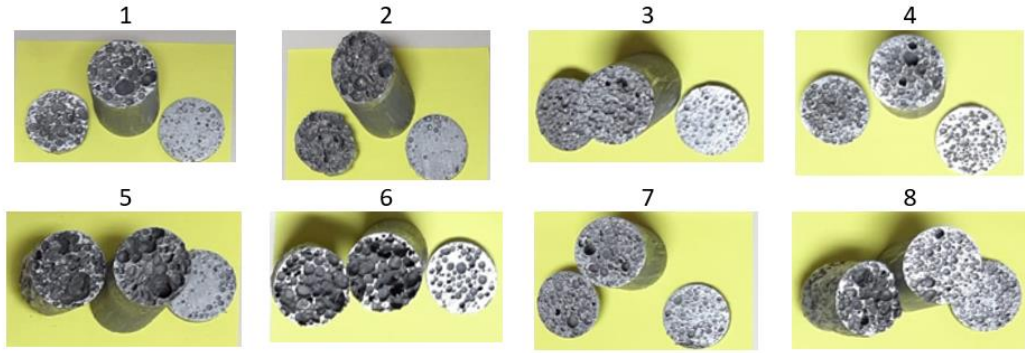

Figure 2. Samples after foaming

Table 2. Foaming parameters of specimens

Specimen	TiH_2 (wt%)	Temperature °C
1	0.25	590
2	0.25	590
3	0.25	610
4	0.25	610
5	0.5	590
6	0.5	590
7	0.5	610
8	0.5	610

The porosity of samples is one of the main properties for comparation of the light-weight structure of the different aluminium foams and it can be measured from the equation:

$$P = \frac{\rho_i - \rho_f}{\rho_i}, \quad (1)$$

where ρ_f is a density of the aluminium foam and ρ_i is density of aluminium which has value of 2,7 g/cm^3 [7], [10], [15].

Relative density ρ_{rel} represents the ratio of foam and aluminium densities and can be expressed as follows [4]:

$$\rho_{rel} = \frac{\rho_f}{\rho_i}, \quad (2)$$

After foaming, base of the specimens were sanded on 600 grit paper and prepared for microhardness testing. This microhardness property was measured using Shimadzu tester HMV 2T at five places on the surface. The average value was calculated. A compression test was carried out using a hydraulic press. Measurement of the force values were carried out with the force sensor HBM C6A.

After completed the tests, compression properties and energy absorption were observed. Compressive behavior is divided into three parts. The first of them is an elastic region with linear growth. It is related to small compressions where foam has large growth in compression stress according to small strain rate. This part finishes when compressive yield stress is reached. After a large slope on a diagram, the curve has a minor slope which represents plastic deformation, and it is called plateau region. Foams with lower densities exhibit an almost constant plateau region, while, with a rise of density, there is a stress rise in the plateau region. It begins with yield stress as a result of local stress concentration which weakens the strength of cell walls. The last part is the densification region, which has a larger slope than the previous one. It is related to merging cell walls of aluminium foam. This whole behavior depends on the density of the foam and its composition. Lower densities lead to lower values of compression strength. One of the parameters that also affects strength properties is heat treatment. It can proceed with alloys that can be age-hardened. From the stress-strain diagram, Young's modulus can be calculated from the elastic region [7], [10], [19], [20]. Plateau stress is given as a ratio of energy absorption and densification strain:

$$\sigma_{pl} = \frac{1}{\varepsilon_d}\int_0^{\varepsilon} \sigma(\varepsilon)\, d\varepsilon, \quad (3)$$

where ε_d are densification strain and $\sigma(\varepsilon)$ stress [13]. Densification strain is linearly dependent on foams relative density:

$$\varepsilon_D = 1 - \alpha\frac{\rho}{\rho_s}, \quad (4)$$

where α is a material constant that can have values from 1.4 to 3. For closed cell foams, this parameter has a value of 1.4 [5], [21], [22]. Energy absorption per unit volume represents the area under the stress-strain curve after compression test and can be calculated from:

$$E_v = \int_0^{\varepsilon} \sigma(\varepsilon)\, d\varepsilon, \quad (5)$$

where $\sigma(\varepsilon)$ is stress related to strain ε. The second part from the compression diagram called the plateau region is the most important for energy absorption. Its calculation starts from the beginning of the elastic region and finishes at densification strain where all pore cell walls are crushed. Foam walls can be deformed in the beginnings of compression test and their plasticity is depended on the density and type of the foam. The start of wall break happens when local stress exceeds critical st

ress levels [5], [7].

3. Results and discussion

The densities and relative densities of the specimens are shown in Table 3. It can be seen that samples (2, 4, 6, 8), which are characterized by an increase of the foaming time, have smaller density and relative density. Longer holding time resulted in a growth of foams pores. A rise in the percentage of TiH_2 led to a reduction of densities due to a release of a larger gas amount. As a consequence, an increase in height of the foam, larger pore space was obtained. There is also a slight decrease of densities with the larger temperature because of the faster decomposition of TiH_2 and higher foaming gas percentage. The first and the second samples with the least TiH_2 content and temperature didn't have the successful growth of the foam, especially the second which needed to have a larger height. That is why the production of the foams with that parameters are not recommended.

Densities have a small impact on the microhardness of the foam, Table 3. There is a small decrease in microhardness with an increase in density. Only the first two samples have a proportional impact. Because of the low difference in temperatures of the foaming process, it can be seen that there is no significant difference between the samples foamed at 590 °C with those foamed at 610 °C. Slightly increase in microhardness is visible with a smaller percentage of TiH_2 where there are fewer pores. With higher densities, there is an increase in plateau stress as well as energy absorption while the densification strain values decrease, Table 4. This fall happens because of the greater resistance of aluminium cells to loads during the compression tests with an increase in density. Furthermore, the potential to resist elastic deformations also rises. With an increase in density, the size of pores is decreased and their collapse space became smaller leading to the conclusion that the plastic stage is shorter and the densification strain begins earlier [13].

Table 3. Densities and microhardness of specimens

Specimen	Density g/cm³	Relative density	Microhardness HV
1	1.029	0.38	78
2	0.909	0.34	77
3	0.985	0.37	81
4	0.804	0.3	92
5	0.874	0.32	60
6	0.688	0.26	68
7	0.907	0.34	64
8	0.764	0.28	75

Foams with higher densities have larger yield strain, Table 4. When yield strength is reached, cell walls deform or fracture, and stress drops. After the compaction of cells, stress continues to grow. Larger pores have a longer compaction distance which means that greater strain is needed for the growth of stress. A greater compressive force is needed for cell walls fracture when the foam is made with greater porosity [11]. From Figure 3. it can be seen that specimens with the lower foaming time have larger engineering stress at the same strain values. This is most visible in the first part of the diagram with elastic properties where specimens 1, 3, 5, and 7 have a larger slope. They also have a more pronounced densification strain while the other four specimens have a similar slope in the plateau region.

The lower size of foam cells and higher densities exhibited larger energy absorption, which is proportional to compressive stress, Table 4. This happened because of the greater resistance of smaller cell walls which are more homogenous distributed in the foam [7]. However, compression test at room temperature results in exceptionally high dislocation densities with high work-hardening which leads to greater energy absorption [10].

Table 4. Compressive properties and energy absorption results

Specimen	Energy absorption			Compressive stress			Plateau stress	$\sigma_{0,2}$	Densification strain
	J/mm³			MPa			MPa	MPa	
	ε = 0,5	ε = 0,6	ε_D	ε = 0,5	ε = 0,6	ε_D			
1	22.3583	28.2617	20.5911	53.867	64.201	56.8	43.99	27.116	0.468
2	11.741	16.21	12.546	37.51	54.08	39.716	23.94	15.77	0.52
3	21.3765	26.8640	20.4474	48.419	64.911	48.498	42.42	27.192	0.482
4	11.892	15.533	14.736	32.946	40.714	39.288	25.41	13.409	0.58
5	11.686	14.564	13.082	22.846	31.994	29.545	23.69	27.674	0.552
6	7.7655	9.4401	10.124	17.133	16.634	23.234	15.92	15.84	0.636
7	18.0642	21.9846	18.9778	37.71	42.284	37.601	36.22	30.469	0.524
8	10.699	13.813	14.092	29.068	34.663	35.32	23.18	10.87	0.608

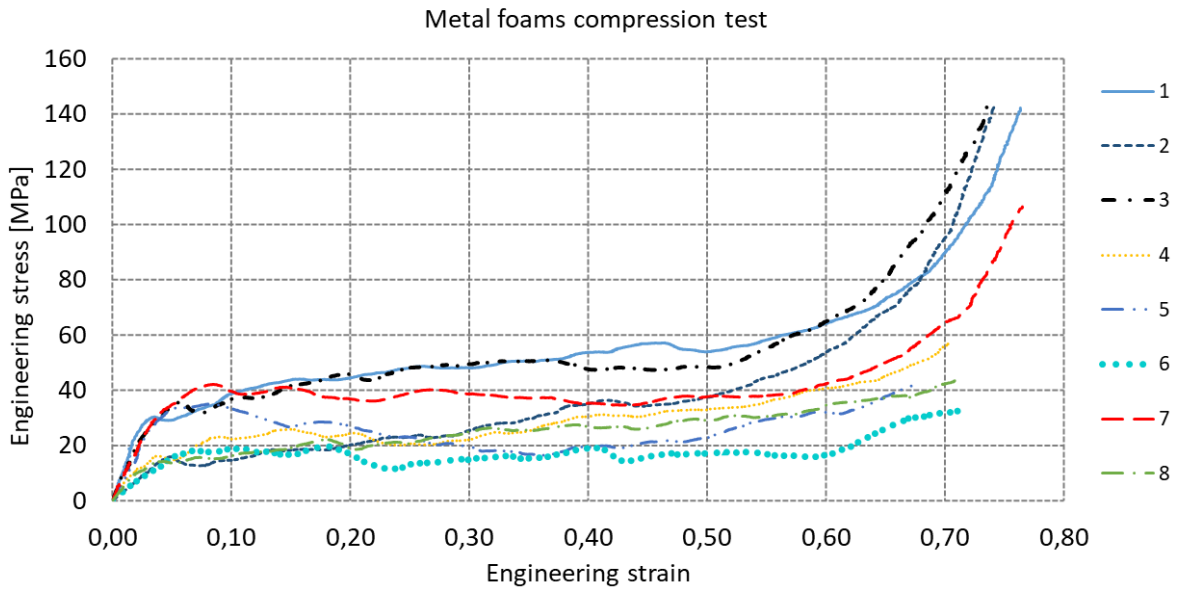

Figure 3. Engineering stress-strain curves

From the previous results, it is visible that the third sample has one of the highest values of compression stress and energy absorption. Its advantage is in the shorter time of foaming. However, it is concluded that with an increase in densities, there is a rise in mechanical properties also. Because of that, the fourth sample can be chosen when reduction of weight represents the main property for the selection. It also has good mechanical properties as well as high densification strain. Production of this kind of foam leads to cost saving because of the use of recycling material.

4. Conclusion

Closed cell foams were successfully made with an addition of TiH_2 as a foaming agent and machine waste which is the main advantage because of the reduction of the cost and time of foaming. The influence of time and temperature of the foaming process as well as a percentage of TiH_2 on densities and mechanical properties was observed.

Longer foaming time and temperature led to a decrease in densities. The smaller TiH_2 percentage increased density. This happens because smaller content of H_2 gas can be released in the process and there is more aluminium core in the foam. It can be concluded that the density of foams doesn't have a significant influence on the microhardness of the samples. A smaller percentage of foaming agent leads to an increase in microhardness.

With the growth of densities, values of compression strength, energy absorption, and plateau stress increase, while densification strain decreases. The larger slope on the stress-strain diagram have specimens with lower foaming time, especially in the elastic part. They also have expressed the beginning of densification region, while others are characterized with a similar slope as in the plateau region. Because of the smaller collapse space of higher density foams, their densification strain decreases.

Acknowledgment

This research has been supported by The Croatian Science Foundation through the project Recycling of aluminum alloys in solid and semisolid state (IP-2020-02-8284).

REFERENCES

[1] Razboršek B., Gotlih J., Karner T., Ficko M., (2019), *The influence of machining parameters on the surface porosity of a closed-cell aluminium foam*, Stroj. Vestnik/Journal Mech. Eng. 66, No. 1, p 29–37.

[2] Papantoniou I. G., Pantelis D. I., Manolakos D. E., (2018), *Powder metallurgy route aluminium foams: A study of the effect of powder morphology, compaction pressure and foaming temperature on the porous structure*, Procedia Struct. Integr. 10, p 243–248.

[3] Gábora A., Mankovits T., (2019), *Quality control of closed-cell metal foam produced by direct foaming*," IOP Conf. Ser. Mater. Sci. Eng. 659, No. 1.

[4] Prados Martín E., (2021), *Microstructural parameters affecting the compressive response of closed-cell aluminum foams*, Mech. Adv. Mater. Struct. 0, No. 0, p 1–20.

[5] Kovacik J., Orovčík Ľ., Jerz J., (2016), *High-temperature compression of closed cell aluminium foams*, Met. Mater. 54, No. 6, p 429–440.

[6] Ulbin M.et al., (2018), *Detailed Analysis of Closed-Cell Aluminum Alloy Foam Internal Structure Changes during Compressive Deformation*, Adv. Eng. Mater. 20, No. 8, p 1–8.

[7] Nammi S. K., Edwards G., Shirvani H., (2016), *Effect of cell-size on the energy absorption features of closed-cell aluminium foams,* Acta Astronaut. 128, p 243–250.

[8] Lei Q., Ren J., Ren H., Chao H., Du W., (2019), *Study on dynamic characteristic of closed-cell aluminum foam,* Vibroengineering Procedia 28, p 142–147.

[9] Novak N., Vesenjak M., Duarte I., Tanaka S., (2010), *Compressive Behaviour of Closed-Cell Aluminium foams at high strain rates*, Composites Part B: Engineering 41, No. 8, p 678-685.

[10] Movahedi N., Linul E., Marsavina L., (2018), *The Temperature Effect on the Compressive Behavior of Closed-Cell Aluminum-Alloy Foams,* J. Mater. Eng. Perform. 27, No. 1, p 99–108.

[11] Yang D. et al., (2019), *Coupling effect of porosity and cell size on the deformation behavior of Al alloy foam under quasi-static compression,* Materials (Basel) 16, No. 6.

[12] Hangai Y.et al., (2020), *Compressive properties of two-layered aluminum foams with closed-cell and open-cell structures,* Mater. Today Commun. 24, No. January, p 101249.

[13] Zhao Y., Ma C., Xin D., Sun M., (2020), *Dynamic mechanical properties of closed-cell aluminum foams with uniform and graded densities,* J. Mater. Res. 35, No. 19, p 2575–2586.

[14] Shen J., Lu G., Ruan D., *Compressive behaviour of closed-cell aluminium foams at high strain rates,* Compos. Part B Eng. 41, No. 8, p 678–685.

[15] Hangai Y., Kobayashi R., Suzuki R., Matsubara M., Yoshikawa N., (2019), *Aluminum foam-filled steel tube fabricated from aluminum burrs of die-castings by friction stir back extrusion,* Metals (Basel). 9, No. 2.

[16] Tsuda S., Kobashi M., Kanetake N., (2006), *Producing technology of aluminum foam from machined chip waste,* Mater. Trans. 47, No. 9, p 2125–2130.

[17] Kanetake N., Kobashi M., and Tsuda S., (2008), *Foaming behavior of aluminum precursor produced from machined chip waste,* Adv. Eng. Mater. 10, No. 9, p 840–844.

[18] Kumar G. S. V., Heim K., Garcia-Moreno F., Banhart J., Kennedy A. R., (2013), *Foaming of aluminum alloys derived from scrap,* Adv. Eng. Mater. 15, No. 3, p 129–133.

[19] Banhart J., Baumeister J., (1998), *Deformation characteristics of metal foams,* J. Mater. Sci. 33, No. 6, p 1431–1440.

[20] Wang X., Zhou G., (2013), *The static compressive behavior of aluminum foam,* Rev. Adv. Mater. Sci. 33, No. 4, p 316–321.

[21] Fleck N., (2002), *Metal Foams: a Design Guide,* vol. 3069, No. February, p 264.

[22] Kádár C., Kenesei P., Lendvai J., Rajkovits Z., (2017), *Energy absorption properties of metal foams,* No. June, p 1–6.

ISSN 1847-7917

Aluminium and aluminium alloys surface protection by the use of anodization technology

Petar LJUMOVIC[1)], ***Inoslav SVALINA***[2)], ***Igor GABRIC***[2)] and ***Anela BARBARIC***[3)]

1) University of Split, Faculty of Electrical Engineering, Mechanical Engineering and Naval Architecture, Rudjera Boskovica 32, 21000 Split, **Croatia**
2) University of Split, University Department of Professional Studies, Kopilica 5, 21000 Split, **Croatia**
3) FEAL d.o.o., Trnska cesta 146, 88 220 Siroki Brijeg, **Bosnia and Herzegovina**

petarlj@fesb.hr
is47355@oss.unist.hr
igabric@oss.unist.hr
anela.barbaric@feal.ba

Keywords

Aluminium
Anodization
Anodizing plant

Professional paper

Abstract: This paper presents specialized systems and plants for anodizing of aluminium and aluminium alloys with a description of each specific operation. It describes each of the specific process baths within the process of anodizing aluminium and aluminium alloys. The anodization procedures are given and explained in chronological order. The advantages of the process of anodizing aluminum and aluminum alloy are given as well. Final products commercial usage is also listed. The example of products quality control is shown, with commonly measured parameters of the anode layer by the use of various measuring instruments, in order to determine if the final product meets the specified technical standards.

1. Introduction

Anodization procedure is done in an anodizing plant which contains tank (depth to 2.5m), standard and special cranes for manipulating and suspenders for hanging samples.

Figure 1. Anodizing plant [1]

Tanks are filled with electrolytes (chemicals and demineralised water), thus form an integral part in anodizing plant for aluminium and aluminium alloys samples. On Figure 1, exhaust ventilation channels are shown, which serve for removal of the gases formed during anodization procedure. Samples are hanged on the suspenders, which are most commonly made from titanium in form of the fish bone. The use of titanium is important, for the reason of its good mechanical properties, described by Kulkami et al. [2], and electricity conduction on aluminium alloys samples. Titanium acts neutral for the most fluids used during anodization procedure, moreover during the repeated use of suspenders.

2. Anodization technology process

2.1. Cleaning

Cleaning procedure is used for the natural aluminium oxide removal purposes, as well as for the elimination of all imperfections and defects on the surfaces of the aluminium and aluminium alloys. Moreover, defects can be stressed out even more after the anodization procedure. Therefore, the samples must be subdued to

cleaning, either chemical or mechanical, or to electrochemical cleaning, if needed. Electrochemical cleaning is conducted by the use of 75 % concentrated phosphorus acid (H_3PO_4), with the procedure lasting from 2 to 10 minutes, at 5 to 10 A/dm² voltage and at 50 to 80 ºC temperature. Before using anodization procedure for the elimination of imperfections on aluminium and aluminium alloys samples, the degreasing and removal of the natural aluminium oxide must take place, which is repeated after the anodization procedure. Cleaning is often done by the use of NaOH because of the simplicity of the process when dealing with serial production of the samples made from aluminium and aluminium alloys. Drawn profiles are most common for bearing structures and door mounts. Mechanical cleaning, therefore conducted with the use of machines or manually is done less often, due to the complexity of the process. According to the previously defined standard (DIN 17611), different levels of cleaning are present for the samples surfaces, by which each one gets its technical mark regarding treatment quality.

2.2. Rinsing in demineralized water

The rinsing procedure in demineralized water is done after each stage of the aluminium and aluminium alloys anodization process. Demineralized water is in fact the quantity of total dissolved solid mass (TDS) between 1 and 10 mg/L, where the water itself has very low electrical conductivity. Additionally purified demineralized water (2. level of purification according to EN ISO 3696:1997), has an electrical conductivity lower than 1 µS/cm. The use of tap water or unpurified industrial water is not recommendable due to the presence of impurities; with the quantity of total dissolved solid mass (TDS) between 50 and 300 mg/L, such as calcium, sodium, magnesium, which leave stains on cleaned samples made from aluminium and aluminium alloys, and affect the final quality of the anodization procedure. Rinsing is used for the removal of residual hydroxide or acid remains, and impurities. Rinsing procedure time duration is between 1 and 3 minutes, in sufficient volume of water.

2.3. Degreasing

Degreasing process is conducted in detergents or in sodium hydroxide (20 % NaOH) in a bath, with temperature between 65 and 75 °C, and time duration between 5 and 10 minutes. This way, usually all impurities are removed. By conducting a simple test, it can be seen if the degreasing process has performed well by spraying the surface of aluminium and aluminium alloys with water. Degreasing process is successfully done if the water flows freely down the aluminium surfaces without leaving any water clusters behind.

2.4 Etching

Etching procedure is done for the purpose of removal of natural surface aluminium oxide layer (Al_2O_3). The procedure is done in saturated sodium hydroxide solution (NaOH) and demineralised water, at bath temperature between 40 i 60 °C and time duration of 5 minutes. Etching occurs due to the chemical reaction as follows (1):

$$2Al + 2NaOH + 2H_2O \rightarrow 2NaAlO_2 + 4H_2 \quad (1)$$

2.5 Rinsing in hydroxide solution

Rinsing in hydroxide solution is done for the purpose of removal of sodium hydroxide (NaOH) remains after the etching process. The procedure is done in the sodium hydroxide (NaOH) and water solution at water temperature 45 °C, no later than one minute after removing the samples made from aluminium and aluminium alloys from etching procedure. This type of rinsing is done to avoid permanent adhesion of hydroxide solution remains left from etching procedure and other impurities on to the aluminium surface. The procedure is to be repeated until the required surface condition quality is reached.

2.6 Neutralization

Neutralization procedure is done for the purpose of removal of sodium hydroxide (NaOH) remains from the aluminium and aluminium alloys samples. It is conducted in water and acid solution where the use of the acid depends on the acid type that will be used in anodization process (H_2SO_4, H_2CrO_4 and $H_2C_2O_4$), in time duration between 10 and 30 seconds.

2.7 Anodization

The anodization process itself is an electrochemical process, with the use of electrical energy and electrolytes (chemicals and deoxidized water), with cathode and anode (samples made from aluminium and aluminium alloys), which are used for obtaining considerably thicker aluminium oxide layer against the height of the natural aluminium oxide layer that protects the aluminium substrate from corrosion.

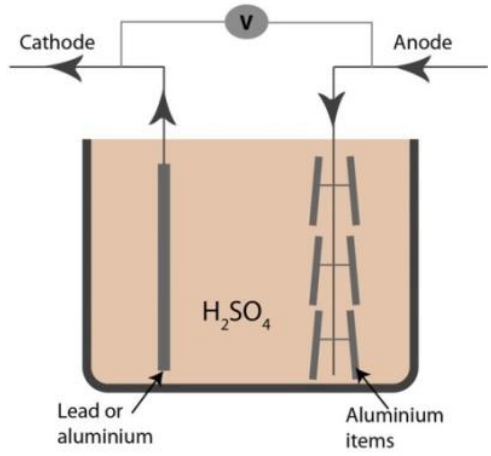

Figure 2. Basic scheme of anodizing process [3]

Tank material is most commonly made from polypropylene reinforced with carbon or steel profiles to insure its mechanical strength. Most common dimensions are 8 meters in length, 1 to 1.5 m width and 2 to 2.5 meters in height, with fluid capacity greater than 1000 liters. Anodization process mostly requires direct current (DC) due to the better efficiency of its stray currents. Positive side of direct current is connected to the anode which allows deposition of the aluminium oxide layer on more samples simultaneously. Superficially obtained aluminium oxide layer (Al_2O_3) due to its hexagonal structure also serves as an electrical isolator, moreover gives good foundation for dyeing procedure. There are several different anodization procedures for aluminium and aluminium alloys and parameters that affect the procedure itself. The properties vary due to the used electrolytes from various acids (H_2SO_4, H_2CrO_4 and $H_2C_2O_4$), dissolved in demineralized water, due to the composition and concentration of the electrolytes and their temperatures, evenly mixed electrolytes, amount of the square area of anode and chemical composition of samples made from aluminium and aluminium alloys. Moreover, properties depend on anodization procedure time duration, electrical voltage [V] and electrical current [A] regulation.

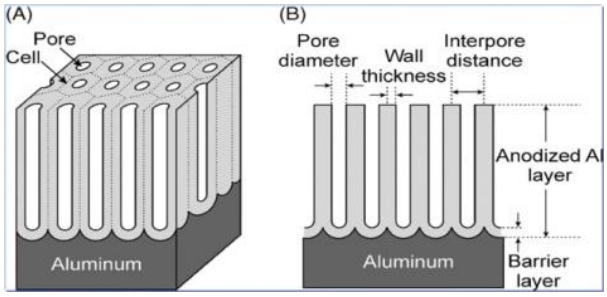

Figure 3. Parameters of aluminium oxide layer [4]

Considering the fact that the oxide layer is an excellent electrical isolator, it provides bigger resistance to electrical energy conduction in relation to its height increase, which automatically decreases the growth of the oxide layer, its mechanical and structural properties therefore its corrosion resistance. Due to this features, it is recommended to use a constant value of electrical current [A] in aluminium and aluminium alloys anodization procedure, moreover to regulate the electrical voltage [V], which provides uniformed mechanical and structural properties of the obtained aluminium oxide layer which, at the same time, requires a lower electrical current [A]. The usual values of the needed electrical current vary from 1-1.5A/dm² anode surface area.

At the beginning of the anodization procedure, electrical current is at its peak in order to generate oxygen on anode surface (a). Afterwards, electrical current steeply decreases due to forming of high electrical resistance because of barium-aluminium oxide layer generating (b). During the formation of porous aluminium oxide layer, electrical current increases (c, d). Electrical current than stabilizes due to the constant rate of porous al-oxide forming (e), explained by Ohgai [5].

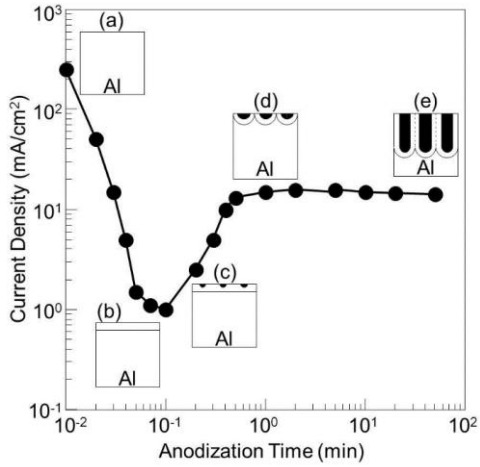

Figure 4. Electrical current by anode square area regulationdue to duration of aluminium and aluminium alloys anodization process in tank [5]

During the anodization process, good electrical conductivity of generated aluminium oxide layer must be insured, therefore anode efficiency of electrical current (ηa), which enables the oxide layer to form evenly. To insure finer oxide layer with balanced texture on the aluminium and aluminium samples surfaces, constant temperature from 18 to 21 °C needs to be maintained, as well as electrical current by samples square surface area. The samples are than immersed in electrolytic bath, thus presenting the anode connected on positive side of direct current (DC), which conduction makes the electrolyte to dissolve, and anode surface area to oxidise with oxygen from the electrolyte. Minimum distance between anode and cathode must be 25 mm, to minimize the electrical bridges to the lowest point. Cathode is mostly made from aluminium, lead, stainless steel and titanium. Aluminium cathodes lifetime is 4 years at best, while stainless steel cathodes last to 10 years. Lead cathodes last between 10 and 15 years, but at the same there are not environmentally friendly due to the fact that their ions could be found in anodization procedure waste waters. Aluminium cathodes are generally made from 1100 or 1350 sheets, or extruded 6063 T5 and 6101 T5 or T6 alloys. Advantages of using these cathodes reflect in lower electrical voltage requirements for the anodization procedure, lower energetic requests and expanses. Anodization procedure parameters regulation is less complicated; less wasted heat during the procedure, cathode lifetime is longer, smaller frontal dimensions could be obtained. Larger cathode surface area can be generated as well, because the extrusion process provides the fish bone profile, which consequently generates

smaller cathode dimensions in relation to its overall surface.

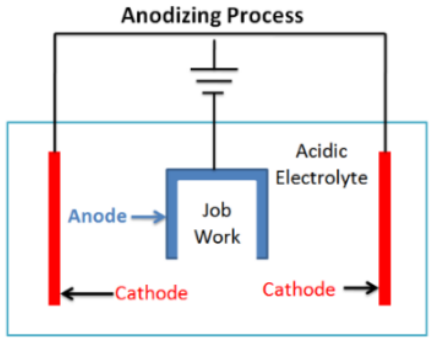

Figure 5. Anode and chatode position scheme [6]

Cathodes may be coated with polymer inserts in order to reduce their effective working area. In order to gain evenly distributed oxide anions on anode and balanced height of the aluminium oxide layer, sufficient amount of electrolyte mixing is necessary, which is commonly done by aeration (compressed air blowing with "oil free" compressors or specialized magnetic mixers). Moreover, heat exchangers are used for eventual heating of the anodization procedure in case of its overcooling. The temperature should not go below its default one.

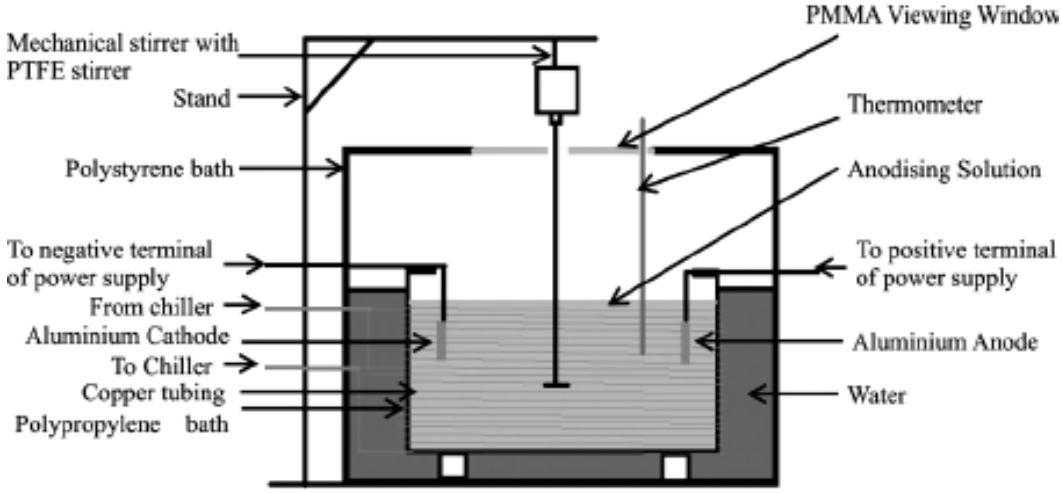

Figure 6. Cross-section of the anodization tank with its constituent parts [7]

The oxide layer inserts into the aluminium and aluminium surface with one part of its height, which creates a very good adhesion between them. Due to the very good connection of aluminium and its oxide which literally merges with aluminium substrate, samples made from aluminium and aluminium alloys are resistant to external abrasive influences and peeling.

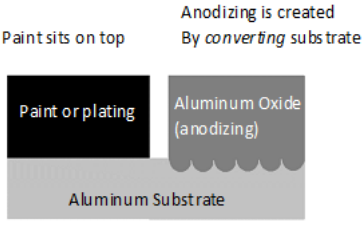

Figure 7. Coating and aluminium oxide layer adhesion on pure aluminium [8]

On Figure 7, the adhesion of coating and aluminium oxide layer on aluminium substrate is shown. Applied coatings overlap the aluminium substrate surface and do not have any physical connection and adhesion to substrate material, thus are subjected to peeling. Obtained oxide layer consists of barrier layer on the surface of aluminium substrate and hexagonal layer with open porosities. The oxide layer has ceramic characteristics. Porosities are needed to be closed in sealing procedure. Quality of anode layer depends on quality of aluminium and aluminium alloys samples which are anodized, made mostly from Al 99.5, than AlMgSi0.5, AlMg1 and AlMg3. Obtained oxide layer provides effective protection from corrosion with considerable mechanical resistance and insulation properties; it is good electrical and heat isolator considering the obtained hardness and height. By reaching the requested height of the oxide layer, anodization procedure is instantly stopped by the use of digital operating system and anodization procedure regulation. Most commonly used electrolyte in anodization procedure is the one from sulphuric acid (H_2SO_4). Few other used electrolytes are from chromatic

acid (H_2CrO_4) and oxalic acid ($H_2C_2O_4$). Quality of obtained oxide layer can be improved by the use of two-stage anodization, where uniformed and highly arranged porosive hexagonal aluminium oxide layer structure is obtained. Considering the fact that primarily obtained aluminium oxide layer is removed, surface of aluminium substrate retains its characteristic web-like structure with concave spots for porosion forming that give better characteristics of oxide layer during the conduction of the second stage of anodization procedure.

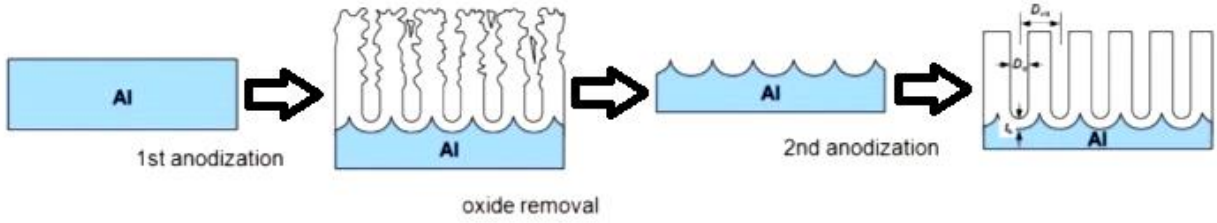

Figure 8. Two-stage anodization of aluminium oxide layer scheme [9]

2.7.1 Chemical reactions in anodization tanks

Sulphuric acid is used in majority of cases. The anodization procedure in based on classic electrolysis process, where electrochemical reaction consists of oxidation process; anode oxygen reaction where negatively charged anions release excess electrons to anode which receives oxygen in process of cathode reduction of hydrogen, where positively charged cations receive the same amount of electrons and release hydrogen. These reactions are necessary for starting and conducting of the anodization procedure where the electricity is transported within mentioned reactions. During electrolysis process, explained by Redkin et al. [10], different chemical agents are released on anode and cathode, galvanic cell is formed, so the electrolysis can proceed only if the electrical voltage of outer electrical energy source is opposite and greater of the electrical voltage (negative anode reaction) of the formed cell. The chemical reaction itself occurs between aluminium substrate and aluminium oxide layer, and between electrolyte and aluminium oxide layer. Electrolyte contains free hydrogen H^+ ions (hydrogen ion formed by proton binding), therefore contains H_3O^+ (hydronium cation formed by binding of proton to water molecules) and SO_2 (sulphur-dioxide in the form of gas). During the electrical energy flow between anode and cathode, dissolution of sulphuric acid occurs, with negatively charged sulphur oxide anions (SO_2) forming on the cathode and traveling to anode, sending oxygen and creating reaction on the aluminium anode's surface where oxygen binds with aluminium forming aluminium oxide (Al_2O_3). Moreover, unstable sulphur dioxide (SO_4) forms, which binds with water atoms (H_2O). Sulphuric acid (H_2SO_4) forms again, while remaining oxygen molecules bind with aluminium and also form aluminium oxide. Aside of exchanging negative and positive ions, electrical energy is spent also on growth of the aluminium oxide extraction of oxygen and ionization of aluminium in cations Al^{3+} between al-substrate and aluminium oxide layer according to Lin et al. [11]. Electrolytic dissociation of water enables it to split on hydrogen H^+ and hydroxide OH^- ions, which than enables gases oxygen
and hydrogen to be released on anode and cathode. Electrochemical reactions of sulphuric acid in water can be shown as follows (2, 3, 4);

$$H_2SO_4 + H_2O \rightarrow HSO_4^- + H^+ \quad (2)$$

$$HSO_4^- + H_2O \rightarrow SO_4^{2-} + H^+ \quad (3)$$

$$H^+ + H_2O \rightarrow H_3O^+ \quad (4)$$

Products formed after the electrochemical anode reaction can be shown as follows (5);

$$2Al + 3H_2O \rightarrow Al_2O_3 + 3H_2 \quad (5)$$

Electrochemical anode reaction can be shown as follows (6);

$$2Al + 3H_2O \rightarrow Al_2O_3 + 6H^+ + 6e^- \quad (6)$$

Electrochemical cathode reaction can be shown as follows (7);

$$6H^+ + 6e^- \rightarrow 3H_2 \quad (7)$$

Electrochemical reaction of water dissociation can be shown as follows (8);

$$H_2O \rightarrow H^+ + OH^- \quad (8)$$

2.7.2 Anodization in chromatic acid

The anodization procedure in chromatic acid (H_2CrO_4) (Type I), provides an aluminium oxide layer height from 5 to 10 μm. Obtained oxide layer has very good corrosion resistance due to noncorrosive properties of chromatic acid. At this particular anodization procedure, the concentration of the acid used is in range of 10 %, electrolyte temperature is at 40 °C, electrical current by anode square area is 0.5 A/dm², electrical voltage

gradually increases during procedure to 40 V, and time duration is calculated in minutes or read from the diagram. These parameters are defined by experience. Obtained aluminium layer has a ceramic characteristic which means it is a good isolator. Due to the low height of aluminium oxide layer, it does not affect the sample dimensions where narrow tolerances are in use.

2.7.3 Anodization in sulphuric acid

Anodization in sulphuric acid (H_2SO_4) (Type II), gives an aluminium oxide layer height from 10 to 25 μm. Obtained width of aluminium oxide layer is further separated on "class 1" with minimal layer width of 18 μm, which is used for outdoor purposes, and "class 2" that has minimal layer width of 10 μm, which is used for internal purposes [12]. Obtained aluminium oxide layer has very good corrosion resistance, mechanical resistance and hardness just next to diamond's. At this anodization procedure in sulphuric acid, the concentration of the acid used is commonly in range of 10 to 20 %, electrolyte temperature is between 18 and 21 °C, electrical current by anode square area is from 1.0 to 1.5 A/dm², electrical voltage varies from 10 to 30 V and time duration is calculated in minutes or read from the diagram. These parameters are defined by experience. At the start of anodization procedure, thin barrier oxide layer forms as well as hexagonal porous layer. Obtained aluminium oxide layer has ceramic characteristics; it is a good electrical isolator.

Aluminium oxide layer inserts in the aluminium and aluminium alloys samples surface with 2/3 of its height, which forms a very good bond and adhesion between them. Therefore, it is important to take dimensions of finished aluminium and aluminium samples into consideration, having in mind that their dimensions increase by 1/3 of the aluminium oxide layer height

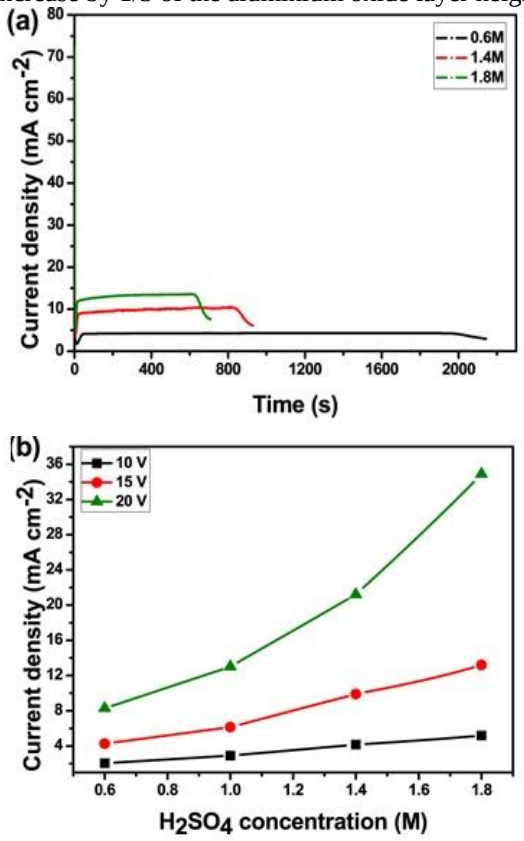

Figure 9. Aluminium and aluminium alloys anodization time duration, sulphuric acid concentration and electrical current by anode square area display due to the needed electrical voltage [12]

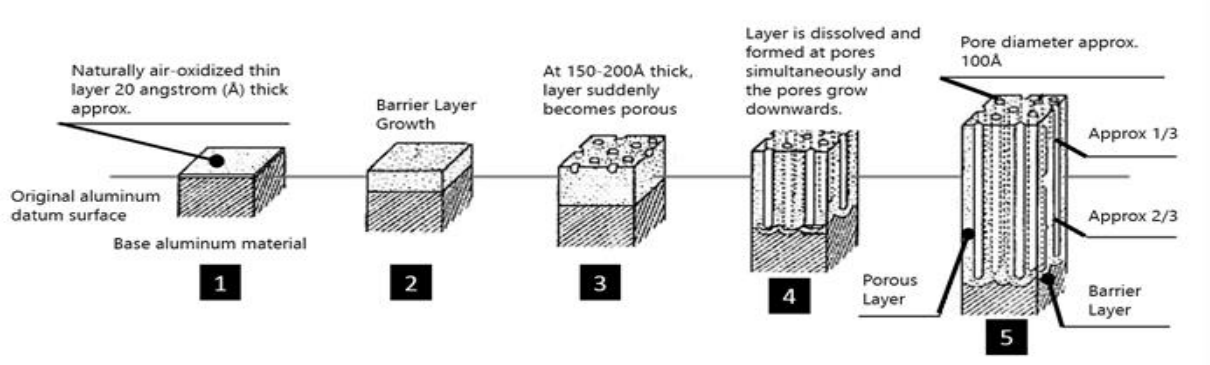

Figure 10. Aluminium oxide layer forming chronology [13]

Porosities are to be closed in sealing procedure or by introducing dyeing procedure instead. The obtained aluminium oxide layer is very pliable for dyeing due to the very highly developed porosities.

2.7.4 Anodization in sulphuric acid – hard anodization

Hard anodization procedure in sulphuric acid (H_2SO_4) (Type III) provides aluminium oxide layer of height between 50 to 100 μm. Obtained oxide layer has very good corrosion and mechanical resistance with hardness from 50 to 70 HR_C. This procedure is suitable for dynamically loaded mechanical parts like sliding rails, gears, revolving joints and pistons, due to their exposure to significant mechanical wear. Obtained aluminium oxide layer has ceramic characteristics; it is a good electrical isolator. For this type of anodization procedure, acid concentration vary from 10 to 20%, electrolyte

temperature goes from 0 to 10°C, direct electrical current by anode square area varies from 2.5 to 3.5 A/dm², electrical voltage is above 100 V and time duration is calculated in minutes or read from the diagram. These parameters are also defined by experience. Aluminium alloys suitable for this type of anodization are from 5000 and 6000 series. Aluminium oxide layer inserts in the aluminium and aluminium alloys samples surface with 1/2 of its height, which forms a very good bond and adhesion between them. Therefore, it is important to take dimensions of finished aluminium and aluminium samples into consideration, having in mind that their dimensions increase by 1/2 of the aluminium oxide layer height. In most cases, porosities are not sealed, due to the excellent corrosion resistance of the obtained aluminium oxide layer height.

2.7.5 Anodization in oxalic acid

The anodization procedure in organic oxalic acid ($H_2C_2O_4$) (Type IC), gives an aluminium oxide layer height up to 50 μm. Obtained oxide layer has very good mechanical resistance with excellent hardness but, unfortunately, weaker corrosion resistance. Obtained aluminium oxide layer has ceramic characteristics; it is a good electrical isolator. For this type of anodization procedure, acid concentration is at 20% range, electrolyte temperature goes from 15 to 35°C, direct electrical current by anode square area varies from 1 to 3 A/dm², electrical voltage is from 30 to 50 V and time duration is calculated in minutes or read from the diagram. It is important to take dimensions of finished aluminium and aluminium samples into consideration, having in mind that their dimensions increase by 1/2 of the aluminium oxide layer height.

2.8 Dyeing

The most common color shades in use are the ones from "EURAS Colour Code" color palette standard. Few other commercial color standards in use are from SANDALOR and SCHÜCO. For aluminium and aluminium alloys samples to be properly colored, oxide layer must be at least 10 μm high. The color deposits at the bottom of the porous layer of the aluminium oxide, after the pores are closed by sealing process and eventually protected from environmental influences. Dyeing procedure is used with coloring bath temperature range between 65 and 75 °C and time duration between 10 and 30 minutes. Metal oxide based colors are in use which are deposited at the bottom of the porous aluminium oxide walls, by the use of electrolytic process in proper baths.

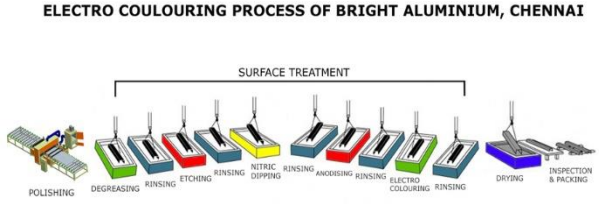

Figure 11. Anodization process chronology with dyeing procedure [14]

2.9 Sealing

Sealing process is used for the purpose of closing of the porous aluminium oxide layer thus increasing corrosion resistance. It is done in two ways; by "warm" or "cold" sealing procedure. "Warm" sealing procedure (hydration sealing) is conducted in demineralized water at boiling temperature, with time duration between 30 and 60 minutes, depending on the height of obtained aluminium oxide layer. This procedure forms "boehmite" ($Al_2O_3H_2O$) at the surface of oxide layer, due to the reaction of aluminium oxide layer (Al_2O_3) and water (H_2O), with ratio of oxide layer 83 % and water 17% and pH values of sealing bath between 5.5 and 6.5. Boehmite layer forms by chemical reaction as follows (9);

$$Al_2O_3 + H_2O \rightarrow 2AlO \cdot OH \qquad (9)$$

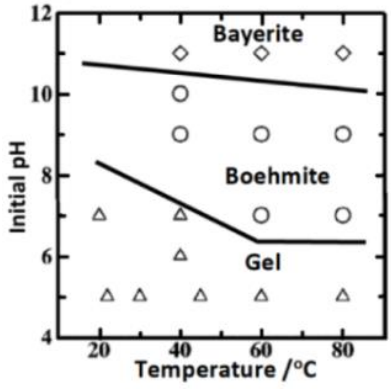

Figure 12. Boehmite formation diagram [15]

Figure 13. Boehmite structure image [16]

Boehmite layer is hard, vitreous layer that has greater volume then aluminium oxide layer; it physically seals (fills) the pores, thus increases the resistance of the layer to corrosion and wear. The "cold" procedure (cold sealing) is conducted in demineralized water, with the addition of 5 to 6 g/l of nical-fluoride at room temperature, with time duration between 20 and 30 minutes. pH values of the bath vary from 5.5 and 6.5. The

procedure is economically acceptable due to the lower bath temperatures, thus more suitable for sealing the samples which are colored. During the conduction of sealing procedure, it is preferable to use inhibitors (acetates, chromates, molybdates), which improve corrosion resistance.

2.10 Drying

Drying procedure is conducted for the purpose of maturation of sealing procedure. It is conducted in natural air, at room temperature with time duration of 48 hours. During drying procedure, samples should not be wrapped up or covered. Ideally, samples should not be removed from suspenders used during anodization procedure, therefore set to drying for 48 hours at anodizing plant.

3. Discussion

Important properties of obtained aluminium oxide layer are corrosion and mechanical resistance, thus resistance to wear due to the hardness of porous oxide layer, where porosity itself enables coloring or good adhesion for gluing. Another important property is dielectricity where the aluminium oxide behaves as an isolator and does not conduct electrical energy. Very important property of the obtained aluminium oxide is its passivity and the fact that it is environmentally friendly. Pourbaix diagram (generally known as the diagram of potential towards pH values), gives an insight in area of acidic and alkalic corrosion therefore passivity of certain metal at room temperature, where the corrosion of metal in electrolytic liquids is surveyed [17]. Aluminium and aluminium alloys are passive in pH range from 4 to 9, at potential from -2 to1, in humid atmosphere, in tap and saltwater and in majority of aerated electrolytes like rain, snow and ice.

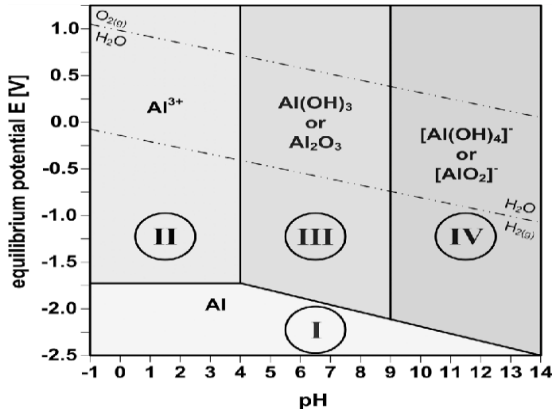

Figure 14. Pourbaix diagram for pure aluminium at 25 °C [18]

Characteristic areas shown on Figure 14, are:

i. area of general immunity
ii. area of acidic corrosion
iii. passive area
iv. area of alkalic corrosion

_.._.._.._ water stability border (H_2O)

Considering the fact that Pourbaix diagram shows an empiric area of corrosion for pure aluminium, corrosion values must be measured for each aluminium alloy combination, in order to obtain the area of immunity at requested polarities and pH values tested by Sukiman et al. [19]. Porous aluminium oxide layer is suitable for coloring procedures, where (considering the applied color), different color tones and shades can be obtained on sample surfaces made from aluminium and aluminium alloys. Obtained colors are resistant to bleaching, outer atmosphere influences and ultra-violet radiation. The height of the obtained aluminium oxide layer can be controlled, so the needed tolerance fields can be acquired.

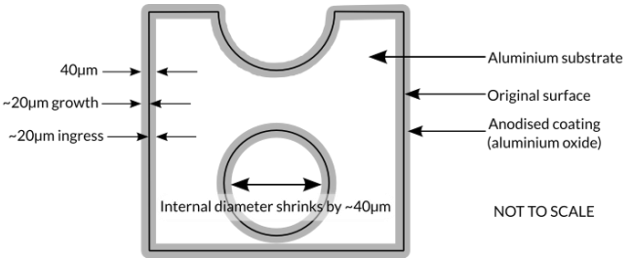

Figure 15. Sample dimensions enlargement due to the use of anodization process [20]

Aluminium oxide layer has good resistance to acids, but not to alkalic atmosphere. While using it in civil engineering, it should be protected from lime influences, because it causes permanent damage to the oxide layer which is hardly corrected. It is possible to gain excellent adhesion properties which enable better glue and coating adhesion as well as welding. Due to the good bond between aluminium substrate and aluminium oxide layer, samples made from aluminium and aluminium alloys are resistant to outer abrasion influences. Their commercial use today is literally limitless:

- various supporting structures in mechanical and civil engineering,
- profiles and walls manufacturing for civil engineering fittings and decorative panels,
- parts for engines with internal combustion, car chassis and rims, bicycle frames,
- outer and internal panels for aeronautical and space industry,
- in naval architecture for vessels hull and superstructure manufacturing,
- household appliances, commercial and industrial mirror manufacturing, scientific telescope mirrors production,
- electrical and electronical parts and components,
- various furniture accessories,

- equipment for food industry; food storage and consuming manufacturing, food and industrial foil production,
- jewellery manufacturing and medicament additives.

4. Conclusion

The main advantage of anodization procedure reflects in obtained aluminium oxide layer that carries very low maintenance demands. It is passive; it does not have any impact to health and environment and does not generate any notable corrosion. The anodization procedure does not produce CO_2 emissions or any solvents. Obtained aluminium oxide layer is permanently bonded with aluminium substrate, on which it evenly forms whether on straight or curved areas or sharp edges, and has uniformed final surface texture. It has great mechanical resistance and does not change its properties through time, like surface coatings do. Aluminium oxide is impermeable, therefore resistant to the majority of chemical influences; moreover gains very good corrosion resistance in humid, sea, industrial and urban atmospheres which are saturated with chlorides and sulphur. It is an isolator, so it does not conduct electrical energy. While being welded, the colors are resistant to all outer influences. 100% recycling is enabled by remelting or pressing. It enables quality control by on-the-spot check, which is done without damaging the oxide layer. For example, quality control can be conducted in chemical laboratory at anodizing plant FEAL Siroki Brijeg (Bosnia and Herzegovina), with the use of specific technologies in order to guarantee the required properties of the final product and treated surfaces. Besides measuring all required parameters of the aluminium profiles anodization procedure, the laboratory also conducts testing of colored aluminium profiles. For the anode layer height measuring, an instrument with eddy current technology is introduced, Fischer DualScope MPOR, that enables measuring height/width of the layers up to 200 μm.

Figure 16. Eddy current hight/width measuring gauge [21]

For conductivity measurements, a WTW Cond 315i instrument is introduced, which enables measuring bath conductivities in micro Siemens by centimeters (μS/cm). For pH measurements, a WTW pH3110 instrument is used, which enables measurements of baths pH values.

REFERENCES

[1] Cmak, https://www.cmak.com/en/cranes/customcranes-special-cranes-and-applications/

[2] Kulkarni M., Mazare A., Schmuki P., Iglic A., (2016), *Influence of anodization parameters on morphology of TiO_2 nanostructured surfaces*, Advanced Materials Letters 7, No 1., p 23-28.

[3] Alumeco, https://www.alumeco.com/knowledgetechnique/surface-treatment/anodising

[4] Lotusproactive, lotusproactive.wordpress.com/2013/11/11/structural-aluminium-anodising/

[5] Ohgai T., (2012), *Magnetoresistance of Nanowires Electrodeposited into Anodized Aluminium Oxide Nanochannels*, Open Acess peer-reviewed chapter

[6] Quora, https://www.quora.com/What-is-the-process-of anodizing

[7] Researchgate https://www.researchgate.net/figure/Schematic-diagram-of-the-anodising-bath_fig1_262993427

[8] Omwcorp http://www.omwcorp.com/understanding-and specifying-anodizing-2/

[9] Lee W., (2010), *The Anodization of Aluminum for Nanotechnology Applications*, The Journal of The Minerals, Metals & Materials Society 62, p 57- 63.

[10] Redkin A., Apisarov A., Dedyukhin A., Kovrov V., Zaikov Y., Tkacheva O., Hryn J., (2012), *Recent Developments in Low-Temperature Electrolysis of Aluminium*, ECS Transactions 50, No. 11.

[11] Lin Y., Lin Q., Liu X., Gao Y., He J., Wang W., Fan Z., (2015), *A Highly Controllable Electrochemical Anodization Process to Fabricate Porous Anodic Aluminum Oxide Membranes*, Nanoscale Research Letters 10, Article number: 495.

[12] Abd-Elnaiem A., Abbady G., Ali D., Asafa T. B., (2019), *Influence of anodizing voltage and electrolyte concentration on Al-1wt %Si thin films anodized in H_2SO_4*, Materials Research Express 6, No. 8, IOP Publishing Ltd.

[13] Anoplate https://www.anoplate.com/news-and-events/the- impact-of-anodize-on-dimensions/

[14] Brightanodising http://brightanodising.com/

[15] Mdpi https://www.mdpi.com/20796412/10/3/226/htm

[16] Rruff https://rruff.info/Boehmite/R120123

[17] Pourbaix M., (1974), *Atlas of Electrochemical Equilibria in - Aqueous Solutions*, Printed by National association of corrosion engineers, Houston, Texas, USA.

[18] Kaminski N., Zorn C., (2015), *Temperature-humidity-bias testing on insulated-gate bipolartransistor modules-failure modes and acceleration due to high voltage*, IET Power Electronics 8.

[19] Sukiman N. L., Zhou X., Birbilis N., Hughes A. E., Mol J. M. C., Garcia S. J., Zhou X., Thompson G. E., (2012), *Durability and Corrosion of Aluminium and Its Alloys: Overview, Property Space, Techniques and Developments*, Open acess peer-reviewed chapter.

[20] Metalfinishing https://metalfinishingsltd.co.uk/articles/anodising-dimensions/

[21] Personal photo database

ISSN 1847-7917

Human-centric approach of the Lean management as an enabler of Industry 5.0 in SMEs

Marko MLADINEO[1)]***, Marijan ĆUBIĆ***[1)]***, Nikola GJELDUM***[1)] ***and Marina CRNJAC ŽIŽIĆ***[1)]

1) University of Split, Faculty of Electrical Engineering, Mechanical Engineering and Naval Architecture, R. Boskovica 32, 21000 Split, **Croatia**

mmladine@fesb.hr
marijancubic00@gmail.com
ngjeldum@fesb.hr
mcrnjac@fesb.hr

Keywords

Industry 5.0
Lean management
Industry 4.0
Sustainability

Original scientific paper

Abstract: From the very beginning, Industry 4.0 was seen as evolution, more than revolution. So, there is nothing strange about first drafts of Industry 5.0, which are published about 10 years after the first draft of Industry 4.0. Very significant is the European Commission's document about Industry 5.0 which promotes sustainable, human-centric and resilient European industry. The European draft of Industry 5.0 is very much affected by the COVID-19 crisis. It is one of the reasons why human-centric aspect is much more important in the Industry 5.0 than in Industry 4.0. However, there are many open questions and challenges how to implement all these ideas about sustainability, human-centricity and resilience. On the other hand, there is a 40-year-old proven methodology for organization and process improvements based on the human-centric approach – the Lean management. The Lean is based on philosophy of the worker's engagement in process improvement, therefore it seems to be suitable philosophy for human-centricity of Industry 5.0. Particularly for Small and Medium-sized Enterprises (SMEs) who are always struggling to adopt new industrial concepts. In this paper, the key success factors for Lean implementation into SME are selected based on the review of large number of studies, analysis and reviews. These factors are then put in the context of Industry 5.0 to explore the possibilities of Lean managements as an enabler of Industry 5.0.

1. Introduction

1.1. Industry 4.0

In the last 10 years, the further development of the idea and possibilities to integrate Information and Communication Technology (ICT) and the Industrial Internet of Things (IIoT) into production systems [1] introduced some new terms in operations management: Industry 4.0 [2], Smart Factory [3] & Cyber-Physical Production System [4]. For a quick distinction of the plethora of different terminology, a commonly agreed description is as it follows: The technology base making use of ICT is named IIoT. A production system making use of an IIoT technology base may be described as a Cyber-Physical Production System (CPPS), which in an ultimate vision may represent a full integration of value-driving strategies: the Smart Factory. Industry 4.0, however, describes the economic impact of the previously described approaches. As this set of definitions does not follow an official agreement, the notions are occasionally used synonymously.

The term Industry 4.0 was first described in Germany in 2011 [1]. It is used as a synonym for the 4th industrial revolution, which is triggered by the introduction of ICT into production systems. The first three industrial revolutions came about as a result of mechanization through steam-powered machines (1st industrial revolution), mass production based on electrical production lines (2nd industrial revolution), and automation based on microcontrollers and IT (3rd industrial revolution). Industry 4.0 as a new industrial platform is based on the Smart Factory concept [1]: Manufacturing systems are vertically connected to business processes within companies, as well as horizontally embedded in distributed value-adding networks that can be managed in real time. Smart Factories allow individual customer requirements to be met and mean that even one-off items can be manufactured profitably. Hence, the main features of Smart Factory can be summarized into the following: Smart personalized products (with the support of Cyber-Physical Production System [4]), Product and service provider (product and service integrated into single product [5], or manufacturing service provider [6]), and High level of collaboration (collaborative manufacturing [7] and all other value adding processes through production networks [8]).

Furthermore, one of the key elements of Industry 4.0 is Cyber-Physical Production System with following advantages and challenges ([1], [3] and [9]):

- *Smart products* – product which fits the customer's exact needs and which is uniquely identifiable, may be located at all times and knows

its own history, current status and alternative routes to achieving customer.
- *Single-item production* – CPPS should help plan and control of the single-item products, and make it as much economical as serial mass production.
- *Production without rigid plans* – CPPS should manage production without rigid plans, since it is needs to manage production of single-item products.
- *Energy-efficiency* – CPPS represents a backbone for more energy-efficient manufacturing and decisions that results with environmental-friendly solutions.
- *Cyber Security* – CPPS and its computer cloud should be more secure from hacker attacks than IT systems of today, since it is a most weak point of the CPPS.
- *Production networks* – collaborative product development, collaborative manufacturing and all other value adding processes supported by mutually networked CPPSs.

1.2. Industry 5.0

Although the new industrial platform – Industry 4.0 – had a significant impact on research community and became one of the most trending topics in last 5 years, the COVID-19 pandemic caused the breaking of global value chains and forced the rethinking of the world manufacturing paradigms [10]. The resilience of the manufacturing system with people as it most valuable, yet very vulnerable part, became important focuses of the new paradigms. In 2020, European Commission's workshop on Industry 4.0 and its new challenges [11], has resulted with completely new paradigm [12]: "Industry 5.0 – Towards a sustainable, human-centric and resilient European industry".

From the very beginning, Industry 4.0 was seen as evolution, more than revolution. So, this change toward Industry 5.0 was expected in the near future, but, due to COVID-19 pandemic, it came sooner. The main change in Industry 5.0 is the focus on its three core elements presented in Figure 1.

Figure 1. Industry 5.0 with three core elements [12]

These core elements should re-found and widen purposefulness of industry, beyond producing goods and services for profit, through [12]:
- *Human-centric approach* – putting human needs and interests at the heart of production process, by sub-ordering and adapting technology to humans, not vice versa.
- *Sustainability* – development of circular processes that re-use, re-purpose and recycle natural resources, to ensure the needs of today's generation, without jeopardizing the needs of future generations.
- *Resilience* – development of higher degree of robustness in industrial production to become resilient for disruptions in global value and supply chains.

It is important to note that Industry 5.0 is the evolution of Industry 4.0. At the beginning, the idea was to have some kind of a "patch" for Industry 4.0 called "Industry 4.1" or similar [11]. The aim was to address some issues like the problem of techno-centric approach of Industry 4.0, concern about the future of shop-floor workers with further automation, etc. However, COVID-19 pandemic occurred and the "patch" grew into the "upgrade" of European industrial paradigm. With Industry 5.0, the industry is seen not just as another sector in economy, but it is seen as a power able to achieve societal goals beyond jobs and growth, to become a resilient provider of prosperity [11].

The Industry 5.0 with its three core elements opens enormous research perspective, and that is the one of its ideas: to promote research and innovation. In this paper, the focus is limited on research about using proven human-centric methodologies, like Lean management, as an enabler of Industry 5.0 in SMEs.

1.3. Lean management

For more than 40 years, Lean management (also known as Lean production, Lean thinking, Lean philosophy, or, simply, Lean) has been on the scene, making all other business improvement approaches outlasted and becoming the most successful approach to business improvement [13]. Lean was born in Toyota in Japan in 1970s and 1980s, but it become world-wide known in 1990s [15].

Lean represents a complete system for management, production planning and control, and continuous improvement of the business processes and whole organization. So, it is clear that Lean is more than a set of methods or toolbox, it is a philosophy and a way of thinking [14]. The main aspects on which Lean focuses are customer, value stream, continuous improvement, and employees' education. Therefore, Lean philosophy is reflected within:

1) System thinking;
2) Value for the customer;
3) Waste elimination;
4) Lead time reduction;

5) Respect for people;
6) Continuous improvement.

Lean is seen as a continuous improvement approach that has spread across almost all type of industries and businesses [16]. But, there is no universal approach, or the best way, to implement Lean [14]. Each enterprise needs to find its own way on a journey toward Lean organization. A whole set of Lean tools and methods are available as a support on that journey.

Although there are many Lean principles, methods and tools, some of them become unavoidable terms in operations management: Just-In-Time, Value Stream Mapping, Kaizen, Jidoka, 5S, etc. Interesting fact is that many of these Lean tools use only pencil and A3 sheet of paper to identify problems and design improvements, and that is the one of the main advantages of Lean approach.

Since Lean is focused on process identification, process measuring and improvement, it is seen by many researchers as a kind of pre-requisition for Industry 4.0 ([17] and [18]). Because, it is not possible to "digitalize" production process without knowing it and measuring it.

Furthermore, Lean has a human-centric approach that puts people in the center of the model, as it can be seen on the well-known model of Toyota Production System (Figure 2) and on HR-ISE (Croatian model of Innovative Smart Enterprise [19]) model (Figure 3).

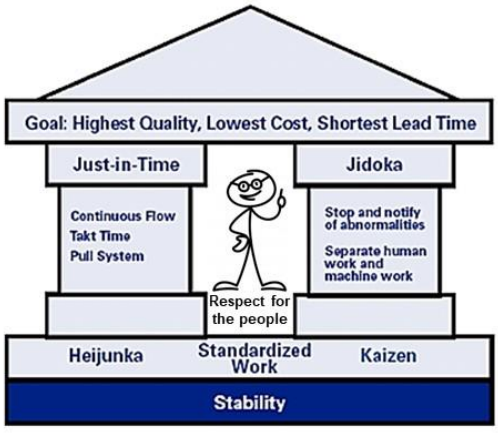

Figure 2. People in the center of model of Toyota Production System

This human-centric approach of the Lean management, i.e. its philosophy of the people engagement in process improvement from shop-floor workers to managers, seems like an excellent perspective for human-centricity of Industry 5.0. This fact has been taken for a base of this research.

Figure 3. People in the center of HR-ISE model – Croatian model of Innovative Smart Enterprise [19]

2. Key success factors of Lean implementation in SMEs

2.1. Methodology

SMEs do not acquire new cutting-edge technologies and modern organizational approaches with ease [20]. Very often, SMEs are hesitators [20], so both, Industry 4.0 and Lean management, are not easily accepted by them.

The problem is that implementation of new technology or organizational approach has exploration phase in which the benefits are not so visible [21]. The enterprise needs to force the implementation until the exploitation phase with high benefits occur [21], but it is not an easy task.

Therefore, a review of large number of studies, analysis and reviews (35 in total) has been made to identify key success factors of Lean implementation is SMEs (Table 1). Most of them are scientific papers, but there are also professional reports and white papers. The focus has been put on key success factors of Lean implementation, but the usage of the Lean tools in SMEs has been investigated as well.

Table 1. Studies, analysis and reviews of key success factors of Lean management and Lean tools implementations in SMEs

No.	*Study / Analysis / Review*	*Key success factors*	*Lean tools*
1)	Achanga P., Essam S., Roy R., Nelder G. (2006). Critical success factors for lean implementation within SMEs. Journal of Manufacturing Technology Management 17 (4).	X	
2)	Hu Q., Mason R., Williams S.J., Found P. (2015). Lean implementation within SMEs: A literature review. Journal of Manufacturing Technology Management 26 (7).	X	

No.	*Study / Analysis / Review*	*Key success factors*	*Lean tools*
3)	Rose A.M.N., Deros B.Md., Rahman M.N.Ab., Nordin, N. (2011). Lean manufacturing best practices in SMEs. Proceedings of the 2011 International Conference on Industrial Engineering and Operations Management, Kuala Lumpur, Malaysia.	X	X
4)	Bakås O., Govaert T., Van Landeghem H. (2011). Challenges and success factors for implementation of Lean manufacturing in european SMEs. MITIP 2011 - Norwegian University of Science and Technology, Trondheim, Norway.	X	
5)	Pearce A., Pons D., Neitzert T. (2018). Implementing lean - Outcomes from SME case studies. Operations Research Perspectives 5.	X	X
6)	AlManei M., Salonitis K., Xu, Y. (2017). Lean Implementation Frameworks: The Challenges for SMEs. Procedia CIRP 63.	X	
7)	Antosz K., Stadnicka D. (2017). Lean Philosophy Implementation in SMEs – Study Results. Procedia Engineering 182.	X	X
8)	Ulewicz R., Kucęba R. (2016). Identification of problems of implementation of Lean concept in the SME sector. Engineering Management in Production and Services 8 (1).	X	
9)	Mirzaei P. (2011). Lean production: introduction and implementation barriers with SMEs in Sweden. Master Thesis, Jönköping University, Sweden.	X	
10)	Kundu G., Manohar B.M. (2012). Critical success factors for implementing lean practices in IT support services. International Journal for Quality research 6 (4).	X	
11)	Noori B. (2015). The critical success factors for successful lean implementation in hospitals. International Journal of Productivity and Quality Management 15 (1).	X	
12)	Seppänen O., González V.A., Arroyo P. (2015). Global Problems - Global Solutions. IGLC 2015, Perth, Australia.	X	
13)	Ainul Azyan Z.H., Pulakanam V., Pons D.J. (2017). Success factors and barriers to implementing lean in the printing industry: A case study and theoretical framework. Journal of Manufacturing Technology Management 28.	X	X
14)	Vermaak T.D. (2008). Critical Success Factors for the Implementation of Lean Thinking in South African Manufacturing Organizations. Doctoral Thesis, South Africa.	X	
15)	Knol W.H., Slomp J., Schouteten R.L.J., Lauche K. (2018). Implementing lean practices in manufacturing SMEs: testing 'critical success factors' using Necessary Condition Analysis. International Journal of Production Research 56 (11).	X	
16)	Alhuraish I., Robledo C., Kobi A. (2014). Key Success Factors of Implementing Lean Manufacturing and Six Sigma. Excellence in Services, Liverpool, UK.	X	
17)	Ward S.A. (2015). Critical Success Factors for Lean Construction Intervention. Doctoral Thesis, University of Dundee, UK.	X	
18)	Belhadi A., Touriki F.E., El Fezazi S. 2016. A Framework for Effective Implementation of Lean Production in Small and Medium-Sized Enterprises. Journal of Industrial Engineering and Management 9 (3).	X	X
19)	Alefari M., Salonitis K., Xu Y. (2017). The Role of Leadership in Implementing Lean Manufacturing. Procedia CIRP 63.	X	
20)	Desai T.N. (2016). Review of lean manufacturing practices – critical success factors and performance measures for SMEs. International Journal of Quality and Innovation 3 (1).	X	
21)	Krichbaum B.D. (2007). Lean Success Factors: 10 Lessons from Lean: White paper, Process Coaching Inc., USA.	X	
22)	Nasrollahzadeh T., Marsono A.K., Masine, M. (2016). Critical Success Factor for Industrialized Building System Process ProtocolMap by Lean Construction management. Journal of Civil and Environmental Engineering 2016.	X	
23)	Minh N., Nguyên N., Tuấn, L. (2015). Framework of Critical Success Factors for Lean Implementation in Vietnam Manufacturing Enterprises. VNU Journal Of Science: Economics And Business, 31 (5E).	X	
24)	Kobus J., Westner M., Strahringer S., Strode D. (2018). Lean Management in IT Organizations: A Ranking-type Delphi Study of Implementation Success Factors. JITTA 19.	X	
25)	Chelangat B. (2016). Critical Success Factors (CSFs) For Implementation of Lean Six Sigma in Commercial Banks in Kenya. IOSR Journal of Business and Management 18 (12).	X	
26)	Albliwi S., Antony J. (2013). Implementation of a lean six sigma approach in the manufacturing sector: a systematic literature review. Proceedings of the 11th International Conference on Manufacturing Research, Cranfield University, UK.	X	
27)	Maleyeff J. (2007). Improving Service Delivery in Government with Lean Six Sigma. Report, IBM Center for The Business of Government, USA.	X	
28)	Salonitis K., Tsinopoulos C. (2016). Drivers and Barriers of Lean Implementation in the Greek Manufacturing Sector. Procedia CIRP 57.	X	X
29)	Sieckmann F., Ngoc H.N., Helm R., Kohl H. (2018). Implementation of lean production systems in small and medium-sized pharmaceutical enterprises. Procedia Manufacturing 21.	X	

No.	*Study / Analysis / Review*	*Key success factors*	*Lean tools*
30)	Baviskar P. (2015). Critical Success Factors For Effective Implementation Of Lean Assessment Tools/ Framework In Manufacturing Industries. Master Thesis, KTH, School of Industrial Engineering and Management, Sweden.	X	
31)	Mishra R.P, Chakraborty A. (2014). Strengths, weaknesses, opportunities and threats analysis of lean implementation frameworks. International Journal of Lean Enterprise Research 1 (2).	X	
32)	Kumar M., Antony J., Singh R.K., Tiwari M.K., Perry D. (2006). Implementing the Lean Sigma framework in an Indian SME: a case study. The Management of Operations 17 (4).		X
33)	Saboo A., Garza-Reyes J.A., Er A., Kumar V. (2014). A VSM improvement-based approach for lean operations in an Indian manufacturing SME. International Journal of Lean Enterprise Research 1 (1).		X
34)	Miina A. (2013). Critical Success Factors of Lean Thinking Implementation in Estonian Manufacturing Companies. Doctoral Thesis, Tallinn University of Technology, Estonia.		X
35)	Matt D.T., Rauch E. (2013). Implementation of Lean Production in small sized Enterprises. Procedia CIRP 12.		X

The data used in this research is gathered from 35 sources (Table 1) of which 31 have identified key success factors of Lean implementation and 10 have identified usage of Lean tools in SMEs. The most common success factors with their importance, and the most common Lean tools have been identified.

2.2. Results

The distribution of most important success factors for Lean implementation in SMEs is presented in Figure 4. The data are from 31 different sources involving several hundred SMEs from all around world.

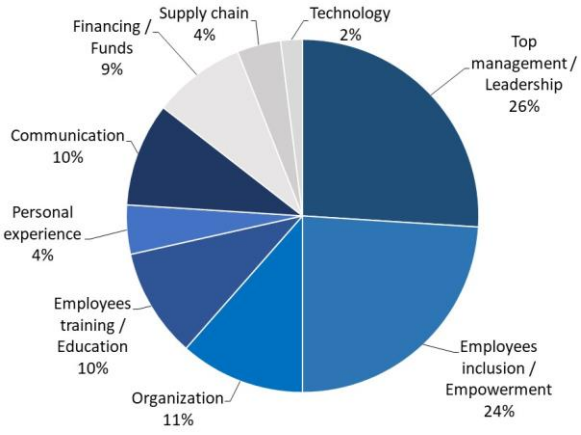

Figure 4. Key success factors of Lean implementation in SMEs and their relative importance

Most of the analyzed researches have evaluated the importance of each success factor, and for the rest of the researches the importance was approximated. Therefore the relative importance represents mean value of 31 inputs. The analysis has shown:

- *Most of the factors are related to people*: Top management / Leadership, Employees inclusion / Empowerment, Organization, Employees training / Education, Personal experience, and Communication. In total, they count for 6 out of 9 key success factors, but they also count for 85% of importance for success!
- *The remaining factors are*: Financing / Funds, Supply chain, and Technology. In total, they count for 3 out of 9 key success factors, but they also count for only 15% of importance for success.

The results are very intriguing, because SMEs are usually not satisfied with their technology level and insufficient funds, but in the case of Lean management, these factors are not important.

Regarding the most common Lean tools in SMEs, the data from 10 different sources, involving dozens of SMEs, have shown what Lean tools are most often implemented in SME (Figure 5).

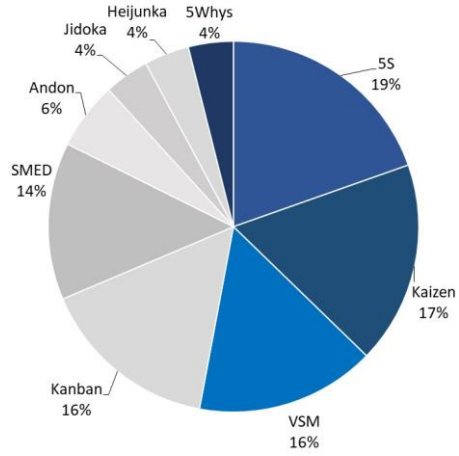

Figure 5. The most common Lean tools implemented in SMEs

Again, the most common tools are people oriented: 5S, Kaizen, VSM, and 5Whys. They count for 4 out of 9 most common tools, but they also count for 56% of the most common tools. Other tools (Kanban, SMED, Andon, Jidoka, and Heijunka), beside employees engagment, also require the purchase of some equipment or tehncology. While 4 most common tools require nothing but a pencil and A3 sheet of paper to identify problems and design improvements.

3. Discussion on Lean as Industry 5.0 enabler

Although the process awareness of the Lean management was seen as a kind of pre-requisition for Industry 4.0, the interest for Lean and organizational changes was

overtaken by the technology-push strategy of the Industry 4.0. However, with Industry 5.0 the human-centric approach is restored with important premise [12]: "rather than asking what we can do with new technology, we ask what the technology can do for us".

Therefore, the Lean management can be seen as one of the enablers of Industry 5.0. First of all, the Lean philosophy has a human-centric approach which cares not just about employees, but also about customers. Second, the Lean approaches are the system thinking and the lead time reduction, which can result with more resilient production process and supply chain which is capable to sustain different kind of crisis. At last, the Lean aims are waste elimination (no over production, scrap reduction, etc) and continuous improvement of the processes, which ultimately lead toward sustainable production without threatening the environment and socio-economic stability. This relationship between Lean and Industry 5.0 has been presented in Figure 6, as a proposal and conclusion of this research.

Figure 6. The relationship between Industry 5.0 and Lean philosophy with identified key success factors of Lean implementation in SMEs

4. Conclusion

This research has shown that a 40-year-old proven methodology for organization and process improvements based on the human-centric approach – the Lean management – shows potential to be one of enablers of the Industry 5.0 in SMEs. The analysis of key success factors of Lean management and Lean tools implementations in SMEs has shown that most of the success factors and tools are people oriented, thus giving the human-centric approach to the organizational and process improvement, as required by Industry 5.0.

REFERENCES

[1] Kagermann H., Wahlster W., Helbig J., (2013), *Recommendations for implementing the strategic initiative INDUSTRIE 4.0*. Heilmeyer und Sernau, Germany

[2] McKinsey & Co., (2015), *Industry 4.0 – How to navigate digitization of the manufacturing sector*. Digital McKinsey, USA

[3] Zühlke D., (2010), *SmartFactory - Towards a Factory-of-Things*. IFAC annual Reviews in control, p 129- 138.

[4] Monostori L., (2014), *Cyber-physical Production Systems: Roots, Expectations and R&D Challenges*. Procedia CIRP 17, p 9-13.

[5] Meier H., Roy R., Seliger G., (2010), *Industrial Product-Service Systems - IPS2*. CIRP Annals – Manufacturing Technology 59, p 607-627.

[6] Meier M., Seidelmann J., Mezgár I., (2010), *ManuCloud: The Next-Generation Manufacturing as a Service Environment*. ERCIM News 83, p 33-35.

[7] Mourtzis D., (2010), *Internet Based Collaboration in the Manufacturing Supply Chain*. 43rd CIRP Conference on Manufacturing Systems - Conference Proceedings, Vienna, Austria

[8] Veza I., Mladineo M., Gjeldum, N., (2015), *Managing innovative production network of smart factories*. IFAC-PapersOnLine 48(3), p 555-560.

[9] Mladineo M., (2020), *Production Networks meet Industry 4.0*. GRIN Publishing, Germany

[10] World Manufacturing Foundation, (2020), *Back to the Future: Manufacturing beyond COVID-19*. World Manufacturing Forum 2020, Cernobbio, Italy.

[11] European Commission – Directorate-General for Research and Innovation, (2020), *Enabling Technologies for Industry 5.0 – Results of a workshop with Europe's technology leaders*. Publications Office of the European Union, Luxembourg.

[12] European Commission – Directorate-General for Research and Innovation, (2021), *Industry 5.0 – Towards a sustainable, human-centric and resilient European industry*. Publications Office of the European Union, Luxembourg.

[13] Jones D.T., Womack J.P., (2017), *The Evolution of Lean Thinking and Practice*. The Routledge Companion to Lean Management, Routledge, USA.

[14] Liker J.K., (2017), *The Toyota Way: Striving for Excellence*. The Routledge Companion to Lean Management, Routledge, USA.

[15] Womack J.P., Jones D.T., (1996), *Lean Thinking: Banish Waste and Create Wealth in your Corporation*. Simon and Schuster, USA.

[16] Netland T.H., Powell, D.J., (2017), *A Lean World*. The Routledge Companion to Lean Management, Routledge, USA.

[17] Gallo T., Cagnetti C., Silvestri C., Ruggieri A., (2021), *Industry 4.0 tools in lean production: A systematic literature review*. Procedia Computer Science 180, p 394-403.

[18] Veza I., Mladineo M., Gjeldum N., (2016), *Selection of the basic lean tools for development of Croatian model of Innovative Smart Enterprise*. Tehnički vjesnik 23, No. 5, p 1317-1324.

[19] Veza I., Crnjac M., Mladineo M., (2018), *The Croatian model of Innovative Smart Enterprise for different sizes of enterprise*. Proceedings of AMME-18, Cairo, Egypt.

[20] Zadra R. (2020), *Digital transformation and Manufacturing 4.0*. WMF 2020, Cernobbio, Italy.

[21] Netland T., Ferdows K., (2016), *The S-curve effect of lean implementation*. Production and Operations Management 25, No. 6, p 1106-1120.

ISSN 1847-7917

Basic advantages of thin-sheet AA5056 alloy joints produced by friction stir welding

Sviatoslav MOTRUNICH[1)], ***Anatoliy POKLATSKY***[1)], ***Ilya KLOCHKOV***[1)] ***Massimo ROGANTE***[2)], ***Anatoliy ZAVDOVEEV***[1)]

1) Paton Electric Welding Institute of the NAS of Ukraine, 03150 Kyiv, **Ukraine**
2) Rogante Engineering Office, Contrada San Michele n. 61, I-62012 Civitanova Marche, **Italy**

avzavdoveev@gmail.com
main@roganteengineering.it

Keywords

friction stir welding
AA5056 aluminium alloy
hardness, microstructure
tensile strength, fatigue, residual stress

Original scientific paper

Abstract: Comparative studies of microstructure, degree of softening, tensile strength, tendency to nucleation and propagation of cracks and fatigue resistance, as well as investigation on the levels of longitudinal residual stresses (RS) have been performed on 1.8 mm thick AA5056 wrought aluminium alloy joints obtained by gas tungsten arc welding (GTAW) and friction stir welding (FSW). It has been shown that the use of FSW ensures the formation of an indispensable joint with a minimum level of stress concentration at the transition points from the weld to the base material and avoids defects in the joints in the form of pores, macro inclusions of the oxide film and hot cracks caused by melting and crystallization of the metal during the fusion welding. As a result of intense plastic deformation of the metal, under the tool collar and in the weld core, a uniform disoriented structure with grain sizes of 3-4 μ and dispersed (≤ 1 μ) phase precipitates is formed and grains are elongated and curved in the movement direction of the plasticized metal. As a result, the hardness of the metal in the joint zone, the tensile strength of the samples under uniaxial tension, their fatigue strength and tendency to crack nucleation and propagation increase. A decrease in the heating temperature of the welded edges provides a decrease in the maximum level of tensile longitudinal RS in welded joints by 25% in comparison with GTAW.

1. Introduction

In the manufacture of welded structures for various purposes, operated at temperatures from -190ºC to + 70ºC, semi-finished products in the form of sheets, plates, strips, extruded panels, profiles, rods, forgings, stampings, etc. from a durable and ductile wrought AA5056 aluminium alloy are widely present [1, 2]. To obtain permanent joints from this alloy, in most cases, various methods of fusion welding are used, in which the weld is formed as a result of melting of a certain amount of materials to be joined and filler wire in a common weld pool and their subsequent crystallization in shield inert gas. This leads to the formation of a cast coarse-grained structure of the weld metal and to structural changes due to high-temperature heating associated with adjacent sections. In addition, due to the melting and crystallization of metal in such welded joints, defects are quite often created in the form of pores, macro inclusions of the oxide film and hot cracks, as a result of which the properties of welded joints are reduced [3-5].

It is possible to avoid the melting of metal in the weld formation zone and to maximally preserve the properties of the semi-finished products, using the method of joining in the solid phase by FSW [6, 7]. As a result of heating the aluminium alloy due to friction in the welding zone only to a plastic state, intensive mixing, deformation in a limited volume and compaction by the working surfaces of the tool, a finely dispersed structure is formed in the seam. The main material in the heat-affected zone (HAZ), furthermore, is weakened to a lesser extent than during melting welding. Consequently, the tensile strength of such compounds under uniaxial tension and their fatigue strength under cyclic loads increase, and the levels of RS and residual strains decrease [8-14].

The purpose of this work is to determine the main advantages of butt joints of a thin-sheet wrought AA5056 aluminium alloy obtained by FSW, compared with those performed by GTAW.

2. Materials and methodology

For research, sheets of aluminium alloy AA5056 1.8 mm thick were used. Butt joints were obtained by GTAW at a speed of 20 m/h and a current of 140 A using a MW-450 installation (Fronius, Austria) and a SvAMg5 filler wire with a diameter of 1.6 mm. FSW was carried out on the laboratory installation using a special tool with a shoulder diameter of 12 mm and a conical tip with a diameter of 2.4 mm at its base [15]. The rotation speed of the tool was 1,420 rpm, and the linear displacement speed was 12 m/h. In this case, the width of the seams obtained by GTAW averaged 6.5 mm, that of FSW was 3.5 mm and the width of the thermomechanical affected zone on the front side of the seam was ≈12 mm.

Sections were made from the welded joints to study their structure and samples with a working part width of 15 mm were produced to determine their tensile strength under uniaxial tension in accordance with GOST 6996-66.

Symbols

HRB	- Brinell hardness	$R\sigma$	- asymmetry of the stress cycle
GTAW	- gas tungsten arc welding	U_i, U_p	- arc voltage in the pulse and in the pause, V
FSW	- friction stir welding		**Greek letters**
RS	- residual stress	μ	- micrometre

The width of the working part of the samples for determining the characteristics of fatigue resistance was 25 mm. The structural features of welded joints were evaluated using a standard optical electron microscope. Mechanical testing of the samples was carried out on a MTS 318.25 universal servo-hydraulic complex. Cyclic tests were carried out at axial loads along a sinusoidal cycle with a coefficient Rσ = 0.1 and a frequency of 15 Hz until the samples were completely destroyed. Under the same conditions, a series of 5-7 samples of the same type was tested. The experimental data of fatigue tests were processed by linear regression analysis methods, generally accepted for such studies. Based on the tests results for each series of samples and on the established restricted endurance limits, the corresponding fatigue curve was constructed - a regression line in the coordinates 2σa – lgN.

The hardness of the metal was measured on the front surface of the polished joints. The softening degree of the metal in the weld zone was evaluated on a ROCKWELL device at a load of P = 600 N. The fracture resistance characteristics of base material and welds of the welded joints were determined on Kahn samples with a sharp (R = 0.1 mm) notch, providing crack nucleation at a relatively low energy level, by using the RU-5 universal testing machine. The incision was positioned so that its apex coincided with the seam axis. According to the results of testing the samples with simultaneous tension and bending, diagrams of "load-deformation" were generated, which made it possible to characterize their resistance to nucleation and propagation of operational cracks [16].

Longitudinal RS in the welded joints were determined experimentally by metal cutting. Using the metal deformation value resulting from ~~its~~ cutting, and the corresponding formulas of the theory of elasticity (Hooke's law), the RS due to welding heating were determined [17].

3. Results and discussion

The studies showed that in FSW~~,~~ the size of the seam is smaller and its shape compares favourably with that obtained by GTAW. It does not have reinforcement and weld melt formed during fusion welding through the use of filler wire and of a lining with a forming groove. This can significantly reduce the level of stress concentration at the points of transition from the seam to the base material, which negatively affects the operational and resource characteristics of the joints.

In addition, the formation of a permanent connection in the solid phase without melting the welded edges avoids oxidation of the metal. Furthermore, the intense deformation and mixing of plasticized metal during the welding process contributes to the mechanical destruction and dispersion of the initial oxide film instantly formed on aluminium alloys located on them. Therefore, in the joints obtained by FSW there are no defects in the form of macro inclusions of the oxide film, which are very often formed during GTAW of aluminium-magnesium alloys (Figure 1).

Figure 1. Longitudinal fractures of the 1.8 mm thick AA5056 alloy joints obtained by FSW (a) and GTAW (b)

The absence of molten metal, in which the solubility of hydrogen increases sharply, avoids the additional saturation of the weld zone due to the migration of this gas from the adjacent surface layers of the metal. Along with intensive mixing and compaction of the weld metal in the joint zone, favourable conditions are provided for the formation of non-porous seams. Since melting and crystallization of the metal are absent during friction welding with stirring, and the seam is formed in the solid phase, it is possible to completely avoid the formation of the most dangerous and inadmissible defects for critical structures in the form of hot cracks created during the crystallization of molten metal at the place of accumulation of low-melting eutectic inclusions.

The formation process of an inseparable compound during FSW combines a whole complex of interconnected phenomena, including: intense local heat release on friction surfaces; rapid heating and cooling of small volumes of metal in a confined space under high

pressure; the movement of a metal heated to a plastic state along a complex path; plastic deformation in microvolumes of a metal; recrystallization, diffusion, and mechanical crushing of constituent particles; intensive dislocation movement; instant formation of an integral connection behind the tool, etc., which determines the structural features of its various sections.

Microstructural studies showed that the intensive movement of plasticized metal by the working surfaces of the tool shoulder over the entire thickness of the welded edges leads to the formation of a specific structure of joints (Figure 2).

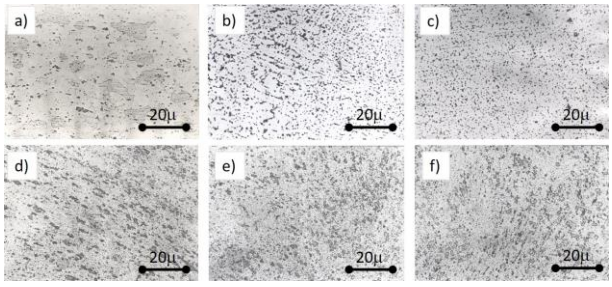

Figure 2. The microstructure of the base metal (a) and welded joints of the AA5056 alloy obtained by GTAW with a SvAMg5 filler wire (b - fusion zones, c - seam) and by FSW (d - thermomechanical impact zone from the ramp side, e - seam core, f - thermomechanical impact zone from the side of the waste)

In the central part (core) of the seam, due to dynamic recrystallization, the formation of a fine-crystalline structure of the seams occurs. In the weld core, thus, the size of grains having an almost globular shape does not exceed 4 μ, and that of dispersed phase precipitates is ≤ 1 μ, which is 5-7 times less than in the base metal. In the zone of thermomechanical impact at the interface between the weld and the main material, in addition to small grains, larger ones (6-7 μ) are also elongated in the direction of movement of the plasticized metal. In the zone of thermal influence, not subjected to deformation, the grain size is 10-15 μ.

The AA5056 alloy joints obtained by GTAW are characterized by a mixed dendritic structure consisting of columnar and equiaxed grains, typical of aluminium-magnesium alloys in a cast state. At the same time, equiaxed dendrites of about 25 μ in size are formed in the central part of the seam. Near the zone of its fusion with the main material, a layered dendritic structure with extended phase precipitates along the boundaries of these grains is more manifested.

Intensive plastic deformation of the metal in the zone of formation of an indispensable compound during FSW not only facilitates grinding of its structure, but also leads to its strain hardening (Figure 3).

Figure 3. Hardness distribution in the AA5056 alloy welded joints obtained by GTAW and FSW

In the central part of the AA5056 alloy joints, hence, the hardness of the metal is at the level of 84 HRB, while in the zones of its conjugation with the main material it is not lower than 83 HRB. In this case, the minimum hardness of the metal (i.e., 78.5 HRB) is observed at the boundary of the zones of thermomechanical and thermal effects. Whereas during GTAW in the central part of the weld the hardness of the metal does not exceed 76 HRB, in the zones of its fusion with the base material it extents to 78 HRB. Therefore, samples of AA5056 alloy compounds made by GTAW using a SvAMg5 filler wire with removed reinforcements and weld penetrations are destroyed under uniaxial tension over the weld metal and have a tensile strength of 300 MPa (Table 1).

The destruction of the samples with reinforcement of the seam occurs on the base metal, as well as samples obtained by friction stir welding. Moreover, their tensile strength is about 320 MPa.

Tests with simultaneous tension and bending of Kahn samples made from GTAW joints showed that the crack nucleation at the top of the concentrator with a sharp notch and its further propagation occurs along the weld metal (Figure 4).

On the other hand, in the samples welded by FSW the crack originating in the seam centre at the top of the concentrator is shifted to the zone of thermomechanical action. Therefore, the load – strain diagrams obtained during testing of Kahn samples indicate that the minimum resistance to nucleation and propagation of cracks is observed in welds with a coarse-grained structure obtained by GTAW (Figure 5).

On the other hand, the nucleation and propagation of a crack during testing of samples performed by FSW is even somewhat slower than in the main material, which indicates a sufficiently high level of their ductility.

As a result, it was found that a decrease in the temperature of heating the metal in the zone of formation of one-piece compound during FSW favourably affects the level of RS arising in it due to the uneven distribution of the thermal field.

Table 1. Strength limit of welded joints of AA5056 alloy obtained by GTAW and FSW

№	Method	Limit σ, MPa	Fracture	Photo of the fractured sample
1	GTAW with reinforced seam	323.7 317.1 **320.2**	base metal	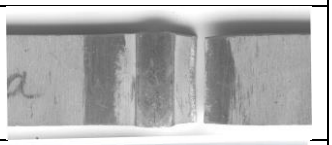
2	GTAW without reinforced seam	301.7 299.1 **300.4**	seam	
3	FSW without reinforced seam	321.1 316.2 **319.7**	base metal	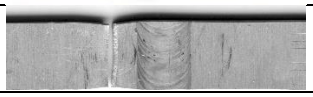

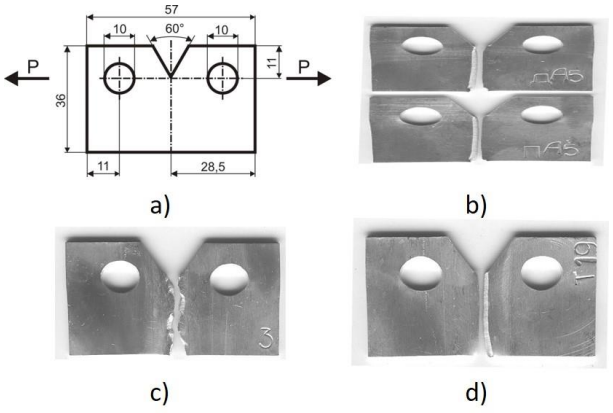

Figure 4. Sketch image (a) and tested samples of Kahn made of the base material (b) and welded joints of the AA5056 alloy obtained by GTAW (c) and FSW (d)

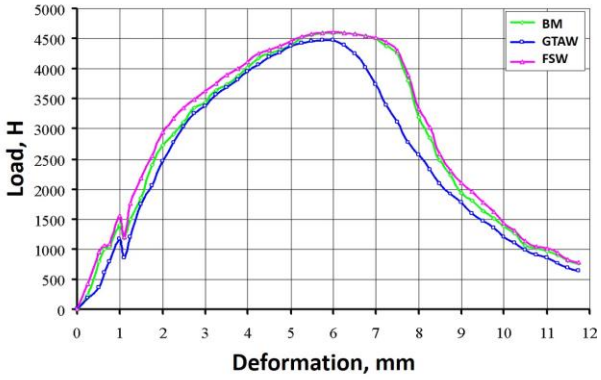

Figure 5. The "load - deformation" diagrams obtained during the testing of Kan samples made of the base material and welded joints of the AA5056 alloy

So, during the GTAW the maximum value of longitudinal tensile RS at a distance of 10 mm from the weld axis is at the level of 103 MPa (Figure 6).
In the centre of the seam, these stresses are 72 MPa. At a distance of about 22 mm from the weld axis, they decrease to zero, then compressive stresses arise with a maximum value of 38 MPa at a distance of 35 mm from the weld axis. In welded joints made by FSW, the maximum value of tensile stresses is only 78 MPa. At the same time, their value in the centre of the weld is at the level of 36 MPa, which is twice less than with GTAW. Accordingly, the maximum value of compressive RS at a 35 mm distance from the weld axis decreases to 23 MPa. The results of experimental studies on fatigue resistance of the AA5056 alloy welded joints obtained in the solid phase by FSW showed that their endurance limit on the basis of 2×10^6 cycles of voltage changes is 85-95% of the corresponding values of the base metal and practically reaches the level of the conditional endurance limit (Figure 7).

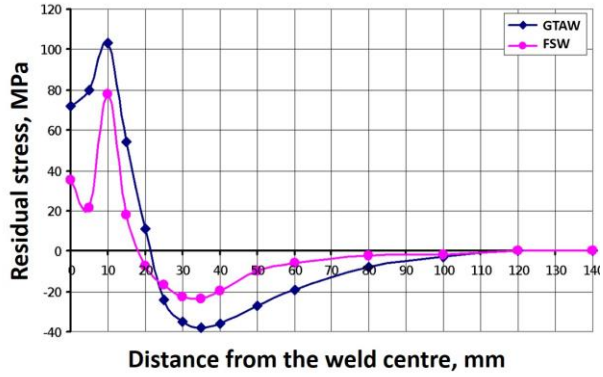

Figure 6. Distribution of longitudinal RS in 1.8 mm thick welded joints of the AA5056 alloy obtained by GTAW and FSW

In turn, the fatigue resistance of welded joints made by GTAW is significantly inferior in the entire durability range based on 10^5 to 2×10^6 cycles of voltage changes. At the same time, the durability of the joints made by FSW is up to 10 times higher in comparison with the joints made by GTAW, and their limited endurance based on 10^6 cycles of voltage changes is 15 to 20% more. The main reason for the lower durability of welded joints made by GTAW is the high concentration of acting stresses due to the geometric parameters of the weld.

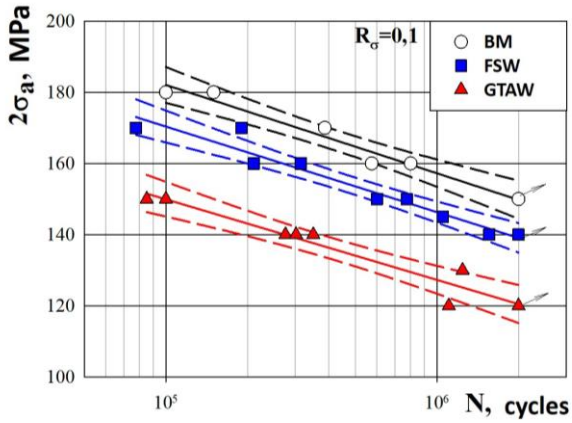

Figure 7. Fatigue curves and the corresponding 95% scattering region of the data for the 1.8 mm thick AA5056 alloy samples with asymmetry of the stress cycle Rσ = 0,1: ○ - base metal; ■ - FSW; ▲ - GTAW

4. Conclusion

1. During the FSW of an AA5056 alloy, as a result of intense plastic deformation of the metal, a uniform disoriented structure with grain sizes of 3-4 μ and dispersed (≤ 1 μ) phase precipitates is formed in the weld core. In the zones of the weld with the base material, some grains elongate to 6–7 μ and they bend in the movement direction of the plasticized metal.
2. The use of FSW ensures the formation of an integral connection with a minimum level of stress concentration at the transition points from the weld to the base material. It also avoids defects in the joints in the form of pores, macro inclusions of the oxide film and hot cracks caused by melting and crystallization of the metal during fusion welding.
3. Owing to the strain hardening of the metal and to grains refinement, FSW of the thermally unstrengthened AA5056 alloy leads to hardness increasement in the joint zone. During GTAW, on the other hand, the metal hardness in this zone decreases due to the formation of a cast coarse-grained dendritic structure of the joints. Therefore, the tensile strength of samples obtained by FSW, under uniaxial tension, is 20 MPa higher than in the case of samples without reinforcements and weld penetrations welded by GTAW. In addition, the samples made by FSW have an increased resistance to the nucleation and propagation of cracks while stretching and bending.
4. Due to the formation of welds in the solid phase at lower temperatures compared to fusion welding, the maximum level of tensile longitudinal RS in the welded joints of the AA5056 alloy obtained by FSW is 30% lower than with GTAW.
5. The durability of the butt joints obtained by FSW is much higher than that of the joints made by GTAW, and their restricted endurance limit based on 2×10^6 cycles of voltage changes almost reaches the durability level of the samples of the base metal, whereas for joints obtained GTAW is 30 to 40 % lower.

REFERENCES

[1] Ishchenko A.Ya., Labour T.M., (2013), *Welding of modern structures from aluminum alloys*, NPP Publishing House of the National Academy of Sciences of Ukraine, Kiev

[2] Beletskiy V.M., Krivov G.A., (2005), *Aluminum alloys (composition, properties, technology, application)* - Directory, Komintech, Kiev

[3] Rabkin D.M., Lozovskaya A.V., Sklabinskaya I.E., (1992), *Metallurgy of welding aluminum and its alloys*, Academy of Sciences of Ukraine, Institute of electric welding them. E.O. Paton, Naukova Dumka, Kiev

[4] Machine V.S., Poklyatsky A.G., Fedorchuk V.E., (2005), *Mechanical properties of joints of aluminum alloys in welding with consumable and non-consumable electrodes*, Automatic welding No. 9, p 43-49.

[5] Poklyatsky A.G., (2001), *Features of the formation of macroinclusions of an oxide film in the weld metal of aluminum alloys*, Automatic welding No. 3, p 38-40.

[6] Klimenko Yu.V., (1967), *Method of friction welding of metals*, Copyright certificate No. 195846. Stated 11/09/1965 (No. 1036054 / 25-27). Published on 05/04/1967. Bulletin No. 10.

[7] Thomas W.M., Nicholas E.D., Needham J.C. et al. (1991), *Friction Stir Butt Welding*, Int. Patent Application No. PCT/GB 92/02203; GB Patent Application No. 9125978.8.

[8] Sato Y., (2002), *Relationship between Mechanical Properties and Microstructure in Friction Stir Welded Alloys*, Journal of the Japan Welding Society 8, p 33-36.

[9] Pietras A., Zadroga L., (2003), *Rozwój metody zdrzewania tarciowego z mieszaniem materiału zgrzeiny (FSW) i możliwosci jej zastosowania*, Biuletyn Instytutu Spawalnictwa w Gliwicach No. 5, p 148-154.

[10] Shibayanagi T., (2007), *Microstructural aspects in friction stir welding*, Journal of Japan Institute of Light Metals No. 9, p 416-423.

[11] Kluken A., Ranes M., (1995), *Aluminum bridge constructions - welding technology and fatigue properties*, Svetsaren No. 3, p 13-15.

[12] Jata K.V., Sankaran K.K., Ruschau J.J., (2000), *Friction Stir Welding Effects on Microstructure and Fatigue of Aluminum Alloy 7050-T7451*, Metallurgical Transactions Vol. 31A, p 2181-2192 Switzerland

[13] Lanciotti A., Vitali F., (2003), *Characterization of friction welded joints in aluminum alloy 6082-T6 plates*, Welding International No. 8, p 624-630 United Kingdom

[14] Larsson H., Karlsson L., Svensson L., (2000), *Friction Stir welding of AA5083 and AA6082 aluminum alloys*, Svetsaren No. 2, p 6-10.

[15] Ishchenko A.Ya., Poklyatskiy A.G., (2010), *Instrument for rubbing graters with mixing aluminum alloys*, Pat. 54096 Ukraine, IPC V23K 20/12, Є.O. Paton National Academy of Sciences of Ukraine, No. u201005315; application 04/30/2010; publ. 25.10.2010, Bul. No. 20.

[16] Poklyatsky A.G., (2011), *Resistance of seams of thin-sheet aluminum alloys against initiation and propagation of service cracks*, Automatic welding No. 10, p 7-11.

[17] Kasatkin B.S., Kudrin A.B., Lobanov L.M., Pivtorak V.A., Polukhin P.I., Chichenev N.A., (1981), *Experimental methods of investigation of deformations and stresses. Handbook*, Naukova Dumka, Kiev

ISSN 1847-7917

Roughness of low carbon steel after cold rolling of reversing mill 700

Miglena PANEVA, Peter PANEV and Nikolay STOIMENOV
Authors' affiliation:
Institute of Information and Communication Technologies – Bulgarian Academy of Sciences, bl. 2, ac. G. Bonchev str, 1113 Sofia, **Bulgaria**
m.paneva7@gmail.com
panevv@gmail.com
nikistoimenow@gmail.com

Original scientific paper

Abstract: This article describes the production process of cold rolling. For the study, a single-cell reversing mill 700 was observed, indicating the tolerances of the input and output dimensions of the rolls, as well as the dimensions of the working rolls and their roughness. The tolerances in the thickness of the rolled strip are indicated. The roughness of the raw material before and after its rolling and the standard it must meet are analyzed. The data are shown in tabular form.

Keywords
Roughness
Working rollers
Turning
Grinding
Rolling
Mill 700

1. Introduction

Rolling is a manufacturing process in which metal, plastic, paper, glass, or other material change shape when passing between two rolls. The process is possible only for materials allowing plastic deformation and in case they are not structurally changed in a previous process [1].

In flat rolling, the final shape of the product is a sheet (less than 3 mm thick) or a plate (more than 3 mm thick). Rolling is classified according to the temperature of the material. If the metal is below its recrystallization temperature, the process is called cold rolling. Cold rolling is applied to materials with a small cross-section. Cold rolling also uses lubricants to reduce rollers wear and friction during the process.

2. Working rollers

The working rollers of the single-cell reversing mill 700 INCO [2] are two with an overall length of 1927 mm and a working part of 700 mm (C, D, E, F), (Fig. 1).

The material used is hot-rolled, pickled and oiled steel strips wound in rolls of low carbon steel grades.

- Size of incoming rolls:

- maximum outer diameter - 1400 mm;
- minimum outer diameter - 900 mm;
- inner diameter - 450 -550 mm;
- width - 250-510 mm;
- maximum thickness - up to 4.5 mm;
- weight up to 6 t.

- Size of outgoing rolls:

- inner diameter of the roll - 508 mm;
- minimum thickness - 0.3 mm.

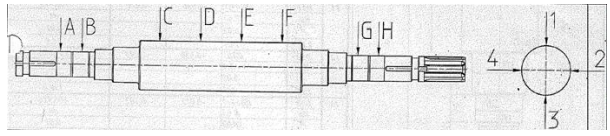

Figure 1. Working roller

The working rollers have a diameter of 210 mm with a permissible circular deviation of 0.02 mm and a roughness of Ra-0.4 μm. The rollers used are from Dee Tee Industries Limited [3], China and NKMZ, Ukraine [4]. The rolling mill has devices for mechanized replacement of the working rollers (Fig. 2) and an emulsion system for their cooling. After using the work rollers, they get over-smoothing, which requires their grinding [5]. The resulting smoothing harms the heat treatment of the rolls. After unpacking them from the furnaces and setting them for the next training operation, the negative effect of over-smoothing is seen, namely gluing the windings to the rolls.

Symbols

Ra	- Roughness, µm	*VHF*	- Very high frequency
L	- length, mm	y_i	- partial values of y within the limits of the base length, mm
n	- number		

Figure 2. Device for mechanized replacement of working roller

3. Rolling technology

After loading the roll of the unwinder, through a system of mechanisms the front end of the strips is set to the mill, passes through the working rollers, and is gripped by a right winder. With a predefined rolling mode, the rolling process itself begins. After completing the first pass, the rear end of the strips is gripped by a left winder and a second pass begins - rolling in the opposite direction.

One roll can be rolled up to five passes under the conditions of continuous submission of lubricating and cooling liquid to the working and support rollers in the direction of rolling.

In both directions of rolling, there is a system for blowing the emulsion from the metal strip. All the time on the rolling utensils on both sides of the cell monitor the thickness of the strips.

The permissible maximum rolling speed is 800 m / min at a total maximum pressure of up to 600 t, according to the standard BDS EN 10140.

The thickness limits are normal (A), fine (B), or precision (C) and are listed in Table 1**.**

Table 1. Tolerance of thickness, mm [6].

Dimensions in millimetres

Nominal thickness		Tolerances on thickness for nominal widths					
		< 125			≥ 125 and < 600[a]		
>	≤	A	B	C	A	B	C
	0,10	± 0,008	± 0,006	± 0,004	± 0,010	± 0,008	± 0,005
0,10	0,15	± 0,010	± 0,008	± 0,005	± 0,015	± 0,012	± 0,010
0,15	0,25	± 0,015	± 0,012	± 0,008	± 0,020	± 0,015	± 0,010
0,25	0,40	± 0,020	± 0,015	± 0,010	± 0,025	± 0,020	± 0,012
0,40	0,60	± 0,025	± 0,020	± 0,012	± 0,030	± 0,025	± 0,015
0,60	1,00	± 0,030	± 0,025	± 0,015	± 0,035	± 0,030	± 0,020
1,00	1,50	± 0,035	± 0,030	± 0,020	± 0,040	± 0,035	± 0,025
1,50	2,50	± 0,045	± 0,035	± 0,025	± 0,050	± 0,040	± 0,030
2,50	4,00	± 0,050	± 0,040	± 0,030	± 0,060	± 0,050	± 0,035
4,00	6,00	± 0,060	± 0,050	± 0,035	± 0,070	± 0,055	± 0,040
6,00	8,00	± 0,075	± 0,060	± 0,040	± 0,085	± 0,065	± 0,045
8,00	10,00	± 0,090	± 0,070	± 0,045	± 0,100	± 0,075	± 0,050

[a] Can be extended to 650 mm: see 6.2.4.

4. Roughness of surfaces

The surface roughness is different in shape, size and direction grooves, depressions and protrusions that form the relief of a surface [7].

Real surfaces differ from geometric ones, which are ideal, ie. without deviations from the form.

The measurement of the actual surface cannot be accurate due to measurement errors. Therefore, the surface that the measurement is obtained is called a real (effectively measured) surface.

Despite their insignificant dimensions, the roughness of the surfaces has a great influence on the performance characteristics of the machine parts and in particular on the accuracy of their joints. They affect the strength of fatigue, impact strength, corrosion resistance, the strength of galvanic coatings, the reflection of electromagnetic waves and more [8].

The conditional line against which the measured real profile is reported is called the baseline. The baseline must be equally spaced and parallel to the midline, and it also does not cross the profile. There is a certain area where the roughness is quantified. This section is called the base length.

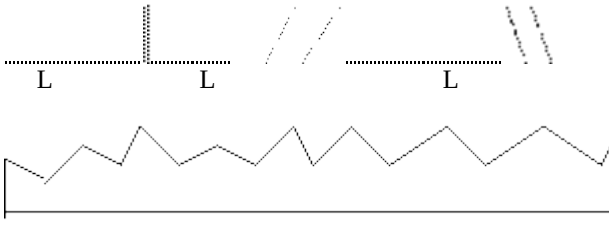

Figure 3. Location of the base length

The dimensions of the base length depend on the degree of surface roughness - for rougher surfaces they are larger, and for smoother surfaces - smaller. The base length is positioned relative to the profile to exclude surface undulation.

The average arithmetic means deviation of the profile - Ra is the deviation from the absolute values of the deviations of the profile within the limits of the base length. When measuring a limited number of deviations, the average arithmetic mean deviation is determined approximately by the formula:

$$Ra \approx \frac{1}{n}\sum_{i=1}^{n}(yi) \quad (1)$$

Ra is the average arithmetic deviation of the estimated profile defined on the sampling length. Ra is used as a global estimate of the roughness amplitude of a profile. It says nothing about the spatial frequency of the irregularities or the shape of the profile. Ra is important for random surface roughness (stochastic), treated with tools that do not leave traces on the surface, such as sandblasting, milling, polishing.

5. Used equipment

For the work, a portable roughness device DIAVITE Compact II VHF [9] was used, with a measuring range of 0 ÷ 19.99 m, with an accuracy of 0.01 m. It is a compact portable roughness tester for standard roughness measurements in production facilities and measuring rooms. The advantages are that it is easy to operate without training; it is safely measured using a permanently connected filter with a scanning road and the power supply module can be integrated into the wireless measuring device.

The roughness measurements of the sheet metal are performed in the direction of rolling to obtain precise results, according to the standard BDS EN ISO 4287: 2006 (Technical requirements for the geometry of products); Surface structure: Profile method. Terms, definitions, and parameters of surface structure (ISO 4287: 1997) [10].

6. Experimental results

To experiment, an analysis of the low-carbon metal roughness was made in several conditions of metal delivery and processing: hot-rolled coil, purchased cold-rolled coil, and cold-rolled coil from a purchased hot-rolled coil, processed on reverse mill 700 for cold rolling. Five measurements were made in each of the metal states and then averaged. The roughness measured after rolling off a reversible mill is made after different stages of deformation: at 5% deformation and 50% deformation.

The roughness of all measured coils is always measured in the rolling direction, according to standards EN 10305-3 and EN 10305-5 for the production of precision electric welded pipes and profiles. The test unit must contain at least 2 tonnes of metal or the quantity of the primary coil for the production of pipes and profiles. The test pieces must be taken from the same place as the samples for mechanical measurement at the end of the roll.

Table 2 presents the results of measuring the roughness of a hot-rolled roll with a size of 2.0x1105 mm. Measurements show an average roughness of 1.39 µm.

Table 2. Roughness of Hot Rolled coil, size 2.0x1105 mm.

Number of measurements	Roughness, µm
1	1,48
2	1,27
3	1,54
4	1,48
5	1,19
Average value	**1,39**

Table 3 presents the results of the roughness measurements of a purchased cold-rolled roll with a size of 0.85x1010 mm. The values show an average roughness of 1.0 µm.

Table 3. Roughness of a purchased cold-rolled roll with a size of 0.85x1010 mm.

Number of measurements	Roughness, μm
1	0,98
2	0,99
3	1,02
4	1,0
5	1,03
Average value	**1,0**

Table 4 presents the results of measuring the roughness of a cold-rolled coil of a reversing machine for cold rolling at 5% and 50% deformation with an initial roughness of 1.4 μm. The results show that when rolling with 5% deformation, the roughness does not decrease significantly, reaching 1 μm and approaching that of the purchased cold-rolled roll. While the roughness at 50% deformation is significantly reduced to 0.39 μm. The values are close to those of the working rollers with which the sheet metal contacts.

Table 4. Roughness of a cold-rolled roll of a reversing mill for cold rolling at different deformations with an initial roughness of 1.4 μm.

Number of measurements	Deformation	Roughness, μm
1	5 %	0,99
2		1,0
3		1,02
4		1,01
5		1,02
Average value		**1,01**
1	50 %	0,31
2		0,30
3		0,32
4		0,32
5		0,34
Average value		**0,32**

7. Conclusion

Low-carbon metal roughness analyzes were performed in several conditions of metal delivery and processing: hot-rolled coil, purchased cold-rolled, and cold-rolled coil from purchased hot-rolled coil, processed on reversing mill 700 for cold rolling. The test specimens were taken from the end of the coil and the measurement was performed in the direction of rolling of the roll. The average values of the hot-rolled coil show a roughness of 1.39 μm. The values of the purchased cold-rolled roll are on average 1.0 μm. The measured roughness after rolling off a reversible mill made after 5% deformation is 1.01 μm, which shows that the roll has not significantly changed its roughness, and at 50% deformation - 0.32 μm. The values show that we have reached the roughness of the working rolls when starting work, which will help to avoid sticking the windings to the rolls. This roughness is also suitable for subsequent finishing of pipes, such as chrome plating and nickel plating.

Acknowledgments

The paper is supported by the Bulgarian Academy of Sciences, a program for supporting young scientists and doctoral students, and by the Bulgarian Ministry of Education and Science National Research Program "Young scientists and postdoc students" approved by DCM#577 /17.08.2018.

REFERENCES

[1] https://bg.wikipedia.org/wiki/%D0%92%D0%B0%D0%BB%D1%86%D1%83%D0%B2%D0%B0%D0%BD%D0%B5 (last visited April 2021)

[2] http://www.sa-inco.com/ (last visited April 2021)

[3] http://bg.conticasting.com/ (last visited April 2021)

[4] http://nkmz.com/ (last visited April 2021)

[5] Paneva M. and Panev P., (2021) *Mechanical treatment and roughness of working rolls for reverse mill for cold rolling*, XXX International Scientific and Technical Conference, ADP - 2021., 29.06 ÷ 02.07.2021, Sozopol, Bulgaria., Publishing house of TU-Sofia ISSN – 2682-9584, Publisher Department "Automation of Discrete Production Engineering" Mechanical Engineering Faculty, Technical University – Sofia.

[6] Standards *BDS EN ISO 10305-3, 10305-5*

[7] Helpos.com, (2008) THESIS on the topic: "*Device for surface treatment of fine - mechanical parts with irregular shape*". (last visited April 2021)

[8] Ruseva Sl., Papazyan K., Atanasov Ass., Petkova St.,(1988) *ESKD, Handbook of design documentation*, State Publishing House "TECHNIQUE", Sofia.

[9] https://www.hahn-kolb.net/-/-DIAVITE-Compact-II/5521CL04_040801020102.cyid/5521.cgid/bg/BG/EUR/ (last visited April 2021)

[10] Standard *BDS EN ISO 4287:2006*

ISSN 1847-7917

Investigation of the shielding ability of concrete samples reinforced with B_4C and iron fillings against neutron radiation

Massimo ROGANTE[1)]***, Osman GENCEL***[2)]***, Erol KAM***[3)] ***and Tuncay TUNA***[4)]

1) Rogante Engineering Office, Contrada San Michele n. 61, I-62012 Civitanova Marche, **Italy**
2) Bartin University, Civil Eng. Dep., Bartin, **Turkey**
3) Yıldız Technical University, Dep. of Physics, Istanbul, **Turkey**
3) TAEK, Cekmece Nuclear Research Center, Kucukcekmece, Istanbul, **Turkey**

main@roganteengineering.it
erolkam@hotmail.com

Keywords

Neutron radiation
Radiation shielding
Composite material
Boron carbide
Concrete

Original scientific paper

Abstract: Neutrons are neutral subatomic particles and, similarly to other particles, protons and electrons, their potential applications fundamentally consist in research and development studies related to industry, medicine, agriculture and other fields. Production of radiopharmaceuticals, assessment of the humidity values of soil and characterization of materials' inner structure can be mentioned as examples of the wide area of employment of these special and spectacular particles. Beside these unique properties, human body should be protected against uncontrolled irradiation with neutrons due to their high ability of penetrating and causing indirect ionization, i.e. the most known dangers of these particles. Works for this purpose have been performed, focused on usable, economic, light weight and high strength shielding resources, and composites with layered or mixed type of different suitable materials are the favorite candidates. There are two steps in neutron shielding works: thermalizing and adsorption of neutrons are the main step, then the shielding of indirect ionization such as alfa, beta or gamma is the second step. Developed materials, thus, should be adequate for both steps.

In the present work, we have investigated the shielding characteristics of concrete blocks reinforced with boron carbide and iron fillings in the field of Am-Be neutron source having 2 Ci activity. Boron carbide has a good reputation along with high thermal neutron cross section and high mechanical values. Concrete too is one of the basic component of constructional field. Energetic neutrons can be thermalized by collisions of light nucleus of concrete then absorbed by boron carbide. Iron fillings take place in the structure, in order to absorb gamma radiation which originated from the indirect ionization of neutrons.

Within the scope of this study, 15 samples were prepared having 100×100 mm width-length values and a 20 mm thickness, with different percentage of boron carbide and iron fillings. According to the results from experiments, the highest (61.34%) and the lowest (20.83%) shielding rates were obtained respectively from the last and the first sample. An adequate indirect radiation shielding resulted from all samples. In the light of these outcomes, this material can be considered as an effective neutron shielding material.

1. Introduction

Concrete is considered to be an excellent and versatile shielding material; it is widely used to shield nuclear power plants (NPPs), particle accelerators, research reactors, laboratory hot cells and medical facilities. Concrete is a relatively inexpensive material, which can be easily handled and cast into complex shapes. It contains a mixture of various light and heavy elements and a capability for attenuation of photons and neutrons [1, 2]. As the human population and industrial demands grow, nuclear technology has oriented humanity towards using synthetic energy to complement conventional energy sources, which are running out. Constructions of NPPs have been increased for many purposes, especially for energy supply all around the world. The issue of the potential impact of nuclear leakage on the environment, and a potential crisis, however, are attracting a considerable interest and stimulating many discussions [3]. Living isolated from radiation is almost impossible in the modern world: humans and animals are subjected to natural or artificial radiation in the environment, due to the increased living standard. Medical facilities too, like radiotherapy devices, need a well-shielded room. To protect living creatures, thus, is a first aim.

Although lead has been used for shielding structures such as NPPs, there is a wrong concept on it. For some cases, e.g., lead has been insufficient to shield neutrons. For this purpose, concrete is considered as an excellent and

versatile shielding material widely used for NPPs, particle accelerators, research reactors, laboratory hot cells and medical facilities. In all nuclear installations, concrete is the most commonly used shielding material to protect from neutron radiation. It is a common practice to add boron to concrete, in order to enhance the thermal neutron attenuation properties and to suppress secondary gamma-ray generation. In neutron shielding studies, the first step is to reduce the energies of the neutrons to thermal levels. For this purpose, elastic or inelastic collisions with light atomic nuclei, such as hydrogen, carbon and boron, are held. In each collision, neutrons lose some energy and reach thermal energies and at this stage they can be easily absorbed by some materials which have high thermal neutron cross-sections [4]. Shielding materials, therefore, should ensure two main steps, namely thermalization and absorption of neutrons. A thermalizer material - or moderator - must be rich with light elements in addition to accommodating the absorber material as the matrix material. An absorption material, on the other hand, must have a high thermal neutron cross-section with high sensitivity to neutron particles and it should be compatible with matrix material including high mechanical properties [5, 6]. Boron carbide has a good reputation along with high thermal neutron cross section and high mechanical values [7]. Concrete is also one of the basic components of constructional field. Energetic neutrons can be thermalized by collisions of light nucleus of concrete, then absorbed by boron carbide. Iron fillings take place in the structure in order to absorb gamma radiation originated from the indirect ionization of neutrons. In the present study, the shielding characteristics of concrete blocks reinforced with boron carbide and iron fillings have been investigated.

2. Materials and Methods

B_4C was supplied from a private Turkish company. Some characteristics of B_4C are given in Table 1.

Table 1. Characteristics and chemical compositions of B_4C

Natural isotopes of boron and ratios	^{10}B - 18.8% / ^{11}B - 81.2%
Molecular weight (g/mol)	55.25
Density (g/cm³)	2.51
Melting temperature (°C)	2763
Boiling temperature (°C)	3500
Neutron cross section (barn)	755
Hardness (Vickers)	20-78 GPa
Particle size analysis	4-4800 mesh
Appearance	Granule and dust/black-gray
Oxidation Resistance	Up to 600 °C in air atmosphere B_2O_3 film decreases the oxidation
Chemical Resistance	Excellence

Average particle sizes of B_4C were 10 µm. The neutron source adopted in this study was a Howitzer-type Am-Be source, which emits 4-5 MeV energetic neutrons with source activity of 2 Curie (see Figure 1).

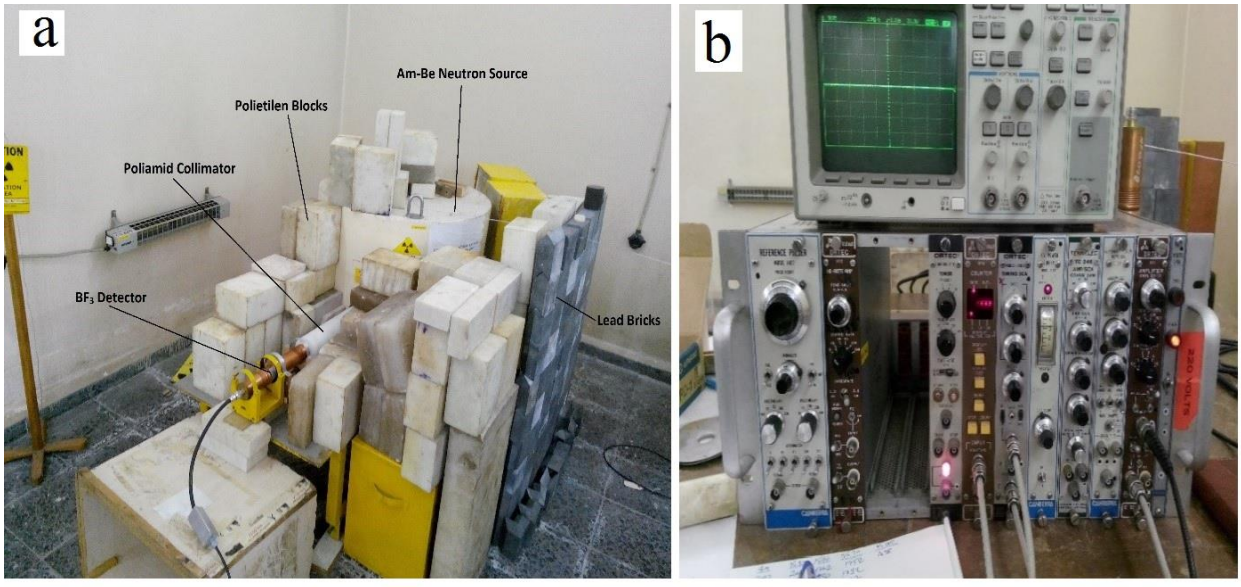

Figure 1. Neutron source and detector system (a) and counting system attached to the neutron source (b)

The list of all equipments used in the experimental setup is given in Table 2.

Table 2. Hardware information used in the neutron shielding tests

Hardware	*Property/Brand*
Neutron Source	^{241}Am-9Be
Energy	4-5 MeV
Activity	2 Ci
Detector	Boron Trifluoride (BF_3) Neutron Detector
Oscilloscope	Hewlett Packard
Counter	Ortec 875
Timing & SCA	Ortec Model 420A
Preamplificator	Ortec
Amplificator	Ortec 571
Power Supply	Canberra Model 3105 H.V. 0-5 kV
Counting Time	5×100 sec

15 samples have been prepared with 100×100 mm width-length values and 20 mm thickness, with different percentages of boron carbide and iron fillings. Table 3 reports the composition of each sample.

Table 3. Composition of the investigated samples (weight %)

sample	B_4C %	iron fillings %	C-50 %
1	5	5	90
2	10	5	85
3	15	5	80
4	20	5	75
5	25	5	70
6	30	5	65
7	35	5	60
8	40	5	55
9	45	5	50
10	50	10	40
11	55	10	35
12	60	10	30
13	65	10	25
14	70	10	20
15	75	10	15

Concrete-50 (C-50) high performance concrete was used, having modulus of elasticity, shrinkage, fire resistance, freeze-thaw resistance, volumetric stability, high early strength, toughness, wear resistance, and other characteristics designed according to performance.

Heavy concretes are concretes with a unit weight between 3,000 and 5,000 kg/dm^3, which are used to create an armor against high energy rays and neutrons. Areas of use may include nuclear reactors and hospital-treated sections. Aggregates of heavy concrete are heavy ferrous minerals such as barite (barium sulfate $BaSO_4$), limonite and magnetite. These materials possess a retarding effect. Heavy aggregates are equivalent to normal aggregates in terms of strength.

3. Results and discussion

The obtained results are shown in Figure 2, which clearly reports the increases of the neutron shielding performance of the considered composites depending on boron carbide and iron filling concentrations in the C-50 concrete body.

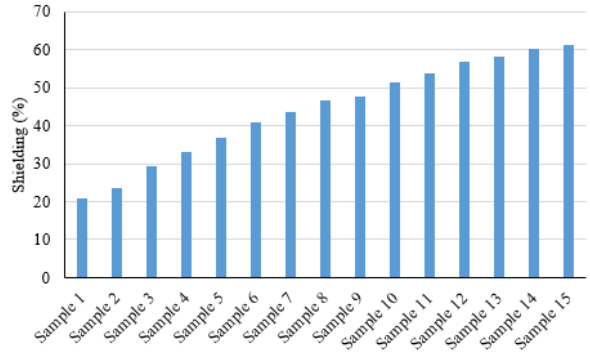

Figure 2. Shielding performances of composites produced

The increase of boron carbide and iron filling in the concrete corresponds to a significant improvement of the shielding performance of the composite. The lowest shielding percentage belongs to the composite containing just 5% boron carbide and 5% iron filling, with 20.83% shielding capacity, while the highest one to the composite containing 75% boron carbide and 10% iron filling, with a 61.34% shielding capacity.

The most significant increases of the shielding performance occur in correspondence with the first samples (in particular, samples 2 to 5), having lower boron carbide content and iron filling.

4. Conclusion

The results of the investigation carried out on fast neutron shielding performance of cement based composites containing boron carbide and iron filling have provided new information about the shielding capacity of these composites. The adoption of boron carbide from 5% to 75% and iron filling from 5% to 10% as replacement material instead of natural aggregates has a significant effect on shielding performance of the concrete. The best neutron shielding performance has been observed with regard to composite containing 75% boron carbide and 10% iron filling, with a 61.34% shielding capacity. The produced composites can be utilized while building the walls of NPPs, as moderator for nuclear reactors, in medical departments and in neutron facilities (e.g., as

protective radiation casing of neutron collimators), to protect from damages due to neutron particles.

REFERENCES

[1] Gencel O., Brostow W., Ozel C., Filiz M., (2010), *Concretes containing hematite for use as shielding barriers*, Materials Science – Medziagotyra 16 No. 3, p 249-256. Lithuania http://matsc.ktu.lt/index.php/MatSc/article/view/26077

[2] Gencel O., Brostow W., Ozel C., Filiz M., (2010), *An investigation on the concrete properties containing colemanite*, Int. J. Phys. Sci. 5 No. 3, p 216-225

[3] Kan Y.C., Pei K.C., Chang C.L., (2004), *Strength and fracture toughness of heavy concrete with various iron aggregate inclusions*, Nucl. Eng. Design 228 No. 1-3, p 119-127 United Kingdom https://doi.org/10.1016/j.nucengdes.2003.06.008

[4] El-Sayed A.A., Kansouh W.A., Megahid R.M., (2002), *Investigation of radiation attenuation properties for baryte concrete*, Japanese Journal of Applied Physics 41/1 No. 12, p 7512-7517 United Kingdom https://doi.org/10.1143/JJAP.41.7512

[5] Korkut T., Gencel O., Kam E., Brostow W., (2013), *X ray, gamma and neutron radiation tests on Epoxy-Ferrochromium slag composites*, International Journal of Polymer Analysis and Characterization 18 No. 3, p 224-231 United Kingdom https://doi.org/10.1080/1023666X.2013.755658

[6] Aygun B., Turgay K., Karabulut B., Gencel O., Karabulut A., (2015), *Production and Neutron Irradiation Tests on a New Epox/Molybdenum Composite*, International Journal of Polymer Analysis and Characterization 20 No. 4, p 323-329 United Kingdom https://doi.org/10.1080/1023666X.2015.1017790

[7] Tuna T., Bayrak K., (2017), *Investigation of the Shielding Capability of Concrete Matrixed Colemanite Reinforced Shielding Material*, Journal of Engineering Technology and Applied Sciences 2, No. 2, p 57-63 Turkey https://doi.org/10.30931/jetas.336562

[8] Tuna T., (2017), *Boron Carbide Reinforced Polyester Matrised Neutron Radiation Shielding Material Development and Characterization*, Master Thesis, University of Istanbul, Turkey

ISSN 1847-7917

Decommissioning of Nuclear Facilities: general considerations and suggestions not regarding activated parts

Massimo ROGANTE[1)]***, Franco G. CESARI***[2)]***, Massimo GIORGI***[3)]
1) Rogante Engineering Office, Contrada San Michele n. 61, I-62012 Civitanova Marche, **Italy**
2) Nuclear Engineering Lab., DIENCA, University of Bologna, Bologna, **Italy**
3) Nuclear Engineering Section, Department of Energy, Politecnico di Milano, **Italy**
main@roganteengineering.it

Keywords
Decommissioning
Nuclear power plants
Research reactors
Neutrons

Original scientific paper
Abstract: Decommissioning of nuclear facilities (NFs) generally consists in safely dismantling and removing a facility or site from service, then decreasing residual radioactivity to a level that consents releasing the land for unrestricted usage, as well as dismissing the license.
Several NFs are currently under decommissioning, in the world, concerning both nuclear power plants (NPPs) and research reactors (RRs). This paper concerns general considerations and suggestions related to this final stage of the life of these facilities, taking into account that decommissioning is not only an ordinary activity of installation end, but also a significant condition of accessibility of materials, parts and worked systems submitted for years to ageing and degradation. It represents, therefore, the suggestion for new diagnostics and for actions to undertake in the installation phase of new NPPs and RRs components in order to enhance their safety and dependability. Application of neutron beam methods for featuring materials problems in decommissioning, finally, is highlighted.

1. Introduction

The decommissioning of a Nuclear Facility (NF) can be described as the cessation of operations and the removal of the facility from its service, followed by its conversion into an out-of-service state and, finally, by its whole elimination, to leave: the buildings free of any radioactive contamination and ready to be demolished or used; the site ready for different industrial purposes [1].
Numerous old NFs in the world have presently reached this final stage of their life. They are both nuclear power plants (NPPs) and research reactors (RRs). While NPPs are primarily used to generate electricity, the latter are nuclear reactors producing radioisotopes and neutrons employed mainly for basic and applied research such as medical and industrial applications, as well as for development, education and training. Over 180 commercials, experimental or prototype reactors, over 500 RRs and several fuel cycle facilities, up to now, have been retired from operation. Some of these have been fully dismantled [2]. Concerning new NFs, designed for a 40 to 60 year or more operating life, their design should include a decommissioning plan, which includes the cleaning up and demolishing steps so that the sites will be made available for other uses. Concerning the decommissioning of old NFs, one should take into account the various difficulties to overcome relating to the dismantling of structures and parts eventually not conceived, since their design, also for their decommissioning. In the phases of planning, training and carrying out the dismantling phase, the need for information about the actual design and the existing state of the NF is a main concern for authorities and staff, to carry out the work professionally, safely and with acceptable economical costs. General safety requirements for the decommissioning of NFs are indicated and updated by the Internaitonal Atomic Energy Agency (IAEA). Decommissioning requires the adoption of specific technologies for disassembling and the improvement of various decontamination processes (i.e., chemical, electrochemical and mechanical) and assorted disassembling techniques such as cutting and splitting. These technologies create a considerable amount of low and medium radioactive materials, which require adaptation into the most appropriate forms for their storage. A cautious preliminary analysis of the activities related to decommissioning is indispensable in addition to the most appropriate preparation of the personnel involved. If a NPP has not been used for a long time, for example, the loss of expertise among the staff could create problems, since the new personnel might not be familiar with the plant - insufficient archival records for structural and engineering details - or the skilled staffs have already left it.

2. Main activities related to NF decomissioning, with exclusion of deeply or weakly activated parts

Decommissioning generally involves several different activities, e.g. the following:

- planning
- licensing adoption of technological tools
- manage of industrial safety and safety analysis
- structural analysis
- treatment technologies and apparatus to process gaseous wastes and ventilation
- treatment technologies to process liquid wastes, particularly regarding lead contamination
- monitoring and security issues and technologies
- minimization of the environmental impact, i.e. low-level waste disposal and waste minimization, waste disposal/storage facilities, waste processing and treatment.

The creation of a Decommissioning Visualisation Unit would permit to test out strategy and procedures for the various dismantlement tasks related to a NPP.

Moreover, experience gained from the dismantlement of NFs under decommissioning is fundamental in order to provide suggestions for dismantling technologies and safe handling of nuclear components upon dismantling.

No distinct optimal approach exists for every NF, as approaches can be largely dissimilar and a range of site specific or, at least, country specific parameters often influence the most favourable option. Organizations operating in research and applied technology related to this sector should possess specific skills to provide consulting both for the various decommissioning issues and activities, and for the conductive phases. Planning and management of works related to suction, ventilation and filtration systems, e.g., include the following activities:

- Protection of the personnel and environment from the gaseous pollutions; treatments and technologies of capture and confinement of polluting substances present in the air
- Tests to determine the quality of present products and substances, to verify the efficiency of the filtering system and to analyze qualitatively and quantitatively the stopped particles
- Drawing up of operating to carry out integrity tests of filtering barrier in situ
- Planning and work management until the dismantlement, of nuclear components - specially of mechanical type - with hot and mechanic cutting processes
- Drawing up of operating procedures for measure, monitor, management and treatment of the gaseous contaminant produced during the operations of dismantling (hot cutting processes such as plasma, laser, oxyacetylene and lance, and mechanical cuts) of plants either in the operating area or in the workshop, in closed nuclear and non-nuclear environments
- Forming and training of the operating personnel and predisposition of proper operation manuals related to:
  - suction/routing/filtration equipments and their use and maintenance
  - execution of cutting activities
- Planning critical analysis with check of the existing procedures and eventual improvement, adjustment or drawing up of new procedures for measures, monitor and surveillance of the work activities
- Selection of manufacturer Companies.

Other consultancies, e.g., can concern base indications of technical specifications and for the supply of materials and components, and activities of checks and controls, including checks of supplier Companies and interconnections with designers.

A main inconvenience of a delayed decomissioning is that possibly the workers will be unfamiliar with the facility and will have to rely on insufficient archival records for structural and engineering details. Dismantlement shall involve metal component segmentations and removal by adopting in situ adequate devices. A range of health hazards (e.g., inhalation as the main form of exposure in the case of material superficially contaminated), moreover, can be postulated for workers involved in metal cutting procedures. Thermal cutting processes based on two options - plasma torch and oxyacetylene device - have been evaluated in a study carried out during the dismantlement of the Caorso NPP, in which a testing campaign to analyse emissions and micronic dust in the cutting hall was settled, and final considerations were evidenced. In particular, plasma torch involves more pollutant and higher cutting temperatures, allowing faster rate in cutting plates, therefore oxyacetylene for pipes of moderated size/schedule. Moreover, the pollutant inhalation by workers can be significant even if depending, e.g., by cut duration, alloy type, wall size/thickness, surface treatment by Pb products, hot cutting type and distance of the worker face from piece under sectioning [3].

A safe dismantling of NPP components should assume important precautions, in order to assess the operative safeguards to defend personnel and create right procedures during the dismantling processes. Such provisions have been explained in [4-6], especially concerning:

- the pollutant inhalation by workers
- the enhancement of the elimination of the worst pollution component (i.e., the micronic dust)
- the employment of absolute filters to capture the gaseous mixture released during the cutting processes

- the need to deeply examine pollutants dissemination outside the cut area, gaseous emissions and dusts concentrations.

Preventive measures have been suggested, in addition, following the experience gained during the mentioned testing campaign, especially to be adopted during the hot cutting processes of pipes and tanks in closed environment, and to limit Pb concentration in the dust (due to the painted pieces), e.g.:

- to increase the frequency of air-changes, also introducing fresh air under pressure
- to eliminate fumes with monitored procedures in order to maintain cleaned, clear and breathable the room atmosphere
- to operate by automatic remote or manual cut with a shielding at the worker inhalation
- to increase the suction capacity, in order to eliminate the dust by filtration
- to separate the cutting room in diverse compartments, also isolating and transfering large dimension components to a specific station of the plant where the cutting procedures can be carried out more safely
- to select sectioning methods generating lower cut temperatures and smaller quantity of thin dusts (e.g., mechanical cut) [7].

3. Treatment of heavy metals polluted wastewater by activated carbon

During NF decommissioning processes, heavy metals poisoning can occur through inhalation by workers.

Toxicity of heavy metals is well known and it is related to its tendency to accumulate in living organisms, unlike organic pollutants are subject to biological degradation.

Heavy metals mostly considered as potentially toxic for living organisms are zinc, cadmium, chromium, copper, mercury, nickel and lead. The need of an effective lead removal from wastewaters in the nuclear industry may come from during decommissioning activities as well as during operational activities. Very stringent standards prevent the release of lead-contaminated industrial liquids into the environment due to its high toxicity and for this reason effective techniques shall be used to reduce lead concentration on aqueous solutions from wastewaters of NFs. During the years, different techniques were developed for lead removal such as chemical precipitation, electrochemical reduction, ion exchange, reverse osmosis and membrane separation.

Adsorption by activated carbon is among the most promising processes to remove traces of heavy metals from waters. For low flow rates and low concentration (i.e. ppb or ppm) usage of activated carbon is the best choice especially for lead removal.

Effectiveness of activated carbon is related to its chemical stability, high efficiency, high selectivity and economic feasibility.

Many laboratory tests have shown that removal of lead from aqueous solutions is highly effective and other tests are in progress to better investigate the influence of different factors on the adsorption process, such as pH value, precipitates or complexes formation, adequate contact time and initial metal concentration. A better investigation of the adsorption mechanisms can lead on a more appropriate development of the understanding of the diffusion models [8, 9].

4. Materials and parts obtained from NF decomissioning

NF decommissioning is not only a mere activity of installation end, but also a significant singular opportunity in which materials, parts and worked systems are available (e.g., piping, welded joints, inside components of pumps, pressurizer, vapour generator, pumps of the primary circuit, concrete as a shield of the reactor), submitted for years to ageing and degradation. It signifies, thus, the suggestion for new advanced diagnostics and a source of stimulus for actions to undertake in the installation phase of new parts to enhance safety and dependability of NFs. Pipes, plates, welded joints and, generally, irradiated materials of the reactor vessel, furthermore concrete compounds and polimeric materials obtained by decommissioning, have a substantial additional value: they can be investigated after a long time of exercise, providing an important help to explain various aspects related to degradation and creating effects towards the enhancement of upcoming NF installations. Materials degradation is a key topic in the NF sector, depending from different origins - e.g., chemical attacks produced by corrosion, embrittlement, radiations, stress corrosion cracking (SCC) and thermal treatments -, whose joined actions may produce an effect significantly increased as compared to those of the considered singular causes. Neutron radiation (NR) damage and thermal ageing are crucial factors defining the reactor's lifetime. NR linked with high operative temperatures can produce critical nano(micro)-structural modifications, deteriorating mechanical characteristics of metallic parts and producing creep, embrittlement, hardening and swelling. Chemical composition of materials submitted to high neutron flux, e.g. in fusion reactors, is modified due to the chemical elements' transmutation during nuclear reactions. Thermal and mechanical features of these materials could be altered during the service, as a consequence of nuclear transmutation and alterations of the chemical composition [10, 11].

The problem of long term service of materials submitted to hard mechanical and thermal load requires the application of both traditional investigation techniques (e.g., mechanical tests assessing the macroscopic changes of the characteristics) and advanced NDT, helping to predict ageing and possible fracture. Ageing

and creep resistance, similar to other mechanical properties, depends to a great extent from the micro– and nano–structure (for example, pores, precipitates and dislocation groups) formed in the metals. A non–uniform degradation, besides, can accelerate the advance of cracks favouring the critical reduction of the life of the component and therefore of the system [12].

A fruitful approach consists in the adoption of neutron techniques, obtaining significant advantages in comparison with fractography or with the typical analyses, since they strongly help the solution of main problems and questions associated to the methodological limitations of the traditional characterization. Neutrons, predicted in the 1920 by E. Rutherford and discovered in 1932 by J. Chadwick, have lately become a progressively substantial probe across many disciplines, revealing key properties about materials, and they are ever more helpful in the non-destructive characterisation of industrial materials and parts of nuclear/traditional interests.

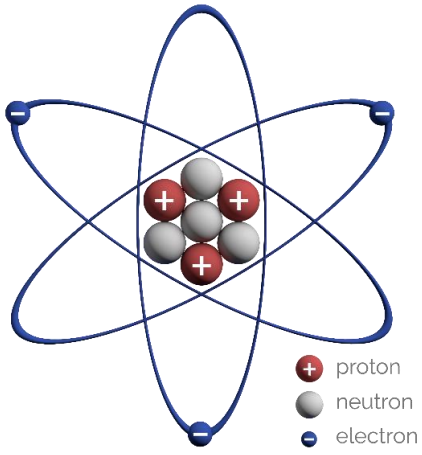

Figure 1. Symbolic representation of an atomic structure

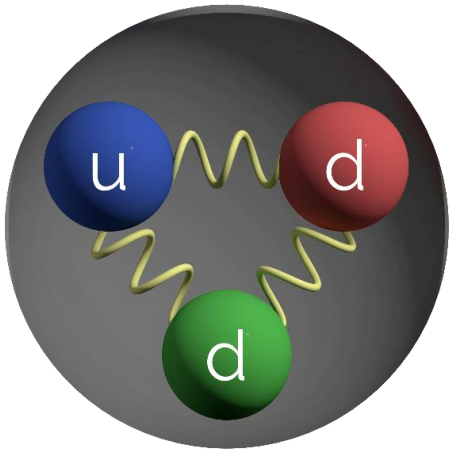

Figure 2. The neutron, containing one up quark and two down quarks

Figure 1 illustrates the atom structure, while Figure 2 represents the neutron.

Industrial applications of neutron techniques are also being developed in various new sectors [13, 14]. Concerning materials and parts obtained from NF decommissioning, the following investigations can be carried out, also providing suggestions to produce parts for new NFs:

– small angle neutron scattering characterization, supplying information at the nano(micro)-scale to check by analyzing specific volumes of the material the evolution of some parameters - e.g., dimension, volume fraction, concentration and interface area - of carbides or other nano(micro)-defects such as porosity, linked with: the degradation and ageing level of the analyzed component; the eventual local deviations in composition and technology [13-15].
– neutron diffraction analysis: to determine internal and sub-surface residual stresses (RS) and their concentration e.g. in correspondence of notches and cracks; to assess the fraction of RS relaxation at the operating temperatures and after a long time; to evaluate the effectiveness of post weld relaxation treatments or the effect of other thermal treatments [13, 14, 17, 18]
– prompt gamma activation analysis to evaluate qualitatively and quantitatively the material's constitutive elements, providing an average composition of the inside material, i.e. of the component in its whole or its fragments [13, 19, 20].

Concerning industrial applications of these techniques, the Rogante Engineering Office has developed special methodological approaches and data processing procedures, adopted in several non-destructive and non-invasive advanced characterization activities [13]. Many studies have been carried out, till now, showing the advantages of adopting neutron techniques to obtain essential data not available by using other means, and the trends in their industrial applications are confirmed, e.g., for the investigations of monolithic and bi–metallic welds, joints based on friction welding, repair welding, effects of radiation on RS and defect formation. Neutron techniques allow also:

– to study the factors monitoring fatigue behaviour of welded components
– to adopt analytical methods to evaluate the total fatigue life of parts subjected to variable-amplitude loading histories and surface treatments, to find possible routes to advance fatigue strength
– to employ probabilistic methods to assess possible nucleation of nano(micro)-cracks within a joint metal (fatigue damage processes) [11, 21].

Acknowledgements

The authors thank Dr. Lorenzo Rogante for his contribution in the graphic realization of Figures 1 and 2.

REFERENCES

[1] Cumo M., (2005), *Experiences and Techniques in the Decommissioning of Old Nuclear Power Plants*, Proc. Workshop on Nuclear Reaction Data and Nuclear Reactors: Physics, Design and Safety, 25 February – 28 March 2002, Trieste, Italy.

[2] *Decommissioning Nuclear Facilities*, (2020), World Nuclear Association, available online: web page https://www.world-nuclear.org/information-library/nuclear-fuel-cycle/nuclear-wastes/decommissioning-nuclear-facilities.aspx (accessed on 04 June 2020).

[3] Cesari F., Rogante M., Giostri A., (2008), *Results of the experimental campaign on contaminated metal components parameters and suggestions for safely NPP component dismantling*, Nuclear Engineering and Design 238, No. 10, p 2801-2810 Netherlands https://doi.org/10.1016/j.nucengdes.2008.05.009

[4] Cesari F.G., Rogante M., Giostri A., (2007), *Precautions arising from the experimental campaign on contaminated metal components parameters for safely nuclear power plant components dismantling*, Transactions, SMiRT 19, Toronto, Canada, p. # W01/4

[5] Cesari F.G., Rogante M., Giostri A., (2006), Conforti G., *Contaminated metal components in dismantling by hot cutting processes*, ASME ICONE14-89451 U.S.A. https://doi.org/10.1115/ICONE14-89451

[6] Cesari F., Giostri A., Rogante M., Sirito E., Sirito M., (2005), *Hot cutting processes and emissions characterization in metal components dismantling*, CAM3S'2005, Gliwice-Zakopane, Poland http://www.acmsse.org/content/plyty/CAMS2005/papers/1258.pdf

[7] Rogante M., Cesari F.G., Migliore G., (2014), *NPP decommissioning: a methodology to evaluate the gaseous emissions produced by thermal cutting processes*, International Nuclear Safety Journal 3 No. 4, p 43-61 U.S.A.

[8] Mido Y., Satake M., (1995), *Chemicals in the Environment*, Discovery Publishing House, New Delhi

[9] Caccin M., Giorgi M., Giacobbo F., Da Ros M., Besozzi L., Mariani M., (2015), *Removal of lead (II) from aqueous solutions by adsorption onto activated carbons prepared from coconut shell*, Desalination and Water Treatment Journal 57 No. 10, p. 4557-4575 United Kingdom

[10] Rogante M., (2014), *Materials and Components From NPP Decommissioning: Opportunities of Investigation by Neutron techniques*, Energy-Environment-Economics, Nova Science Publishers, Hauppauge, New York, Chapter 7, p 109-124 U.S.A.

[11] Rogante M., (2011), *Considerations on the investigation of materials and components obtained from NPP Decommissioning*, Nuclear Power Plants, Series Nuclear Materials and Disaster Research, Physics Research and Technology, Nova Science Publishers, Hauppauge, NY, Chapter 5, pp. 119-138 U.S.A.

[12] Rogante M., Lebedev V.T., (2007), *Nanostructure characterisation by SANS for investigation on ageing*, 31st ESReDA, Smolenice Castle, Slovakia, JRC European Commission, Vuje EUR 22887 EN

[13] Rogante M., (2008), *Applicazioni Industriali delle Tecniche Neutroniche*, 1st Italian Workshop for Industry "Industrial Applications of Neutron Techniques", Civitanova Marche, Italy

[14] Rogante M., Rosta L., (2005), *Nanoscale characterisation by SANS and residual stresses determination by neutron diffraction related to materials and components of technological interest*, Proc. SPIE 5824, p 294-305 https://doi.org/10.1117/12.606090

[15] Glatter O., Kratky O., (1982), *Small Angle X-ray Scattering*, Academic Press, New York, U.S.A. p. 515.

[16] Rietveld H.M., (1969), *Profile refinement method for nuclear and magnetic structures*, Journal of Applied Crystallography, No. 2, p 65-71 United Kingdom

[17] Noyan I.C., Cohen J.B., (1987), *Residual Stress - Measurement by Diffraction and Interpretation*, Springer-Verlag, New York, U.S.A

[18] Rogante M., *Caratterizzazione, mediante scattering neutronico, di materiali e componenti per l'impiantistica nucleare ed industriale*, (1999), Ph.D. thesis, University of Bologna, Italy

[19] Révay Zs., Belgya T., Kasztovszky Zs., Weil J.L., Molnár G.L., (2004), *Cold neutron PGAA facility at Budapest*, Nucl Instrum Meth B No. 213, p 385–388 Netherland https://doi.org/10.1016/S0168-583X(03)01653-7

[20] Révay Zs., Molnár G.L., Belgya T., Kasztovszky Zs., Firestone R.B., (2001), *A new gamma-ray spectrum catalog and library for PGAA*, J Radioanal Nucl Chem No. 248, p 395-399 Switzerland https://doi.org/10.1023/A:1010684210532

[21] Rogante M., Lebedev V.T., Kralj S., Rosta L., Tőrők Gy., (2006), *Neutron techniques for welding project methods development in nuclear/traditional industrial application*, Multidiscipline Modeling in Materials and Structures, No. 2(4), p 419-433 United Kingdom

ISSN 1847-7917

Optimization of density of microwave sintered alumina ceramics due to the corrosion in nitric acid

***Ivana ROPUŠ*[1)], *Hrvoje CAJNER*[2)] *and Lidija ĆURKOVIĆ*[2)]**

1) Energoatest zaštita d.o.o., Potočnjakova 4, 10000 Zagreb, **Croatia**

2) University of Zagreb, Faculty of Mechanical Engineering and Naval Architecture, Ivana Lučića 5, 10000 Zagreb, **Croatia**

ivanaropus@gmail.com,
hrvoje.cajner@fsb.hr,
lcurkovic@fsb.hr

Keywords

alumina ceramic
density
response surface methodology
optimization

Original scientific paper

Abstract: The objective of this study was to investigate and analyse the bulk density of cold isostatically pressed and microwave sintered high purity alumina ceramics. Bulk densities were determined before and after the corrosion in aqueous HNO_3 solutions in a concentration range of 0.5 mol dm^{-3}, 1.25 mol dm^{-3} and 2 mol dm^{-3} with different exposure times – up to 10 days. The influence of temperature (25, 40 and 55 °C) on corrosion was also monitored. Ceramic bulk density was determined by the Archimedes' method. Response surface methodology was used for optimization of density within experimental "sample-corrosive media" area. Exposure to corrosive media was conducted according to the Box-Behnken design. After regression function was defined, conditions to achieve maximal corrosion resistance of sintered ceramics (retention of maximal density achieved after sintering) were determined by optimization within experimental area.

1. Introduction

Alumina (Al_2O_3) ceramics are well known as corrosion resistant materials, highly resistant to vapours and slag up to high temperatures [1–4]. Due to those characteristics, alumina is used in many aggressive environments such as food industry, chemical industry, machine, plant construction, medical application etc. [1,5,6]. However, alumina's chemical resistance depends on the chemical composition of raw powder, granules preparation, shaping and sintering process, as well as conditions at which the final product is exploited [6]. Corrosion resistance of ceramics can be monitored in the way of observing mass loss, change of morphology, mechanical properties (e. g. hardness, fracture toughness) etc. [4,7].

Parameters that influence the chemical resistance of ceramics may be monitored by one factor at a time (OFAT) or according to design of experiment. In contrary to OFAT, design of experiment enables to detect interactions among process factors. Moreover, economically effective and time saving is to monitor the process parameters according to the design of experiment [8–10]. Furthermore, optimal parameters prediction is enabled by optimization within defined experimental "sample-corrosive media" area.

Response surface methodology is often used to understand the impact of independent variables on responses (dependent variable) i.e. to analyse the response of independent variables on different levels [8]. Response surface methodology is also used for optimization purposes [8,9,11–13].

Examples of response surface methodology designs are central composite design (CCD), face centred composite design (FCCD), Box-Behnken design [9]. Number of experiments at three levels without replications of central point that are necessary to conduct the experiment for CCD and FCCD designs are 16 and for Box-Behnken design 13. Lower number of experiments may be decision making point in the case of limitations of the resources available to conduct experiments (time, material etc.).

In framework of this research alumina samples were sintered by hybrid microwave kiln as nonconventional sintering method. As opposed to conventional sintering where heat is conducted from the outside to the inside of the material, in the microwave heating process the heat is generated internally and transferred to the outside of the material. This ensures a uniform microstructure of the final product [14].

This research was conducted in order to understand in a better way the impact of temperature, time and concentration of acid environment on chemical stability of high purity alumina. Furthermore, the aim was to define optimal conditions at which bulk density of microwave sintered alumina exposed to nitric acid (HNO_3) with time and temperature will remain maximal as possible. Box-Behnken design, as response surface methodology design, was used for statistical modelling and analysis of a process in which the response of interest (bulk density) is affected by various variables (temperature, time and concentration of nitric acid).

Symbols

m (A)	- mass of the sample in the air, g	X_0	- actual value of independent variable at centre point
m (B)	- mass of the sample in liquid, g	α	correction factor (atmospheric pressure; α = 0,99985)
R^2	- coefficient of determination, %	ρ	- density, g cm^{-3}
V	- volume of sample, cm^3	ρ_0	- density in liquid, g cm^{-3}
x_i	- coded value of an independent variable	ρ_L	- density in air, g cm^{-3} (ρ_L = 0,0012 g cm^{-3})
X_i	- actual value of independent variable	ΔX	- step change value of independent variable

2. Experimental part

2.1. Materials

Alumina powder (Alteo, France) of high purity (99.83 wt. %) was used in this research. Alumina granules were produced at Applied ceramics d.o.o., Croatia, where they were also cold isostatically pressed in cylindrical shapes. Numbers were engraved on each sample (ceramic's green body) in order to easily follow the properties each one of them during the experiment. Hybrid microwave kiln (OVER industrijska elektronika d.o.o., Croatia) was used for sintering. Magnetron of 1.5 kW at 2.45 GHz was applied. Sintering was conducted isothermally during 1 h at 1600 °C.

2.2. Methods

Sintered cylindrical pellets were rinsed with alcohol and dried in sterilizer at 150 ± 5 °C for 4 h prior to measurements of Archimedes density. After that, pellets were immersed in 10 cm^3 of nitric acid in polypropylene tubes. Concentrations of HNO_3 used in this research were 0.5 mol dm^{-3}, 1.25 mol dm^{-3} and 2 mol dm^{-3}. Sealed tubes containing pellets and nitric acid were held at room temperature, 40 °C and 55 °C for 24 h, 132 h and 240 h, according to Box-Behnken design. After predetermined holding time, samples were taken out from the tubes, rinsed with distilled water and dried in an oven for 3 h at 150 °C in order to measure density of the samples after corrosion test.

Archimedes density (ρ, g cm^{-3}) of alumina samples before and after corrosion experiments was measured by analytical balance Mettler Toledo (Mettler Toledo GmbH, Switzerland) with addition of Mettler Toledo density kit MS-DNY-43 for density measurement. Mass of the samples was measured in the air and then in liquid (distilled water) at known temperature. Density was determined by computing program according to the standard ASTM C373-88 (Standard Test Method for Water Absorption, Bulk Density, Apparent Porosity, and Apparent Specific Gravity of Fired Whiteware Products, Ceramic Tiles, and Glass Tiles).

According to the standard, volume of the sample can be determined as:

$$V = \alpha \frac{m\,(\mathrm{A}) - m(\mathrm{B})}{\rho_0 - \rho_\mathrm{L}}, \qquad (1)$$

and density as:

$$\rho = \frac{m\,(\mathrm{A})}{m\,(\mathrm{A}) - m\,(\mathrm{B})}(\rho_0 - \rho_\mathrm{L}) + \rho_L\,. \qquad (2)$$

2.3. Box-Behnken design

In this research, lower number of experiments was desirable because of duration of the experiment - up to10 days as well as limited availability of the resources necessary to apply during that period. Those were the reasons why Box-Behnken design was chosen as response surface methodology design.

Parameters such as time, temperature and concentration of acid were identified as those influencing the corrosion stability of the alumina ceramics according to the preliminary experiments and literature survey [4,15–19]. Therefore, those parameters were chosen as independent variables for Box-Behnken design (Table 1).

Table 1. Independent variables used in Box–Behnken design

Independent variable	-1 level	0	+1 level
c (HNO_3), mol dm^{-3}	0.5	1.25	2
Temperature, °C	25	40	55
Time, h	24	132	240

Independent values may be coded according to the following equation [20]:

$$x_\mathrm{i} = \frac{X_\mathrm{i} - X_0}{\Delta X} \qquad \mathrm{i} = 1, 2, 3. \qquad (3)$$

Density was observed as response (dependent variable) in this experiment while it is a property of ceramic material that easily may indicate the impact of aggressive media on degradation of material. It may indicate mass loss or change of volume of the ceramic material caused by its exposure to the aggressive media.

The analysis of regression and variance were conducted by Minitab 18® statistical software.

3. Results and discussion

3.1. Model building and statistical significance test

Box-Behnken design with three factors and three levels, as well as 5 replicates of the central point, altogether 17 experiments (Table 2), was used to determine second order response surface. Centre point was run for five times to ensure process stability and inherent variability.

Table 2. Experimental parameters

No	Concentration	Temperature	Time
1	1.25	25	240
2	1.25	40	132
3	2	40	24
4	2	55	132
5	0.5	40	24
6	2	40	240
7	1.25	40	132
8	1.25	40	132
9	0.5	25	132
10	1.25	40	132
11	1.25	40	132
12	1.25	25	24
13	0.5	40	240
14	1.25	55	240
15	2	25	132
16	0.5	55	132
17	1.25	55	24

Analysis of variance was used for statistical analysis. The *p*-value lower than 0.05 was considered as statistically significant. According to ANOVA (Table 3), obtained model consisting of main factors (A, B, C) interaction (AB, AC, BC) and quadratic (A^2, B^2, C^2) factors was significant since *p*-value < 0.05. Moreover, no significant lack of fit of the model was present (*p*-value > 0.05).

The suitability of the model was also confirmed by determination coefficient (R^2) that equals 0.8493 indicating that 84.93 % of the variability in the response could be predicted by the model.

Normal probability plot of observed response (bulk density) is shown at Figure 1(A). Residuals are not showing unwanted convex, concave or S-shape behaviour, indicating that residuals are normally distributed. That means there is sufficient agreement between the actual data and the model data.

Pareto chart allows to understand magnitude and importance of an effect [21–23]. Standardized Pareto chart for density (Figure 1(B)) shows bars proportional to the standardised effect. Red line indicating the *p*-value equals to 0.05. The most significant factors of density of microwave sintered ceramics exposed to aggressive nitric acid are linear and quadratic term of temperature (marked as B and B^2).

Table 3. Analysis of variance of density of alumina sintered in hybrid microwave kiln after exposure to HNO_3

Source	*F* - Value	*p* - Value
Model	4,38	0,0321*
A-c, mol dm^{-3}	4,74	0,0660
B-T, °C	18,47	0,0036
C-t, h	4,50	0,0717
AB	0,01	0,9393
AC	0,02	0,8790
BC	0,10	0,7614
A^2	1,96	0,2040
B^2	9,12	0,0194
C^2	0,21	0,6584
Lack of Fit	3,52	0,1279**

* significant; ** not significant; R^2 = 0,8493

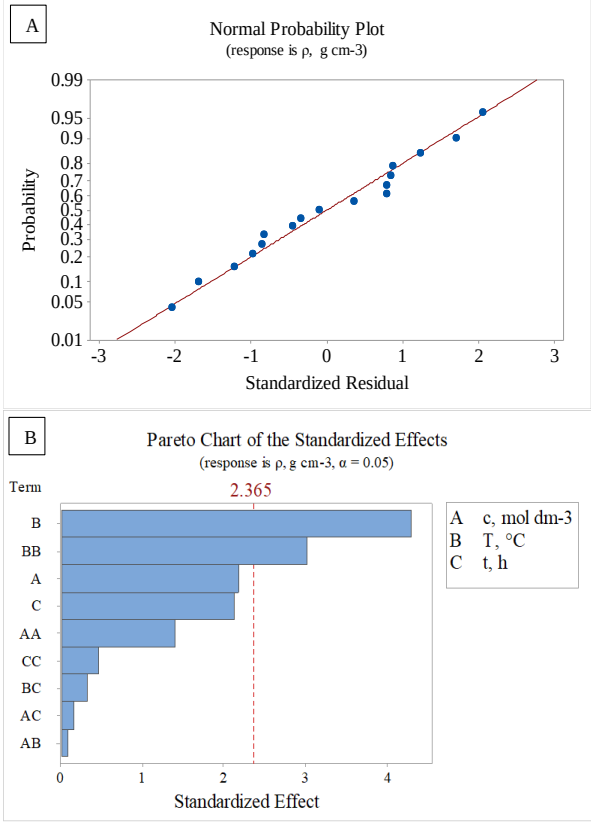

Figure 1. (A) Normal probability plot for density, (B) Pareto chart of the effect (density) obtained by ANOVA

Polynomial model for density is shown in the following equation:

$$Y = 3.77 - 4.875 \cdot 10^{-3}A - 9.625 \cdot 10^{-3}B - 4.75 \cdot 10^{-3}C - 2.5 \cdot 10^{-4}AB + 5 \cdot 10^{-4}AC - 1 \cdot 10^{-3}BC + 4.325 \cdot 10^{-3}A^2 + 9.325 \cdot 10^{-3}B^2 - 1.425 \cdot 10^{-3}C^2, \quad (4)$$

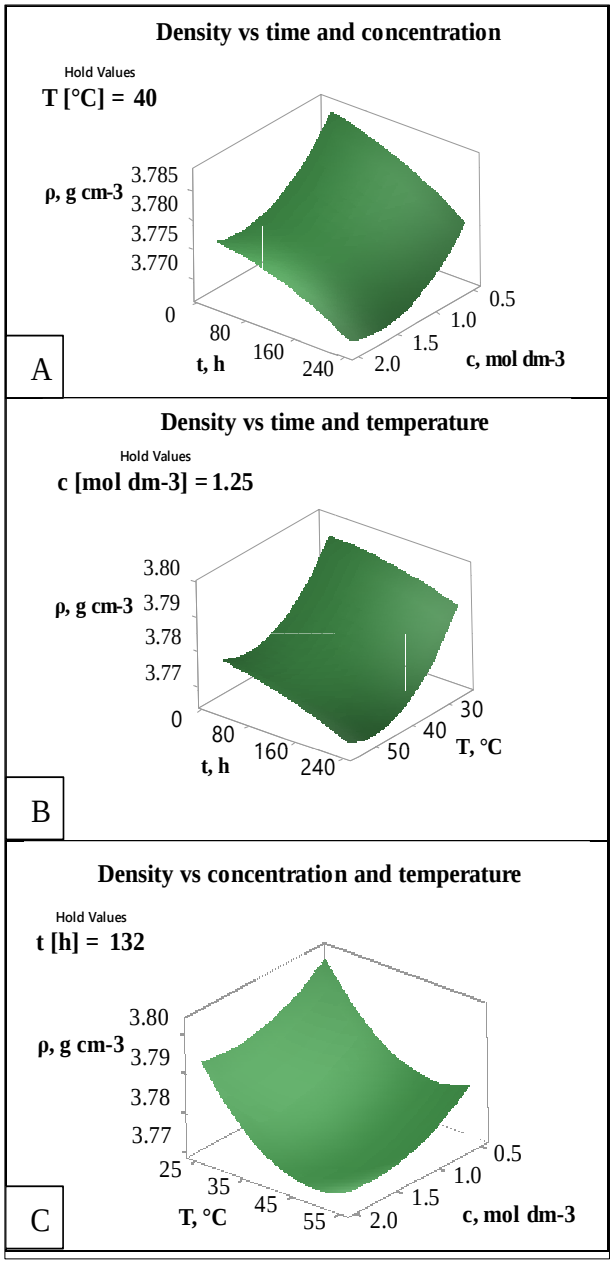

Figure 2. 3D diagram of response surface plots showing the effects of (A) time and HNO_3 concentration at constant temperature (40 °C), (B) time and temperature at constant HNO_3 concentration (1.25 mol dm^{-3}) and (C) HNO_3 concentration and temperature at constant time (132 h) on the density of high purity alumina

Response surface plots of density, representing built model, are shown in Figure 2. It is visible that increase of temperature and concentration with time, leads to the decrease of the density of sintered high purity alumina. Obtained results are contrary to the research of Ćurković et al. [15] where the corrosion stability of conventionally sintered high purity alumina decreased by the decrease of the concentrations of applied acids (HCl and H_2SO_4). It might be that sintering method i.e., obtained morphology, impacts differently the corrosion stability of alumina.
However, density range of high purity alumina sintered in hybrid microwave kiln used in this research, is narrow.

3.2. Optimization

Optimum conditions for the corrosion resistance process of high purity alumina were deduced to achieve minimum decrease of density values i.e., retention of maximal density achieved after sintering.
Methodology of the desired function was used to obtain the optimised process variables. It indicated that lowest temperature (25 °C) and lowest exposure time (24 h) to the lowest nitric acid concentration (0.5 mol dm^{-3}) contribute to the maximum corrosion resistance of the high purity alumina sintered in hybrid microwave kiln with desirability of 91.25 %.

3.3. Verification

Verification of the validity of the optimized conditions was carried out by the experiment at optimized conditions (25 °C, for 24 h at 0.5 mol dm^{-3} HNO_3) to evaluate the experimental results vs predicted values obtained by model equation. The results listed in table 4 show that values obtained by confirmation experiment are within 95 % of predicted values meaning that optimal values are valid under specified range of corrosion process variables.

Table 4. Verification of experimentally obtained values of density and density values predicted by the model at optimal corrosion resistance conditions

Response	Experimental value	Predicted value	Low CI (95 %)	High CI (95 %)
Experimental conditions: 0.5 mol dm^{-3} HNO_3, 25 °C, 24 h, desirability 91 %				
ρ, g cm^{-3}	3.8150	3.8053	3.7878	3.8228

4. Conclusion

In this research high purity alumina ceramics sintered by means of hybrid microwave sintering method was tested under aggressive conditions to explore its corrosion resistance. Bulk density of alumina ceramics was determined before and after the corrosion in three different concentrations of HNO_3 solutions, different exposure times – up to 10 days at three different temperatures (25, 40 and 55 °C).
Box-Behnken response surface design was used to conduct the experiment, build the regression function and to predict optimal corrosion resistance values in order to define minimum decrease of density values i.e., retention of maximal density achieved after sintering. Within

experimental area optimal corrosion resistance conditions are achieved at 25 °C for 24 at 0.5 mol dm^{-3} HNO_3. Results obtained by the quadratic model were verified by the experiment. Experimental results are in the range of 95 % of confidential interval of obtained model confirming suitability of the model to predict the corrosion resistance of the monitored ceramics within experimental area.

High purity alumina sintered in hybrid microwave kiln may be considered resistant to nitric acid at given conditions.

Further research may be taken in the way of determining the impact of sintering methods (conventional and non-conventional) on the chemical stability of high purity alumina within monitored experimental area.

Acknowledgements

This work has been fully supported by the Croatian Science Foundation within the project IP-2016-06-6000: Monolithic and Composite Advanced Ceramics for Wear and Corrosion Protection (WECOR).

REFERENCES

[1] Vukšić M., Žmak I., Ćurković L., Ćorić D., (2019), Effect of Additives on Stability of Alumina—Waste Alumina Suspension for Slip Casting: Optimization Using Box-Behnken Design, Materials, 12, p 1–16

[2] Žmak I., Ćorić D., Mandić V., Ćurković L., (2020), Hardness and Indentation Fracture Toughness of Slip Cast Alumina and Alumina-Zirconia Ceramics, Materials, 13, p 1–17

[3] Hirata T., Ota S., Morimoto T., (2003), Influence of impurities in Al2O3 ceramics on hot corrosion resistance against molten salt, Journal of the European Ceramic Society, 23, p 91–97

[4] Medvedovski E., (2013), Influence of corrosion and mechanical loads on advanced ceramic components, Ceramics International, 39 No 3, p 2723–2741

[5] Frankel GS., Vienna JD., Lian J., Scully JR., Gin S., Ryan J V., et al., (2018), A comparative review of the aqueous corrosion of glasses, crystalline ceramics, and metals - review, Npj Materials Degradation, 2 No 1, p 1–17

[6] Wu T., Zhou J., Wu B., (2017), Effect of Y2O3 on acid resistance of alumina ceramic, Ceramics International, 43 No 6, p 5102–5107

[7] Baitalik S., Kayal N., (2017), Processing and properties of cordierite-silica bonded porous SiC ceramics, Ceramics International, 43 No 17, p 14683–14692

[8] Yolmeh M., Jafari SM., (2017), Applications of Response Surface Methodology in the Food Industry Processes, Food and Bioprocess Technology, 10 No 3, p 413–433

[9] Mäkelä M., (2017), Experimental design and response surface methodology in energy applications: A tutorial review, Energy Conversion and Management, 151, p 630–640

[10] Wahid Z., Nadir N., (2013), Improvement of one factor at a time through design of experiments, World Applied Sciences Journal, 21, p 56–61

[11] Chaker H., Ameur N., Saidi-Bendahou K., Djennas M., Fourmentin S., (2020), Modeling and Box-Behnken design optimization of photocatalytic parameters for efficient removal of dye by lanthanum-doped mesoporous TiO2, Journal of Environmental Chemical Engineering, 1 No 9, p 104584

[12] Wahyudi S., Gapsari F., Awali H., (2014), Optimization of Chemical Environment Condition towards Corrosion Rate of Sulfuric Acid Resistant Alloy Metal (Saramet) using Response Surface Methodhology, Applied Mechanics and Materials, 493, p 733–738

[13] Li J., Peng J., Guo S., Zhang L., (2013), Application of response surface methodology (RSM) for optimization of the sintering process of preparation calcia partially stabilized zirconia (CaO-PSZ) using natural baddeleyite, Journal of Alloys and Compounds, 574, p 504–511

[14] Ćurković L., Veseli R., Gabelica I., Žmak I., Ropuš I., Vukšić M., (2021), A Review of Microwave-Assisted Sintering Technique, Transactions of FAMENA, 1 No 45, p 1–16

[15] Ćurković L., Fudurić Jelača M., Kurajica S., (2008), Corrosion behavior of alumina ceramics in aqueous HCl and H2SO4 solutions, Corrosion Science, 50, p 872–878

[16] Kurajica S., Ćurković L., Tkalčec E., Mandić V., (2013), Acid corrosion behavior of sol – gel-prepared mullite ceramics with and without addition of lanthanum, Journal of the American Ceramic Society, 96 No 3, p 923–927

[17] Gutiérrez AV., Cuevas JL., Ángeles AG., Pilalua N., (2019), Addition of ceramics materials to improve the corrosion resistance of alumina refractories, SN Applied Sciences, 1 No 7, p 1–7

[18] Ćurković L., Fudurić Jelača M., (2009), Dissolution of alumina ceramics in HCl aqueous solution, Ceramics International, 35, p 2041–2045

[19] Schacht M., Boukis N., Dinjus E., (2000), Corrosion of alumina ceramics in acidic aqueous solutions at high temperatures and pressures, Journal of Materials Science, 5, p 6251–6258

[20] Pasma SA., Daik R., Maskat MY., Hassan O., (2013), Application of Box-Behnken design in optimization of glucose production from oil palm empty fruit bunch cellulose, International Journal of Polymer Science, 2013, p 1-8

[21] Douglas C. Montgomery GCR., (2003), Applied Statistics and Probability for Engineers. 3rd ed. John Wiley & Sons, Inc., New York

[22] Spoerk M., Gonzalez-Gutierrez J., Lichal C., Cajner H., Berger GR., Schuschnigg S., et al., (2018), Optimisation of the adhesion of polypropylene-based materials during extrusion-based additive manufacturing, Polymers, 10 No 5, p 490

[23] Spoerk M., Arbeiter F., Cajner H., Sapkota J., Holzer C., (2017), Parametric optimization of intra- and inter-layer strengths in parts produced by extrusion-based additive manufacturing of poly(lactic aci*d)*, Journal of Applied Polymer Science, 134 No 41, p 1–15

ISSN 1847-7917

Cell cytoskeleton structure and conduction of environmental biophysical signals through microtubules and microfilaments

Claudio SANTELLI
Santelli Medical Office, Viale Europa n. 81, 63831 Rapagnano (FM), **Italy**
claudiosantelli8@gmail.com

Keywords
Biological structural materials
Cytoskeleton
Microtubules
Microfilaments
Environment protection

Review article
Abstract: The cytoskeleton, as biological structural material made up of different types of fibrous protein structures (microtubules, microfilaments and intermediate filaments), creates a cytoplasmic structural scaffold. In microtubules and microfilaments, the ability to transmit environmental information from the cell membrane to the nuclear membrane to control gene expression has been demonstrated. In recent experiments conducted by VID art/science (www.vidartscience.org), it has been highlighted that the microtubules of adult stem cells emit different electromagnetic spectra in response to sound signals produced during a live artistic performance. In this paper, the histological structure of the cell cytoskeleton and the review of the functions of support, mobility, duplication and conduction of intra and extra cellular biophysical signals are described. New perspectives are opened both for regenerative and antiaging medicine and for the understanding of the epigenetic effects that art and environment exert on biology.

1. Introduction

Inside the cell, the cytoplasm surrounding the various organelles was originally considered to be devoid of any structural characteristics considering that the various intracellular organelles (mitochondria, Golgi apparatus, ribosomes, etc.) were free to float in the cytoplasmic solution [1]. Subsequent research revealed that the cytoplasmic ground substance, on the contrary, is supported and stabilized by a complex three-dimensional network of cytoskeletal elements. The cytoskeleton, formed by different types of fibrous structures (Microtubules, Intermediate Filaments, Microfilaments) (Figure 1), connected by a series of transverse protein bridges, creates a cytoplasmic scaffold that extends from the plasma membrane to the nuclear envelope.

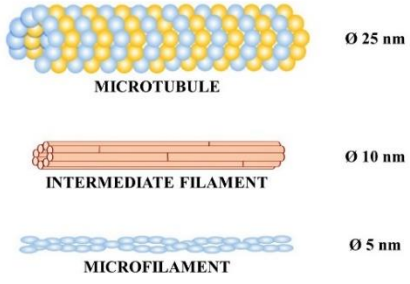

Figure 1. Cytoskeleton components (Microtubule, Intermediate filament, Microfilament)

The microtubules are formed by 13 protofilaments composed of dimers of two proteins (tubulin α and tubulin β): they are hollow inside and have a diameter of about 25 nm (Figure 2).

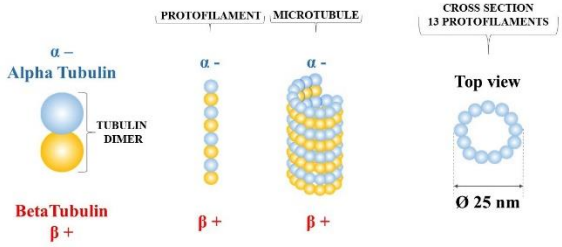

Figure 2. Microtubule structure

The ends of the microtubules are polarized. Tubulin α - and tubulin β + represent an oscillating electric dipole.
The microtubules create their mobility thanks to structural instability as they polymerize and depolymerize continuously [2] (Figure 3).
This cytoskeletal network that orders and supports the different membranous structures, organelles and cytoplasm is composed, for the most part, of proteins that make the structure highly dynamic, in continuous assembly/disassembly, able to modify its appearance and spatial structure as the cell develops, differentiates, and moves.

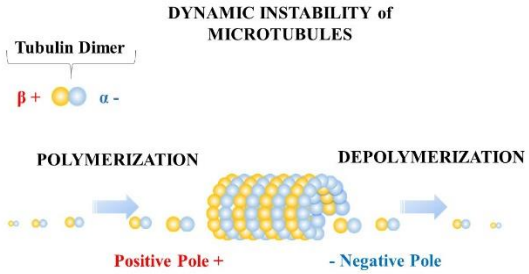

Figure 3. Dynamic instability of Microtubules

Microfilaments are globular protein formations of actin with a diameter of approximately 5 nm (Figure 4).

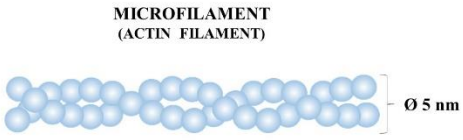

Figure 4. Microfilament structure

The elements of the cytoskeleton are mainly involved in the shape of the cell (especially the Intermediate Filaments with a diameter of about 8-10 nm, which are the most rigid), in cell duplication, in cell movement, in the formation of cilia, in cell polarization and, as biomechanical conduits, in favouring the transport of molecules through protein molecular motors (Kinesin and Dynein).

The most recent studies have highlighted the ability to receive and transmit signals of physical information (electrical, mechanical, electromagnetic, vibrational, etc.) intra and extra cellular that can modulate gene expression. The ability of microfilaments and microtubules to conduct electrons and ions has already been documented. The dynamics governing the transmission of information have been extensively studied by the pioneering work of Fisher, Shannon and others [3].

The cell membrane, as the interface between a cell and its environment, is the site where much of this environmental information is received via its surface receptors [3] and it is able to detect, process and respond rapidly to external threats and opportunities [4].

Cytoskeletal structures function as information channels. An environmental perturbation that causes a transmembrane flow of ions from the adjacent cytoplasm generates a transient ion gradient along the cavity of a microtubule or a potential gradient along the microfilament that forms a wire conductor for the ion flow. Signal transmission through the ion flow along the cytoskeleton is highly optimized. In particular, the microtubules carry coarse-grained Shannon information in the centrosome (containing two centrioles) and adjacent to the nucleus for a rapid and dynamic assessment of the environment. The microfilaments, which generally connect to the protein complexes of the nuclear envelope, transmit the maximum fine-grained Fisher information by transmitting detailed information on the spatial and temporal variations of the environment to the nucleus [3]. Microfilaments and microtubules often interface through direct physical contact and through cross-linking proteins. This suggests a complex network for signal transmission and analysis [3] (Figure 5).

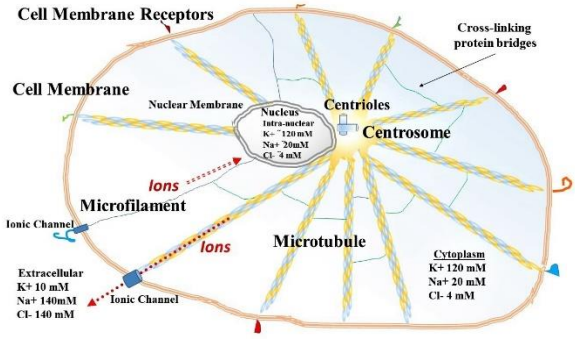

Figure 5. Cytoskeleton structure

Microfilaments, which are composed of highly negative surface charge actin, are highly conductive and transmit information showing fluctuations in the order of microseconds (fine grain) via ion waves and solitons [3], [5]. The finding that microtubular activity is associated with the generation of electric fields, potentially capable of spreading information through cells, provides new clues for understanding intra- and inter-cellular communication [6]. Some proteins have characteristics of the "helix-loop-helix" type and can be considered as oscillatory units, with alpha-helices comparable to oscillating springs and the loops that act as connectors between oscillators. Proteins are phase-resonant vibrational units and, through the use of the "Near-Terahertz Field Microscopy", it has recently been possible to record their vibrations. The proteins of the body vibrate, with different frequencies, like the strings on a violin. Mostly cellular proteins "walk" on microtubules with the help of "molecular motors", such as kinesins and dyneins [6] (Figure 6). The molecules involved in cellular information could be considered as oscillators walking on the elastic network of the cytoskeleton, in which the microtubules act as dissipative

structures of the vibrational differences between the various oscillators until synchronization is achieved.

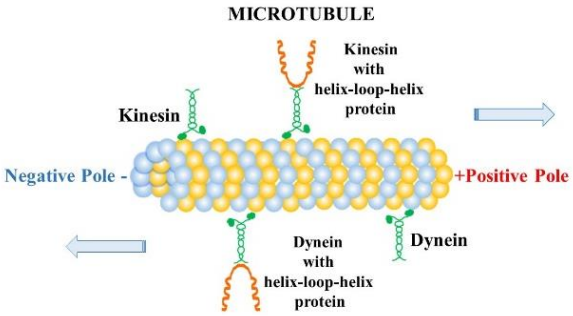

Figure 6. Transport of helix-loop-helix protein by molecular motors Kinesin and Dynein on the surface of a microtubule

Thanks to the network of connections of the cytoskeleton, the synchronization between cellular oscillators could be transmitted, by resonance, to the cell surface and recorded [6].

Heritable information in the genome encodes the structure and function of cellular macromolecules, but this information remains fixed over time. On the contrary, a cell must access, analyse and respond quickly and continuously to a wide range of spatial and temporal information interacting dynamically with the external environment. Since the genome does not have the ability to locate external signals, however, the cell membrane, via its surface receptors, is the site where most of the external information is received and processed [7].

The cytoskeleton then conducts this information towards the nucleus through electromagnetic signals and mechanical vibrations and it has the ability to communicate also through the emission of light with frequencies close to infrared [6].

In photobiomodulation, in fact, light - with frequencies close to infrared - can modulate stem cells and stimulate them to differentiate [8].

By sending electromagnetic waves with different frequencies on microtubules growing in vitro, with the "tunnel effect microscopy" (STM, Scanning Tunnelling Microscopy), resonances between the structure of the tubulin protein and the applied electromagnetic field were identified. There is an increasing evidence that mechanical vibration affects stem cells and organ physiology. Pressure waves, such as sound waves, could also affect cells by generating micro-vibrations or resonances [6].

An important demonstration was given by the "Cell Melodies" live experiment conducted in Bologna in 2016 by the artists and scientists movement (VID art / science www.vidartscience.org) curated by Prof. Carlo Ventura of the University of Bologna, Italy, and Julia von Stietencron with the participation of the drummer Mildford Graves, the actor Alessandro Bergonzoni and of adult human stem cell cultures visualized by a multispectral imaging (MSI) microscope capable of detecting the electromagnetic emission (light) spectra produced by the stem cells. Such MSI microscope revealed that human stem cells produce very different electromagnetic emission spectra in response to the different sound, vocal and musical signals produced by the artists. For the first time, the authors of the experiment provided evidence that human stem cells are able to respond with different vibrational characteristics to the sound generated by the artists in the form of music or vocal dialogues in live performances [9].

As demonstrated by recent studies conducted by Prof. Ventura, this latter function has important prospects both for regenerative medicine for the possibility of modulating, through specific signals, the differentiation potential of stem cells, as well as for counteracting the process of cellular aging through the elongation of the telomere of chromosomes [10] and the optimization of cell polarity [6].

Polarization is a fundamental property of cellular health, being the result of the modulation of ion fluxes and oscillatory dynamics of microtubules. The results indicate that the response of stem cells to physical energy applied by means of an electromagnetic field can restore cell polarity, improving physiological processes [11].

These aspects, furthermore, can represent a new paradigm in the virtuous relationship between "Environmental Protection" and psycho-physical well-being. All interventions that protect and improve the environment in which we live and work can provide biological well-being through the biophysical signals received and processed by the dynamic network of microtubules and microfilaments of the cell cytoskeleton. The care of the landscape, the historical-artistic redevelopment of the villages, the insertion of environmental sculptures, the "site specific" artistic and musical events acquire a new value, not only economic and tourist, but also health-conscious.

Acknowledgements

Prof. Franco Rustichelli and Dr. Ing. Massimo Rogante are acknowledged for useful discussions.

The VID art / science international movement of artists and scientists created by Prof. Carlo Ventura and Julia von Stietencron is also acknowledged, for kindly allowing me to refer to their illuminating and magnificent "Cell Melodies" live experiment.

REFERENCES

[1] Wolfe S.L., (1996), *Introduzione alla Biologia Cellulare e Molecolare*. EdiSES s.r.l. Napoli, Italy

[2] Kapoor, V., Hirst, W.G., Hentschel, C., Preibisch S., Reber S., (2019), *MTrack: Automated Detection, Tracking, and Analysis of Dynamic Microtubules*,

Scientific Reports 9, 3794 United Kingdom https://doi.org/10.1038/s41598-018-37767-1

[3] Frieden, B.R., Gatenby, R.A., (2019), *Signal transmission through elements of the cytoskeleton form an optimized information network in eukaryotic cells*, Scientific Reports 9, 6110 United Kingdom https://doi.org/10.1038/s41598-019-42343-2

[4] Gatenby, R.A., (2019), *The Role of Cell Membrane Information Reception, Processing, and Communication in the Structure and Function of Multicellular Tissue* Int. J. Mol. Sci. 20 No. 15, 3609 Switzerland https://doi.org/10.3390/ijms20153609

[5] Adamatzky, A., Huber, F., Schnauß, J., (2019), *Computing on actin bundles network*, Scientific Reports 9, 15887 United Kingdom https://doi.org/10.1038/s41598-019-51354-y

[6] Ventura C., Gullà D., Graves M., Bergonzoni A., Tassinari R., Cavallini C., Von Stietencron J., (2017), *Melodie cellulari - Elettromagnetismo, Musica e Suono della voce per parlare alle dinamiche più profonde della nostra biologia*, La Medicina Biologica 3, p 3-9 Italy https://medibio.it/medicina-biologica/2013/163/1242/pdf/MB1703_01.pdf

[7] Frieden, B.R., Gatenby R., (2020), *Ion-Based Cellular Signal Transmission, Principles of Minimum Information Loss, and Evolution by Natural Selection."* Int. J. Mol. Sci. 21, No. 1, 9 Switzerland https://doi.org/10.3390/ijms21010009

[8] Zomorrodi, R., Loheswaran, G., Pushparaj, A., Lim L., (2019), *Pulsed Near Infrared Transcranial and Intranasal Photobiomodulation Significantly Modulates Neural Oscillations: a pilot exploratory study*, Scientific Reports 9, 6309 United Kingdom https://doi.org/10.1038/s41598-019-42693-x

[9] Ventura C., Gullà D., Graves M., Bergonzoni A., Tassinari R., Von Stietencron J., (2017), *Cell melodies: when sound speaks to stem cells*, CellR4 5 No. 2, e2331 U.S.A. https://www.cellr4.org/article/2331

[10] Rinaldi S., Maioli M., Pigliaru G., Castagna A., Santaniello S., Basoli V., Fontani V., Ventura C., (2014), *Stem cell senescence. Effects of REAC technology on telomerase-independent and telomerase-dependent pathways* Scientific Reports 4, 6373 United Kingdom https://doi.org/10.1038/srep06373.

[11] Florian M.C., Geiger H., (2010), *Concise review: polarity in stem cells, disease, and aging*, Stem Cells 28, p 1623-1629 U.S.A. https://doi.org/10.1002/stem.481

ISSN 1847-7917

Determination of the friction coefficient of 3D printed materials

Part I – Rolling Friction

Nikolay STOIMENOV, Stanislav GYOSHEV, Miglena PANEVA and Peter PANEV
Institute of Information and Communication Technologies – Bulgarian Academy of Sciences, Acad. G. Bonchev str., bl. 2, 1113 Sofia, **Bulgaria**

nikistoimenow@gmail.com
stanislavgyoshev@mail.bg
m.paneva7@gmail.com
panevv@gmail.com

Professional article

Abstract: For most 3D printing materials, the basic physical and mechanical parameters such as tensile strength, modulus of elasticity, and coefficient of elongation are known and investigated. The coefficients of friction of the materials relative to each other and other materials are not determined. This paper is considered the determination of the coefficient of friction in rolling 3D printed spheres of different materials (PLA, PETG, Flex, and Stainless Steel). The aim is to determine the coefficient more precisely, thus in the presented work experiments with different diameters of the sphere for each of the listed materials are made. Experiments have also been made with different pairs of materials.

Keywords
Rolling
Friction
3DPrinting
3DModelling
3DMaterials

1. Introduction

The milling processes are widely used in different technological operations such as the mining industry, food, pharmacy, etc. The milling processes of different materials is an important industrial process in which the material is crushed and milled to a certain pre-desired size by the interaction between material, grinding bodies, and grinding media. The milling in most cases is carried out with the help of grinding bodies and grinding media (lifters / internal lining), which are subjected to an aggressive working environment, in addition to the grinding bodies themselves. The grinding process is extremely energy-intensive (worldwide about 20% of the energy is used for this process). For this reason, it has been widely researched. Of great importance is the proper functioning of the mill, grinding bodies, lifters, speed, separation angle (shoulder angle), angle of incidence (toe angle), and other factors to achieve good performance and high productivity. Costs in the process of grinding (enrichment) of copper ore are as follows: for electricity are allocated 50%, for grinding bodies about 30%, about 10% for lining (lifters) of mills, and 10% for labor and other costs [1]. The experiments with industry mills are expensive and time-consuming. The experiments with modeling and simulations are preferable in that type of experiments. For a proper simulation, all input parameters must be set up as much as possible to the original one. For simulation and investigation of the interaction between grinding bodies and media, it must be set parameters such as coefficient of rolling friction, coefficient of static friction, coefficient of restitution, etc. The rolling friction coefficient is an important parameter that is frequently used in numerical simulations but without proper justification for its value [2]. The paper aims to determine the coefficient of rolling friction of 3D printed materials, which will be used for simulation modeling.

Symbols

r	- Ball radius, *mm*	*CRF*	- Coeficient of rolling friction
m	- Mass of the ball, *kg*	f	- Static friction
g	- acceleration due to gravity, ms^{-2}		
F	- frictional force, *N*	**Greek letters**	
N	- normal force, *N*	μ	- Coefficient of friction
COF	- Coeficient of friction	θ	- Angle of inclination

2. Coefficient of friction

The coefficient of friction (COF), often symbolized by the Greek letter μ, is a dimensionless scalar value which describes the ratio of the force of friction between two bodies and the force pressing them together. The coefficient of friction depends on the materials used; for example, ice on steel has a low coefficient of friction, while rubber on pavement has a high coefficient of friction. Coefficients of friction range from near zero to greater than one. It is an axiom of the nature of friction between metal surfaces that it is greater between two surfaces of similar metals than between two surfaces of different metals hence, brass will have a higher coefficient of friction when moved against brass, but less if moved against steel or aluminium [3], [4], and [5]. Coulomb friction, named after Charles-Augustin de Coulomb, is an approximate model used to calculate the force of dry friction. It is governed by the model:

$$F = \mu N \quad (1)$$

Where:

F- is the force of friction exerted by each surface on the other. It is parallel to the surface, in a direction opposite to the net applied force.

μ- is the coefficient of friction, which is an empirical property of the contacting materials,

N- is the normal force exerted by each surface on the other, directed perpendicular (normal) to the surface.

The COF is the ratio of a force to a force and hence has no units.

The Coulomb friction F may take any value from zero up to μN, and the direction of the frictional force against a surface is opposite to the motion that surface would experience in the absence of friction.

The COF is an empirical measurement – it has to be measured experimentally, and cannot be obtained by calculations.

2.1. Rolling friction

When an object rolls over a surface, it experiences resistance to its motion. This resistive force is a type of kinetic friction and known as rolling friction [4, 5]. The point at which the object is in contact with the surface is critical in understanding rolling friction. At this point, both the object and the surface deform due to factors like elasticity, weight, and roughness. The cause of rolling friction is the mentioned deformation. The constant of proportionality is called the coefficient of rolling friction. It takes a constant value depending on the nature and material of the surfaces. The rolling friction also is known as rolling resistance.

The rolling friction over an inclined surface is shown in Figure. 1. It is shown a rigid body with radius (r) of rolls down a plane inclined at an angle (θ) with the horizontal. When a body is placed on an inclined plane, it tries to slip down and hence a static friction (f) acts upwards. This friction provides a torque which causes the body to rotate. The normal force (as the contact surface reaction) is:

$$N = mg\cos\theta. \quad (2)$$

The basic equilibrium equations for the ball rolling on the inclined surface lead to expression for the calculation of the coefficient of the rolling friction as:

$$CRF = \tan\theta \quad (3)$$

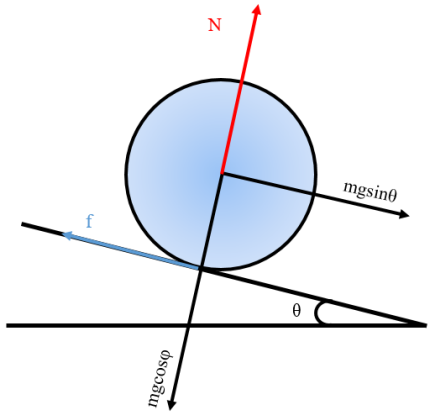

Figure 1. Coefficient of rolling friction

3. Experimental setup

3.1. Sample preparation

The tested samples were produced with a 3D printer. 3D printing is a modern technology that provides various new possibilities for complex-shaped objects to be made. It helps designers, based on a CAD model, to build real objects [6]. This technology is already making a significant impact in numerous fields such as industry, agriculture, and medicine [7], [8], and [9]. Fused deposition modeling (FDM) is one of the most common additive manufacturing techniques, comprising extrusion of thermoplastic filaments for deposition as layer by layer [7]. Among other thermoplastic (filaments) materials utilized in the FDM technique, ABS, PLA, PETG, and PC are the most popular ones [9]. The printed sample materials were with the following settings: a dimension of the printed surface – 120x60x10 mm; Infill surfaces – 20%; Spheres with a radius of 4.5 mm; Layer thickness – 0.16 mm. The printing temperature, as well as the printing speed, was different for the different materials, in compliance with the manufacturer's requirements.

3.2. Test preparation

For the experimental determination of the rolling friction coefficient is used one of the six categories, which can be used – the gravitation-based device [10]. On the gravitation-based device, shown in Figure 3 is mounted 3D printed material plate. The test was performed with pairs as follows: PLA+PLA; PLA+PETG; PLA+Steel; PETG+PLA; PETG+PETG; PETG+Steel; Flex+PLA; Flex+PETG; Flex+Steel. For each material pairs were performed with 3 experimental tests, and the average result was taken. Part of the experimentally tested angles are shown in Figure 4 (a – pair PLA+PETG; b – pair PETG+PLA; c – pair Flex+Steel), where is taken the moment when the object rolls over a surface. A graph of the rolling friction pairs is shown in Figure 5.

Figure 2. Coefficient of rolling friction

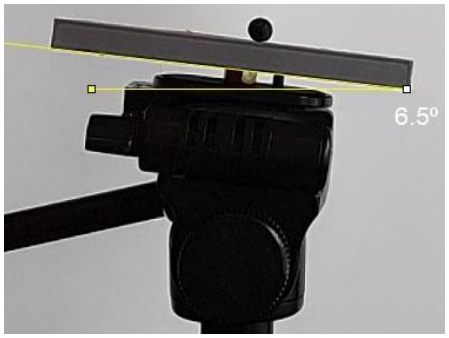

a – pair PLA+PETG;

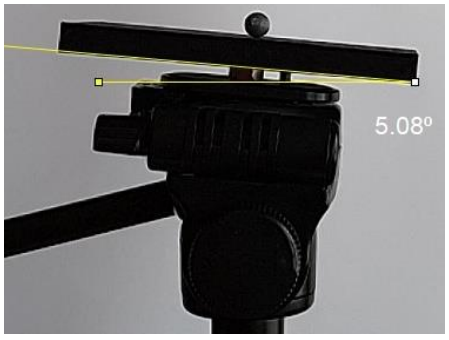

b – pair PETG+PLA;

c – pair Flex+Steel.

Figure 3. Coefficient of rolling friction in different material pairs.

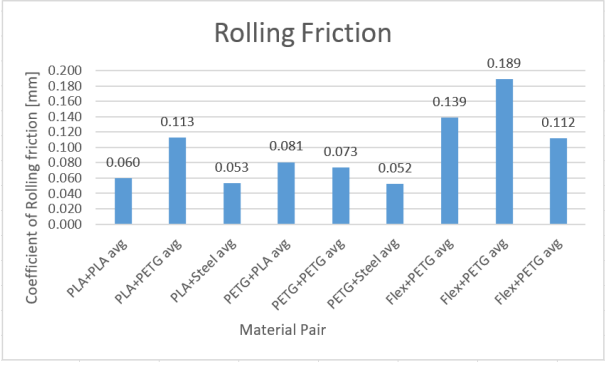

Figure 4. Rolling friction material pairs

4. Future work

The experimentally determined coefficients of rolling friction will be used for setting the parameters of a specialized software EDEM Software, used mostly for modeling and optimization of milling processes. The measured coefficient of rolling friction gives more accurate results in the simulation process. The coefficient of rolling friction must not be underestimated. If the coefficient is not set to the required one, mistakes and discrepancies can occur. If the coefficient is calibrated properly, the results would be closer to the real ones [11, 12]. The simulations from the software will be verified with a laboratory mill.

5. Conclusion

The coefficient of rolling friction was experimentally determined by the gravitation-based device method. The rolling friction coefficients were conducted with different material pairs as follows: PLA+PLA; PLA+PETG; PLA+Steel; PETG+PLA; PETG+PETG; PETG+Steel; Flex+PLA; Flex+PETG; Flex+Steel. The material pairs, except Steel material, were 3D printed by FDM 3D Printer. The experimentally obtained results will be used for simulations in EDEM Software aiming at optimization of the interaction between grinding bodies and media with innovative shapes.

Acknowledgments

This research was carried out as part of the project № KP-06-N47/5 "Research and optimization of the interaction between grinding bodies and media with an innovative shape", financed by the Bulgarian National Science Fund.

REFERENCES

[1] *Metso Crushing and screening solutions* – Brochure www.metso.com – last visited June 2021.

[2] Jankowiak T., Rusinek A., List G., Sutter G., Abed F., *Numerical analysis for optimizing the determination of dynamic friction coefficient*, Tribology International, Volume 95, pp. 86-94, ISSN 0301-679X, 2016.

[3] Piljek P., Keran Z., Pavličić L., Horvatic A., Runje B., *Experimental and Numerical Determination of Friction Coefficient in Metal Forming Processes*, 8th International Conference on Mechanical Technologies and Structural Materials (MTSM 2019), Split, Croatia, September 26-27, 2019, Croatian Society for Mechanical Technologies, Croatia, ISSN: 1847-7917, pp. 133-138

[4] J O Bird BSc, CEng, MIEE, CMath, FIMA, FCollP, MIEIE, P J Chivers BSc, Ph.D., in Newnes *Engineering and Physical Science Pocket Book*, 1993

[5] V.N. Malyshev, in Advances in *Friction-Stir Welding and Processing*, Woodhead Publishing, ISBN: 978-0-85709-454-4, 2014

[6] N. Ayrilmis, M. Kariz, J.H. Kwon, M. Kitek Kuzman, *Effect of printing layer thickness on water absorption and mechanical properties of 3D-printed wood/PLA composite materials*, Int. J. Adv. Manuf. Technol., 102 (5-8) (2019), pp. 2195-2200, 10.1007/s00170-019-03299-9

[7] H. Bikas, P. Stavropoulos, G. Chryssolouris, *Additive manufacturing methods and modelling approaches: a critical review*, Int. J. Adv. Manuf. Technol., 83 (1-4) (2016), pp. 389-405, 10.1007/s00170-015-7576-2

[8] H. Rezayat, W. Zhou, A. Siriruk, D. Penumadu, S.S. Babu, *Structure–mechanical property relationship in fused deposition modelling*, Mater. Sci. Technol., 31 (8) (2015), pp. 895-903, 10.1179/1743284715Y.0000000010

[9] J.T. Cantrell, S. Rohde, D. Damiani, R. Gurnani, L. DiSandro, J. Anton, A. Young, A. Jerez, D. Steinbach, C. Kroese, P.G. Ifju, *Experimental characterization of the mechanical properties of 3D-printed ABS and polycarbonate parts*, Rapid Prototyp. J., 23 (4) (2017), pp. 811-824, 10.1108/RPJ-03-2016-0042

[10] Ünlü B.S., Atik E., *Determination of friction coefficient in journal bearings*, Materials & Design, Volume 28, Issue 3, pp. 973-977, ISSN 0261-3069, 2007

[11] Song X., Zhang G., *The role of the friction coefficients in the granular segregation in small systems*, Powder Technology Vol. 372, pp. 40-47, ISSN: 0032-5910, 2020

[12] Xiong G., Gao Z., Hong C., Qiu B., Li S., *Effect of the rolling friction coefficient on particles' deposition morphology on single fibre*, Computers and Geotechnics, Vol. 121, 103450, 2020

ISSN 1847-7917

Fatigue numerical analysis comparison on bicycle pedal example using different software

Kenan VARDA[1)]***, Ernad BEŠLAGIĆ***[1)]***, Josip KAČMARČIK***[1] ***and Nermina ZAIMOVIĆ-UZUNOVIĆ***[1)]

1) Mašinski fakultet, Univerzitet u Zenici Fakultetska 1, 72000 Zenica, **Bosna i Hercegovina**

kenan.varda@unze.ba
ernad.beslagic@unze.ba
josip.kacmarcik@unze.ba
nermina.zaimovic.uzunovic@unze.ba

Original scientific article

Abstract: The topic of this paper is the analysis of the stress states and material fatigue on the example of a bicycle pedal. The bicycle pedal was made of unnotched 6061-T6 aluminum alloy and the data used in the analysis were created using the S/N curve for a given material. In the SolidWorks Simulation and Ansys software, a static load was applied on the pedal and Von Mises stresses and locations with the highest deformation were obtained. After that, a numerical analysis of material fatigue was created and the results for three parameters were obtained. Those parameters are damage, life and load factor. These numerical simulations represented a stress cycle with an alternating stress above the endurance limit and show a measurable permanent damage in few locations.

Keywords

Fatigue
Analysis
Damage
Pedal

1. Introduction

This paper is a classic example of the application of numerical simulations in the testing of a machine part, in this case the bicycle pedal. As is known, numerical simulations are increasingly used in the testing of machine parts subjected to different loads. On the example of a bicycle pedal, a numerical simulation of fatigue and the number of cycles that the pedal can withstand before entering the plastic area, i.e., the area of permanent deformation, was performed.

First, it was necessary to create a credible CAD model of the bicycle pedal. The sizing and shape of the CAD model is done on the basis of the European standard EN 14764. The subject of this standard are city and recreational bicycles. The tests covered by this standard are designed to ensure the strength and durability of both individual parts and the bicycle as a whole, requiring consideration of safety aspects and high quality throughout the product development process. The fourth chapter of EN 14764 covers the requirements that are set for all parts of a bicycle and describes the methods for testing them [1]. The test methods are grouped according to a certain principle, and the recommendations for testing the bicycle pedal are included in the methods for testing the pedals and the drive system of this standard.

After creating the CAD model of the bicycle pedal, and before the numerical testing procedure, it was necessary to define the standard material and its characteristics that are necessary to know in the simulation procedure. In the numerical simulation of material fatigue, it is necessary to enter the main characteristics of the material as well as the values of stress and cycles of the S/N curve for a particular material, which is done.

Numerical simulations of material fatigue were performed in two different commercial software, SolidWorks and Ansys. The aim was to show possible deviations of individual parameters of interest, that are life and safety (load) factor and the results of conducted numerical simulations in both software.

2. Fatigue properties and S/N curve

Fatigue properties of materials are often described using the fatigue limit or the S-N curve (fatigue curve, Wöhler curve). The S-N curve describes the relation between cyclic stress amplitude and number of cycles to failure. The figure 1 below shows a S-N curve of 6061-T6 aluminium alloy material which is used for fatigue analysis in this paper [2]. This material was used because it is recommended by Military handbook - metallic materials and elements for aerospace vehicle structures which is standardized for bicycle pedals. On the horizontal axis the number of cycles to failure is given on logarithmic scale. On the vertical axis (either linear or logarithmic) the stress amplitude (sometimes the maximum stress) of the cycle is given.

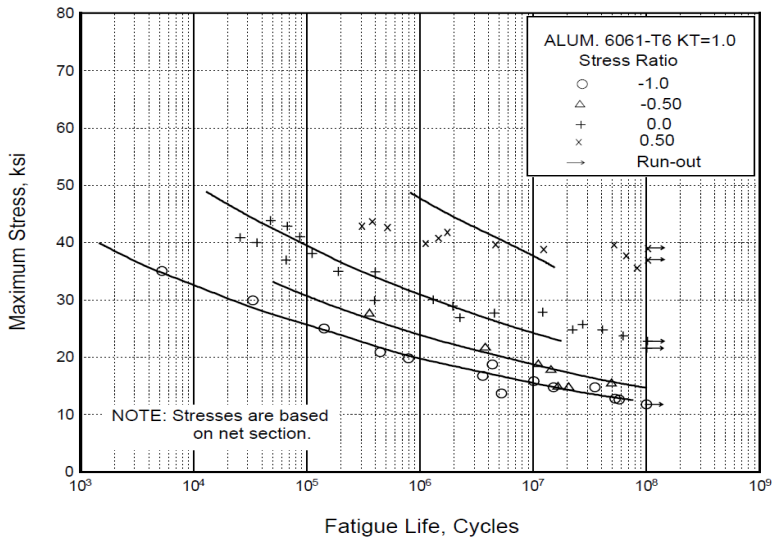

Figure 1. Best-fit S/N curves for unnotched 6061-T6 aluminum alloy, various wrought products, longitudinal direction [2]

S-N curves are derived from fatigue tests. Tests are performed by applying a cyclic stress with constant amplitude on specimens until failure of the specimen. In some cases, the test is stopped after a very large number of cycles (N>10^6). The results are then interpreted as infinite life. In this case, all numerical simulations were performed for 10^6 number of cycles, as it is recommended in the above-mentioned European standard.

Fatigue curves are often given for KT=1 (unnotched specimens) and in the particular case, KT is also 1. Those curves describe the fatigue properties of a material.

3. CAD model for numerical simulations

As mentioned earlier, all parameters and dimensions of the model used in the numerical simulations were taken on the basis of the European standard. When creating the CAD model used for numerical simulations in both software, it was important to create the surfaces of importance and define the main basic dimensions of the model. A credible model of a bicycle pedal has been created, the shape of which corresponds to standard pedals, which has curves and places intended for stress reduction (Figure 2).

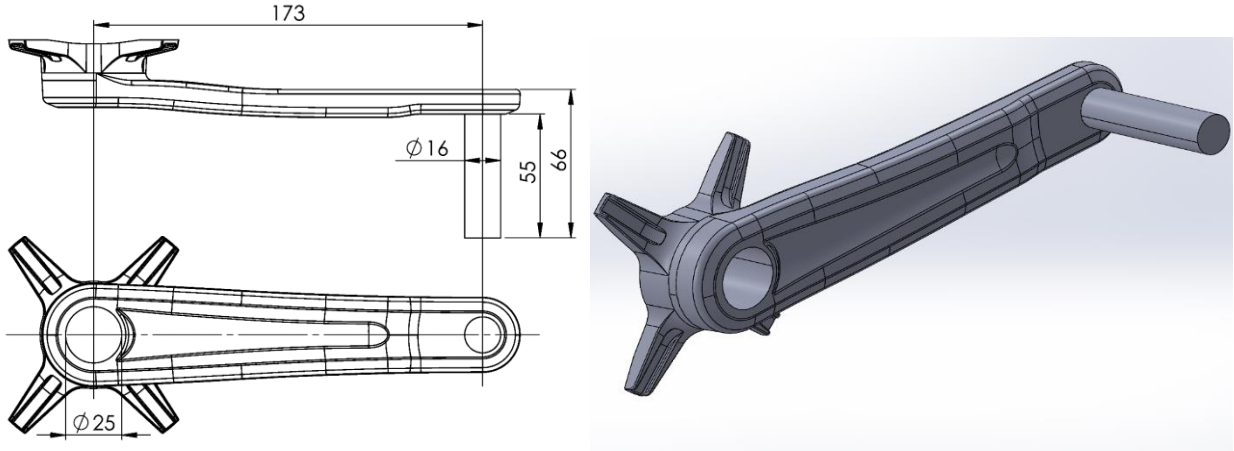

Figure 2. Basic dimension and CAD model of bicycle pedal

The CAD model consists of two parts, a support and a shaft at the end of which a force is applied [3]. The force of the foot is applied on the middle of the support on the foot pedal. The force F, acting on the support, consists of two components, Fy and Fz:

$$Fy=1000N * cos(7,5°)$$
$$Fz=1000N * cos(7,5°)$$

Boundary conditions for both software are the same. When defining boundary conditions, as a precondition for creating a mathematical model, the supports and connections on the model itself are determined. There are two types of supports, fixed and cylindrical support. Cylindrical support was defined on cylindrical face, with no radial movement. The carrier and the shaft to which

the force is applied are connected with bonded connection (Figure 3).

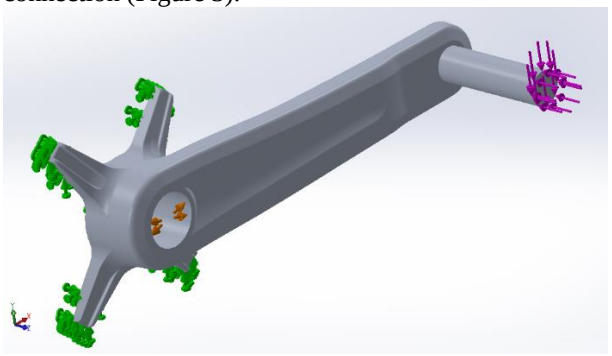

Figure 3. Boundary conditions for mathematical model

After creating of CAD model and boundary conditions for mathematical model, numerical simulations were performed.

4. Numerical simulation in SolidWorks

When creating a mathematical model, before conducting the simulation, it is important to define the material of the part we are examining. As mentioned earlier, the material of the bicycle pedal is 6061-T6 aluminium alloy. The characteristics of its S/N curve and the specific numerical values of the stress and the number of cycles are entered in a table in the material properties dialog box. Parameters like elastic modulus, Poisson's ratio, shear modulus, mass density, tensile strength etc., were defined (Figure 4) [4].

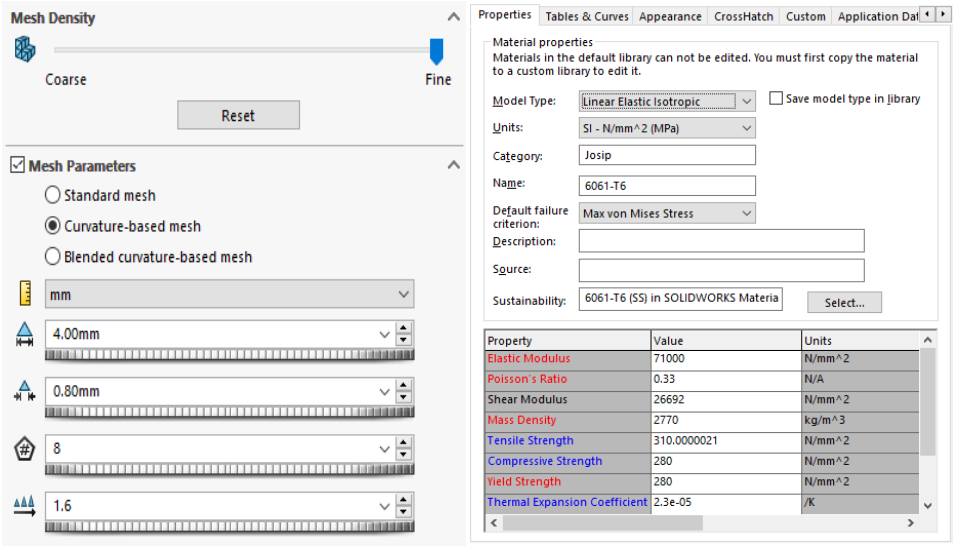

Figure 4. Defining material parameters and mesh parameters in SolidWorks

The next step is to create a mesh. For a specific simulation, SolidWorks has created an automatic mesh of the finest quality. Some parameters were manually corrected (Figure 5). The size of the basic elements is 4 mm. The sizes of the elements are specially defined in two characteristic places, namely at the transition between the shaft and the support, the size of 1 mm, and on the cylindrical surfaces of the pedal and the cylinder joint, the size of 2 mm (Figure 5).

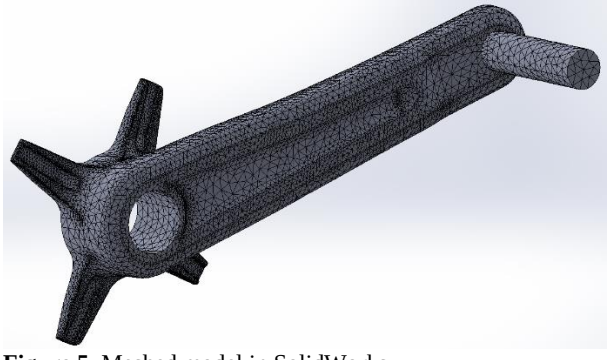

Figure 5. Meshed model in SolidWorks

Curvature-based method of mesh creation was used in SolidWorks, and default options of 8 elements in the circle and 1,6 ratio of element growth were applied. A tetrahedral mesh of 167167 nodes and 107501 elements was created.

5. Numerical simulation in Ansys

An automatic mesh has been created in the Ansys software, by an automatic mesh has been created in the Ansys software, by default. The shape of the elements is automatically selected. Element order is quadratic, element size is 4 mm, like in SolidWorks software. Resolution is default, transition is slow and smoothing is medium (Figure 6) [5].

The mesh is combination of tetra, hex and wedge elements (TET10, HEX20 i WED15). 193206 nodes and 128877 elements were created (Figure 7).

Details of "Mesh"	
Display	
Display Style	Use Geometry Setting
Defaults	
Physics Preference	Mechanical
Element Order	Quadratic
Element Size	4, mm
Sizing	
Use Adaptive Sizi...	Yes
Resolution	Default (2)
Mesh Defeaturing	Yes
Defeature Size	Default
Transition	Slow
Span Angle Center	Medium
Initial Size Seed	Assembly
Bounding Box Di...	259,36 mm
Average Surface ...	96,792 mm²
Minimum Edge L...	3,3427e-003 mm

Quality	
Check Mesh Qua...	Yes, Errors
Error Limits	Standard Mechanical
Target Quality	Default (0.050000)
Smoothing	Medium
Mesh Metric	Aspect Ratio
Min	1,1733
Max	40,372
Average	2,1129
Standard Devi...	0,94237
Inflation	
Advanced	
Statistics	
Nodes	193206
Elements	128877

Figure 6. Defining material parameters and mesh parameters in Ansys

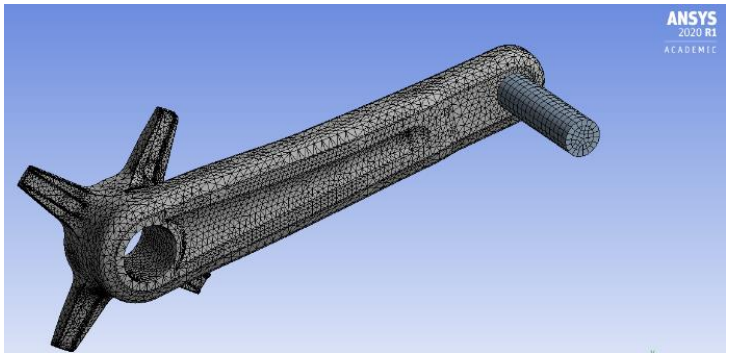

Figure 7. Meshed model in Ansys

6. Simulation results

Three characteristic faces (face A, B and C) and three points (1, 2 and 3) were determined on the CAD model, and results of performed simulations in both software were compared in these six characteristic parameters (Figure 8). On these surfaces, only maximum and minimum values were showed [6].

In both software, classical static stress analyses were performed, where the results of Von Mises stresses were obtained. Conducted static analyses are a prerequisite for numerical simulation of material fatigue. In both simulations, as mentioned in the introduction, results were obtained for three factors: life, damage and safety (load) factor.

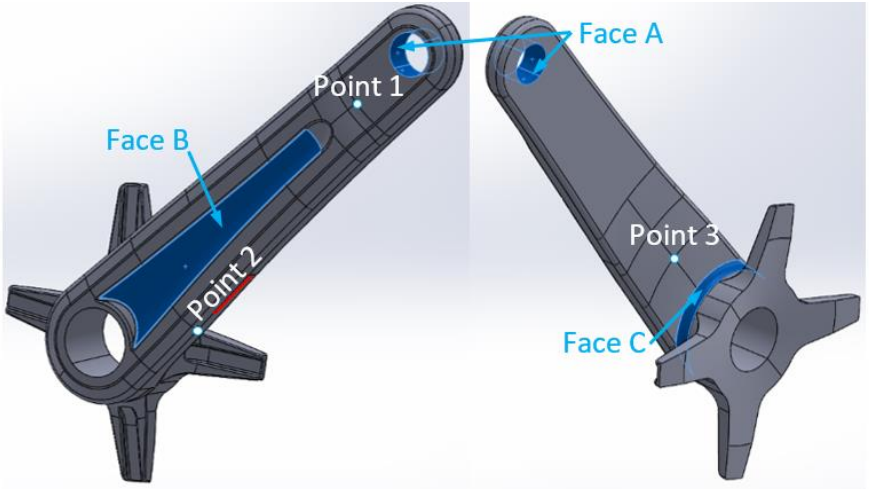

Figure 8. Characteristic faces and points on the CAD model

By SolidWorks definition, parameters of interest are:

- Life - Available only when the fatigue study is defined with one event. Shows the number of cycles (for constant amplitude event studies) or the number of blocks (for variable amplitude studies) that cause fatigue failure at each location. The plot is based on SN curves and the alternating stress at each location. A block is the full load history of a variable amplitude event (including the number of repeats).
- Load factor - Available only when the fatigue study is defined with one event. Shows the load factor of safety for fatigue failure at each location. A load factor of safety of 3.5 at a location indicates that the defined fatigue event will cause fatigue failure at this location if you multiply all loads defined for the static study by 3.5.

After the simulations were performed, results for these three parameters were visualized (Figure 9).

By Ansys definition, three parameters of interest are:

- Life - This result contour plot shows the available life for the given fatigue analysis. If loading is of constant amplitude, this represents the number of cycles until the part will fail due to fatigue. If loading is non-constant, this represents the number of loading blocks until failure. Thus, if the given load history represents one month of loading and the life was found to be 120, the expected model life would be 120 months. In a constant amplitude analysis, if the alternating stress is lower than the lowest alternating stress defined in the S-N curve, the life at that point will be used.

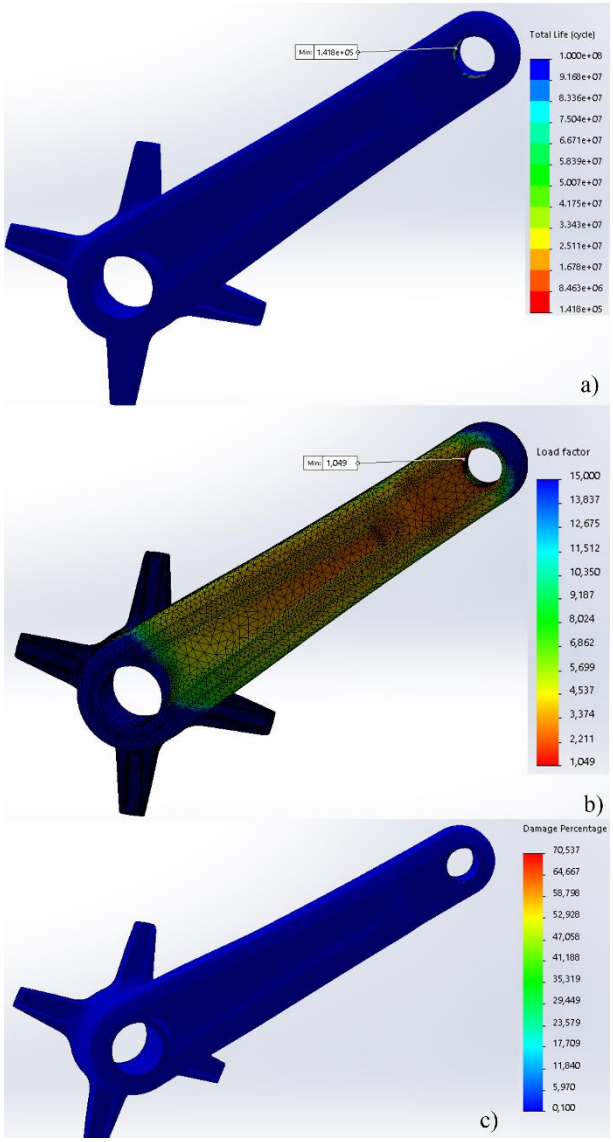

Figure 9. Results for life (a), load factor (b) and damage (c) in SolidWorks

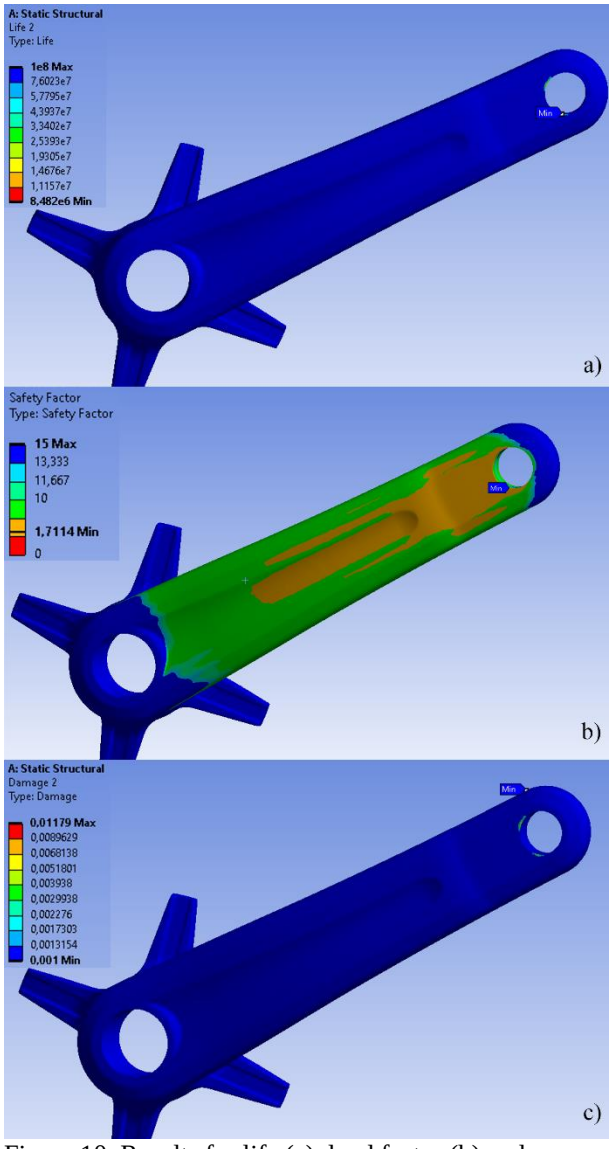

Figure 10. Results for life (a), load factor (b) and damage (c) in Ansys

– Safety factor - This result is a contour plot of the factor of safety (FS) with respect to a fatigue failure at a given design life. The maximum FS reported is 15.

These are the steps at each node to calculate Safety Factor:

1. Calculate the alternating and mean stress tensor.
2. Collapse alternating and mean stress from tensor to scalar using selected stress component.
3. Calculate Safety Factor from the mean stress equation using Seqv as queried from the SN curve for the design life.

Life and damage parameters are the same by definitions, and load and safety factors are different by definition, but we can assume that those two parameters are very similar, and those results are also showed in table 1, [7].

Table 1. Results of performed simulations in both software

	VonMises stress / Mpa		Life cycles		Safety (load) factor	
	Ansys	SW	Ansys	SW	Ansys	SW
Face A	210,38	251,23	8,48E+06	1,42E+05	1,7114	1,049
Face B	100,57	100,99	1,00E+08	1,00E+08	3,58	2,609
Face C	137,03	137,19	1,00E+08	1,00E+08	2,6275	1,92
Point 1	104,01	103,73	1,00E+08	1,00E+08	3,4615	2,54
Point 2	45,121	45	1,00E+08	1,00E+08	7,9795	5,855
Point 3	52,096	52,16	1,00E+08	1,00E+08	6,9111	5,052

7. Conclusion

The procedure of preparation of CAD and mathematical model for the mentioned simulations was done in the same way. So, the dimensions and geometry of the model are identical. The main difference in the implementation of the procedure of numerical simulation of material fatigue in these two simulations is that the meshes are created automatically with both software. The main finite element parameters are the same. In the process of testing parameters of importance, which are life, damage and load (safety) factor, the difference occurs in the algorithm for solving the third parameter, where in the end the results on characteristic surfaces and points also differed significantly. For the first two parameters, the results are equal apart from the results on the edge on the face A. It is concluded that these results deviations are mesh dependent, and even that the location is possible singularity so no further efforts were made to obtain better results agreement at the face A.

The further testing should be based on performing a practical experiment based on which the percentage deviation of the results from the nominal values should be established. Certainly, when it is impossible to use an experiment, performed numerical simulations are a good platform for scientific research.

REFERENCES

[1] European Parliament and of the Council, (2005), EN 14764:2005, City and trekking bicycles - Safety requirements and test methods, EU

[2] MIL-HDBK-5H, (1998), Military handbook, metallic materials and elements for aerospace vehicle structures, USA

[3] Porča A., (2018), Numerička analiza uticaja zamora materijala na sigurnost rama bicikla u skladu sa en 14764, Mašinski fakultet u Zenici, Zenica, BiH

[4] Dassault systemes, (2021), SolidWorks Help

[5] Ansys, Inc., (2021), Ansys Help, USA

[6] Chetan N. Madivalar1a, Tony Shay, Shreedhar Kolekar, (2018), Fatigue failure analysis of bike crank arm using solidworks simulation, Journal of Mechanical Engineering Research and Developments (JMERD), Michigan University, USA

[7] Ansys, Inc., (2020), Evaluating Fatigue on a Bicycle Frame, Webinar, USA

ISSN 1847-7917

Application of heat treatment in wear protection for working parts of agricultural machinery

Ivan VIDAKOVIĆ[1)]***, Goran HEFFER***[1)]***, Katica ŠIMUNOVIĆ***[2)]***, Goran ROZING***[1)]

1) University of Osijek, Faculty of Agrobiotechnical Sciences Osijek, Vladimira Preloga 1, 31000 Osijek, **Croatia**
2) University of Slavonski Brod, Mechanical Engineering Faculty in Slavonski Brod, Trg Ivane Brlić Mažuranić 2, 35000 Slavonski Brod, **Croatia**
3) University of Osijek, Faculty of Electrical Engineering, Computer Science and Information Technology Osijek, Kneza Trpimira 2b, 31000 Osijek, **Croatia**

ividakovic@fazos.hr
gheffer@fazos.hr
ksimunovic@unisb.hr
grozing@ferit.hr

Original scientific paper

Abstract: In this paper, the results of investigating the wear by abrasive particles with different velocities of the samples made of C45 steel in the normalized state, and samples of the same steel subjected to quench hardening as well as boronizing. As an abrasive in the experiment, a soil sample with a sandy loam texture label was applied. The research was conducted with the aim of determining the best application of the above-mentioned heat treatment procedures of wear protection on agricultural machinery. During the exploitation of agricultural machinery, the working parts of machines and tools for tillage are exposed to the different types of wear. The most dominant wear mechanism is abrasion, which occurs due to the direct contact of the working surfaces of the tool with the soil particles. This wear is manifested by a change in the shape of the working parts, which causes a decrease in the efficiency of machines thus requiring frequent renewal of worn parts and increased maintenance costs of agricultural machinery. The research proved a significantly lower wear of samples subjected to quench hardening as well as boronizing compared to steel in the normalized state, thus proving the justification of the application of these treatments as wear protection of parts of agricultural machinery.

Keywords

Boronizing
Normalization
Quench hardening
Steel C45
Wear by abrasive particles

1. Introduction

Material wear can be found in various segments of the economy, especially those that incorporate mechanical systems or machinery with movable working parts. The negative consequences of wear other than a significant loss of material are also observable in significant financial costs related to the frequent maintenance and repair of worn parts [1]. Because of the significant financial costs, the processes of material wear are constantly being researched with the aim of better understanding the problem and finding ways to save money by applying various wear protection measures. Material wear by soil particles can be found on numerous machines and devices with working parts in direct contact with soil particles during exploitation. Parts of agricultural, construction, or mining machinery are most often exposed to this form of wear, [1] and [2].

Agricultural tillage machinery is exposed to various forms of wear during the exploitation. The wear of the material by abrasive particles is the most significant part of the overall forms of wear. Thereby, the basic mechanism of wear is abrasion. The working parts of tools such as plows, disc harrows, harrows, cultivators, etc. that are in direct contact with soil particles during operation are most exposed to this type of wear. The most common abrasive in the soil is quartz along with some other modifications of silicon dioxide. Also, various metal oxides with abrasive effects on the surface of tillage tools can be found in the soil (e.g., calcium, iron, aluminum oxides, etc.). The surface of the material is exposed to wear during exploitation due to sliding and impact of soil particles, which cause marks of abrasion on the tool surface as a mixture of different forms – stripes, grooves, and scratches. The authors [1] state that the process of indenting abrasive particles and the mechanism of material removal is based on particle size and morphology, where round and polyhedral particles cause gradual abrasion wear, while sharp-edged particles cause material cutting. This difference can lead to distinct wear characteristics and material separation mechanisms. The presented form of wear is limited to the tool surface only and does not affect the inner layers of the material. The abrasive wear can cause various consequences, but the most prominent include the change in the geometric shape and the mass loss of the working parts of the tool (e.g., blade). The change in the geometric shape of the blade leads to poor performance quality and higher fuel

consumption [3], which ultimately results in lower performance of the working unit.

The intensity of material wear by soil particles is affected by soil properties, material properties, and tool velocity. The research of the abrasive wear was in most cases conducted during the application of certain working parts, i.e., tools in exploitation due to the specific conditions of exploitation. Most of the research tried to tackle finding possible protection measures against the wear, development, and application of different materials of tool parts with pronounced wear resistance and different designs of working parts, which mainly aimed to reduce the area in contact with the ground. Based on the research [4] and [5] it can be stated that the life cycle of tillage tools depends on wear and abrasion characteristics of materials due to problems associated with the interaction of tool surfaces with soil. The basic requirements when choosing materials for the working parts of the tool include high resistance to abrasion wear and high surface hardness in the range of 38 – 45 HRC.

Carbon steels for hardening and tempering with more than 0.5% of carbon (e.g., C45, C60, Č1730) are mainly used in the production of tillage tools. In the standard (normalized) state, these carbon steels have the appropriate technological properties required for making the tools, while in quench-hardened and tempered state, they possess the satisfactory wear resistance [6]. In this case, all tool parts are made of the same material that provides the optimal ratio of performance properties and cost. On the surfaces that are exposed to the increased wear (tool blades), protection measures are applied, which mostly consist of different technological processing procedures that change the structure of the working surface of the tool's base material, thus improving its wear resistance. Regarding that, various procedures are applied, which can generally be divided into procedures for changing the structure of the working surface material and procedures for changing the type of the working surface material of the tool. The most commonly used are hardfacing processes [3] and processes of hard coating [7], followed by thermal processes [8] and thermo-reactive diffusion techniques [9] as well as thermal chemical processes [10].

The aim of the present research is to determine if the application of quench hardening and boronizing (thermal-chemical treatment) is justified in the protection of tillage tools from wear in the abrasive environment.

2. Materials and methods

The justification for the application of quench hardening and boronizing (thermal-chemical treatment) for protecting the working parts from wear in the abrasive environment was determined by laboratory research of wear on appropriate samples. The wear resistance was defined by measuring the mass loss of samples.

2.1. The material

The samples were made of C45 steel (Č1531), cylindrical in shape, Ø 20 x 40 mm in size, shown in Figure 1. This steel belongs to the group of non-alloy or low-alloy structural steel for hardening. By quench hardening and high tempering (> 500°C), this steel achieves adequate yield strength, tensile strength, and toughness [11]. This structural steel with increased carbon content (0.42 – 0.52%) in its normalized or hardened and tempered state is used for the manufacture of medium strength machine parts, e.g., shafts, bearing drawn cups, piston rod, etc. By quench hardening and thermal-chemical processes (case-hardening, nitriding, boronizing) the wear resistance is improved, so it can be used to make parts that will be exposed to mild wear. The samples were finely ground to prepare the surface so that it has minimal roughness and unevenness, otherwise this could lead to uneven wear.

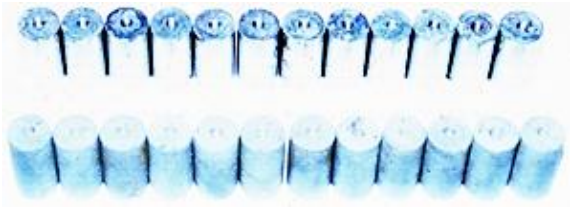

Figure 1. Samples of the material used in the experiment

After the grinding procedure, the cross-section surface hardness was measured in three replications for each sample by Shimadzu Microhardness Tester Type M. Also, the microstructural analysis was performed by metallographic microscope Olympus GX51F-5 with digital camera DP25 and software for image analysis.

The normalized state is the delivery condition by the steel manufacturer. The measured hardness of the samples in such a state ranged from 207 to 210 HB. Figure 2 presents the ferrite-perlite microstructure of the C45 steel in the normalized state.

The quench-hardened state is a conventional (common) process for tillage tools, as most such tools (plow blades, harrow discs, cultivator hoes, etc.) are subjected to quench hardening prior to exploitation, which increases the hardness and wear resistance of these working parts.

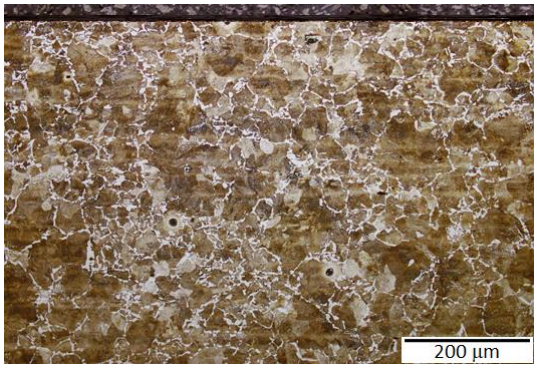

Figure 2. Microstructure of the C45 steel in the normalized state

The quench hardening process was carried out in the workshop for the heat treatment of tools in the "Unior" company in Vinkovci by heating in the electric furnace at 850°C, followed by quenching in room-temperature water. This procedure was used to achieve martensitic microstructure along the entire sample cross-section. The measured surface hardness of the samples ranged from 601 to 626 HB. The martensitic microstructure of a quench hardened sample is presented in Figure 3.

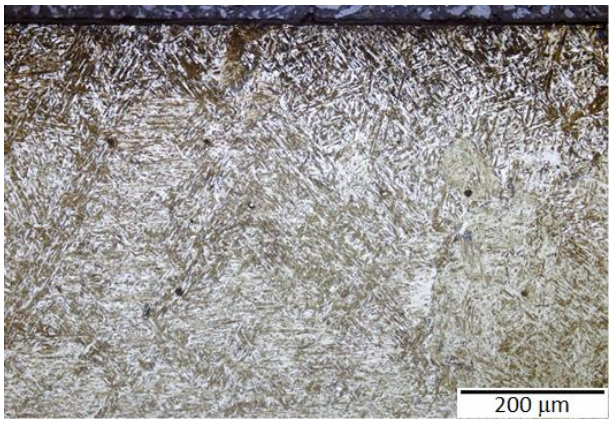

Figure 3. Microstructure of the quench hardened C45 steel

Boronized state was obtained by the boronizing process in the laboratory of the Department of Heat Treatment and Surface Engineering at the Faculty of Mechanical Engineering and Naval Architecture in Zagreb. The boronizing process consisted of heating the samples in "Ekabor 3" granulate at a temperature of 1000°C for four hours, after which the samples were air-cooled.
The boronizing process created a hard boron layer, 65 – 135 µm thick, with average measured microhardness values of about 1320 HV0.2. The base material retained a lower microhardness value of about 270 HV0.2 in the area below the transition zone. The microstructure of boronized C45 steel is presented in Figure 4.

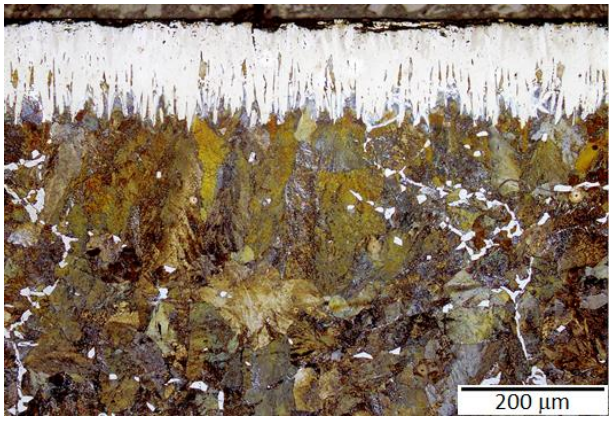

Figure 4. Microstructure of the boronized C45 steel

A clearly visible hard boron layer can be observed in contrast to the base material. "Jagged" parts of the boronized layer in the transition zone can also be observed.

2.2. Wear experiment

The method used in the experiment was the simulation of the wear process of the sample during its motion in the abrasive (soil particles) at specified kinematic parameters. The wear process took place in a specifically constructed tribometer within the appropriate wear system (tribosystem). During the operation of the device, the wear process largely corresponds to the actual tillage conditions, while ensuring the change of the same conditions in accordance with the experiment design [12]. The motion of the sample in the experiment was circular, with the sample immersed in the abrasive throughout the experiment. The abrasive was loosened before each passage of the sample due to its homogeneity and for preventing the formation of permanent traces within the abrasive, which could change wear conditions. The device was constructed at the Department of Agricultural Engineering and Renewable Energy Sources at the Faculty of Agrobiotechnical Sciences Osijek according to [13] and [14]. The schematic representation of the device is provided in Figure 5.

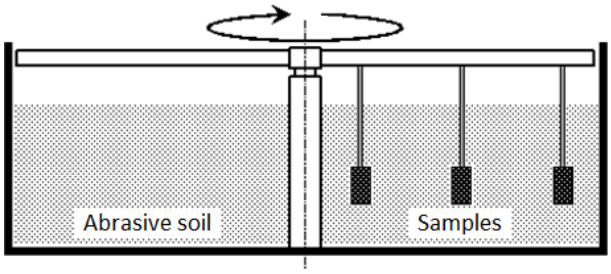

Figure 5. Schematic representation of the wear device in the abrasive

This device, designed for measuring wear of the sample in the abrasive environment, enables:

- The simulation of the wear process of materials of different qualities
- The application of different types of abrasives in the amount required to perform the experiment
- The selection of various kinematic parameters of the motion of the sample
- Designing and replicating the experiment for the statistical processing of the results
- Simultaneous testing of multiple samples under the equal experiment conditions.

2.3. The abrasive used in the experiment

In the wear experiment, which was conducted in this research, it is possible to use different types of soil as an abrasive. After selecting the type of soil, it is necessary to perform a pedological analysis of the soil to accurately determine its composition and texture. The selected soil

type should also be prepared for laboratory use by a specific research method. In this research, a soil sample of sandy loam texture, which was taken from the arable layer at a depth of 30 cm, was used as an abrasive. Pedological analysis, conducted at the Department of Pedology of the Faculty of Agriculture in Zagreb, found that there is approximately 65% of sand in the mechanical composition of the soil sample. The mechanical composition of the soil used in the experiment is presented in Table 1.

Table 1. Mechanical composition of the abrasive used in the experiment

Particle size, [mm]	Share, %	Particle type
2.0 – 0.2	11.5	coarse sand
0.2 – 0.05	53.5	fine sand
0.05 – 0.02	4.6	silt
0.02 – 0.002	18.4	silt
< 0.002	12.0	clay

For the wear test, the soil was brought to a loose state (2 mm, fine) by manual crushing of lumps, air drying, and sieving. The moisture of the soil was measured immediately before and after the wear test and ranged from 1.2 to 1.6%.

2.4. Experiment parameters

The samples of the material in the wear experiment move in the abrasive at a selected velocity and simultaneously reach a certain total wear rate.

The velocities of the sample were selected at approximately the appropriate velocity for conducting agrotechnical operations with tillage tools under operating conditions [15] and [16]. The applied velocities in this study are presented in Table 2.

Table 2. Sample velocity

Velocity	m/s	km/h
v_1	1.0	3.6
v_2	2.0	7.2
v_3	3.0	10.8

The total wear rate of the sample was determined per the assumption of abrasiveness of the soil in which the experiment was performed, the performance indicators of the wear of tillage tools, and similar previously conducted research [7] and [9]. It was set to 50.000 meters.

2.5. Identifying mass loss

Identifying the total wear rate of the sample was performed by measuring the loss of mass of the sample after reaching the total wear rate. The mass loss of the sample represents the difference between the mass of the sample in the initial state (before the wear experiment) and after the wear experiment. The sample's mass was measured by an analytical balance Adam PW 124, with the accuracy of 10^{-4} grams and a measurement interval of 0 – 120 grams, in the Laboratory of Phytopharmacy at the Department of Phytomedicine, Faculty of Agrobiotechnical Sciences Osijek. Before each measurement, the samples were thoroughly cleaned with acetone, rinsed in water, and dried in stream of warm air.

3. Research results

In order for the analysis to be objective, the wear experiment of the samples in the abrasive environment was performed in three replications for each condition, which was determined by the material's microstructure and the velocity of the sample. Table 3 and Figure 6 show the average mass losses of the samples after three replications for each material at all velocities.

Table 3. Average mass losses of the samples and dispersion measures of results

Velocity [m/s]	Mass loss [g]	Material sample condition		
		Normalized	Quench hardened	Boronized
1.0	Average	0.0456	0.0095	0.0093
	SD	0.0026	0.0008	0.0007
	CV [%]	5.7116	8.3258	7.6014
2.0	Average	0.0579	0.0165	0.0113
	SD	0.0044	0.0010	0.0005
	CV [%]	7.5348	6.2869	4.3951
3.0	Average	0.3380	0.0442	0.0216
	SD	0.0202	0.0016	0.0012
	CV [%]	5.9651	3.5144	5.3591

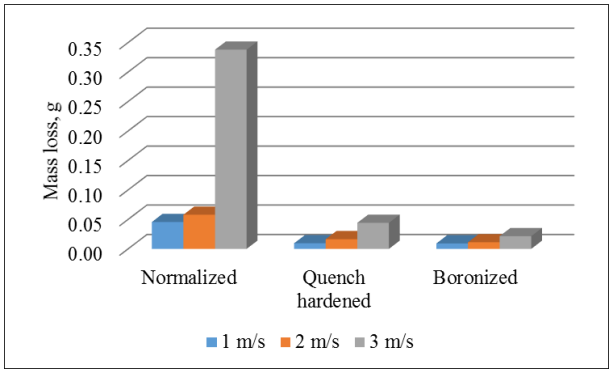

Figure 6. Diagram representation of the average mass loss of the samples

Based on the research conducted on the wear resistance of samples in the normalized, quench hardened, and boronized state by motion in the abrasive environment, the following was determined:

By comparing the mass loss in samples in the normalized, quench hardened and boronized state, a significantly lower mass loss was observed in quench hardened and boronized samples. This indicates that the heat treatment of quench hardening and thermal-chemical treatment of boronizing increase the wear resistance in motion in the abrasive environment multiple times compared to the samples in the normalized state.

By analyzing the average mass losses according to Figure 6 and Table 3, the mass loss in the normalized state at a sample velocity of 1 m/s was 4.8 (0.0456/0.0095) times higher than the mass loss of the quench hardened sample and 4.9 (0.0456/0.0093) times higher than the mass loss of the boronized sample. At a sample velocity of 3 m/s, the difference in the mass loss is even more pronounced, so the mass loss of the normalized samples is 7.6 (0.3380/0.0442) times higher than the mass loss of the quench hardened sample and 15.6 (0.3380/0.0216) times higher than the mass loss of the boronized sample. By comparing the mass loss of the quench hardened sample and boronized sample, the mass loss of the quench hardened sample at a sample velocity of 1 m/s was 1.02 (0.0095/0.0093) times higher than the mass loss of the boronized sample, i.e. the similar mass losses occurred. The increase in velocity of the samples led to an increase in the difference in mass loss, so at the sample velocity of 3 m/s, the mass loss of the quench hardened sample was 2.04 (0.0442/0.0216) times higher than the mass loss of the boronized sample.

4. Conclusion

The research confirmed that thermal and thermal-chemical treatments of steel can significantly improve its wear resistance in motion in the abrasive environment. This result indicates that the application of these procedures is fully justified.

The comparison of the mass loss of individual material states (microstructures) found that the quench hardened and boronized samples have significantly higher wear resistance in the abrasive environment compared to the normalized sample, while the boronized sample has higher wear resistance in relation to the quench hardened sample.

The results of the research indicate that in all samples, the mass loss increases with velocity, which in the practical application of agricultural machinery indicates that the wear of working parts of tillage tools increases with increasing their working velocity.

This research indicates the need to continue the investigation of the problem with better preparation and control of the experiment, application of other wear-resistant materials, and better statistical processing of the results for the scientific proof of the influence of certain factors (sample velocity, impact angle, abrasive granulation) on the wear process of agricultural tillage machinery.

REFERENCES

[1] Narayanaswamy, B., Hodgson, P., Beladi, H., (2016), *Effect of particle characteristics on the two-body abrasive wear behaviour of a pearlitic steel*, Wear 354-355, p 41-52 Netherlands

[2] Ivušić, V., (1998), *Tribologija*, Hrvatsko društvo za materijale i tribologiju, Zagreb

[3] Singh Kang A., Singh G., Singh Cheema, G., (2017), *Improving wear resistance via hardfacing of cultivator shovel*, Materials Today: Proceedings, 4 No. 8, p 7991-1999 Netherlands

[4] Heffer G., Vujčić M., (1996), *Čimbenici trošenja poljoprivredne mehanizacije pri obradi tla*, „Aktualni zadaci mehanizacije poljoprivrede", Opatija

[5] Bhakat A.K., Mishra A.K., Mishra N.S., (2007), *Characterization of wear and metallurgical properties for development of agricultural grade steel suitable in specific soil conditions*, Wear 263, p 228-233 Netherlands

[6] Novosel M., Krumes D., (1998), *Posebni čelici*, Sveučilište Josipa Jurja Strossmayera u Osijeku, Strojarski fakultet u Slavonskom Brodu, Slavonski Brod

[7] Heffer G., Samardžić I., Schauperl Z., Vidaković I., (2018), *Wear of Induction Cladded Coating in the Abrasive Mass at Various Speeds and Impact Angles*, Technical Gazette 25 No. 6, p 1776-1782 Croatia

[8] Mann P.S., Brar N.K., (2015), *Tribological aspects of agricultural equipments: a review*, International Research Journal of Engineering and Technology 2 No. 3, p 1704-1708 India

[9] Heffer, G., Šimunović, K., Samardžić, I., Vidaković, I., (2020), *Effect of Speed and Impact Angle on Solid Particle Erosion of Vanadium Carbide Coatings Produced by Thermo-Reactive Diffusion Technique*, FME Transactions, 48 No. 3, p 497-503 Serbia

[10] Bartkowski D., Młynarczak A., Goscianski M., (2012), *The effect of diffusion boriding on durability of the agricultural tools used in the soil*, Archives of Mechanical Technology and Automation 32 No. 4, p 7-14 Poland

[11] Kožuh S., (2010), *Specijalni čelici*, Sveučilište u Zagrebu, Metalurški fakultet, Sisak

[12] Heffer G., (1995), *Utjecaj brzine gibanja i mikrostrukture materijala na abrazijsko trošenje česticama tla*, Magistarski rad, Sveučilište u Zagrebu, Fakultet strojarstva i brodogradnje, p 77.

[13] Vinogradov V.N., Sorokin G.M., Kolokolnikov M.G., (1990), *Abrazivnoe iznašivanie*, Mašinostroenie, Moskva Russia

[14] Yu, H.-J., Bhole, S.D., (1990), *Development of a prototype abrasive wear tester for tillage tool*

materials, Tribology International 23 No. 5, p 309-316 Netherlands

[15] Kareem K.I., Sven P., (2019), *Effect of Ploughing Depth, Tractor Forward Speed, and Plough Types on the Fuel Consumption and Tractor Performance*, Polytechnic Journal 9 No.1, p 43-49 Iraq

[16] Mattetti M., Varani M., Molari G., Morelli F., (2017), *Influence of the speed on soil-pressure over a plough*, Biosystems Engineering 156, p 136-147 Netherlands

ISSN 1847-7917

The influence of chloride concentration end electrolyte temperature on CuAlMnZn alloy corrosion in NaCl solution

Ladislav VRSALOVIĆ[1)]***, Senka GUDIĆ***[1)]***, Radosna JERČIĆ***[1)]***, Ivana IVANIĆ***[2)]***, Stjepan KOŽUH***[2)]***, Mirko GOJIĆ***[2)]

1) University of Split, Faculty of Chemistry and Technology, Ruđera Boškovića 35, 21000 Split, **Croatia**
2) University of Zagreb, Faculty of Metallurgy, Aleja narodnih heroja 3, 44000 Sisak, **Croatia**

ladislav@ktf-split.hr
sgudic@ktf-split.hr
radosna.jercic@gmail.com
iivanic@simet.hr
kozuh@simet.hr
gojic@simet.hr

Keywords

CuAlMnZn
corrosion
polarization
microscopy

Original scientific paper

Abstract: The objective of this study was to investigate the influence of chloride ion concentration (from 0.1 to 1.5%) and temperature (from 20 to 40 °C) on corrosion behavior of CuAlMnZn alloy in NaCl solution stirred with a magnetic stirrer (150 rpm). Electrochemical techniques such as open circuit potential measurement, linear, potentiodynamic polarization and cyclic voltammetry methods have been applied. The results have been shown that increase in concentration and temperature of NaCl solution leads to a lowering open circuit potential values of alloy, increase in corrosion current density and a decrease in values of the polarization resistance. After polarization measurements, corroded electrode surfaces, were examined with an optical microscope.

1. Introduction

Copper and its alloys are one of the significant metal construction materials of extensive use. A special group of copper alloys consists of the so-called Shape Memory Alloy (SMA) alloys, which can be plastically deformed at lower temperatures to return to their original shape by exposure to elevated temperatures.

Copper-based shape memory alloys present an alternative to NiTi alloys due to their excellent thermal and electrical properties, easier production and lower price [1-3]. The corrosion behavior of copper alloys significantly depends on the electrolyte composition in contact with the alloy surface and the alloying elements present in Cu-alloys, the method of alloy production, and subsequent thermal treatment. The most common alloying elements found in alloys with a copper-based shape are aluminum, nickel, manganese, and zinc. The presence of zinc in the Cu-Al-Mn alloy with shape recollection significantly lowers the temperature of martensite formation. The amount of Zn or the Mn: Zn ratio plays a significant role in controlling the temperature of the phase transitions [4]. From the corrosion resistance aspect, aluminum is one of the alloying elements that increase the corrosion resistance of copper alloys due to forming a protective layer of Al_2O_3, together with Cu_2O, which is rapidly formed on the surface exposed to the corrosive environment. The formation of these stable passive layers on Cu-Al alloys is mainly due to the higher affinity of aluminum for oxygen and the more significant stability of Al_2O_3 compared to Cu_2O [5-7]. The presence of manganese as an alloying element in Cu-alloys affects the crystal grain size and the mechanical and corrosion properties of alloys. Namely, Mn is easily and quickly dispersed through the mass of the alloy and accumulates at the grain boundaries and thus prevents further grain growth. Investigations have shown that such refining of the microstructure leads to improved mechanical properties and increases alloys' corrosion resistance [6-8].

Due to their wide application, these alloys can interact with various aggressive media that often contain chloride ions resulting in corrosion processes. As chloride ions represent one of the most common corrosion agents in nature, in this paper, we investigated the corrosion behaviour of an alloy of CuAlMnZn composition of 11% Al, 3.4% Mn, 3.2% Zn, the rest of Cu, obtained by continuous casting, in NaCl solution.

Symbols

E_{OC}	- open circuit potential, V	R_p	- polarization resistance, kΩ cm^2
E_{corr}	- corrosion potential, V	*wt.%*	- weigh percentage
i_{corr}	- corrosion current density, μA cm^{-2}		

2. Experimental procedure

CuAlMnZn alloy of composition (wt.%) 11% Al, 3.4% Mn, 3.2% Zn, rest Cu, was produced by melting technically pure components in a vacuum induction furnace in argon protective atmosphere and then by continuous vertical casting according to the procedure described in more detail in the work of Vrsalović and associates [9]. This process yielded 8 mm diameter alloy rods, from which small cylindrical specimens were obtained by cutting, which were joined by soldering to insulated copper wires. After soldering and ultrasonic cleaning of the solder joint in ethanol, the samples were placed in appropriate silicone molds into which a polyacrylate mixture was poured to insulate the samples. In this way, electrodes were made on which further electrochemical measurements were performed. The non-insulated base of the cylindrical alloy roller was the working surface of the electrode, which was treated by grinding with water-sanding papers of different gradation (up to P 2500) using a grinding and polishing device Metkon Forcipol 1V. After grinding, the alloy surface was polished on the same device using a suitable fabric on which a polishing suspension (alumina) was applied with particle size of 0.5 μm. The electrode was then ultrasonically cleaned in ethanol for 3 minutes and in deionized water for 2 minutes to remove residual fine particles from its surface. Electrochemical investigations were performed in 0.1, 0.5, 0.9 and 1.5% NaCl solution which were prepared by weighing the calculated mass of NaCl on an analytical balance and then dissolving with deionized water in a 1-liter volumetric flask. The appropriate pH of the solution (pH = 7.4) was adjusted by precise dosing of 0.1 mol dm^{-3} NaOH solution using a pH meter Seven Multi manufactured by Metler Toledo, Switzerland.

The electrochemical studies were carried out in a double wall termostated glass electrochemical cell at 20 °C, 30 °C and 40 °C. The electrochemical methods used were open-circuit potential, linear, potentiodynamic and cyclic polarization measurements using an EG&G PAR Model 273A Potentiostat/Galvanostat, coupled to a computer. The volume of electrolyte for each experiment was 200 ml. An Ag/AgCl electrode, connected to the solution through a Luggin capillary, was used as reference, and a Pt-sheet of geometric area 4.5 cm^2 was used as the auxiliary electrode.

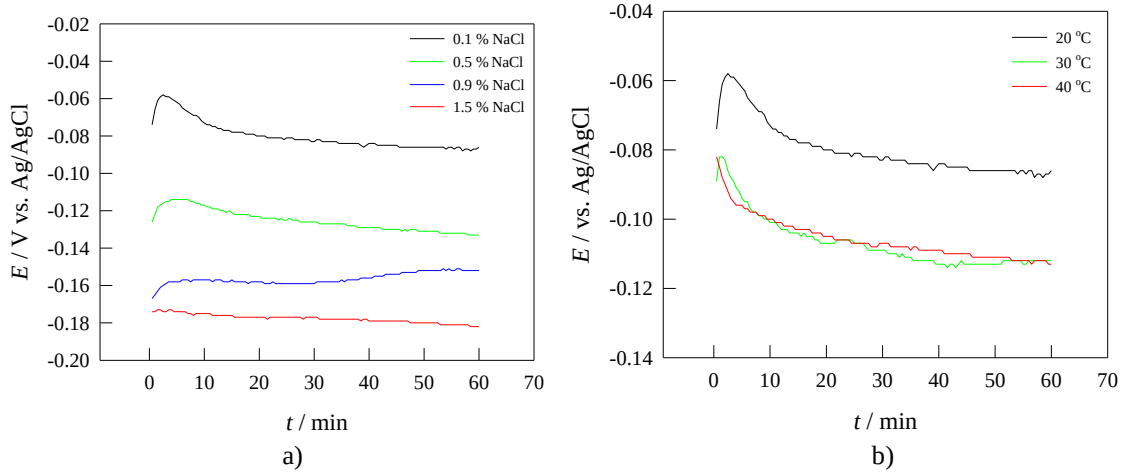

Figure 1. Open circuit potential changes for CuAlMnZn alloy in different concentration of NaCl solution (a), and in 0.1 % NaCl solution at different temperatures (b)

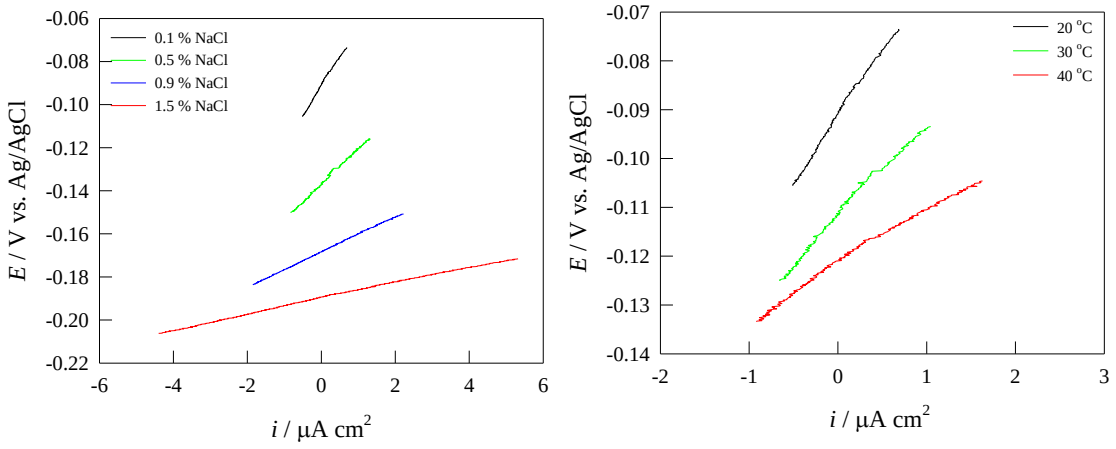

a) b)

Figure 2. Linear polarization measurements for CuAlMnZn alloy in different concentration of NaCl solution (a), and in 0.1 % NaCl solution at different temperatures (b)

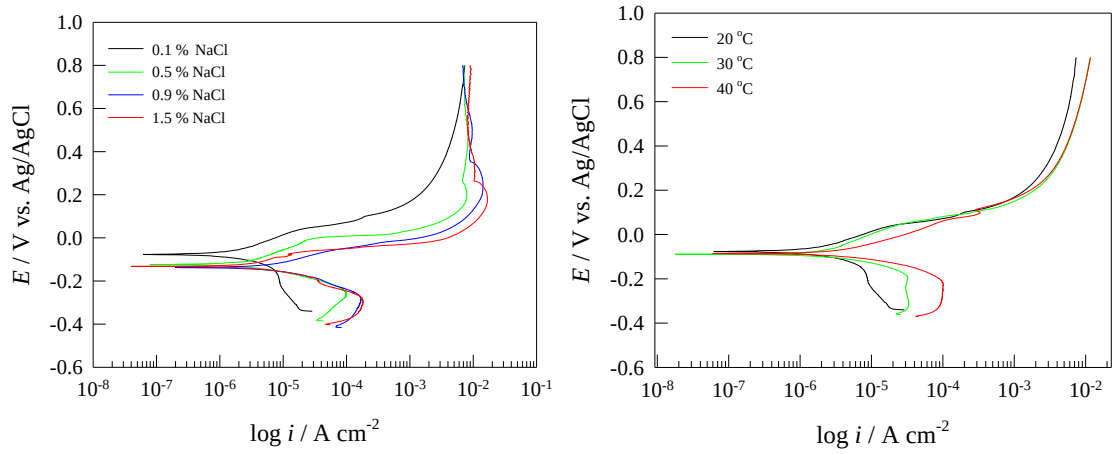

a) b)

Figure 3. Potentiodynamic polarization measurements for CuAlMnZn alloy in different concentration of NaCl solution (a), and in 0.1 % NaCl solution at different temperatures (b)

3. Results and discussion

Changes in the value of the open circuit potential (E_{OC}) with time for CuAlMnZn alloy in NaCl solution of different concentration and temperature are shown in Figure 1a and 1b. The investigations were performed by recording the potential value every 10 seconds for a period of 60 minutes.

It can be noted that there are significant differences in the results related to the immersion potential as well as the steady-state one, which is related to the concentration of chloride ions and electrolyte temperature. At higher NaCl concentration, the potential decay is noticed at the four different NaCl concentrations analysed. This decay is probably explained in terms of the dissolution of copper oxide film naturally formed into the air once Cu is the primary element in the alloy composition.

After E_{OC} measurement, the linear polarization method was performed in a narrow range of potentials (±20 mV) with the scan rate of 0.2 mVs^{-1}, in order to determine the value of the polarization resistance, and the results are shown by Figure 2 and Table 1.

Table 1. Values of corrosion parameters determined from potentiodynamic polarization measurements

Solution / temperature °C	E_{corr} V	i_{corr} μA cm^{-2}	R_p kΩ cm^2
0.1 % NaCl; 20 °C	-0.072	1.49	27.356
0.5 % NaCl; 20 °C	-0.108	2.92	16.535
0.9 % NaCl; 20 °C	-0.118	3.70	8.230
1.5 % NaCl; 20 °C	-0.177	5.35	3.652
0.1 % NaCl; 30 °C	-0.084	1.91	19.295
0.1 % NaCl; 40 °C	-0.086	4.88	11.350

Presented results in Figure 2 as well as the calculated values of polarization resistance (Table 1) show the negative impact of increasing chloride ion concentration and electrolyte temperature on the corrosion resistance of the material, which can be shown as a decrease in the slope of linear curves.

Figure 3 present the polarization curves obtained in different concentration of NaCl solution and different temperature of electrolyte. The potentiodynamic polarization plots were recorded at 0.25 mVs^{-1}, starting from the -250 mV from E_{OC} to the final positive value (+800 mV). The parameters extracted from the curves in Figure 3 are listed in Table 1.

A significant difference in the values of cathodic current densities is visible in the investigation with the lowest NaCl concentration, while the values of cathodic current densities at higher NaCl concentrations are similar. Increasing the concentration of NaCl solution significantly affects the values of anodic current densities, which increase highly with increasing concentration of chloride ions, similar to the polarization investigation performed with CuAlNi alloy [10]. The most significant difference in the anodic parts of the curve can be observed in measurements with 0.1% and 0.5% NaCl solution. In contrast, in investigations with higher concentrations of chloride ions, this difference is smaller.

Thus, the initial part of the anode curve for CuAlMnZn alloy, when tested in 0.1% NaCl solution immediately after the corrosion potential, has the steepest slope, which decreases with increasing chloride ion concentration due to more intense anodic dissolution. After the area with a steeper slope, there is an area with a much smaller slope in which a relatively significant increase in current is visible with a relatively small change in potential, which shows that in this area, there are a continuous dissolution of Cu in the form of Cu (I) ions. The third area is the area of relatively high anode current densities.

In the case of anodic curves for CuAlMnZn alloy in 0.5, 0.9 and 1.5% NaCl solution, the appearance of an anode current maximum is visible, the value of which is higher with the higher concentration of chloride ions. After reaching the maximum, there is a slight decrease in the anodic current densities due to the formation of a layer of corrosion product on the electrode surface which creates additional resistance to the dissolution of the alloy. This phenomenon was observed by examining the corrosion behaviour of other shape memory Cu-alloys such as CuAlNi, CuAlMn, and CuAlAg [7,9-12]. However, in contrast to the above and previously investigated alloys, in the case of CuAlMnZn alloy, this decrease in the anodic current density is less pronounced, which indicates that the layer of corrosion products is less bound to the alloy surface or has higher solubility compared to corrosion products formed on CuAlNi and CuAlMn alloys.

Values of corrosion parameters determined from potentiodynamic polarization curves and linear polarisation curves were shown in Table 1.

It can be seen that with the increase of the electrolyte concentration, there is a shift of the corrosion potential towards negative values as well as an increase of the corrosion current density and decrease of polarization resistance values, which also occurs with the rise of the electrolyte temperature.

Figure 4 shows the cyclic voltammograms for CuAlMnZn alloy in NaCl solutions of different concentrations, at 20 °C. The tests were performed on electrodes that had been pre-machined by grinding and polishing and sonicated in ethanol and deionized water. Measurements were performed in a wide potential range from -1.2 V to 1.2 V with a potential change rate of 10 mV s^{-1}. It can be seen that with an increase in the concentration of chloride ions, there is a significant increase in the values of the current density.

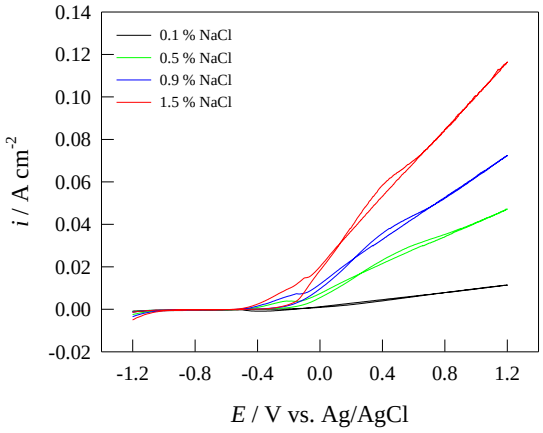

Figure 4. Cyclic polarization curves for CuAlMnZn alloy in different concentration of NaCl solution

After potentiodynamic polarization measurements, the surface of the CuAlMnZn electrode was examined using an optical microscope to determine its degree of corrosion. The test results are shown in Figure 5 after potentiodynamic polarization in 0.1 % and 1.5 % NaCl at 20 °C, while Figure 6 shows alloy surface after measurements at 30 and 40 °C.

Figure 5 a), which shows the surface of the CuAlMnZn electrode after polarization measurement in 0.1% NaCl solution, clearly shows the grain boundaries of the alloy as if the surface had been etched with a suitable etching solution. This indicates the appearance of general surface corrosion, and slight point damages which are a consequence of a localized form of pitting corrosion. Increasing the concentration of chloride ions leads to more intense corrosion of the CuAlMnZn alloy surface, which is visible in Figure 5 b), where small cracks and grooves on the surface formed by the corrosion process can be seen. Rising the temperature of the 0.1 mol dm^{-3} NaCl solution leads to greater surface damage (Figure 6). The high number of small pits is clearly visible at Figure 6 a), and raising the temperature leads to their growth and interconnection into larger pits (Figure 6 b). For a more detailed insight into the corrosion and the elementary composition of the surface, it would be necessary to make an SEM/EDS analysis, which will be done in further investigations.

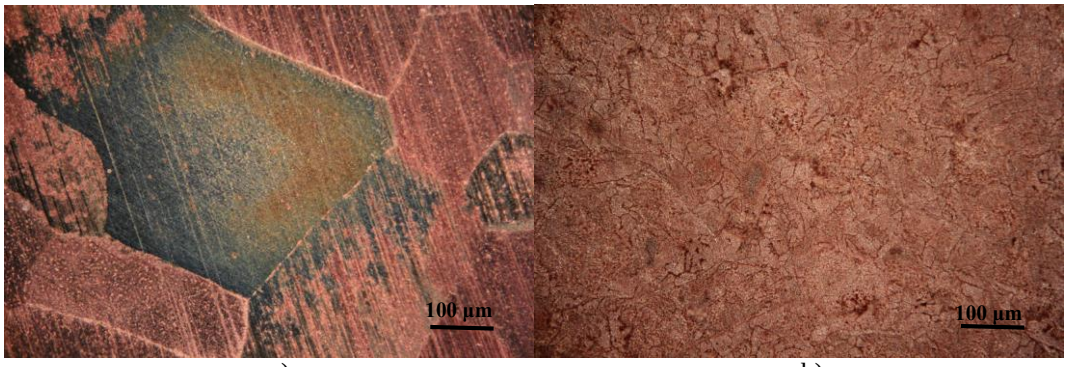

a) b)

Figure 5. The surface of CuAlMnZn alloy after polarisation measurement in 0.1 % NaCl (a) and 1.5 % NaCl solution at 20 °C (b)

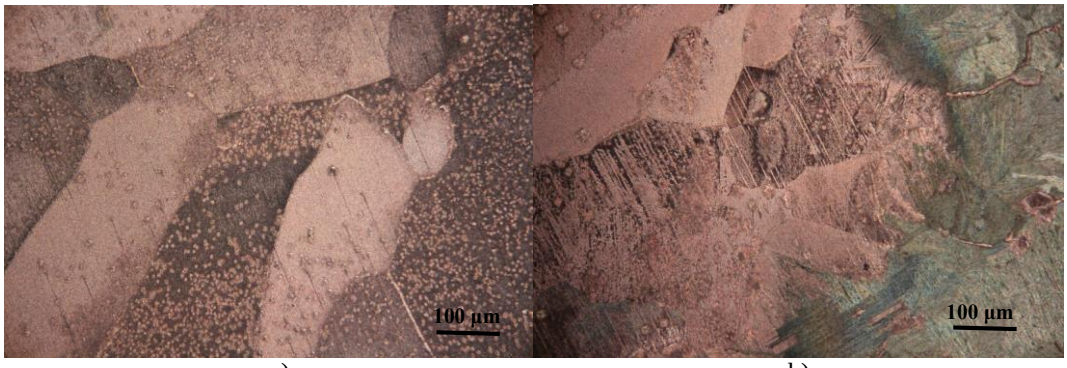

a) b)

Figure 6. The surface of CuAlMnZn alloy after polarisation measurement in 0.1 % NaCl at 30 °C (a) and 40 °C (b)

4. Conclusions

- The open-circuit potential of CuAlMnZn alloys shift towards negative values with increasing chloride ion concentration and increasing electrolyte temperature.
- Polarization resistance values decrease with increasing chloride ion concentration and increasing electrolyte temperature.
- Potentiodynamic polarization measurements have shown that an increase in electrolyte concentration leads to a significant increase in anode current densities and thus to an increase in corrosion current, and an increase in electrolyte temperature has a similar effect.
- Cyclic voltammograms for CuAlMnZn alloy in different concentrations of NaCl solutions show that with increasing concentration of chloride ions, there is a significant increase in current density, which indicates a more intense electrode reaction.
- Examinations of the electrode surface with an optical microscope after potentiodynamic polarization measurements showed that increasing the concentration of chloride ions leads to more intense corrosion of the CuAlMnZn alloy surface.

REFERENCES

[1] Saud Al-Humairi S. N., (2019), Cu-Based Shape Memory Alloys: Modified Structures and Their Related Properties, DOI: 10.5772/intechopen. 86193

[2] Ivanić I., Gojić M., Kožuh S., (2014), *Slitine s prisjetljivosti oblika (I. dio): najznačajnija svojstva*, Kem. Ind. 63 No. 9-10, p 323-330.

[3] Ivanić I., Gojić M., Kožuh S., (2014), *Slitine s prisjetljivosti oblika (II. dio): podjela, proizvodnja i primjena*, Kem. Ind. 63 No. 9-10, p. 331-344.

[4] Dasgupta R., (2014), *A look into Cu-based shape memory alloys: Present scenario and future prospects*, Journal of Materials Research, 29 No. 16, p 1681-1698.

[5] Shaik M. A., Syed K. H., Golla B. R., (2019), *Electrochemical behavior of mechanically alloyed hard Cu-Al alloys in a marine environment*, Corros. Sci., 153, p 249-257.

[6] Saud S. N., Hamzah E., Abubakar T., Bakhsheshi-Rad H. R., (2015), *Correlation of microstructural and corrosion characteristics of quaternary shape*

memory alloys Cu-Al-Ni-X (X=Mn or Ti), Trans. Nonferrous Met. Soc. China 25 No. 4, p 1158-1170.

[7] Gojić M., Vrsalović L., Kožuh S., Kneissl A., Anžel I., Gudić S., Kosec B., Kliškić M., (2011), *Electrochemical and microstructural study of Cu-Al-Ni shape memory alloy*, J. Alloys Compd. 509, p 9782-9790.

[8] Moghaddam A. O., Ketabchi M., Bahrami R., (2013), *Kinetic grain growth, shape memory and corrosion behavior of two Cu-based shape memory alloys after thermomechanical treatment*, Trans. Nonferrous Met. Soc. China, 23 No. 10, p 2896−2904.

[9] Vrsalović L., Ivanić I., Kožuh S., Kosec B., Bizjak M., Kovač J., Gabor U., Gojić M., (2019), *Influence of heat treatment on the corrosion properties of CuAlMn shape memory alloys*, Corros. Rev. 37 No. 6, p 579-589.

[10] Vrsalović L., Ivanić I., Čudina D., Lokas L., Kožuh S., Gojić M., (2017), *The influence of chloride ion concentration on the corrosion behavior of the CuAlNi alloy*, Tehnički glasnik / Technical Journal. 11 No. 3, p 67-72.

[11] Vrsalović L., Ivanić I., Kožuh S., Gudić S., Kosec B., Gojić M., (2018), *Effect of heat treatment on corrosion properties of CuAlNi shape memory alloy*, Trans. Nonferrous Met. Soc. China, 28 No. 6, p 1149−1156.

[12] Benedetti A. V., Sumodjo P. T. A., Nobe K., Cabot P. L., Proud W. G., (1995), *Electrochemical studies of copper, copper–aluminium and copper–aluminium–silver alloys: impedance results in 0.5 M NaCl*, Electrochim. Acta 40, p 2657–2668.

ISSN 1847-7917

Influence of pulse current arc welding modes on changing the parameters of the weld and HAZ of welded joints made by low alloyed materials

Anatoliy ZAVDOVEEV[1] ***Massimo ROGANTE***[2], ***Valeriy POZNYAKOV***[1], ***Mark HEATON***[3], ***Thierry BAUDIN***[4], ***Alexander GAYVORONSKI***[1], ***Yuriy DEMCHENKO***[1], ***and Serj ZHDANOV***[1]

1) Paton Electric Welding Institute of the NAS of Ukraine, 03150 Kyiv, **Ukraine**
2) Rogante Engineering Office, Contrada San Michele n. 61, I-62012 Civitanova Marche, **Italy**
3) ANT, Advanced Nano Technology, Nandor Rd, Park West Business Park, Dublin, **Ireland**
4) Université Paris-Saclay, CNRS, Institut de chimie moléculaire et des matériaux d'Orsay, 91405 Orsay, , **France**

avzavdoveev@gmail.com
main@roganteengineering.it
mark.heaton@antsltd.com
thierry.baudin@universite-paris-saclay.fr

Keywords

Pulsed current gas metal arc welding
thermal cycles of welding
heat affected zone
low-alloyed welding materials

Original scientific paper

Abstract: Pulsed current gas metal arc welding (PC-GMAW) is characterized by periodically changing arc power and, thanks to its features, it allows solving complex technological issues in the creation of unique designs, and increasing the productivity of welding processes and surfacing corrosion-resistant alloys on steel. Many manufacturers of welding equipment, presently, have implemented the idea of impulse welding in their production. The data on the influence of PC-GMAW on thermal cycles of welding (TCW), however, are scattered and therefore it is difficult to compare with thermal cycles of welding characteristic for continuous current gas metal arc welding. During welding of high-carbon steels, the task is to reduce the mixing of the weld metal with the base metal and to increase the resistance of welded joints to the formation of cold cracks. For the successful application of PC-GMAW in solving the above-mentioned problems, it becomes necessary to compare the effect of pulse current gas metal arc welding regimes on the parameters of welds, heat affected zone (HAZ) and TCW with continuous current gas metal arc welding made with low-alloyed welding materials. This has been the main goal of the research, the results of which are reported in the present paper.

1. Introduction

Pulse-current gas metal arc welding (PC-GMAW) is qualitatively different from traditional shielded gas metal arc welding (GMAW), as well as from manual arc welding with modulated current [1-7]. This process is increasingly used in the manufacture of welded structures of aluminum alloys, titanium and structural steels with a strength of up to 500 MPa [8,9], as well as wire arc additive manufacturing [10,11]. This is explained by the fact that PC-GMAW expands the possibilities of controlling the processes of melting and transfer of the electrode metal in different spatial positions, improves the formation of seams, reduces the mixing of the electrode metal with the base metal and the size of the heat affected zone (HAZ) [7], [12-17]. This is due to the fact that such well-known companies as Fronius (Austria), Bohler (Germany), ESAB (Sweden) and others, pay considerable attention in their activities to the development and manufacture of equipment for the implementation and expansion of pulse-arc welding process. Much less in the technical literature is the question of the influence of the parameters of PC-GMAW [18,19] on the thermal processes occurring in the HAZ metal of welded joints, and how they affect the structure and mechanical properties of this metal [20], its resistance to cold cracking and brittle fracture, etc. It is the uncertainty of these issues that constrains the use of pulse-arc welding technologies in the manufacture of metal structures from steels that are sensitive to thermal processes and prone to hardening.

2. Materials and methodology

To solve this problem, we performed surfacing of the high-alloy welding wire 1.2 mm diameter G3Si1. The surfacing was carried out on 10 mm thick plates made of 9MnSi5 steel (DIN, wt %: C 0.09, Si 0.5-0.8, Mn1.3-1.7). Surfaces were made from the surfacing plates, which measured the parameters of the seams and the HAZ. Pulse current arc welding ($f \geq 25$ Hz, PC-GMAW) and pulsed arc welding ($f \leq 25$ Hz, PA-GMAW) are distinguished by the frequency of pulses. Using a pulsating arc, the optimal pulsation modes were selected. In this case, the welding mode was as follows: pulse welding current - I_p = 140 A, pause current (base current) was 80% of the pulse current I_p = 112 A;

Symbols

f	- frequency of pulses, Hz	t_p	- pause time, s
I_{av}	- average current of the arc welding, A	U_i, U_p	- arc voltage in the pulse and in the pause, V
Ief	- effective current of the arc welding, A		**Greek letters**
I_p	- pulse welding current, A	δ	- duty cycle
t_i	- pulse time, s	τ	- cooling time

Arc voltage in the pulse is U_i = 22 V, arc voltage in the pause U_p = 18 V, welding speed equal to 15 m/h, while the pulse time t_i and the pause time t_p, as well as the current in the pause and duty cycle varied. To detect HAZ, the metallographic samples were macro etched with chlorine iron. Recording of the welding thermal cycles (WTC) of the HAZ overheating section was performed using a 0.5mm type K thermocouple, installed on the HAZ section, which was heated to a temperature of 1200°C. The following values were selected to assess the effect of pulsed arc welding modes on the weld parameters: I_{av} = 120, 140, 160, 180, 200, 220 A; U = 21, 22, 24, 26, 28, 30 V; V = 15 m/h; shield gas Ar + 18% CO_2. The modes for the automated pulsed arc welding were as above mentioned, with:

$$I_{av} = \frac{I_{pulse} t_{pulse} + I_{pause} t_{pause}}{t_{pulse} + t_{pause}} \quad (1)$$

where I_{av} is the average current of the arc-arc welding, I_{pulse} = 450 A, I_{pause} = 160 A, t_{pulse} and t_{pause} are the pulse duration and pause, respectively. In addition to I_{av}, the effective current of the arc-arc welding also applies:

$$I_{ef} = \sqrt{(1 - \delta) \times I_{pause}^2 + I_{pulse}^2} \quad (2)$$

where δ = duty cycle. Thus, given the above-mentioned parameters of pulsed-arc welding, I_{ef} results almost 25% higher than I_{av} (Figure 1).

Pulse current arc welding ($f \geq 25$ Hz, PC-GMAW, Figure 2) and pulsating arc welding ($f \leq 25$ Hz, PA-GMAW) are distinguished by the frequency of pulses.

Using a pulsating arc, the optimal pulsation modes were selected. In this case, the welding mode was as follows: pulse welding current I_p = 140 A, pause current (base current) = 80% of I_p = 112 A; arc voltage in the pulse U_i = 22 V, arc voltage in the pause U_p = 18 V, welding speed = 15 m/h, while the pulse time t_i, the pause time t_p as well as the current in the pause and duty cycle varied.

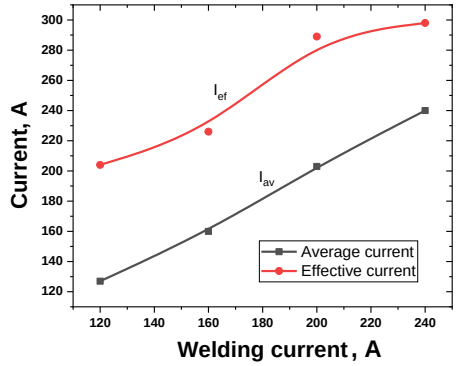

Figure 1. Dependence of the average and effective currents from the welding current at PC-GMAW

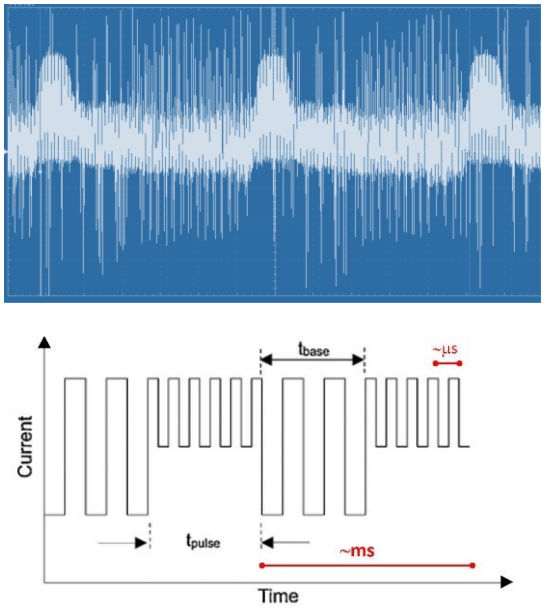

Figure 2. Waveform of pulsed current GMAW: real time oscillogram, and schematic view adapted from [11, 21]

3. Results and discussion

3.1. Pulse current gas metal arc welding (PC-GMAW)

When comparing stationery and PC-GMAW modes, it is clear that in PC-GMAW seam roller is more homogeneous and uniform without traces of spraying [1]. Measurements of metal losses on sputtering showed that in pulse-arc welding it decreases by an order of magnitude, from 0.7% in the stationary process to 0.07% in PC-GMAW.

Analysis of the cross-section of surfacing performed in different modes showed that the depth of penetration in PC-GMAW increases in comparison with the stationary welding process in the same modes (Table 1). The form of seam penetration in PC-GMAW is significantly different from the process performed by a stationary burning arc.

Table 1. Macro samples of surfacing performed in different modes: PC-GMAW (left), GMAW (right)

I = 120 A U = 21 V	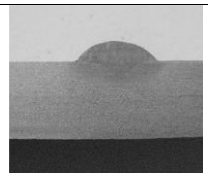	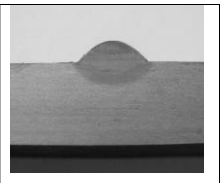
I = 140 A U = 22 V	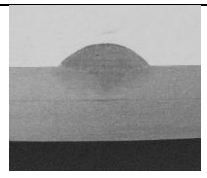	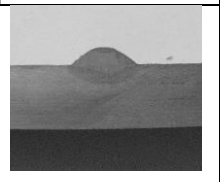
I = 160 A U = 24 V	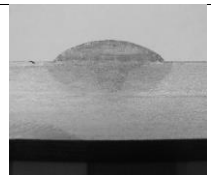	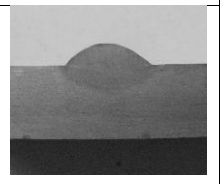
I = 180 A U = 26 V	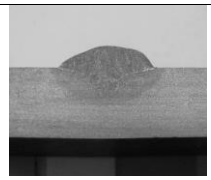	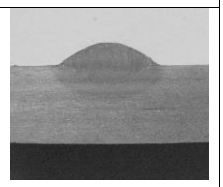
I = 200 A U = 28 V	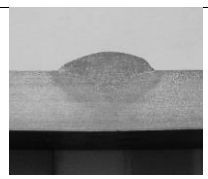	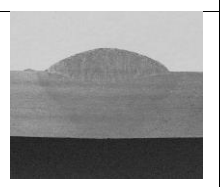
I = 220 A U = 30 V	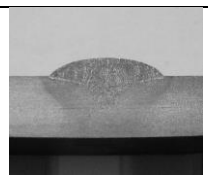	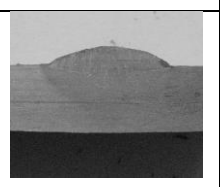

Quantitative analysis showed that with increasing welding current, the width of the seam also increases. The nature of the change of this value is the same for welding with a stationary burning arc, and for PC-GMAW. A similar relationship is observed for the height of the seam. As for the penetration depth, in general, with increasing welding current it increases. But in the case of PC-GMAW, the penetration depth is almost twice as much as in the case of welding with a stationary burning arc (Figure 3). Also, at PC-GMAW, the area of cross section of a seam exceeds the given indicators for welding by a stationary burning arc. The value of HAZ under the root is comparable for both types of welding, and at the root of the HAZ seam during PC-GMAW is less (Figure 3).

3.2. Pulsating arc (PA-GMAW)

According to the experiment, it was found (Figure 4) that with increasing pause current, the width of the seam increases, with a smaller value of duty cycle corresponds to a larger value of the width of the seam. The height of the seam increases evenly with increasing pause current. The change in the penetration depth has similar patterns, i.e. with increasing pause current increases. Changing the parameters of HAZ under the root is monotonous. The less duty cycle corresponds to large values of HAZ width. It is important to note that the average values of HAZ under the root is lower than when welding stationary burning arc (GMAW) (Figure 4). In the PA-GMAW welding mode - pulse current I_{pulse} = 140 A and a pause current I_{pause} = 112 A (fixed pulse time = 0.5 s) with increasing pause time increases the height of the seam, slightly decreases the width of the seam and decreases the width of the HAZ, and the penetration depth at t_p = 0.5 s increases and further practically does not change (Figure 4). In the case of fixing the pause time (0.5 s) and increasing the pulse time, the penetration depth also initially increases and then stabilizes, but confirmation of this fact requires further research. The width of the HAZ changes nonlinearly, and in the case of a fixed pulse time, is less than in the case of GMAW. In the case of fixing the pause time and increasing the pulse time, the width of the HAZ is greater than for PC-GMAW and less than for GMAW.

3.3. Welding thermal cycles

The analysis of welding thermal cycles allowed us establishing the following features: in the case of PC-GMAW, the rate of increase of the metal temperature in the coarse-grained HAZ is greater than in the case of GMAW; in the high-temperature region from 1,350 °C to 1,000 °C (stage I), the cooling of the metal when PC-GMAW occurs faster, and in the temperature range less than 1,000 °C (stage II) is slower (Figure 5). The data show that the cooling rate of the metal in the temperature range of the lowest austenite resistance 600-500 °C (stage III) for PC-GMAW is less than in the case of GMAW, and $\tau_{8/1}$ has close values. The peculiarities of WTC during

PC-GMAW revealed from the graph of the derivative (Figure 5b) made it possible to establish that the cooling rate of the metal at the HAZ sections, which are heated to temperatures of 1.000 °C are higher than during the GMAW.

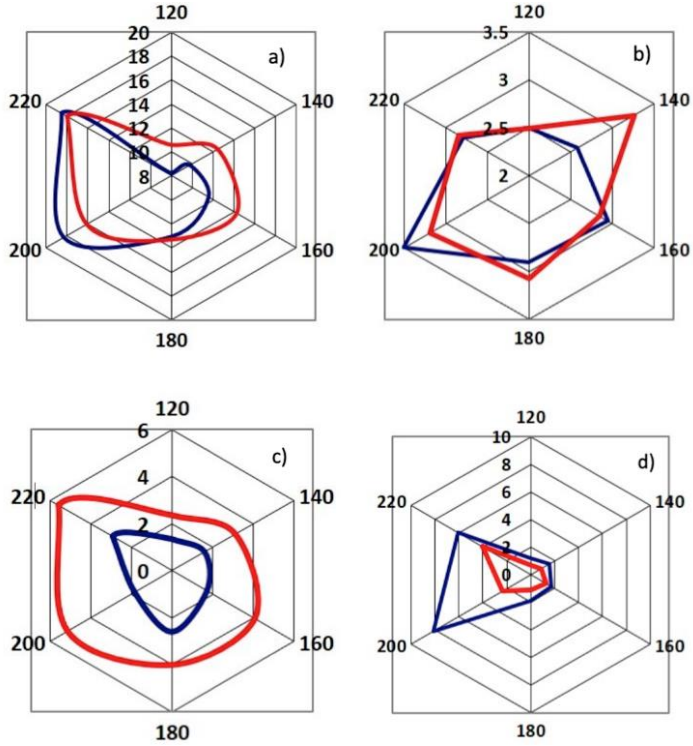

Figure 3. Quantitative characteristics of the parameters of the seams made by GMAW (blue line) and PC-GMAW (red line): a - seam width; b - seam hight; c - penetration deeps; d - HAZ in the root (mm)

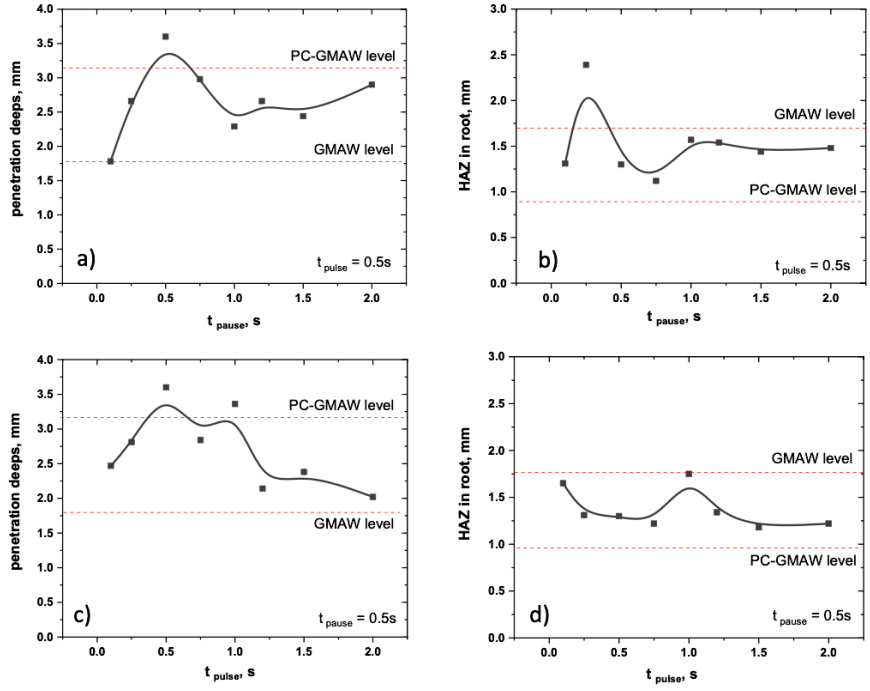

Figure 4. Quantitative characteristics of the seam's parameters made by PA-GMAW

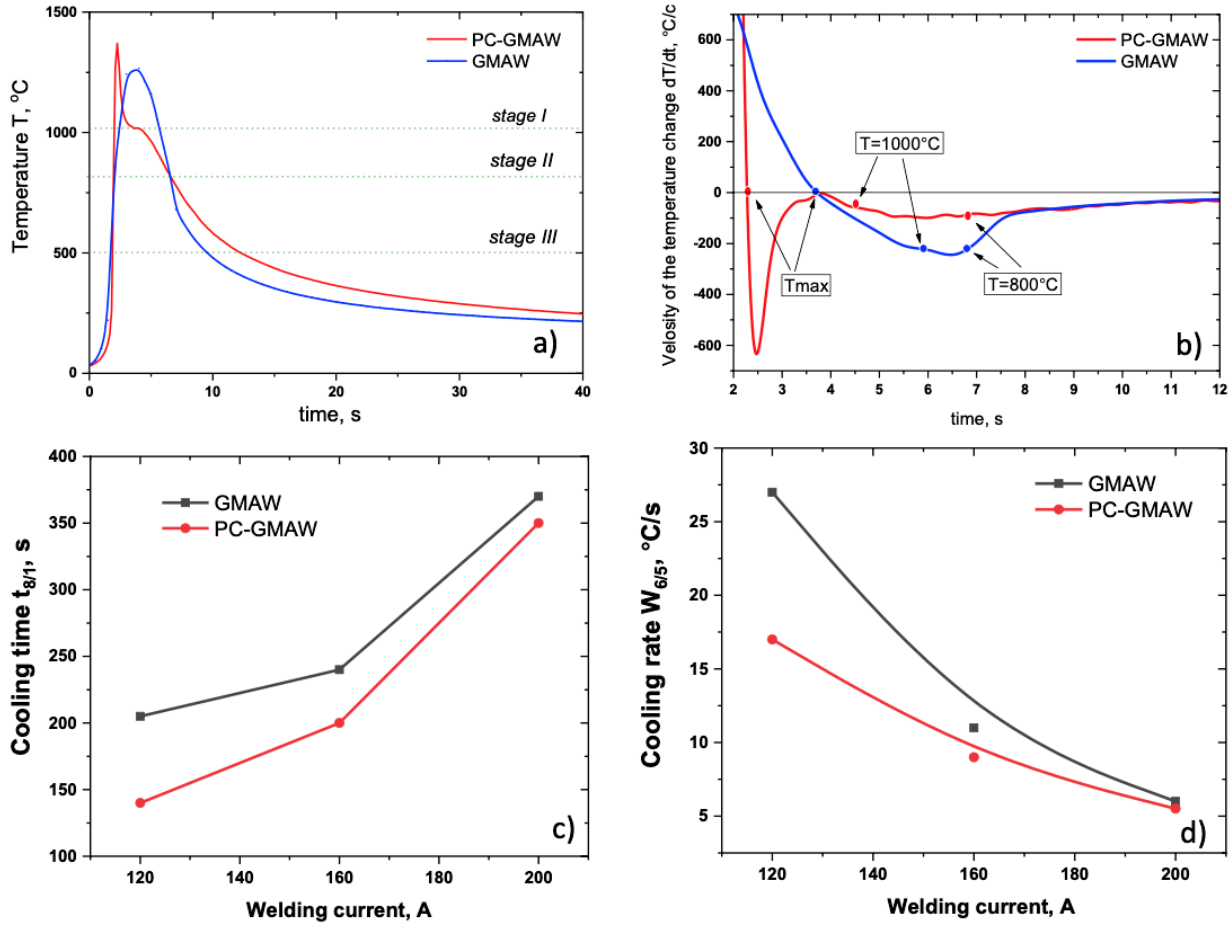

Figure 5. Characteristics of the welding thermal cycle: a – WTC, b – derivative of the WTC, c – cooling time $t_{8/1}$, d – cooling rate $W_{6/5}$

4. Conclusion

PC-GMAW allows reducing the amount of metal spatter and the width of the heat-affected zone, and increasing the penetration depth (almost 2 times) in comparison with GMAW. The cooling rate of the HAZ metal in the temperature range of 600-500 °C is reduced by almost 1.5 times.

The use of PA-GMAW allows increasing the width of the seam and reducing the width of the HAZ in comparison with the GMAW.

The processes of PC-GMAW and PA-GMAW have greater opportunities to control the weld parameters and the amount of heat input, and could be applied in a wide range of manufacturing problems including wire arc additive manufacturing (WAAM).

REFERENCES

[1] Zavdoveev A.V., Denisenko A.M., (2018), Gajvoronsky A.A., Poznyakov V.D., Maksymenko A.A., *Effect of pulsed-arc welding modes on the change of weld metal and haz parameters of welded joints produced with Sv-08kh20N9G7T wire*, Pat. Weld. J. 9, p 7-12 Ukraine https://doi.org/10.15407/tpwj2018.09.02

[2] Palani P.K., Murugan N., (2006), *Selection of parameters of pulsed current gas metal arc welding*, J. Mater. Process. Technol. 172 No.1, p 1-10 Netherlands https://doi.org/https://doi.org/10.1016/j.jmatprotec.2005.07.013

[3] Zavdoveev A., Rogante M., Poznyakov V., Heaton M., Acquier P., Kim H.S., Baudin T., Kostin V., (2020), *Development of the PC-GMAW welding technology for TMCP steel in accordance with welding thermal cycle, welding technique, structure, and properties of welded joints*, Reports in Mechanical Engineering 1 No. 1, p 26-33 Serbia https://www.frontpres.rabek.org/index.php/asd/article/view/3

[4] Tong H., Ueyama T., Harada S., Ushio M., (2001), *Quality and productivity improvement in aluminium alloy thin sheet welding using alternating current pulsed metal inert gas welding system*, Sci. Technol.

Weld. Join. 6 No. 4, p 203-208 United Kingdom https://doi.org/10.1179/136217101101538776

[5] Zavdoveev A.V., Poznyakov V.D., Rogante M., Zhdanov S.L., Kostin V.A., Solomiychuk T.G., (2020), *Features of structure formation and properties of joints of s460m steel made by pulsed-arc welding*, Pat. Weld. J. 6, p 9-13 Ukraine https://doi.org/https://doi.org/10.37434/tpwj2020.06.02

[6] Maruo H., Hirata Y., Nada Y., (1984), *Effects of Welding Current Waveform on Metal Transfer and Bead Formation in Pulsed MIG Welding*, Q. J. Japan Weld. Soc. 2, p 12-18 Japan https://doi.org/10.2207/qjjws.2.12

[7] Rajasekaran S., (1999), *Weld bead characteristics in pulsed GMA welding of Al-Mg alloys*, Weld. J. 78 No. 12, p 397-407 U.S.A. http://files.aws.org/wj/supplement/WJ_1999_12_s397.pdf

[8] Berdnikova O., Pozniakov V., Bernatskyi A., Alekseienko T., Sydorets V., (2019), *Effect of the structure on the mechanical properties and cracking resistance of welded joints of low-alloyed high-strength steels*, Procedia Struct. Integr. 16, p 89-96 Netherlands https://doi.org/10.1016/j.prostr.2019.07.026

[9] Haivorons'kyi O.A., Poznyakov V.D., Markashova L.I., Ostash O.P., Kulyk V.V., Alekseenko T.O., Shyshkevych O.S., (2016), *Structure and mechanical properties of the heat-affected zone of restored railway wheels*, Mater. Sci. 51, p 563-569 Switzerland https://doi.org/10.1007/s11003-016-9876-6

[10] Cunningham C.R., Wikshåland S., Xu F., Kemakolam N., Shokrani A., Dhokia V., Newman S.T., (2017), *Cost Modelling and Sensitivity Analysis of Wire and Arc Additive Manufacturing*, Procedia Manuf. 11, p 650-657 Netherlands https://doi.org/https://doi.org/10.1016/j.promfg.2017.07.163

[11] Cunningham C.R., Flynn J.M., Shokrani A., Dhokia V., Newman S.T., (2018), *Invited review article: Strategies and processes for high quality wire arc additive manufacturing*, Addit. Manuf. 22, p 672–686 Netherlands https://doi.org/https://doi.org/10.1016/j.addma.2018.06.020

[12] Murray P.E., (2002), *Selecting parameters for GMAW using dimensional analysis*, Weld. J. 81, p 125-131 U.S.A. https://app.aws.org/wj/supplement/WJ_2002_07_s125.pdf

[13] Amin A., (1983), *Pulse current parameters for arc stability and controlled metal transfer in arc welding*, Metal Construction 15 No. 5, p 272-278 United Kingdom

[14] Amin M., Ahmed N., (1987), *Synergic control in MIG welding 2—Power-current controllers for steady DC open arc operation*, Metal Construction 19 No. 1, p 331-340 United Kingdom

[15] Lambert J., (1988), *Assessment of the Pulsed MIG technique for tube attachment welding*, Weld. J. 68 No. 2, p 35–43 United Kingdom

[16] Essers W.G., Van Gompel M.R.M., (1984), *Arc control with pulsed GMA welding*, Weld. J. 63 No. 6, p 26-32 U.S.A.

[17] Dorn L., Devakumaran K., Hofmann F., (2009), *Pulsed current gas metal arc welding under different shielding and pulse parameters; Part 2: Behaviour of metal transfer*, ISIJ Int. 49 No. 2, p 261-269 Japan https://www.jstage.jst.go.jp/article/isijinternational/49/2/49_2_261/_pdf

[18] Wu K., Ding N., Yin T., Zeng M., Liang Z., (2018), *Effects of single and double pulses on microstructure and mechanical properties of weld joints during high-power double-wire GMAW*, J. Manuf. Process. 35, p 728-734 Netherlands https://doi.org/https://doi.org/10.1016/j.jmapro.2018.08.025

[19] Sen M., Mukherjee M., Singh S.K., Pal T.K., (2018), *Effect of double-pulsed gas metal arc welding (DP-GMAW) process variables on microstructural constituents and hardness of low carbon steel weld deposits*, J. Manuf. Process. 31, p 424-439 Netherlands https://doi.org/https://doi.org/10.1016/j.jmapro.2017.12.003

[20] Demarque R., Dos Santos E.P., Silva R.S., De Castro J.A., (2018), *Evaluation of the effect of the thermal cycle on the characteristics of welded joints through the variation of the heat input of the austhenitic AISI 316L steels by the GMAW process*, Sci. Technol. Mater. 30 Suppl. 1, p 51-59 Spain https://doi.org/https://doi.org/10.1016/j.stmat.2018.09.001

[21] Wang L., Xue J., (2017), *Perspective on Double Pulsed Gas Metal Arc Welding*, Appl. Sci. 7 No. 9, 894 Switzerland https://doi.org/10.3390/app7090894